HHS Public Access

Author manuscript

Chem Rev. Author manuscript; available in PMC 2023 July 27.

Published in final edited form as:

Chem Rev. 2022 July 27; 122(14): 11900–11973. doi:10.1021/acs.chemrev.1c00914.

Second and Outer Coordination Sphere Effects in Nitrogenase, Hydrogenase, Formate Dehydrogenase, and CO Dehydrogenase

Sven T. Stripp,
Freie Universität Berlin, Experimental Molecular Biophysics, Berlin 14195, Germany

Benjamin R. Duffus,
University of Potsdam, Molecular Enzymology, Potsdam 14476, Germany

Vincent Fourmond,
Laboratoire de Bioénergétique et Ingénierie des Protéines, Institut de Microbiologie de la Méditerranée, Institut Microbiologie, Bioénergies et Biotechnologie, CNRS, Aix Marseille Université, Marseille 13402, France

Christophe Léger,
Laboratoire de Bioénergétique et Ingénierie des Protéines, Institut de Microbiologie de la Méditerranée, Institut Microbiologie, Bioénergies et Biotechnologie, CNRS, Aix Marseille Université, Marseille 13402, France

Silke Leimkühler,
University of Potsdam, Molecular Enzymology, Potsdam 14476, Germany

Shun Hirota,
Nara Institute of Science and Technology, Division of Materials Science, Graduate School of Science and Technology, Nara 630-0192, Japan

Yilin Hu,
Department of Molecular Biology & Biochemistry, University of California, Irvine, California 92697-3900, United States

Andrew Jasniewski,
Department of Molecular Biology & Biochemistry, University of California, Irvine, California 92697-3900, United States

Hideaki Ogata,
Nara Institute of Science and Technology, Division of Materials Science, Graduate School of Science and Technology, Nara 630-0192, Japan; Hokkaido University, Institute of Low Temperature Science, Sapporo 060-0819, Japan; Graduate School of Science, University of Hyogo, Hyogo 678-1297, Japan

Markus W. Ribbe

Corresponding Author: Sven T. Stripp – Freie Universität Berlin, Experimental Molecular Biophysics, Berlin 14195, Germany; sven.stripp@gmail.com.

Complete contact information is available at: https://pubs.acs.org/10.1021/acs.chemrev.1c00914

The authors declare no competing financial interest.

Department of Molecular Biology & Biochemistry, University of California, Irvine, California 92697-3900, United States; Department of Chemistry, University of California, Irvine, California 92697-2025, United States

Abstract

Gases like H_2, N_2, CO_2, and CO are increasingly recognized as critical feedstock in “green” energy conversion and as sources of nitrogen and carbon for the agricultural and chemical sectors. However, the industrial transformation of N_2, CO_2, and CO and the production of H_2 require significant energy input, rendering routines like steam reformation or the Haber process economic and environmental dead ends. Nature, on the other hand, performs similar tasks efficiently at ambient temperature and pressure, exploiting gas-processing metalloenzymes (GPMs) that bind low-valent metal cofactors based on iron, nickel, molybdenum, tungsten, and sulfur. Such systems are studied to understand the biocatalytic principles of gas conversion including N_2 fixation by nitrogenase and H_2 production by hydrogenase as well as CO_2 and CO conversion by formate dehydrogenase, carbon monoxide dehydrogenase, and nitrogenase. In this review, we emphasize the importance of the cofactor/protein interface, discussing how second and outer coordination sphere effects determine, modulate, and optimize the catalytic activity of GPMs. These may comprise ionic interactions in the second coordination sphere that shape the electron density distribution across the cofactor, hydrogen bonding changes, and allosteric effects. In the outer coordination sphere, proton transfer and electron transfer are discussed, alongside the role of hydrophobic substrate channels and protein structural changes. Combining the information gained from structural biology, enzyme kinetics, and various spectroscopic techniques, we aim toward a comprehensive understanding of catalysis beyond the first coordination sphere.

Graphical Abstract

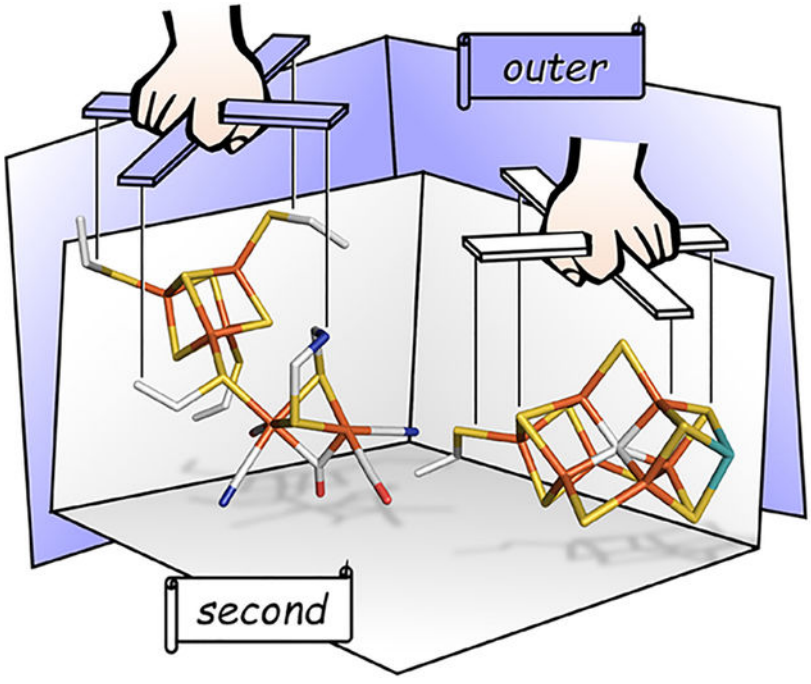

1. INTRODUCTION

Enzymes enhance the probability of a chemical reaction to proceed on biologically relevant time scales. Kinetic rates may differ by a factor of up to 10^6, from the exclusively diffusionlimited enzymes carbonic anhydrase, catalase, or superoxide dismutase to average performers like RuBisCO that produces only three equivalents of product per second. To catalyze a given reaction, the enzyme must provide a specific binding pocket for reactants, for example, offering electrostatic interactions with polar and charged amino acid side chains, the protein backbone, and water molecules. Additionally, hydrophobic interactions play an important role (e.g., in the binding pockets of ATP synthase the separation of reactants and water drives ATP formation). Many enzymes rely on essential cofactors that are not formed by the protein fold. These may be organic "coenzymes" (covalently bound prosthetic groups and loosely bound "cosubstrates") or inorganic clusters of metal ions. The later defines the class of metalloenzymes.[1–3]

Metalloenzymes catalyze important energy conversion reactions throughout all kingdoms of life. The fast-performing enzymes carbonic anhydrase, catalase, and superoxide dismutase are metalloenzymes as well. Introducing two prominent examples, photosystem II (PSII, oxygenic photosynthesis) and cytochrome *c* oxidase (C*c*O, aerobic respiration) are high-valent, gas-processing metalloenzymes (GPMs). At the "oxygen evolving complex" of PSII, a high-potential heterometallic manganese cluster (Mn^{III}–Mn^{V}, $E° \approx 1.0$ V vs SHE) catalyzes water splitting,[4–6] whereas C*c*O catalyzes the reverse reaction at a binuclear heme-copper center (Fe^{II}–Fe^{IV}, $E° \approx 0.8$ V vs SHE).[7–9]

In contrast, low-valent GPMs operate under reducing conditions, exploiting soft, electron-rich metal ions in the catalytic activation of N_2, H_2, CO_2, and CO ($E° \approx -0.4$ V vs SHE).[10] Such systems carry cofactors reminiscent of abiotic metal clusters like pyrite, mackinawite, and pentlandite. These minerals show residual activity catalyzing CO_2, N_2, and proton reduction,[11–13] but efficient turnover can only be achieved as "molecularly tuned derivates"[14] within the active sites of GPMs like nitrogenase, hydrogenase, or CO dehydrogenase. From an evolutionary perspective, it is debated whether mineral cofactors were a prerequisite for catalysis or optimized the activity of protoenzymes. Russell and co-workers argue that metalloenzymes seem to be older than all-organic enzymes,[15] suggesting atmospheric CO_2 and hydrothermal H_2 and CH_4 as earliest sources of electrons and carbon.[16] Similarly, Martin and co-workers argue that life could have evolved from gases that reacted with the help of transition metals.[17] Embedding metal ions or mineral cofactors, simple peptide "nests" may represent the onset of metalloenzyme evolution[18–20] that produced the GPMs discussed in this review including nitrogenase (Section 2), hydrogenase (Section 3), formate dehydrogenase, and carbon monoxide dehydrogenase (FDH and CODH, Section 4 and Section 5). All of these enzymes rely on iron, either as part of the active site cofactor (hydrogenase and nitrogenase) or in iron–sulfur clusters that primarily serve in long-range electron transfer.[21] Further metal ions include nickel (CODH and [NiFe]-hydrogenase) and molybdenum (FDH and nitrogenase). In certain isoenzymes, molybdenum is replaced with tungsten (FDH), vanadium, or iron (nitrogenase). Such systems are studied to understand the biocatalytic principles of gas conversion that

may inspire the design of biomimetic catalysts for the activation of N_2, CO_2, and CO as well as the production of H_2 as a climate-neutral fuel.

Second and outer coordination sphere effects critically impact the catalytic performance of GPMs. Although the influences are manifold and difficult to predict *a priori*, comparing the reaction stoichiometries (eqs 1–4) certain similarities become evident:

$$N_2 + 8H^+ + 8e^- \rightarrow 2NH_3 + H_2 \text{ (nitrogenase)} \quad (1)$$

$$H_2 \rightleftharpoons 2H^+ + 2e^- \text{ (hydrogenase)} \quad (2)$$

$$CO_2 + H^+ + 2e^- \rightleftharpoons HCOO^- \text{ (FDH)} \quad (3)$$

$$CO + H_2O \rightleftharpoons CO_2 + 2H^+ + 2e^- \text{ (CODH)} \quad (4)$$

Each enzyme catalyzes a redox reaction that involves one proton per electron, which hints at proton-coupled electron transfer (PCET)[22–24] as a common principle in GPMs. This demands (*i*) electron transfer to or from a redox site or redox partner in the outer coordination sphere of the metal ion coupled to (*ii*) proton transfer via polar amino acid residues or functional water molecules in the second coordination sphere (Figure 1). Proton transfer pathways and (*iii*) hydrophobic gas channels further modulate the exchange of reactants between active site and bulk solution, sometimes across several nanometers.[25] [FeFe]-hydrogenase, shown in Figure 1, illustrates how individual second coordination sphere effects may comprise (*iv*) hydrophobic interactions and (*v*) hydrogen-bonding contacts.[26] Moreover, the protonation state and polarity of the active site niche influences the (*vi*) charge distribution across the cofactor and redox centers in channeling distance.[27]

Long-distance effects play a crucial role in enzyme catalysis. Within each enzyme family, defined by a common active site structure, homologous enzymes may have very different catalytic properties in terms of turnover rates, catalytic bias (defined here as the ratio of the maximal rates in both directions[28]), reversibility (the requirement for a thermodynamic driving force to trigger catalysis[29]), and resistance to “stress” (e.g., sensitivity to O_2 or visible light). The immediate environment of the active sites in each family is very much conserved, but these enzymes differ by their protein sequences, cofactor composition, and quaternary structures. Nature therefore provides a quasi-infinite playground for examining outer coordination sphere effects in catalysis. For example, certain microorganisms produce many homologous enzymes to catalyze the same reaction (isoenzymes), which suggests that distinct catalytic properties are needed for different physiological functions.

In this review, we highlight and compare the role of second and outer coordination sphere effects on the activation of gaseous substrates such N_2, H_2, CO_2, or CO by various low-valent GPMs. We provide a comprehensive overview on protein variants that were found to affect the catalytic properties of nitrogenase, hydrogenase, FDH, and CODH. To understand

or mimic GPMs, we emphasize that second and outer coordination sphere effects must not be neglected.

2. NITROGENASE

Nitrogen is an essential element for life, necessary for the synthesis of biomolecules such as deoxyribonucleic acid (DNA), ribonucleic acid (RNA), and amino acids. While nitrogen can be found in many different chemical forms throughout atmospheric and geological sources, the largest reservoir of nitrogen on the surface of the Earth is found in the form of dinitrogen (N_2): a small, gaseous, nonpolar, diatomic molecule with a strong triple bond.[30] The strength of this bond is on the order of ~940 kJ/mol, which makes its scission into bioavailable forms, also called "N_2 fixation", one of the most challenging transformations in Nature.

Two main processes are recognized as natural engines for N_2 fixation within the global nitrogen cycle: lighting strikes and biological N_2 fixation (BNF).[31–33] The high temperature environment in the air surrounding lightning causes N_2 to react with other components in the atmosphere, such as dioxygen (O_2), ozone (O_3), or oxygen-based radical species, forming various nitrogen oxides (NO_x).[31,34,35] The NO_x species are then converted to nitric acid (HNO_3) in the atmosphere, and brought down to the ground through rainfall or surface deposition, where the fixed nitrogen species can be utilized.[30,36] This lightning-based process requires extreme conditions such as high temperature, and is completely unregulated which causes many chemical pathways to converge and ultimately produce the highly oxidized HNO_3. In contrast, biological N_2 fixation occurs in diazotrophic microorganisms that span across multiple phyla between bacteria and archaea.[37–39] These organisms are found in many environments, such as surface soils, sediments, marine and fresh waters, and geothermal sources, in both the presence or absence of oxygen.[40–43] Some organisms can live freely within microbial communities, such as the obligate aerobe *Azotobacter vinelandii*,[44] or the thermophilic methanogen *Methanococcus thermolithotrophicus*,[45,46] while others, such as *Rhizobium leguminosarum*, form symbiotic relationships with specific plant species.[47,48] In all cases, N_2 is converted into the highly reduced nitrogen species ammonia (NH_3), although more often ammonium (NH_4^+) is the observed product.[30] Despite the wide variation in living conditions, each of the diazotrophs have genes that encode for the common enzyme nitrogenase.

Nitrogenase is a gas-processing metalloenzyme composed of two proteins, the reductase component NifH (also called the "Fe protein"), as well as the catalytic component NifDK (also called the "MoFe protein") that contains a unique molybdenum-containing iron sulfur cluster called the M-cluster (or "FeMoco").[49,50] There are also so-called "alternative" nitrogenases that replace the Mo ion in FeMoco for either vanadium ("FeVco" in the VFe protein) or iron ("FeFeco" in the FeFe protein).[51] All nitrogenases are capable of reducing small molecule substrates, such as acetylene (C_2H_2) and cyanide (CN^-), under ambient temperature and pressure, but the native reaction catalyzed by the enzyme is the reduction of N_2 to NH_3.[51–53] In comparison, humans have developed the Haber-Bosch process that takes N_2 and dihydrogen (H_2) under high temperature and intense pressure conditions to yield NH_3.[54] Nitrogenase also catalyzes the reduction of protons (H^+) to H_2, and in all reactions with other substrates (including N_2), some portion of the electron equivalents (or electron

flux) is diverted to produce H_2.[50,55] During the native nitrogenase reaction, H_2 is generated as an additional product (eq 1), but the mechanism of its synthesis is distinct from simple proton reduction.[52,56–60]

The complexity of nitrogenase has captivated researchers for decades as they seek out answers to the question, how does nitrogenase carry out these difficult chemical transformations? Many scientific approaches have been utilized in its study, each providing complementary information that can add to the larger picture. Since nitrogenase has been extensively reviewed,[50–52,61–63] this section shall primarily focus on secondary and outer sphere effects that modulate the function of the Mo-dependent enzyme.

2.1. Structural Features of Nitrogenase

The Mo-nitrogenase from *A. vinelandii* is the most extensively studied nitrogenase protein, and under N_2 fixing conditions up to 10% of all cell proteins are nitrogenase related.[44,64] The MoFe protein is an $\alpha_2\beta_2$ heterotetramer of the *nif D* and *nif K* gene products that form NifDK (~220 kDa), where two $\alpha\beta$-dimer units pair together.[61] Each $\alpha\beta$-dimer houses two different metalloclusters that are critical for enzyme function, the P- and M-clusters, such that each NifDK tetramer binds a total of four metalloclusters (Figure 2).[61,65,66] The *nif H* gene product, NifH, serves as the reductase partner of NifDK, and is composed of a homodimeric protein (γ_2) with a molecular weight of ~60 kDa that binds an [4Fe-4S] cluster at the subunit interface.[67] Additionally, each subunit can bind one molecule of MgATP.[63,67,68] One NifH protein can bind to each $\alpha\beta$-dimer of NifDK, forming an Fe:MoFe protein stoichiometry of 2:1.[69,70]

The P-cluster mediates electron transfer between the reductase component, NifH, and the M-cluster during catalysis.[71] The cofactor is composed of an [8Fe-7S] cluster positioned at the α/β interface of NifDK, ~ 10 Å below the surface of the protein.[65,72] It appears as the fusion of two [4Fe-4S] clusters that share a μ_6-sulfide vertex, with ligation from six cysteine residues, α-C62, α-C88, α-C154, β-C70, β-C95, β-C153, three of which come from each subunit (Figure 3). Interestingly, the cysteine residues bind terminally to some of the Fe centers, as is typically found with canonical [4Fe-4S] clusters, but two of them bind in bridging modes between the two cubane halves of the P-cluster. Structurally, this fused cubane geometry of the P-cluster is unique and has not been identified elsewhere in biology. The P-cluster has three interconvertible oxidation states that have been identified as relevant for catalysis: the as-isolated P^N state, the one-electronoxidized P^{1+} state and the two-electron oxidized P^{OX} (or P^{2+}) state.[62,73] The P^N-cluster has been characterized as an all ferrous (Fe^{2+}) cluster,[74–77] and subsequent oxidations result in reversible structural changes that physically open the cofactor.[78–80] This structural fluctuation of the P-cluster during redox changes has been proposed as a means of regulating or “gating” electron transfer within NifDK.[62,81–83]

The M-cluster is an asymmetric [Mo-7Fe-9S–C-*R*-homocitrate] species, with the Mo-capped end ligated by the organic acid *R*-homocitrate through the 2-hydroxy and carboxyl groups, as well as by the α−442His residue, and the opposite, Fe-capped end ligated by α-C275 residue (Figure 4A).[65,66,85] The cluster is buried within the α subunit of NifDK and is positioned ~19 Å from the P-cluster and over 60 Å from the clusters of the partner

$\alpha\beta$-dimer. The structure of the M-cluster is similar to the P-cluster, as both are a fusion of two different cubane species with a common vertex, but the two partial cubane units of the M-cluster, [Mo-3Fe–3S] and [4Fe-3S], are not identical, and the common vertex is an interstitial μ_6-carbide as opposed to a sulfide.[66,86–88] Additionally, there are three "belt" μ_2-sulfido ligands that bridge between the Mo- and Fe-capped halves of the cofactor. These belt sulfide ligands have been shown to exhibit lability in both Mo- and V-nitrogenases, and this apparent flexibility has been implicated to be important during catalysis.[89–95] In V-nitrogenase (or VnfDGK), the V-cluster is a structural analog of the M-cluster (Figure 4B), but with a V ion in place of the Mo ion, and one of the μ_2-sulfide ligands replaced with a carbonate (CO_3^{2-}) ligand of unknown origin.[92–95] There are physical metrics that vary between the M- and V-clusters, but they are still remarkably similar.[51]

The electronic description of the M-cluster has been of interest for decades, as the M-cluster is capable of supporting many redox states,[56] and so the cluster has been experimentally studied using combinations of Mössbauer, X-ray absorption (XAS), magnetic circular dichroism (MCD), and electron paramagnetic resonance (EPR) spectroscopic techniques.[62,75,96–98] Many of these techniques probe the sample in an ill-defined state, and as such, there can be great difficulty in deconvoluting the specific contributions of individual clusters. The most commonly observed state of the M-cluster is the resting, dithionite ($S_2O_4^{2-}$) reduced M^N state that is associated with the diagnostic S = 3/2 rhombic signal from EPR spectroscopy (g = 4.3, 3.7 and 2.0).[73,96,99,100] Computations and high-energy resolution fluorescence detected (HERFD) Mo K-edge XAS experiments identified that the Mo center of the M^N-cluster is best described as an S = 1/2 Mo^{3+} center, as opposed to the classical assignment of Mo^{4+}.[98] This indicates that the Mo exists in an atypical "non-Hund" configuration, and additional spectroscopy and density functional theory (DFT) calculations support a $[3Fe^{2+}{:}4Fe^{3+}{:}Mo^{3+}]^{1-}$ assignment.[97,98,101,102] Further, a crystallographic spatially resolved anomalous dispersion (SpReAD) analysis compared electron densities to Fe K-edge XAS experiments to determine the oxidation states of specific Fe atoms of the M-cluster, and this study agreed with the previously described oxidation assignment.[103] The M^N-cluster can also be oxidized by one electron to the M^{OX} form, which coincides with a loss of the S = 3/2 EPR signal, and is generally not believed to be relevant for catalysis.[73,104,105]

While NifH binds a smaller, more prevalent type of biological [4Fe-4S] cluster, the Fe protein is far from simple. NifH has three recognized physiological functions: (1) Mo and homocitrate insertase in the biosynthesis of the M-cluster, (2) reductase involved in P-cluster biosynthesis on NifDK, (3) obligate reductase for nitrogenase catalysis that couples electron transfer to MgATP hydrolysis.[68] The [4Fe-4S] cluster binds between the two subunits of NifH and is positioned on a C_2 rotation axis with cysteine coordination by two residues (γ-C97 and γ-C132) from each subunit.[67] This cluster is located in a solvent-exposed position, which differs from [4Fe-4S] ferredoxins that have clusters buried within the protein.[63] Further, MgATP molecules that bind to the Walker motif A protein fold have been shown to affect the position of the [4Fe-4S] cluster despite being bound ~20 Å away from the cluster (Figure 2).[68,106,107] This apparent cluster movement has been studied by various structural and spectroscopic methods and is associated with modulation of the reduction potential of NifH.[63,108–112] The protein can support $[4Fe\text{-}4S]^{2+}$, $[4Fe\text{-}4S]^{1+}$,

and $[4Fe\text{-}4S]^0$ oxidation states, which is abnormal compared to other iron–sulfur cluster containing proteins that only support two redox states.[113] In NifH, the $[4Fe\text{-}4S]^{1+}$ state is favored in the presence of dithionite[51,100] and interestingly exists as a mixture of two different spin states, $S = 1/2$ and $S = 3/2$, the composition of which changes with additives such as glycerol or urea.[96,114] During catalysis, the $[4Fe\text{-}4S]^{2+/1+}$ couple is proposed to be operative, transferring one electron to NifDK for every two molecules of MgATP cleaved by NifH, and NifH becomes reduced *in vivo* through physiological reductants such as ferredoxins or flavodoxins.[63,83,115–118] The $[4Fe\text{-}4S]^0$ "all ferrous" or "super-reduced" state has been implicated in reactivity of NifH with carbon substrates like CO and CO_2, yet has also been proposed to play a role in nitrogenase catalysis, but the characterization of this species is fraught with complications that make understanding a physiological role difficult.[51]

2.2. Assembly of Nitrogenase Cofactors

Nitrogenase is a complicated system, not only because of the multimeric metalloprotein composition and unique cofactors, but also because of the requirement of many genes for the regulation and biosynthesis of nitrogenase.[50,51,119] For the NifDK protein from the model organism *A. vinelandii*, a minimum set of nitrogenase proteins that includes NifU, NifS, NifB, NifEN, NifH, NifV, and NifZ are required for *in vitro* activation of N_2 fixation.[49,120] These proteins are encoded by *nif* or "nitrogen fixation" genes, and the *nif* operon is specific to the Mo-nitrogenase system. Organisms that encode for V- or Fe-only nitrogenase (*vnf* and *anf* genes, respectively) still require some of the *nif* operon for proper function.[51] For Mo-nitrogenase, the biochemistry and assembly of the MoFe protein and the cofactors bound therein have been extensively studied over the past two decades, yielding crucial insights into the process.

The biosynthesis of NifDK involves the assembly of both the P- and M-clusters in addition to the polypeptide, but cofactor generation occurs through different routes (Figure 5). While the P-cluster is assembled *in situ* on the NifDK polypeptide scaffold, the M-cluster is assembled *ex situ* on a series of different proteins before terminally reaching NifDK.[49,50,120] The P-cluster originates from a pair of [4Fe-4S] clusters, called the P*-cluster, that are synthesized at the α/β subunit boundary of apo NifDK.[84,121–124] The iron–sulfur fragments are assembled and delivered to apo-NifDK through the action of NifU, a scaffold protein that binds iron–sulfur clusters, and NifS, a cysteine desulfurase that provides sulfide from cysteine.[125,126] The P*-cluster is then fused together with concomitant loss of sulfur by the stepwise action of NifH and NifZ in a MgATP- and electron-dependent process. The result is an apo-NifDK protein with two equivalents of P-cluster bound but lacks M-cluster.

In contrast, the assembly of the M-cluster starts with the construction of [4Fe-4S] clusters by NifU and NifS that are subsequently delivered to NifB, a radical *S*-adenosyl-L-methionine (SAM)-dependent enzyme.[127,128] NifB binds three [4Fe-4S] clusters; one is specifically for catalyzing SAM reactivity, while the other two are the substrate clusters (K1 and K2) known collectively as the K-cluster.[129–131] Under reducing conditions, two equivalents of SAM are cleaved to first transfer a methyl group to the K2 cluster on NifB, and the second equivalent of SAM initiates a hydrogen atom abstraction of the transferred methyl group.[87,88,131] In a

series of uncharacterized subsequent steps, carbide (C_4^-) is generated upon removal of the remaining hydrogen atoms. Concurrently, the two K-cluster cubane units are fused yielding a [8Fe-8S–C] cluster, called the L*-cluster, that contains an interstitial carbide bound to the six central Fe atoms of the cluster.[132,133] A final "9th sulfur" is then incorporated into the L*-cluster through the reduction of a sulfite (SO_3^{2-}) ion to produce the [8Fe-9S–C] L-cluster. The L-cluster on NifB is transferred to another scaffold protein, NifEN, that facilitates the conversion of the L-cluster into the M-cluster through the loss of an Fe atom and the incorporation of Mo and *R*-homocitrate.[134–137] *In vitro* experiments demonstrate that M-cluster-loaded NifEN can then interact directly with apo NifDK (containing only P-clusters) to transfer the M-cluster and produce active NifDK, although additional chaperone proteins have been suggested to assist with this process *in vivo*.[49,50]

2.3. Nitrogen Reduction Mechanism

N_2 reduction requires a high degree of regulation to successfully carry out the reaction, and one of the key factors to this process is the shuttling of electrons. Electrons are transferred from NifH to NifDK through direct complexation of both proteins and the hydrolysis of two MgATP molecules for each electron delivered.[63] This creates a complex system that has been the subject of study for decades. Extensive investigation of the mechanism of N_2 reduction in the 1970s and 1980s led to a kinetic framework known as the Lowe-Thorneley model or cycle.[51,52,63] This model can be viewed from two different perspectives; one is an Fe protein-centric view known as the "Fe protein cycle" and the other, more common view is that of the MoFe protein, or the "MoFe protein cycle".

The Fe protein cycle begins with the NifH protein being in the reduced $[4Fe\text{-}4S]^{1+}$ state ($NifH^R$), binding two equivalents of MgATP.[63,83] The reduction to $NifH^R$ has been facilitated *in vitro* by dithionite, but other reducing agents such as Eu(II) chelates have been used as well. The nucleotide-bound Fe protein then interacts with NifDK, forming a 2:1 complex that has been crystallographically characterized.[69,70,138] Subsequently, there are a series of steps that involve conformational changes, electron transfer, ATP hydrolysis, and phosphate release, resulting in oxidized NifH ($NifH^{OX}$, $[4Fe\text{-}4S]^{2+}$) with two equivalents of MgADP bound in complex with NifDK.[63,83] $NifH^{OX}$ and NifDK undergo dissociation, releasing the reductase before $NifH^{OX}$ is reduced back to the $NifH^R$ state, which becomes capable of exchanging MgADP for MgATP, thereby restarting the cycle. This cycle is presumably active during the reduction of most substrates by NifDK, though in the absence of NifDK, NifH has also been shown to carry out C1 substrate reduction through alternative mechanisms.[51,68]

The Lowe-Thorneley model for N_2 reduction by NifDK, or the MoFe protein cycle, describes the catalytic intermediates in the reaction, each designated by an E_n notation where n is the number of proton and electron equivalents that have accumulated on one $\alpha\beta$-dimer of NifDK (Figure 6).[56] However, the value of n does not indicate where proton and electron equivalents are located, only that they have been delivered to the system, which has sparked considerable research efforts in the field.[52] The first state, E_0, reflects the resting, as-isolated state of NifDK associated with the well-characterized $S = 3/2$ EPR signal of the M-cluster.[62] As each proton and electron pair is accumulated through the

early (n = 2–4) steps of the cycle, it is possible for a "relaxation" to occur, releasing H_2 with concomitant transition to an n − 2 state.[52,60] N_2 has been proposed to bind to the M-cluster in the E_3 and E_4 states, but reduction of N_2 only occurs in the E_4 (or E_4(4H)) state.[52,56,139] This makes the E_4 state one of the most studied of the cycle, because either E_4 can relax backward to lower E_n with release of H_2, or the cycle can proceed forward with the cleavage of the N_2 bond. Intriguingly, when N_2 binds to E_4(4H), one equivalent of H_2 is produced with concomitant formation of the E_4(2N2H) state through a proposed mechanism of reversible reductive elimination or oxidative addition.[52,60,140] The E_4(4H) to E_4(2N2H) reaction represents the first lowering of the N_2 bond order, though several possibilities have been put forward as to the identity of the resultant E_4(2N2H) species.[51,52]

The subsequent steps of the MoFe protein cycle E_5–E_8 promote the further reduction of the N_2 bond. Initially, there were two competing proposals for this latter half of the cycle that differed in the location where proton and electron equivalents are delivered to the reduced nitrogen species: a "distal" and an "alternating" pathway. The distal pathway posits that protons are delivered to the unbound N atom of N_2 first, forming an M = N–NH_2 hydrazido species that undergoes further proton/electron addition to yield one equivalent of NH_3 and a terminal M ≡ N metal nitrido species by the E_5 state.[141–146] The E_5 species is then sequentially protonated to release the second equivalent of NH_3 after the E_8 state. The alternating pathway, based on synthetic Fe-catalyzed versus Mo-catalyzed N_2 reduction,[147,148] proposes that protons are distributed between both N atoms of N_2, starting with diazene (HN=NH), proceeding through hydrazine (H_2N–NH_2) and releasing NH_3 after E_6 and E_8. While there is still uncertainty in distinguishing between these two mechanistic possibilities, mounting evidence supports the alternating pathway for biological N_2 reduction,[51,52] including crystallographic evidence of a putative N_2-bound species.[91] However, evidence from the V-dependent nitrogenase potentially suggests a distal pathway may be operative in that system, but kinetic analysis and calculations propose that the Mo-, V-, and Fe-only nitrogenases all share a common mechanism.[51,93,149,150] Clearly, further investigation will be necessary.

2.4. Nitrogenase Active Site Pocket

To understand the outer sphere environment surrounding the M-cluster, it is necessary to take a critical look at the residues that make up the active site pocket. However, there is no "best" way to discuss the location of amino acid residues with relation to the catalytic cofactor of nitrogenase. High resolution crystallography has provided three-dimensional representations of nitrogenase and the cofactors with precision, but it can be difficult to gain a sense orientation of the cofactor with respect to its protein environment. The 3-fold rotation axis that runs from the Mo-capped end to the Fe-capped end of the cluster does not inherently provide a landmark around the M-cluster by which relative position can be compared other than the Mo and Fe subcubanes. The crystallographic labeling of the cofactor atoms provides some basis of orientation, but the labeling convention is also not particularly intuitive; for instance, the three belt sulfur positions are given labels of S2B, S3A, and S5A, whereas other SXA and SXB labeled sulfur atoms are bound to the Fe-capped (or Fe1) and Mo-capped subcubane structures, respectively (Figure 7). In this discussion, a helpful means to navigate the M-cluster site is to establish an origin at

the central carbide atom, followed by an "*x*-axis" that incorporates the C_3 symmetry axis running between Fe1 and Mo. The Fe1 end of the M-cluster is pointed toward the surface of the α-subunit adjacent to the bulk solvent (designated as the "negative" *x* direction), whereas the Mo end of the cluster is directed toward the $\alpha\beta$-subunit interface (designated as the "positive" *x* direction). The S2B sulfur site has been established as a labile position on the catalytic cofactor,[89,90] and is adjacent to several residues critical for reactivity, so a "*z*-axis" would bisect S2B as well as the central carbide atom of the cluster, with the direction of the S2B atom being positive. There is no convenient atom to position a "*y*-axis" relative to the carbide, but the S3A side of the *xz* plane can be the positive direction of *y* and the S5A side can be negative. Within this framework of (*x*, *y*, *z*) coordinates, α-H442 would be in the (+, +, −) direction relative to carbide, α-C275 would have a (−, 0, 0) position, and the nearest P-cluster would have a bearing of (+, −, +). While also an imperfect system due to constraints, such as α-R359 (Figure 8) and the *R*-homocitrate ligand (HC) running through positive and negative values of *y*, the coordinates should generally provide a spatial navigation within the active site.

The catalytic M-cluster of nitrogenase is one of the largest, most complicated biological cofactors known so far but it is only bound to the protein scaffold through two amino acid residues, α-C275 and α-H442.[61,65,66,85,151] While *R*-homocitrate does bind to the Mo-end of the cluster, the lack of additional ligation to the M-cluster indicates that second coordination sphere effects play a crucial role in catalysis. Many amino acids have side chains with nitrogen-containing functional groups such as histidine, arginine and glutamine that are capable of hydrogen-bonding interactions. Nonpolar or otherwise bulky residues such as valine, phenylalanine and tryptophan have been found to play roles in the steric environment for substrate access and binding, as well as appropriate positioning of the M-cluster within the active site. All of these residues are connected to each other in a tightly regulated way, and disruptions in this network tend to be detrimental to the function of the enzyme. Figure 8 shows the positions of some of the important residues discussed within this review relative to the M-cluster.

In 1991, before crystal structures of NifDK were solved, a series of point mutations of conserved histidine residues were reported, hoping to identify those interacting with the M-cluster. Making use of electron spin echo envelop modulation (ESEEM) spectroscopy,[152] microwave pulses are used in a specific sequence within an EPR experiment to probe nuclei (such as ^{14}N or ^{1}H) that are coupled to a paramagnetic species.[62] Specifically, the intense $S = 3/2$ EPR signal (Figure 9) associated with the M-cluster was probed to search for ^{14}N atoms from histidine residues that may be hyperfine-coupled with or covalently bound to the cofactor.[152]

Residues α-H83 (+, −, +), α-H195 (−, 0, +), α-H196 (−, 0, +), α-H274 (−, −, −), and β-H90 (+, +, +) were targeted for single point mutations. ESEEM studies on whole cells were carried out and signals assigned to N atoms from histidines were observed in all variants, only the variant α-H195 NifDK proteins showed no ESEEM signal, and it was concluded that α-H195 must bind to the M-cluster. However, once the crystal structure of NifDK became available in 1992, it was clear that α-H195 was too far from the M-cluster to bind directly, but instead was likely involved with a hydrogen-bonding interaction to the

S2B sulfur of the cofactor. In 1995, Dean, Hoffman, and co-workers studied the EPR and ESEEM signature of partially purified NifDK variants, namely α-H195N and α-H195Q.[153] Consistent with the previous observations, it was found that the ESEEM signal was dramatically attenuated in the α-H195N NifDK variant but α-H195Q NifDK showed nearly identical signals in both EPR and ESEEM experiments to those of the wild-type enzyme. If the hydrogen bond of α-H195 was responsible for the ESEEM signals, then both variants should display similar spectra, but they did not. This suggested that a nitrogen-containing residue that is sensitive to the position of the α-H195 residue was responsible for the signal. Subsequently, ESEEM studies were expanded to include purified variant proteins targeting residues α-R96 (+, −, 0), α-H195 (−, 0, +), α-R359 (0, +, −), α-F381 (0, +, +), and α-H442 (+, +, −).[154] The spectra of α-H195N NifDK showed that the ESEEM signal (labeled as "N1") was indeed eliminated as previously reported,[152,153] but a weaker signal "N2" that was buried underneath was also observed.[154] Mutation at α-R96 only showed the N1 signal, eliminating this residue as the source of N1, and substitution of α-H442 resulted in a lack of observable EPR signal, consistent with loss of the M-cluster entirely. However, mutation of α-R359 or α-F381 resulted in a loss of the N1 signal while the N2 signal remained intact. Together, these experiments were used to assign the N1 signal to α-R359 and the N2 signal to the peptide NH groups of one or both of the residues α-G356 (+, +, 0) and α-G357 (−, +, 0).[154] However, the catalytic activity of the variant NifDK proteins could not be correlated to the ESEEM signals. Despite this, the study demonstrates that changes in the second coordination sphere on one side of the M-cluster can perturb the interactions occurring on the other side of the cluster, as seen by the loss of the N1 signal at α-G359 (0, +, −) when α-H195 (−, 0, +) is modified. In fact, changing the steric environment as seen with α-F381L NifDK variants (0, +, +) was enough to disrupt hydrogen-bonding interactions around the cluster even though α-F381 is not directly involved in such an interaction, reinforcing that the active site residues are highly interconnected.

Another salient observation about the active site of nitrogenase comes from the crystal structure of an M-cluster depleted NifDK, called Δ*nif B* NifDK.[155] In 2002, Burgess, Rees, and co-workers managed crystallized the NifDK protein without the catalytic cofactor, which resulted in changes to the tertiary structure as compared to wild-type enzyme. Rearrangements of the amino acids left a "funnel" on the surface of the protein that was positively charged, with a loop of residues from α−353 to α−364 positioned at the entrance to the funnel. This loop also contained residues that had positively charged, nitrogen-containing side chains, and the authors proposed that the electrostatic charge of the funnel would help direct the negatively charged M-cluster into the appropriate position so it could be locked into the active site through movement of the funnel loop. Interestingly, a similar concept was discussed for the insertion of the active site cofactor of [FeFe]-hydrogenase (Section 3.2.2). Subsequent point mutation studies further explored this proposal by targeting specific residues that may assist in guiding the M-cluster into NifDK.[156–158] Thus, the side chain selection within the nitrogenase active site has the demonstrated capability to support a robust network of hydrogen bonds, while at the same time functioning in a biosynthetic capacity to orient the M-cluster optimally within the protein for catalysis.

2.5. Assessing the Nitrogenase Second Coordination Sphere

Before the publication of the crystal structures in the 1990s,[65,67,69,80,85,159] the study of nitrogenase was based on genetic, spectroscopic, and reactivity experiments that were used to gain insight into the structure of the protein as well as the bound metallocofactors. At that time, direct information regarding the properties of the individual P- and M-clusters was scarce, and their three-dimensional relationship. Even after the appearance of high-quality crystallographic data, the study of structure–function relationships in nitrogenase was difficult due, in no small part, to the multiple, unique iron–sulfur clusters that are bound to the enzyme. Some of the early efforts to characterize and understand the nitrogenase cofactors involved chemical extraction into organic solvents.[160,161] The P-cluster is integral to the nitrogenase structure, so the acid quenching required for extraction destroys the P-cluster and disrupts the protein fold such that the M-cluster can be removed. This allowed for new avenues of study and analysis, but to date, there have been no successful reports of recrystallized M-cluster outside of the nitrogenase protein.[162]

To better assess the nitrogenase protein structure, amino acid sequencing was carried out through genetic analysis and protein digestion in the 1970s and 1980s to compare nitrogenases from different species.[163–168] Conserved residues were identified and targeted for single-point mutations as a way to connect information about the cofactors to the protein structure and function. Initially, conserved cysteine residues were investigated for their widespread use in biology as ligands for iron–sulfur clusters, as it was understood that nitrogenase likely contained multiple [4Fe-4S] clusters. These cysteine residues were changed into serine or alanine, and the resulting bacterial strains (of *A. vinelandii* or *Klebsiella pneumoniae*) were studied.[169–172] Growth rates in the absence of a fixed nitrogen source were used to establish the N_2 fixation phenotype, and whole cell and/or crude extract activity assays were carried out in an acetylene atmosphere to compare diazotrophic growth rates with nitrogenase activity.[169,172] In addition, EPR spectra of whole cell variants or crude extracts of these cells would be collected to search for the intense $S = 3/2$ signal associated with the M-cluster as a means to cross reference the observed reactivity.[172] Generally, when the cysteine residues (that would later be found to bind to the P- and M-clusters) were mutated to alanine, diazotrophic growth and acetylene-based nitrogenase activity would be eliminated. Serine subsitutions of cysteine residues bound to cofactors would also eliminate activity, but in one case, Newton and co-workers found that substitution of C183 (+, −, +) on the NifD subunit (or α-C183) from *A. vinelandii* to serine did not arrest activity but resulted in diminished diazotrophic growth rates.[169] Conserved residues such as α-Q191 (+, +, +) were mutated to change the polarity or charge; for instance, changing the polar, amide-bearing amino acid side chain of glutamine to the carboxyl group of glutamate (α-Q191E).[169] In this case, the activity was eliminated, despite the fact that glutamine residues are not typically found as ligands to iron–sulfur clusters in biology.[113,173] These findings were unanticipated, but provided indications of the active site of nitrogenase in the absence of structural data, and marked the beginning of targeted efforts to understand the secondary sphere effects within nitrogenase. In the years that followed, many mutagenic studies were reported with a focus on determining effects to nitrogenase activity as well as the number and location of substrate binding sites on the M-cluster. The

residues that have been targeted for mutagenic studies related to the M-cluster site in NifDK from *A. vinelandii* have been summarized in Table 1 and Table 2.

One complicating factor when discussing the results of site-directed mutagenic studies is that often the modification substantially reduces or eliminates nitrogenase activity, but it is not always clear why this occurs. In studies of the MoFe protein from *K. pneumoniae*, Buck and co-workers tested the activity of cell extracts from several cysteine to alanine variants and found almost no acetylene reduction, implying their mutations have made nitrogenase nonfunctional.[172] They employed a parallel experiment to assess the stability of the variant proteins where wild-type apo NifDK (Δ*nif B* NifDK) was added to their cell extracts and would show activity only if free M-clusters were present in the extracts to enable reconstitution of the Δ*nif B* NifDK protein. Low acetylene reduction activity was observed for many variants following such a treatment, but the α-C275A NifDK protein that targeted the M-cluster-binding residue showed an increased activity by an order of magnitude.[172] This indicated that some variant proteins are unable to retain the M-cluster, a conclusion that was validated by adding additional M-cluster to cell extracts of the NifDK variants alone with no observed increase in activity. Indeed, extracts were commonly used because of the difficulty associated with purification, and this problem becomes exacerbated when the stability of the protein is affected. Several reports from Newton and Dean acknowledge that certain proteins could only be partially purified because they would not survive heat treatment steps.[139,153,183,185,191] In some instances where purification was successful, the Mo content of the NifDK variant would be lowered in the wild-type enzyme (<50%), implying that cofactor loading was impaired resulting in variable mixtures of apo and holo NifDK proteins.[139,183,191] These studies still provide valuable insight, but it is important to recognize that it can be difficult to make definitive assessment of outer sphere effects when activities can be attenuated from simple loss of the M-cluster or degradation of the protein.

However, there are investigations targeting the assembly of NifDK that use the retention or loss of the M-cluster as means to probe the function of certain amino acids.[156–158] Ribbe and co-workers have carried out site-directed mutagenesis on several outer coordination sphere residues ≥6 Å from the M-cluster (Figure 10): α-W444 (+, −, −), α-H274 (−, −, −), α-H362 (−, +, −), and α-H451 (−, −, −). A crystal structure of apo NifDK from a Δ*nif B* background revealed that α-H442 in the absence of the M-cluster shifts ~5 Å within the active site.[155,158] The α-H442 residue is rearranged and placed nearby two other histidine residues, α-H274 and α-H451, forming a “triad” while another residue, α-W444, is found to take up the same space as α-H442 does in the holo enzyme (Figure 10). The apparent position swapping of α-H442 and α-W444 was intriguing, so mutagenesis was carried out to replace α-W444. In the α-W444Y and α-W444F NifDK variants, the M-cluster loading was ~90% of the wild-type enzyme, whereas α-W444A and α-W444G contained only 14% and 3% of wild-type M-cluster, respectively.[158] As the side chain of the α−444 residue was changed to smaller, less sterically bulky groups, the Mo concentration decreased. The reactivity assays of the variant proteins with N_2, C_2H_2, and protons, as well as the intensity of the EPR signals all roughly decreased by the same magnitude as the Mo concentration. Paired with heat treatment studies, it was suggested that the variant proteins themselves were stable, leading to the conclusion that α-W444 must be involved in a steric interaction that keeps the M-cluster secure within the active site pocket.[158] It was also observed that in

the α-W444A and α-W444G variants, the EPR signal of the P-cluster appeared to distort relative to the larger substituent-containing variants, implying that α-W444 may also have longer range effects in NifDK than immediately around the M-cluster site.

The other two residues of the histidine triad, α-H274 and α-H451 (Figure 10), were also targets for point mutations.[156] *A. vinelandii* cells separately expressing NifDK variants α-H274A, α-H451A and a double mutant α-H274A/α-H451A grew more slowly under N_2-fixing conditions, indicating issues with nitrogenase activity, with the double mutation having the most deleterious effect on the growth rate. Assessment of the standard substrate reduction assays showed decreased activity of 67%, 56%, and 43% for the α-H274A, α-H451A, and α-H274A/α-H451A NifDK variants, respectively. The decreased activity also correlated well to the Mo concentration, and to the intensity of EPR signals for each of the variants. The α-H451A NifDK protein in the dithionite-reduced state had a very similar EPR spectrum for the $S = 3/2$ M-cluster as wild-type NifDK, but the introduction of α-H274A as either the single or double mutant yielded a spectrum with large distortions in g-values as well as line shapes. The rationalization for this observation was that α-H274 is adjacent to α-C275, which binds the M-cluster and may have more of a direct impact on the M-cluster environment than the more distant α-H451.[156] Additionally, none of the studied mutations affected the EPR signals of the P-cluster, indicating that these residues have less of a long-range steric effect than α-W444. Introduction of isolated M-cluster into solutions of M-cluster deficient α-H274A, α-H451A, and α-H274A/α-H451A Δ*nif B* NifDK variants did not allow for full activation of the protein to wild-type levels of reactivity. Thus, it was concluded that both α-H274A and α-H451A are required during the biosynthesis of NifDK through sequential binding events that draw the M-cluster into the protein.[156] These residues may also play roles in the proton shuttling within the active site, as seen from shifts from N_2 reduction toward proton reduction in the variants, but one factor that was not explored is what steric effect the size of the side chain played in going from histidine to alanine. Alanine substitutions were certainly deleterious, but it would be interesting to see how the protein would retain the M-cluster if uncharged residues larger in size than alanine were studied.

Along similar lines, a final outer coordination sphere residue, α-H362 (−, +, −), had been studied with respect to M-cluster insertion into the NifDK protein (Figure 10).[157] In the crystal structure of the apo NifDK protein, α-H362 is surface exposed and is at the entrance to the insertion funnel of positively charged residues that have been proposed to guide a negatively charged M-cluster into the protein.[155,157] After M-cluster incorporation, the residue moves with the protein secondary structure to pin the cofactor in place. Single point mutants were generated and two variant NifDK proteins were studied, α-H362D and α-H362A.[157] Much like the previous mutations described, the α−362 variants grew more slowly under N_2-fixing conditions, expressed a decreased reactivity profile that correlated with Mo content, and had perturbations to the line shape and intensity of EPR signals, relative to wild-type enzyme. The decreased activities of the α-H362D and α-H362A NifDK variants are ~80% and ~40%, respectively. While modification of this residue did not cause a cessation of activity like that observed for α-W444,[158] substitution of α-H362 for aspartate induces a ~ 20% reduction in activity while alanine substitution results in a more drastic reduction of ~60%. This suggests that either α-H362 is involved in directing the M-cluster into the NifDK active site (supported by the decreased Mo concentration), or the residue

is structurally important for adequately positioning the M-cluster within the active site (supported by the observed perturbations of the M- and P-cluster signals). The best answer is likely a combination of both, but further structural characterization of these NifDK variants may shed light on the M-cluster insertion process.

2.5.1. Reduction of Nitrogen, Acetylene, and Protons.—As mentioned earlier (eq 1), the reduction of N_2 by nitrogenase is a challenging transformation that requires the delivery of 8 electrons, 8 protons, and 16 equiv of MgATP to produce NH_3, H_2, and MgADP.[51,52,100] Not only is NH_3 produced, but H_2 is generated as an integral part of the N_2 reduction mechanism.[57,58,192] As discussed in Section 2.2, electron and proton equivalents are sequentially delivered to the catalytic cofactor by way of NifH and the P-cluster, leading to distinct E_n steps along the Lowe-Thorneley model reaction pathway.[56,60] At the E_4(4H) level, N_2 has been proposed to bind through a reductive elimination/oxidative addition mechanism, forming a reduced nitrogen species E_4(2N2H) and liberating one equivalent of H_2 (Figure 6). It is important to emphasize that while the bond order of N_2 is lowered when binding to E_4, the conversion between E_4(4H) and E_4(2N2H) technically requires no additional energy input, and the process is reversible in the presence of H_2. In fact, this reversibility is what allows H_2 to act as an inhibitor of N_2 reduction. This phenomenon has also been exploited to investigate N_2 binding. If isotopically labeled D_2 ($^2H_2$) is mixed with N_2, the wild-type NifDK can produce HD gas, and, if separately, T_2 ($^3H_2$) is mixed with N_2, NifDK does not significantly accumulate mixed label TOH.[56–60] This means that the reversible H_2 production through N_2 binding is not a simple proton exchange process with solvent, which supports the notion that hydrides (H^-) are generated in the Lowe-Thorneley model.[52,60] Moreover, the relative rates between the forward and reverse reactions have been proposed to favor N_2 reduction over N_2 release,[52,149,150] but these rates change when moving to the alternative nitrogenases.

Protons are also reduced by nitrogenase in a hydrogenase-like process (hydrogenases are discussed in Section 3) that competes with other substrate reduction reactions, but also occurs in the absence of substrates such as N_2, C_2H_2, or CO.[55] Additionally, there is no known additive that can increase the proton reduction of the wild-type enzyme, and it is unclear what the site(s) of proton reduction is. This can complicate analysis of nitrogenase catalysis, as often enough N_2 or acetylene reduction is reported without proton reduction under the same conditions. Consequently, it becomes difficult to rigorously compare systems, particularly from single-point mutagenic studies. For instance, if N_2 reduction decreases between two NifDK variants, the proton reduction under those same conditions could either increase or decrease, and each scenario would lead to a different conclusion. There is also difficulty in the accurate measurement of NH_3/NH_4^+ produced from catalysis compared to gaseous H_2, particularly at low concentrations. For this reason, acetylene is often used as an N_2 surrogate due to the analogous triple bond and gaseous nature of both the substrate and product states. Acetylene was first discovered as a competent substrate for nitrogenase in 1966 by Michael J. Dilworth,[193] and since then it has become crucial to the study of the nitrogenase mechanism despite the nonphysiological role the substrate plays.[51,52,100,194] Wild-type Mo-nitrogenase reacts with C_2H_2 such that >90% of electron equivalents are funneled to produce exclusively ethylene (C_2H_4), substantially

attenuating the H^+ reduction pathway.[100,195] The alternative substrate is thought to bind to the nitrogenase E_1 or E_2 states, although, C_2H_4 is not released from the protein until three proton/electron equivalents are delivered to the M-cluster so that the E_1 state can be reformed.[195] This is in contrast to the proposed N_2 binding states of E_3 or E_4, the latter of which is proposed to be the only productive binding state that results in N_2 reduction (Figure 6). Further, the analysis of acetylene reduction in the presence of the nitrogenase inhibitor carbon monoxide (CO) has led to the proposal that there are multiple substrate binding sites on the M-cluster, and that N_2, C_2H_2 and CO occupy different positions.[195] Finding where the substrate binding sites are located as well as the properties of each has been a driving force behind the analysis of single-point mutations of NifDK. There have been many amino acid residues that have been targeted for single-point mutagenesis, and herein, only examples pertinent to the outer sphere effects on catalysis will be discussed. Table 3 summarizes some of the available assay data for NifDK variant proteins.

In the 1990s, NifDK variants at the α-Q191 (+, +, +) and α-H195 (−, 0, +) residues were reported based on sequence conservation among NifDK analogs, and between NifDK and the biosynthetic protein NifEN.[182,185,187,188] The cells of variant α-Q191K and α-H195N NifDK expressing strains had a Nif^- phenotype where the cells did not appear to grow without the addition of a nitrogen source (such as ammonium chloride or urea).[182] This indicated that these NifDK variants were unable to reduce N_2 under standard conditions. Crude extracts of cells expressing α-Q191K and α-H195N NifDK variants were found to yield no N_2 fixation products, however, reaction with C_2H_2 produced C_2H_4 with <10% of the activity of the wild-type enzyme. Furthermore, ethane (C_2H_6) was found as a product from the variant protein strains, with 12.5% and 35% of the electron equivalents diverting toward ethane production for the α-Q191K and α-H195N NifDK proteins, respectively.[182] This was an interesting result at the time because it demonstrated that the M-cluster site was likely nearby the targeted residues prior to the publication of crystallographic data.

The α-Q191K NifDK protein was purified in 1992 and the reactivity of the enzyme was found to be ~30% of the activity of the wild-type NifDK. It produced no N_2 reduction products, and diverted 90% of electron equivalents to the production of H_2 in the presence of C_2H_2, compared to wild-type enzyme that uses 90% of electron flux to generate C_2H_4.[185] Subsequent characterization has shown that the Michaelis constant (K_m) for C_2H_2 to produce C_2H_4 is 35 kPa, 2 orders of magnitude higher than that for the wild-type enzyme (K_m = 0.5 kPa), indicating that acetylene is not a great substrate for α-Q191K NifDK.[183] It has been further demonstrated that α-Q191K NifDK does not react with C_2H_4 to produce C_2H_6, in contrast to wild-type NifDK that will produce only a small amount (<1% of electron flux) of C_2H_6 from C_2H_4 when C_2H_2 is absent. This and isotope labeling experiments led to the assertion that there must be a longer-lived, common ethylenic intermediate that can be differentiated to release ethylene, or ethane.[183] The lack of N_2 reduction was also explored through the introduction of N_2 gas into C_2H_2 and proton reduction assays.[139] Under standard conditions, wild-type NifDK will divert electron flux from proton reduction to N_2 reduction if N_2 is introduced into the reaction vessel, indicating that N_2 binds to or otherwise interacts with the M-cluster. HD will also be observed as a product in the presence of both N_2 and D_2. In contrast, α-Q191K NifDK does not appear to even bind N_2 because the catalytic performance is unaffected when N_2

is added into the typical acetylene or proton reduction assays.[139] When mixtures of N_2 and D_2 are added to reactions of α-Q191K NifDK, the product HD is absent, consistent with a lack of N_2 binding as well as an inability to access the E_4 state. A rationalization provided for these observations is that the α-Q191K variant is unable to even reach the E_3 level of the Lowe-Thorneley cycle (Figure 6).[139] From crystallography, it is known that α-Q191 is in proximity to the *R*-homocitrate ligand, and both the protein residue and the ligand are involved in hydrogen-bonding interactions,[65,85,151] potentially causing deleterious modulation of the redox properties of the M-cluster. Interestingly, when *R*-homocitrate is exchanged for citrate in a Δ*nif V* variant of NifDK from *K. pneumoniae* (see below), N_2 reduction decreases to 40% of the wild-type activity, diverting more electron flux toward the production of H_2 that exceeds that for the wild-type NifDK; yet, the Δ*nif V* NifDK variant is still capable of binding N_2.[196] Clearly, α-Q191 plays a key role in regulating the energetics in the active site, but the mechanism by which this is accomplished remains elusive.

In parallel, α-H195 (−, 0, +) variants have also been purified and studied.[139,183,187,188] The initial report of α-H195N showed that the enzyme was relatively unstable, did not have a high reactivity toward C_2H_2 and proton reduction compared to wild-type, and was unable to form N_2 reduction products.[182,185] EPR spectra of whole cells indicated that while α-H195N NifDK showed a low intensity $S = 3/2$ M-cluster signal, the α-H195Q variant had an EPR signal of comparable intensity to wild-type enzyme with some perturbations of the *g*-values, suggesting that the electronic properties of the cluster had not substantially changed.[187] The α-H195Q variant showed a modest decrease in activity toward C_2H_2 compared to wild-type enzyme, but there was no observable products of N_2 reduction, even under acid-quenched conditions that would yield N_2H_4 in wild-type NifDK.[198,199] However, in the presence of N_2, the α-H195Q protein proton reduction was reversibly inhibited by slowing the reaction rate, but did not divert electron flux toward other observable products.[187] This indicated that N_2 would bind to the M-cluster of the variant, but would not become reduced. To further explore this notion, Fisher and co-workers increased the pressure of N_2 used in reduction assays of α-H195Q NifDK and saw that under hyperbaric conditions, NH_3/NH_4^+ was observed at a rate <2% of the wild-type enzyme.[188] Additionally, in the presence of a mixture of N_2 and D_2, α-H195Q NifDK produced measurable HD gas, indicating that the protein variant could access the same E_4 state as the wild-type enzyme, but could just not reduce N_2 well. A crystal structure of the α-H195E NifDK protein was later published, showing that in agreement with EPR spectra, the N–H–S2B hydrogen bond stayed intact in the α-H195Q variant like that in the wild-type protein.[184] Thus, the hydrogen bond does not sufficiently control N_2 reduction capabilities, and additional factors, such as proton donors and redox potentials, should be considered. The α-H195N variant was also tested for the ability to bind N_2, and it was found that N_2 would inhibit proton reduction much like in the α-H195Q variant, but no HD evolution was measured. This suggests that the α-H195N variant could bind N_2 (that is, achieve the E_3 state) but was unable to reduce N_2 (that is, unable to access the E_4 state).[139] In this case, it is unlikely that any hydrogen-bonding interaction between α-N195 and the M-cluster exists, but the protein is still able to bind, but not reduce, N_2. In comparison, α-Q191K NifDK likely maintains the hydrogen bond between α-H195 and S2B of the cofactor, but the protein variant is unable to bind N_2 at all.

Acetylene reduction was also investigated with the variant α-H195 proteins, and it was found that N_2 would inhibit the production of both C_2H_4 and C_2H_6, but this inhibition could be reversed with H_2.[139,183,188] In the presence of 10% acetylene, the α-H195N and α-H195Q proteins used 69% and 55% of electron equivalents to generate reduced products, but the former protein yields both C_2H_4 and C_2H_6 while the latter yields C_2H_4 exclusively.[183] The α-H195Q protein behaves similarly to wild-type enzyme, with a K_m for C_2H_2 of 0.5 kPa for both enzymes, and neither producing C_2H_6 from C_2H_2; however, the α-H195Q NifDK variant is less efficient than the wild-type enzyme in C_2H_2 reduction. In comparison, the α-H195N variant has an affinity for C_2H_2 (K_m = 1.0 kPa) similar to that of the wild-type enzyme but produces ethane which accounts for 23% of the total electron flux. Ethylene was also tested as a substrate for the variant proteins in comparison to the wild-type enzyme, with a K_m value of 120 kPa measured for both wild-type and α-H195Q proteins (though the latter uses less than 1% of total electron flux toward ethane production) and a K_m value of 48 kPa measured for the α-H195N variant (alongside a 10-fold increase in activity). These experiments revealed that the high affinity for acetylene in the wild-type enzyme and α-H195Q variants likely prevents ethane production, because once ethylene is produced, it is rapidly replaced by a new molecule of acetylene.[183] The slightly lowered affinity for the substrate in α-H195N NifDK may explain why ethane can be observed as a product, but it is possible that the steric environment also contributes, as asparagine has a shorter side chain than glutamine. These acetylene reduction experiments, in comparison to N_2 reduction, illustrate that more rigorous conditions are required for the cleavage of the triple bond of N_2 compared to alkyne or alkane substrates.

To better identify and understand substrate binding sites on the M-cluster, additional mutations of nitrogenase were studied.[174–178,180] In wild-type NifDK, several observations have been made with respect to the competition between N_2 and acetylene binding to the catalytic cofactor; specifically, it has been shown that two binding sites with different affinities for acetylene exist, and that acetylene is a noncompetitive inhibitor of N_2 reduction while N_2 is a competitive inhibitor of acetylene reduction.[193,200–203] Additionally, C_2H_2 has also been found to be a more potent inhibitor of N_2 reduction under low electron flux conditions, where the rate of electron delivery is decreased, compared to those under high flux conditions.[204] In 2000, a study was reported that used an *Azotobacter vinelandii* strain expressing a NifDK variant with a β-Y98H (+, −, +) mutation, which was shown to have a lower electron flux, as a progenitor for a genetic study.[174] The β-Y98H variant would not grow well under diazotrophic conditions in the presence of 2.5% C_2H_2, because N_2 reduction by the low flux NifDK protein would be strongly inhibited by C_2H_2. The goal was to screen for a mutation that would remove the acetylene sensitivity while maintaining similar levels of N_2 reduction activity. After analysis, it was found that in addition to the β-Y98H mutation, an α-G69S (+, −, +) mutation would allow for cells to grow under N_2 fixing condition in the presence of C_2H_2. A separate protein was then generated that only possessed the α-G69S mutation. The Michaelis–Menten parameters of the α-G69S NifDK protein for C_2H_2, N_2, and proton reduction were similar to those of the wild-type enzyme, indicating that this mutation did not affect nitrogenase activity. In contrast, the affinity for C_2H_2 decreased for α-G69S NifDK (K_m = 14.2 kPa) compared to wild-type enzyme (K_m = ~0.71 kPa), and the variant protein now showed a competitive inhibition of N_2 reduction

in the presence of C_2H_2, instead of a noncompetitive inhibition.[174] The rationale for these observations was that the mutation of α-G69 removed the high-affinity C_2H_2 binding site through steric changes nearby the M-cluster. However, the authors proposed that α-V70 was the actual residue that blocked the substrate binding site, due to the closer proximity to the cofactor. They also identified that α-R96 is positioned nearby α-V70 and is likely to be involved in determining access to the binding site. A separate study concluded that using the α-G69S NifDK protein, two substrate binding sites could be better distinguished on the α-V70 (0, −, +) face of the cluster.[175] One site is denoted as a "high-affinity site" for acetylene binding that may also accommodate CO but not N_2, N_2O, and N_3^-. The other site is designated the "low-affinity" acetylene-binding site that also binds CO, N_2, N_2O, and N_3^-.

Substitutions of the α-R96 (+, −, 0) and α-V70 (0, −, +) positions in NifDK were then explored for their effects on the access and binding of substrates and inhibitors.[176,180] In 2001, multiple mutations of α-R96 were reported, and it was shown that the EPR spectra of all of the NifDK variants were essentially the same as the spectrum of the wild-type enzyme.[180] This result was used to conclude that the substitution had little to no effect on the electron properties of the M-cluster, and as such, the authors selected the α-R96L NifDK variant as a representative example to further study. When high concentrations of C_2H_2 were added to the protein, a new EPR signal appeared in a 70% acetylene atmosphere with g-values of 4.5, 3.5, and <2.0, constituting 40% of the total spin (Figure 11). The addition of N_2 or CO did not affect the appearance of this signal, which is totally absent in the wild-type enzyme. It was found that addition of CN^- to α-R96L NifDK would yield a new paramagnetic species with a g-value at 4.5, that also was absent from the wild-type system. Pulsed electron nuclear double resonance (ENDOR) experiments with ^{13}C-enriched acetylene and cyanide showed that CN^- definitively binds to the M-cluster, while it was inconclusive if C_2H_2 did as well, but in both cases the new EPR signals were derived from the M- as opposed to the P-cluster.[180] These results led to the conclusion that α-R96 must play a steric "gatekeeping" role during catalysis. The change in size of the α-R96 residue presumably opened the active site allowing the small molecules to bind on or near the M-cluster. However, this finding should be taken with some scrutiny: the concentrations required to affect a change in the EPR spectrum are far beyond what is required under usual catalytic conditions, and other molecules, such as N_2, CO, and N_3^- do not cause perturbations in the EPR spectrum of α-R96L NifDK. Interestingly, the α-R96 variants do not product ethane, in contrast to α-Q191 and α-H195 variants.[205] The α-R96 variants do all have different affinities and rates for the reduction of C_2H_2, some similar to wild-type enzyme while α-R96L NifDK has a 3-fold higher affinity, so it is unclear to what extent physiologically relevant conclusions can be made.

In 2002, a follow up to the mutagenesis study of α-G69 NifDK was reported with the substitution of α-V70 (0, −, +) for alanine.[176] The α-V70A NifDK protein was able to grow under diazotrophic conditions, indicating that N_2 reduction was unaffected by the substitution. The active site access of the variant compared to wild-type enzyme was assessed through the introduction of the water-soluble acetylene derivate propargyl alcohol ($HC{\equiv}C–CH_2–OH$). When added to the growth media, the wild-type enzyme was unaffected while the α-V70A protein was unable to grow, presumably due to a larger substrate pocket

that allows the larger alcohol in. Propargyl alcohol was a potent inhibitor of α-V70A NifDK with respect to proton and N_2 reduction, but direct reduction of propargyl alcohol resulted in propene ($H_2C = CH–CH_3$; 4-electron product) as a minor product, as well as allyl alcohol ($HC = C–CH_2–OH$; 2-electron product) as the major product. Propyne ($HC{\equiv}C–CH_3$) was also found to serve as a substrate for α-V70A NifDK, producing the 2-electron product propene, in contrast to the wild-type enzyme where propyne is a poor substrate.[55,59] Additionally, α-V70A NifDK was unable to produce ethane from the reduction of acetylene.[176] Dean, Seefeldt, and co-workers then published a study of the NifDK protein, using the smaller (α-V70A) and larger (α-V70I) side chain variants to study the effect the substitutions at α-V70 had on N_2 reduction.[177] The ability of the α-V70I variant to reduce N_2 was decreased by ~70% compared to wild-type enzyme while electron flux was diverted toward proton reduction, with a concomitant increase in the K_m values for N_2 reduction from K_m = 0.1 atm to >1.5 atm. Acetylene reduction was analogously affected with a substantial decrease in C_2H_4 production, and an increase to both proton reduction and the K_m value compared to wild-type NifDK. These results were rationalized by stating that the longer side chain of isoleucine must impinge on the “catalytic face” of the M-cluster where N_2 and C_2H_2 bind, including Fe2, Fe3, Fe6, and Fe7 from the crystallographic labeling scheme (Figure 7). Substitution of glycine at position α−70 resulted in a nitrogenase protein (α-V70G) that is unable to react with N_2 at all, but maintains activity with acetylene and larger carbon-based substrates.[178] The lack of N_2 reduction with the smallest side chain variant was attributed to the inability to access higher redox states of the M-cluster, but this hypothesis was not further tested. A double mutation consisting of α-V70A and α-Q191A was also generated, and the enlarged substrate pocket allowed for longer chain alkynes, such as 2-butyne ($H_3C–C{\equiv}C–CH_3$), to be reduced near the proposed reactive site at Fe6 on the M-cluster.[178] Undoubtedly, the second coordination sphere environment is important for determining substrate access through steric effects, but with the drastic changes that sometimes occur “globally” in variant proteins, it is logical to be cautious in extending insights gained from the variants to the native system. The α-V70I and α-V70A NifDK proteins have been used to trap and study a variety of intermediate states with a battery of spectroscopic and computational techniques, the like of which have been described at length elsewhere[52,60,206] and will not be further discussed in this review.

Recently, a crystal structure was published by Ribbe, Hu, and co-workers that provides some structural insight into substrate binding on wild-type NifDK.[91] Previous attempts at trapping intermediates of nitrogenase have employed single-point mutations in combination with rapid freeze-quench techniques that can capture transient species.[52,60,206] The strategy used in the recent crystallographic study involved isolation of NifDK in an anaerobic environment that did not contain the exogenous reductant dithionite ($S_2O_4^{2}$).[91] Previous work has shown that when dithionite and other sulfur sources are stringently excluded from *in vitro* maturation assays, an M-cluster precursor called the L*-cluster ([8Fe-8S–C]) can be isolated on NifB that lacks a μ_2-sulfide ligand that it otherwise binds in the presence of dithionite.[133] This sulfur-deficient cluster cannot be matured into the active M-cluster unless a source of SO_3^{2-} is added, which is usually provided by the decomposition of dithionite. Drawing from this inspiration, it was reported that when NifDK was anaerobically purified under a N_2 atmosphere in the absence of dithionite (denoted NifDK*), the resultant

protein was initially unreactive toward substrate reduction.[91] However, reactivity could be restored upon the addition of dithionite. When cells expressing NifDK* were grown in the presence of $^{15}N_2$, the subsequent protein was reported to have $^{15}N_2$ bound, as acid quenching samples of NifDK* yielded labeled N_2 by gas chromatography mass spectrometry (GC-MS) analysis. The labeled N_2 ligand was not observed when dithionite was included as part of the purification protocol.

Isolated NifDK* was then crystallized, and a structure was solved that contained M-clusters with additional electron density between central Fe ions of the cluster (Figure 12).[91] Not only that, the two M-cluster sites within the heterotetrametric NifDK each had different sets of electron density; at 'Site 1', this density appeared in the usual place of S2B (0, 0, +), and at 'Site 2', density was observed in the location of S3A (0, +, −) and S5A (0, −, −). On the basis of anomalous sulfur density, it was concluded that Site 1 lacked a sulfur atom at the S2B position, and Site 2 lacked sulfur atoms at both S3A and S5A. During refinement, best fits of the data resulted in N_2 molecules displacing the respective sulfur atoms at the two different M-cluster sites. At Site 1 (Figure 12A), the N_2 unit appears in a pseudo $\mu_{1,2}$-bridging mode with N6A sitting 1.8 Å from Fe2 and N6B being 2.3 Å from Fe6. N6A is also within 2.9 Å of α-H195 (−, 0, +), indicative of a potential hydrogen-bonding interaction. A stabilizing interaction between the putative N_2 unit and α-H195 would be consistent with observations from the mutagenesis studies described in this review.[139,182–185,187] At Site 2 (Figure 12B), the N_2 units are bound in asymmetric $\mu_{1,1}$-bridging modes where the proximal N atom is within 1.8 Å of one Fe ion, and 2.1 Å from the other Fe (with the Fe pairs Fe4/Fe5 for the "S3A position" and Fe7/Fe3 for the "S5A position", respectively).[91] The distal N atom at the S3A position is 2.9–3.4 Å from the backbone amide groups of α-G356 (+, +, 0) and α-G357, and at the S5A position, the distal N is within 3.2 Å of the side chain of α-R96 (+, −, 0) and a water molecule, also suggesting potential hydrogen-bonding interactions. These positions have not been previously proposed as substrate binding sites, which is an interesting finding, although in crystal structures of V-nitrogenase, an unusual carbonate (CO_3^{2-}) ligand is found to displace the equivalent S3A atom.[92–95] Additionally, in both Site 1 and 2 of sulfur-deficient NifDK*, the *R*-homocitrate ligand appears to be bound to the Mo center through one O atom exclusively; at Site 1 the O atom from the −OH group is 2.7 Å from Mo and the $-COO^-$ group is closer, while at Site 2 the opposite is observed.[91] This could potentially indicate protonation, which may elongate the refined Mo–O distances, consistent with the proposed role *R*-homocitrate may play in proton transfer, but additional evidence is required to validate the protonation states. Strikingly, when NifDK* is put under turnover conditions in the presence of dithionite and then recrystallized (PDB ID 6VXT), the cofactor returns to the normal resting state of NifDK, indicating that the displacement of sulfur is not deleterious but rather reversible.[91] The resolution of the crystallographic data for NifDK* does not allow for the absolute determination of the N_2 unit as a reduced species or otherwise;[207–209] however, the assignment of the N_2 unit is supported by available structural data, and it would further validate the importance of residues such as α-H195 and α-R96, as well as the "catalytic face" of the M-cluster, while putting forward sulfur displacement as a critical mechanistic necessity for substrate reduction by Mo-nitrogenase. A recent study by Hu, Ribbe and coworkers[723] confirmed binding of N_2 to NifDK* in a catalytically competent conformation, showing formation of C_2H_3D in the C_2H_2 reduction

assay (an equivalent to HD formation in the absence of C_2H_2) of NifDK* where only D_2 was supplied instead of a D_2/N_2 mixture, appearance of new $S = 1/2$ features in the EPR spectrum of NifDK* concomitant with a decreased intensity of the M-cluster-associated $S = 3/2$ signal, and release of $^{15}NH_3/NH_4^+$ upon turnover of the $^{15}N_2$-bound NifDK*. In addition, this report revealed that product release only occurred via displacement by sulfite-derived belt-sulfide, and that catalysis involved all belt sulfur locations that were shown to be labeled with selenite-derived selenides in a XAS pulse chase experiment. These observations provide support to a previously proposed mechanism involving a stepwise reduction of N_2 at position S3A, S2B, and S5A that occurs asynchronously in the two $\alpha\beta$-dimers of NifDK.[91] Further crystallographic, biochemical, spectroscopic, and computational work will be required to explore and validate these unique findings.

2.5.2. Inhibition by and Reduction of Carbon Monoxide.—Carbon monoxide has long been characterized as an inhibitor of nitrogenase reactivity in the Mo-dependent systems that affects the reduction of all substrates apart from protons.[52,100,200,210] Mo-nitrogenase has multiple CO-related states that have been spectroscopically characterized under different conditions and concentrations of CO.[52,62] Under low electron flux conditions (1:5 Fe:MoFe protein) and in the presence of low concentration of CO (<1% in argon), the typical $S = 3/2$ EPR signal associated with the M-cluster converts to an $S = 1/2$ signal with g values of 2.09, 1.97, and 1.93 (designated the “lo-CO state”), whereas under high concentrations of CO (>50% in argon) a new $S = 1/2$ signal arises (designated the “hi-CO state”) with $g = 2.17$ and 2.06 (Figure 13).184,202,203,211–213 Under higher electron flux conditions (1:1 Fe:MoFe protein) and high concentrations of CO, a third state known as “hi(5)-CO” was observed in wild-type NifDK, with g values of its EPR signature at 5.78, 5.15, and 2.7 (Figure 13).[181,184,211] A low intensity EPR signal was observed for VnfDGK in the presence of 1 atm of CO with g values at 2.09, 1.99, and 1.91, and the intensity of this signal could be increased with more potent reducing agents.[214,215] By comparison to NifDK, the EPR signal in VnfDGK was assigned to the lo-CO form of the enzyme. In the presence of strong Europium-based reducing agents and 2.6 atm of CO, a new set of EPR signals were observed that could be described as the superposition of the lo-CO state, and a newly identified species with g-values at 2.13, 2.01, and 1.97.[215,216] Although not identical, this new signal was assumed to be analogous to the hi-CO state of NifDK. No equivalent of the hi(5)-CO state has been reported for the VFe protein.

As the crystallographic characterization of CO-bound states was not reported until 2014,[89] many of the earlier studies employed competitive substrate reduction experiments, where separate N_2, C_2H_2, and proton reduction assays were compared in the presence and absence of CO.[51,52] The behavior of nitrogenase in the presence of multiple substrates could then be analyzed and extrapolated to provide insight into CO-bound states of the M-cluster. Additionally, a series of spectroscopic and computational studies revealed EPR signals associated with CO binding to Mo-nitrogenase. As described above, an $S = 1/2$ spin species trapped under low concentrations of CO was designated “lo-CO”, and at higher CO concentrations, another $S = 1/2$ signal would appear that was assigned “hi-CO”.[202,211,217–221] When the initial characterization of V-dependent nitrogenase was undertaken, it was found that CO inhibited reactivity in a similar manner to Mo-nitrogenase,

so it was reasonable to anticipate analogous EPR signals in V-nitrogenase. Hales and co-workers constructed a hybrid nitrogenase that used the polypeptide of V-nitrogenase from *A. vinelandii* and the M-cluster from the *A. vindelandii* Mo-nitrogenase (hereafter labeled M-VFe protein).[222] It was found that the hybrid M-VFe protein had an activity profile more like the native V-nitrogenase. However, in the presence of CO, no EPR signals analogous to the lo-CO or hi-CO signals of Mo-nitrogenase could be observed, although the M-VFe protein carried the same cofactor as the native Mo-nitrogenase. This result was puzzling, but was a strong indication that second and outer coordination sphere effects played a pivotal role in determining the properties of nitrogenase.[51,222] Later, it was shown by Ribbe and co-workers that *Av* V-nitrogenase (and to a lesser degree, wild-type *Av* Mo-nitrogenase) could catalyze the coupling of gaseous CO into longer chain hydrocarbon products following Fischer–Tropsch-like chemistry, but with an observed decrease of ~75% in the specific activity for proton reduction by the V-nitrogenase.[223–225] This finding further expanded the known capabilities of the Mo- and V-nitrogenases, but still lacked a comprehensive structural understanding of CO activity.

With the advent of crystallographically characterized, CO-bound intermediates, insight into structural features of CO binding to nitrogenase could be obtained.[89,94,95,226] In 2014, Spatzal, Rees, and co-workers published the first structure of CO binding to the M-cluster of NifDK (designated NifDK-CO), which corresponded to an inhibited state of the enzyme (Figure 14A).[89] The CO molecule is ligated between Fe2 and Fe6 of the M-cluster in a μ_2-binding mode, apparently displacing the μ_2-S2B sulfur atom that is usually found in resting state structures of NifDK.[61,66,151] The CO ligand is bound symmetrically between the two Fe ions, with Fe–CO distances of 1.86 Å to both metal centers, and the oxygen atom of the CO moiety within close proximity to the side chains of residues α-H195 (2.8 Å) and α-V70 (3.4 Å). The interaction between α-H195 and CO is within the range of a hydrogen bond, which would affect the stability of the CO moiety, while nonbonding interactions from α-V70 may provide stability. When crystals of NifDK-CO were dissolved into buffer in the absence of exogenous CO, the S2B atom and acetylene reduction activity were quantitatively recovered.[89] EPR spectra of NifDK-CO in the solution state, obtained under analogous conditions to crystallography, demonstrated the appearance of an $S = 1/2$ signal previously assigned to the lo-CO species, connecting observation derived from spectroscopy and structural biology.[214]

Recently, Spatzal, Rees, and co-workers reported another CO-bound crystal structure of NifDK (Figure 14B), but with two CO ligands (designated NifDK-(2CO)) as opposed to one.[226] This species was isolated when crystals of NifDK-CO were pressurized with CO at 5.4 atm. The first CO ligand ("μCO") is found in a bridging position between Fe2 and Fe6 of the M-cluster in a μ_2-binding mode analogous to that in NifDK-CO, with Fe–CO distances of 1.93 and 1.92 Å, respectively. The second CO ligand ("tCO") is bound in a terminal mode to Fe6, with an Fe–CO distance of 2.03 Å. Binding of tCO causes the Fe6–C distance to slightly elongate from 2.01 Å in NifDK-CO to 2.06 Å in NifDK-(2CO).[89,226] The oxygen atom of tCO may interact with the amide N of the α-Q191 residue (~3.3 Å) and a carboxylic acid group of *R*-homocitrate (~2.7 Å), while μCO maintains analogous interactions with the side chains of α-V70 and α-H195, in a similar manner as in NifDK-CO. Compared to μCO that is modeled with 100% occupancy, tCO is modeled with only 50% occupancy, likely

because the binding of this ligand is relatively weak. Parallel EPR spectra of the solution state and crystal slurry of NifDK-(2CO) were subsequently used to assign μCO and tCO to the lo- and hi-CO states, respectively.[226]

Analogous crystal structures were solved by Einsle and co-workers of the V-dependent nitrogenase with one (VnfDGK-CO) and two (VnfDGK-(2CO) CO molecules bound (Figure 15).[94,95] In the 1.0-Å resolution structure of VnfDGK-CO, the CO molecule is bound in a μ_2-bridging mode between Fe2 and Fe6, much like that found in the lo-CO state of NifDK-CO, but with a slight asymmetry (Fe2–CO = 2.03 Å, Fe6–CO = 1.94 Å).[94] The μCO ligand has similar interactions with local amino acid side chains, being within 2.9 Å of α-H180 and 3.6 Å of α-V57 (analogous to α-H195 and α-V70 in NifDK), respectively. Unlike NifDK-CO, when VnfDGK-CO crystals were used for activity assays in the absence of exogenous CO, the typical S2B ligand was not found between Fe2 and Fe6. Instead, a monatomic ligand interacting with the nearby α-Q176 residue was observed and assigned as a putative μ_2–OH species. The authors proposed that this oxygen-based ligand might result from reduction of a previously bound CO ligand.[94] When crystals of VnfDGK-CO were pressurized with 1.5 atm of CO for 1 min, a 1.05 Å crystal structure of the VnfDGK-(2CO) was obtained (Figure 15B).[95] The μCO ligand in VnfDGK-(2CO) is positioned in the same manner as that in VnfDGK-CO, and the terminal CO ligand is bound to Fe6 with an occupancy of 50%, analogous to that observed in the structure of NifDK-(2CO); however, the tCO in VnfDGK-(2CO) has an Fe6–tCO distance of 1.89 Å, compared to 2.03 Å in NifDK.[95,226] The oxygen atom of tCO in VnfDGK-(2CO) is also in close proximity to the *R*-homocitrate ligand (~2.9 Å) and the α−176Gln residue (~3.1 Å). Despite the high degree of similarity in active site for the two structures, the tCO ligand appears to be more strongly bound in VnfDGK-(2CO) versus NifDK-(2CO), which may align with the difference in reactivity observed for both systems.[51] However, there are strong indications that the lo-CO and not the hi-CO state of V-nitrogenase is catalytically competent for CO reduction.[215,216] A parallel set of EPR measurements using solution and crystal slurry samples of VnfDGK-(2CO) was not reported by Einsle and co-workers,[95] so the crystallography could not be directly connected to the available spectroscopic characterization of the lo- and hi-CO states. Instead, *in situ* Fourier-transform infrared (FTIR) difference spectroscopy was conducted using a film of VnfDGK in the presence of N_2 and CO isotopes.[95] Supporting the crystallographic assignment, isotopically sensitive features at 1931 and 1888 cm^{-1} were assigned to $t^{12}CO$ and $t^{13}CO$, respectively. Because of strong background signals at lower frequencies, a vibration for the $\mu^{12}CO$ could not be assigned unambiguously, but a putative signal was identified at 1720 cm^{-1}. More work will be needed in the future to fully understand the structure–function relationships gleaned from these structural studies.

On the basis of the crystallographic information, what can be said is that α-Q191, α-H195, and α-V70 in NifDK (and equivalent analogs in VnfDGK) are residues that can interact with the catalytic cofactor when CO molecules are bound. The α-H195 residue is in hydrogen-bonding distance to the μCO ligand and has been proposed to be generally involved in proton delivery during substrate turnover.[227–229] The α-Q191 residue is within an appropriate distance from the tCO ligand to potentially interact with this ligand; additionally it helps stabilize the *R*-homocitrate ligand that binds to the Mo or V ion of the catalytic

cofactor.[95,226] As stated previously, the hi-CO state does not appear to be competent for CO catalysis,[215,216] thus binding to tCO may not be relevant, although the equivalent residue in VnfDGK, α-Q176, has been shown to stabilize a putative N_2 reduction intermediate through a hydrogen-bonding interaction, which further reinforces the importance of this residue.[93] These details regarding CO-bound species provide a measure of perspective that was previously inaccessible and allows for a retrospective look on experiments conducted to assess the structural basis of CO inhibition within nitrogenase.

2.5.2.1. Influence of Point Mutations on the Reaction with CO.: The research groups of Dean and Newton have generated a multitude of single-point mutants of NifDK that have been used to study substrate interactions with the enzyme, including CO. Many of these studies yield overlapping information regarding the properties of NifDK variants, including insights gleaned from experiments with crude extracts of *A. vinelandii* cells and purified variant proteins, so it can be difficult to comprehensively describe the results. Instead of addressing every possible variant reported, the effects of mutations to the α-H195 and α-Q191 residues on CO reactivity will be the primary focus of our discussion below, as well as relevant comparisons to other variants, as necessary.

As described earlier, the site-directed mutagenesis in NifDK of α-H195 (−, 0, +) and α-Q191 (+, +, +) to α-H195N and α-Q191K were reported for *A. vinelandii*.[182] The crude extracts of variant cells were individually assayed in an atmosphere of 10% acetylene (C_2H_2), demonstrating that the variant NifDK proteins were much less active than wild-type enzyme for the generation of C_2H_4, but they also produced some amount of ethane (C_2H_6), whereas wild-type NifDK does not. This raised interest in these variants, as crystallographic evidence would not be available for several years, and the pattern of reactivity was similar to that found for V-nitrogenases.[51] When C_2H_2 reduction assays were carried out, the α-H195N variant was less sensitive to inhibition by CO, showing 50% activity in the presence of 0.5% CO, compared to wild-type NifDK that showed the same decrease in activity already at 0.02% CO. It is important to note that these effects were observed with only the crude extracts, as the protein could not be purified at that time. EPR spectra of whole cells indicated that the $S = 3/2$ M-cluster signal was still present in the variant, albeit with axial perturbations, and at a low intensity (~6% compared to wild-type enzyme).[182,185] Several years later, five additional variants of α-H195 were reported.[187] Similar to the previous reports of α-H195N,[182,185] the crude extracts of the tyrosine, threonine, and glycine variants were not particularly active, but the glutamine and leucine variants expressed slightly higher activity, with α-H195Q NifDK maintaining ~70% the activity of crude extracts of wild-type enzyme.[187] Whole cell EPR of all variants had similar line shapes to wild-type enzyme, but the glycine and leucine variants had much lower intensities of the $S = 3/2$ signal (≤10%), whereas α-H195Q NifDK had comparable intensity to native enzyme, with slight perturbations of the g-values. The proton reduction activities in the presence and absence of CO were assayed, and it was demonstrated that the asparagine, glutamine, and leucine variants were relatively insensitive to CO, but α-H195T NifDK was sensitive to the presence of CO, with ~50% reduction of activity. The α-H195Q NifDK protein was further purified for more accurate comparisons to wild-type enzyme. It was found that CO was a noncompetitive inhibitor of C_2H_2 and N_2 reduction for both proteins, but CO

had a more potent inhibition of α-H195Q NifDK compared to wild-type enzyme. The authors suggested that α-H195 could be involved in steric interactions, as the much smaller glutamine residue would be unable to fill the same space as a histidine side chain, leaving room within the active site. Additionally, it was noted that the glutamine residue could still provide a hydrogen-bonding interaction to the S2B sulfur and, although the differential electronic effect of the histidine- and glutamine-derived interactions could modulate the redox potential of the M-cluster, it was not sufficient to completely change the activity profile. We now know that the S2B site is the location of the μCO ligand in the lo-CO state,[89] and by comparing a 2.5 Å crystal structure of α-H195Q NifDK[184] to the structure of the wild-type NifDK, we know that glutamine and histidine residues at position 195 have a similar distance to the S2B sulfur (Figure 16). This could rationalize why some of the other α-H195 variants do not generally exhibit any sensitivity to CO, that is, the responsible residues are simply too far from the μCO site to strongly interact with CO. The crystal structure also shows that the substitution of histidine with glutamine greatly destabilizes the local hydrogen-bonding network surrounding the M-cluster, complicating the interpretation. Moreover, different substitutions at α-H195 result in protein variants with CO-insensitive proton reduction and CO-inhibited acetylene reduction,[187] leading to the proposal of multiple CO binding site at the M-cluster. In pursuit of this idea, Newton, Fisher, and co-workers used the α-H195Q and α-H195N NifDK proteins in reactivity experiments with HCN, CN^-, and N_3^- in combination with CO.[183,188,191] For the variants, CO was found to remove the inhibitory effects of CN^- and N_3^-, implying that these classic nitrogenase inhibitors all bind to the same sites, albeit with different affinities. In this context, it should be noted that other GPMs like formate dehydrogenase (Section 4) and CO dehydrogenase (Section 5), CN^- and N_3^- inhibit activity, which highlights a functional connection between the low-valent metalloenzymes discussed herein. With respect to the binding site(s) of CO in nitrogenase, recent structural analysis shows that a second CO binds terminally to Fe6 of the M-cluster, and α-H195 is located near Fe2 and is generally unperturbed going from the NifDK-CO structure to the NifDK-(2CO) structure.[89,226] It may be possible for CO molecules (or other inhibitors) to bind to the Fe2 site on the M-cluster in α-H195 variants due to the change in the relative steric protection provided by the imidazole ring, underlining the importance of second coordination sphere effects. Additional structural information with other inhibitory molecules would be important for better understanding these complex effects.

The α-Q191 (+, +, +) residue of NifDK has been a target of mutagenic studies for as long as α-H195.[182,185] Crude extracts of α-Q191E and α-Q191K NifDK were assayed with C_2H_2 and in the presence of 0.02% CO, activities were inhibited by 50% and 75%, respectively.[185] The α-Q191K NifDK was then further purified, but the α-Q191E variant was not stable enough to sustain such a treatment. The purified α-Q191K NifDK protein exhibited an EPR spectrum that had similar line shape to that of the wild-type NifDK, but with perturbations to the g-values, suggesting that the M-cluster was bound to the protein similarly in both proteins. The introduction of 3% CO into substrate reduction assays showed that electron flux for reactions with α-Q191K NifDK decreased by about 70%, 40%, and 50% for N_2, C_2H_2, and proton reduction, respectively, compared to in the absence of CO.[185] This is an unusual finding considering that wild-type NifDK generally redistributes electron

equivalents from the reduction of N_2 and C_2H_2 toward proton reduction in the presence of CO.[51,185] Much like for the α-H195 variants, the purified α-Q191K NifDK was also assayed for proton reduction in the presence of both CN^- and CO.[191] The α-Q191K variant showed a mild inhibition of proton reduction in the presence of CN^-, and subsequent introduction of a 10% CO atmosphere further decreased the proton reduction activity. In contrast, the wild-type and α-H195 variant proteins show inhibition of total electron flux by CN^- but this activity is restored in the presence of CO. The result agrees with the previous observation of CO-derived inhibition of the electron flux for α-Q191K NifDK,[185] and additionally supports that α-Q191 likely can interact with both substrates and inhibitors.

It is now possible to glean additional insight from the crystal structures of NifDK-CO and NifDK-(2CO). Figure 14 shows how the α-Q191 residue of NifDK in both structures is bent away from the M-cluster, but the residue is in proximity to several molecules, 3.6 Å from an H_2O molecule, 3.3 Å from the tCO ligand and 2.9 Å from a terminal carboxylate of the *R*-homocitrate ligand.[89,226] Similar distances are also found for the analogous α-Q176 residue in the CO-bound structures of the V-nitrogenase (Figure 15).[94,95] In addition, it has been noted that the α-Q176 residue can swing in to interact with the V-cluster at the S2B position, so the residue is less static.[93] The closest and likely strongest interaction is between α-Q191 and *R*-homocitrate, so when glutamine is mutated to lysine, the side chain is extended by an additional carbon atom, which may introduce steric misalignment of the Lys residue in the active site. Lysine may clash with the tCO binding site, preventing substrate molecules from properly accessing the M-cluster. This would be consistent with an observation made by Hales, Newton, and co-workers that α-Q191K NifDK does not generate a hi-CO EPR signal and, by inference, does not bind tCO; instead, it only shows the lo-CO signal even under 100% CO atmosphere.[181]

2.5.2.2. Role of the Homocitrate Ligand.: While a physical blockage by lysine may be the source of the aberrant properties of α-Q191K NifDK, another important factor is that a disruption of the α-Q191–homocitrate interaction may destabilize the hydrogen-bonding network within the active site M-cluster, which is thought to be critical for proton delivery during catalysis.[102,181,229–232] When the *nif V* gene is deleted in a nitrogenase-expressing organism, the resulting Δ*nif V* NifDK protein has an M-cluster with citrate in place of *R*-homocitrate.[196,197] In the presence of 3% CO, crude extracts of Δ*nif V* NifDK from *K. pneumoniae* (*Kp*) demonstrated a ~50% decrease of proton reduction, similar to what was observed for α-Q191K NifDK.[185,196,233] Further investigation showed that CO would decrease the electron flow through *Kp* Δ*nif V* NifDK, and uncouple MgATP hydrolysis from electron transfer with a corresponding decrease to the observed proton reduction.[233] This analysis by Dixon and co-workers also indicated that CO was unlikely to be reduced by the variant Mo-nitrogenase from *K. pneumoniae*. Analogous Δ*nif V* NifDK variants were also generated in *A. vinelandii* (*Av*), showing a range of activities in the presence of CO.[181,234,235] Newton, Hales, and co-workers showed that proton reduction by *Av* Δ*nif V* NifDK was inhibited by ~40% in the presence of CO, a similar magnitude to that of *Kp* Δ*nif V* NfiDK, and that *Av* Δ*nif V* NifDK was capable of adopting the lo-CO, hi-CO, and hi(5)-CO states.[181,234] However, CO reduction by a Δ*nif V* NifDK protein was not reported until 2021 by Ribbe, Hu, and coworkers.[235] This protein, compared to wild-type

NifDK, expressed lower activities for all substrates, including CO. It was reported that the Mo content of the *in vivo* isolated *Av* Δ*nif V* NifDK was only ~30% of that in the wild-type protein, which may in part explain the observed low reactivity of the protein. To improve cofactor incorporation, an *in vitro* reconstitution of Δ*nif V* NifDK was carried out, which increased the M-cluster content and rendered the *in vitro* reconstituted variant higher in activity but similar in reactivity pattern as compared to its *in vivo* isolated counterpart. In the presence of CO, Δ*nif V* NifDK diverts more electron flux from proton reduction toward hydrocarbon formation while still maintaining lower specific activity than the wild-type enzyme. These observations were not made previously for the *A. vinelandii* variant because it was not reported that *Av* NifDK could reduce CO to hydrocarbons until 2011 when scaled up reaction conditions were used to detect low-yielding products for V-nitrogenase.[223] An analogous Δ*nif V* variant was also generated for V-nitrogenase, showing that citrate also binds to the V-cluster.[236] However, unlike the scenario in the Mo-dependent system, the Δ*nif V* VnfDGK protein produces a decreased amount of longer chain hydrocarbon products compared to wild-type VnfDGK, favoring a slight increase in proton reduction.

Initially, it was unclear what role the *nif V* gene product played in nitrogenase biosynthesis, but in 1990, Burris and co-workers reported that the organic ligand bound to the M-cluster was identified as citrate, which was subsequently confirmed in 2002 by Lawson and co-workers, who reported a 1.9 Å resolution crystal structure of the *Kp* Δ*nif V* NifDK.[197,237] The structure of the Δ*nif V* protein is highly similar to wild-type NifDK, but while *R*-homocitrate can form hydrogen-bonding interactions with the backbone amide of α-I423 (~2.8 Å), the citrate ligand in Δ*nif V* NifDK is further away from α-I423 (~3.7 Å) and requires H_2O molecules to facilitate an interaction.[237] This would potentially leave the citrate ligand loosely bound to the protein scaffold, disrupting the hydrogen-bonding network necessary for proton delivery to the M-cluster. An additional ramification would be that the loss of second coordination sphere interactions may also modulate the redox properties of the catalytic cofactor, similar to what was proposed for certain α-H195 NifDK variants (*vide infra*). This also means that it might be rather difficult to deconvolute the effects of α-Q191 substitutions from those of Δ*nif V* knockout proteins, because the Gln residue is involved in stabilizing interactions with the citrate ligand. However, there are distinct differences. The α-Q191K NifDK protein only supports the lo-CO EPR signal, while *Av* Δ*nif V* NifDK supports all three CO-based EPR signals. In fact, Newton and co-workers expanded investigations of CO on the reactivity of NifDK by introducing mutations to residues α-R96 (+, −, 0), α-R277 (−, +, +), and α-R359 (0, +, −).[181,186] In this study, CO-bound states were generated for a series of NifDK variants and EPR spectra were collected along with data from proton reduction assays to correlate the spectroscopic signals to catalytic activity. Wild-type NifDK, as well as α-R96Q NifDK, and *Av* Δ*nif V* NifDK all showed the lo-CO, hi-CO, and hi(5)-CO states. However, the variants α-R96K, α-R277C, and α-R359K adopted only the lo-CO and hi(5)-CO states, but not the hi-CO state. Interestingly, α-R277H only showed the hi(5)-CO signal. Inhibition of proton reduction by CO was also equally dynamic, with instances of no inhibition in α-R96Q but ~50% inhibition with the α-R96K substitution, among others.[181] Based on these observations, the authors concluded that the CO-related EPR signals and proton reduction activity could not be correlated, noting that the single-point mutations did not introduce

additional CO-binding sites.[181] The α-R277C NifDK variant was slightly different, in that it demonstrated a 70% increase in proton reduction in the presence of 10% CO compared to the wild-type enzyme.[186] With higher electron flux conditions, the proton reduction activity was enhanced, but dropping tchhe flux resulted in a lack of inhibition of proton reduction, although this reaction occurred at slower rates, similar to that observed in the case of the wild-type NifDK. It was proposed that CO binding to α-R277C NifDK affected catalytic proton transfer and additionally prevented the M-cluster from accessing more reduced states (i.e., E_3 and E_4 from the Lowe-Thorneley cycle). Instead, the variant may divert all the electron equivalents into the E_2 state which subsequently generates H_2.[186] It is unclear why CO binding would have such a different effect on the reactivity of the α-R277C variant as compared to the others, and more work is needed to gain further understanding of CO reactivity.

2.5.2.3. Reduction of Carbon Monoxide.: Attempts to stimulate CO reduction in Mo-nitrogenase have been carried out using combinations of point mutations to α-V70 (0, −, +), α-R96 (+, −, 0), α-H195 (−, 0, +), and α-Q191 (+, +, +).[179] Modifications of α-V70 in *Av* NifDK have been shown to increase the substrate scope of the enzyme by changing the steric environment around the M-cluster.[52,194] The α-V70G and α-V70A NifDK variants, were reported to react with CO, producing hydrocarbons ethylene (C_2H_4), propene (C_3H_6), ethane (C_2H_6), and propane (C_3H_8) in a ratio of 7:4:2:1.[179] These rates are much lower than those reported for the V-nitrogenase[223] and not directly compared with those for the wild-type Mo-nitrogenase under the same experimental conditions. Double mutations were then incorporated to assess the effect of α-R96, α-H195, and α-Q191 on the α-V70-mediated CO reactivity.[179] The α-V70A/α-R96H and α-V70A/α-Q191A NifDK variants show a different product pattern than the single substitutions, with similar values for all C_2 and C_3 products, as well as the inclusion of trace amounts of methane (CH_4). The α-V70A/α-Q191A NifDK, though, produces twice as much C_3H_6 than the α-V70A/α-R96H variant. Additionally, α-V70A/α-H195Q was shown to drastically decrease product formation compared to the single α-V70A NifDK variant. It is difficult to make definitive statements about the exact effect of point mutations in this case because of the interconnected nature of the second coordination sphere effects. What can be said is that the α-V70 residue seems important for regulating the size of substrates and products, consistent with previous observations.[52] The size reduction of the α−70 residue side chain presumably enlarged the active site to accommodate multiple CO molecules, and by extension, additional modification of α-R96 and α-Q191 further expanded the active site to favor the generation of longer chain hydrocarbons. However, the loss of activity in the α-V70A/α-H195Q NifDK protein shows that the size of the cavity is not the only factor governing reactivity toward CO. The α-Q191 and α-H195 residues are known to be involved in proton transfer,[102,181,229–232] but the present data may reflect a more direct role of α-H195 in protonation of reduced, CO-coupled species whereas α-Q191 may play more of a structural role. It may also be possible that substitution of α-Q191 could affect the rate of protonation and allow for intermediate species to accumulate, increasing the hydrocarbon length. Rigorous studies involving additional mutations that vary the size and proton donor ability of the side chains may be necessary to shed further light on the “steric

vs protonation" arguments for the reaction of CO with nitrogenase. It is also possible that yet unidentified factors, such as electron transfer rate or allosteric changes, may play a role.

2.5.3. Reduction of Carbon Dioxide.—The triatomic carbon dioxide (CO_2) is a highly oxidized small molecule that was found to react with Mo-nitrogenase in 1995.[238] CO was initially found as the product of the reaction, as the concentration of CO would increase only in the presence of NifH and MgATP, indicating it was a nitrogenase-dependent phenomenon. However, the exact substrate form, CO_2, CO_3^{2-}, or HCO_3^-, was unclear because of the equilibrium between CO_2 and bicarbonate (HCO_3^-) in solution. It was later reported by Ribbe and coworkers that NifDK was capable of generating CH_4 and C_2H_4 from from CO_2, although the rate of hydrocarbon formation was an order of magnitude slower than CO formation.[239] Interestingly, V-nitrogenase was found to reduce CO_2 to CO in H_2O buffers, but in deuterated buffers, deuterated hydrocarbons (CD_4, C_2D_4, C_2D_6) were observed while NifDK was unable to generate deuterated products under these same conditions. For both Mo- and V-nitrogenase, the specific activity of CO evolution from CO_2 increased in the deuterated buffer system resulting in an inverse kinetic isotope effect (KIE).[239] This could indicate that the formation of CO is carried out through similar mechanisms in both nitrogenases, but the change in hydrocarbon product profile between the two nitrogenases is reflective of something more complex that requires further investigation.

Subsequently, Mo-nitrogenase variants α-V70A and α-H195Q were shown to convert CO_2 into methane (CH_4), confirmed by use of ^{13}C-labeled bicarbonate.[240] Under the reported conditions, C_2 and C_3 hydrocarbon products were not observed. As the NifH:NifDK ratio in the reaction was increased, the rate of the competing proton reduction reaction decreased, diverting electron flux to the formation of CH_4. Even with a high electron flux (50:1), the primary product was H_2, which makes sense considering that proton reduction is a two-electron process, while the conversion of CO_2 to CH_4 requires eight electrons. To separate the reaction of the α-V70A and α-H195Q NifDK variants between CO and CO_2, deoxyhemoglo-bin was added to the activity assays so that any released CO molecule would be rapidly removed from the analysis.[240] The resultant reactions demonstrated a ~25% decrease in the production of CH_4, indicating that two different processes were being observed: one where CO_2 remains bound to nitrogenase throughout the reduction reaction and the other where CO dissociates and presumably rebinds to the M-cluster before reduction to CH_4. CO_2 reduction was further explored when the NifDK variant was incubated in an atmosphere of 45% CO and Ar, including 1–3% acetylene. Propylene (C_3H_6) was observed as the major product with propane (C_3H_8) as a minor component, and isotopically labeled ^{13}C atom from bicarbonate was found to incorporate into propylene. This indicates that one molecule each of CO_2 and acetylene can couple to form the product. Adjustments of the electron flux would favor CH_4 formation at a higher nitrogenase ratio and C_3H_6 formation at lower ratios. Additionally, introduction of ethylene to the CO_2 reaction did not yield propylene, suggesting that the mechanism requires that both molecules must bind and be activated by the cluster before they can be coupled.

It is interesting that in the double mutant α-V70A/α-H195Q NifDK, the reactivity with CO is inhibited compared to α-V70A NifDK, but the same α-H195Q mutation enhances the reactivity of the variant NifDK with CO_2. Electron transfer rates seem to be important

factors for determining the result of CO_2 reduction. A slower rate would favor reduced intermediate species that are long-lived, encouraging C–C bond formation, whereas faster electron delivery appears to more quickly generate CH_4, discouraging carbon coupling.[240] However, electron transfer in nitrogenase must also be understood in the context of proton transfer, because the two events are closely linked to each other.[63] In the α-V70A NifDK variant, CO molecules are readily coupled to form longer chain hydrocarbons, but this activity becomes disrupted when the α-H195 residue is exchanged for one less capable of proton transfer. The timing of proton-coupled electron transfer to the substrate is affected for CO reduction but happens to function well for the eight-electron reduction of CO_2. What should be emphasized is that a new activity was generated by controlling the second coordination sphere via the steric environment to house larger substrates in the active site niche and by tuning protonation of one of the oxygen atoms of CO_2 to generate CO and H_2O. Recently, CO_2 has also been converted to CH_4 by the wild-type Fe-only nitrogenase from *Rhodopseudomonas palustris*,[241] but without additional mutational or structural information about the Fe-only nitrogenase it is difficult to gain further insight into the factors that control CO_2 reduction. The structure and catalytic mechanism of other low-valent GPMs active in CO_2 reduction like formate dehydrogenase and CO dehydrogenase are discussed in Section 4 and Section 5, respectively.

3. HYDROGENASE

Hydrogen turnover (eq 2) is a important reaction in many microorganisms that thrive under reducing, anoxic conditions, and also plays a role in certain aerobes.[242–244] Trace amounts of H_2 provide electrons to power the anabolism of numerous archaea and bacteria in the soil, aqueous environments, or host tissue (H_2 oxidation or "H_2 uptake").[245–247] Under fermentative or "microaerobic" conditions, proton reduction and H_2 release have been shown to be a key in the redox regulation of autotrophs like photosynthetic bacteria and algae.[248–250] Additionally, H_2 contributes to the cellular redox equilibrium as a side product of N_2 fixation by nitrogenase, as discussed in Section 2. The GPMs responsible for proton reduction and H_2 oxidation are referred to as hydrogenases.[251]

Three classes of phylogenetically unrelated hydrogenases have been defined.[252] In archaea, [Fe]-hydrogenase is involved in the conversion of CO_2 to CH_4 (methanogenesis), catalyzing H_2 splitting and hydride transfer at a cofactor with a monometallic iron center.[253–255] Not much is known about the influence of second or outer coordination sphere effects, thus we will focus on the remaining two classes in this article. Unlike [Fe]-hydrogenase, [NiFe]- and [FeFe]-hydrogenase are iron–sulfur enzymes and carry a bimetallic active site cofactor (Figure 17).

[NiFe]-hydrogenases have been found in archaea and bacteria, and are typically involved in heterotrophic H_2 uptake and the "recycling" of H_2 during methanogenesis or N_2 fixation (Section 2).[255–257] A classification into Groups 1–4 has been proposed,[246] in which the water-soluble "standard" [NiFe]-hydrogenases are distinguished from membrane-bound, multimeric, as well as O_2-tolerant and bidirectional [NiFe]-hydrogenases.[257–259] Although highly diverse, all [NiFe]-hydrogenases share the same active site cofactor. It is composed of a nickel and an iron ion, covalently attached to the enzyme by either four cysteine residues,

or three cysteines and one selenocysteine (Figure 17A). The iron ion is coordinated by two CN^- and one CO ligand, the latter being a common feature of hydrogenases.[260]

[FeFe]-hydrogenases have been found in bacteria, lower eukaryotes, and green algae, representing the phylogenetically most recent class.[261–263] The physiological diversity among [NiFe]-hydrogenases is less pronounced than in [FeFe]-hydrogenases:[246] often, [FeFe]-hydrogenases are involved in redox regulation (H_2 release upon proton reduction) but in complex with other metalloproteins, additional roles in CO_2 reduction (Section 4) or bifurcation have been suggested.[264–266] "Standard" [FeFe]-hydrogenases belong to group A and have been investigated intensively whereas knowledge about group B–C [FeFe]-hydrogenase is only beginning to emerge.[267,268] Figure 17B shows the active site cofactor including the covalently attached [4Fe-4S] cluster. The metal ions of the diiron site are modified with a bridging carbonyl ligand (μCO) and two terminal CN^- and a CO ligand. Here, we shall elaborate on the active site architecture, catalytic mechanism, and second/outer coordination sphere effects in [NiFe]-hydrogenase (Section 3.1) and [FeFe]-hydrogenase (Section 3.2).

3.1. [NiFe]-Hydrogenase

3.1.1. Structural Features of [NiFe]-Hydrogenase.—

[NiFe]-hydrogenases are divided into Groups 1–4, according to the classification by Morales, Greening, and co-workers.[246] In these groups, [NiFe]-hydrogenases are further distinguished into "H_2 uptake" (Groups 1 and 2), "bidirectional" (Group 3), and "H_2 evolving" (Group 4) clades. Each group is divided into subgroups, for example, the O_2-sensitive prototypical or standard-type hydrogenases in Group 1b and the O_2-tolerant membrane-bound hydrogenases in Group 1d. The complete list is available in the "hydrogenase database", HydDB.[269] [NiFe]-hydrogenases are multisubunit proteins, which contain at least the catalytic subunit and an iron–sulfur cluster subunit. For example, standard [NiFe]-hydrogenases (Group 1b) are composed of two subunits, large and small, with molecular weights of approximately 60 kDa and 30 kDa, respectively (Figure 18A).[270] The large subunit binds the catalytic cofactor and the small subunit embeds the accessory iron–sulfur cluster. The first crystal structure of a standard [NiFe]-hydrogenase was determined for the enzyme from *Desulfovibrio gigas* (*Dg*) in 1995 at 2.85 Å resolution,[271] followed by the structures of [NiFe]-hydrogenases from *Desulfovibrio vulgaris* Miyazaki F (*Dv*MF)[272–276] and other species.[277–290] The Ni–Fe active site cofactor is located inside the large subunit, where the Ni and Fe ions are bridged with two cysteine thiolates, and two other cysteine residues are bound to the Ni ion in a terminal fashion.[273,291,292] In addition to two CN^- ligands and one CO ligand coordinated to the Fe ion, a bridging hydride ligand (μH^-) may exist between the metal ions (Figure 18B).[273] The Ni site changes its oxidation state (i.e., Ni^{3+}, Ni^{2+}, and Ni^+) among various intermediate states, some of which (Ni^{3+} and Ni^+) have been characterized by EPR spectroscopy. On the other hand, the Fe site maintains the low oxidation, low spin state (Fe^{2+}, $S = 0$).[251,293–298] In the O_2-tolerant NAD^+-reducing [NiFe]-hydrogenase (Group 3d) from *Hydrogenophilus thermoluteolus* TH-1, three cysteine thiolates bridge the Ni and Fe ions while one cysteine residue terminally ligates to the Ni ion in the oxidized state.[284] In the case of [NiFeSe]-hydrogenase, a terminal cysteine is replaced by a selenocysteine.[299–303] In standard [NiFe]-hydrogenases, three iron–sulfur clusters are

located in the small subunit and mediate the electron transfer between the Ni–Fe active site and physiological redox partners.[304–307] In the crystal structure of the O_2-tolerant membrane-bound [NiFe]-hydrogenase (Group 1d, see Figure 18C), a proximal [3Fe-4S] cluster harbored by six cysteine residues has been identified.[286,288,289]

The substrate (H_2) or inhibitors (O_2 and CO) are transferred via hydrophobic channels from the molecular surface to the Ni–Fe active site.[308–311] After splitting H_2 into electrons and protons (eq 2), proton transfer pathways provide an exit route to the molecular surface where protons are release into the solvent. The crystal structures of [NiFe]-hydrogenases revealed that highly conserved amino acid residues like arginine, serine, glutamate, and histidine are located in the second coordination sphere of the Ni–Fe active site (Figure 19). The CO ligand on the Fe ion interacts with the hydrophobic side chains of valine and leucine (V500 and L482 in *Dv*MF). On the other hand, the two CN^- ligands accept hydrogen bonds from arginine R479 and serine S502, respectively, in *Dv*MF.[273] One of the bridging cysteine thiolates is hydrogen-bonded to histidine H88.[312] These interactions have been confirmed in the electron density map of the hydrogen atoms in the subatomic resolution structure of *Dv*MF [NiFe]-hydrogenase.[273]

3.1.2. Ni–Fe Cofactor and Catalytic Cycle.—Standard [NiFe]-hydrogenases form two inactive oxidized states, Ni-A and Ni-B (Ni^{3+}, $S = 1/2$).[259,313,314] In the presence of H_2 or other reductants, activation of Ni-A requires long times, whereas the Ni-B is readily activated.[251,296] A hydroxide is present at the bridging position in the Ni-B state (μOH^-, Figure 20C);[275] however, the identification of the bridging ligand in the Ni-A state remains controversial.[312,315,316] The crystal structure of the Ni-A state in *Dv*MF was interpreted to represent a peroxide ligand (μOOH^-, Figure 20A), while a μOH^- ligand was found in *Allochromatium vinosum* (*Av*, Figure 20B).[275,277,278] The later is in agreement with DFT calculations and single-crystal ENDOR spectroscopy that indicated a μOH^- ligand in both Ni-A and Ni-B.[315] It was proposed that the differences in the EPR spectra of the two states are caused by a ligand rotation of 7–10° involving C546 and C549 in *Dv*MF. Accordingly, the bridging μOH^- ligand of the active site could be same in Ni-A and Ni-B, and the differences of the activation rates between these states may result from the slight distortion in the coordination of the cysteine residues. Further investigation is needed to clarify the difference of these states.

One-electron reduction of the Ni-A and Ni-B states leads to the EPR-silent inactive states, Ni-SU and Ni-SI_r (Ni^{2+}), respectively (Figure 21).[317] The midpoint redox potential for the interconversion between the Ni-A and Ni-SU states was shown to decrease by ~60 mV per pH unit in various [NiFe]-hydrogenases, indicating that the one-electron reduction of Ni-A is coupled to the uptake of one proton.[296,308–311,318–321] While the crystal structure of the Ni-SU state is not yet available, DFT calculations proposed coordination of a water molecule to the Fe ion and modification of the Ni coordination structure.[322]

A glutamate residue in the second coordination sphere of the Ni–Fe cofactor plays an important role for the inactivation process. This highly conserved glutamate residue (E34 in *Dv*MF) is located next to the Cys residue which is terminally bound to the Ni ion (C546 in *Dv*MF, see Figure 19). When the catalytically active [NiFe]-hydrogenase is oxidized under

anaerobic conditions, the enzyme converts from the Ni-SI_a state to the Ni-B state via the Ni-SI_r state (Figure 21). The first order rate constant of the anaerobic inactivation process in the E25Q (equivalent E34 in *Dv*MF) variant of [NiFe]-hydrogenase from *Desulfovibrio fructosovorans* (*Df*) was 5.6 times smaller than that of the wild-type enzyme, although the activation rate constant was hardly affected by the replacement.[323,324] Thus, the glutamate residue is important for the incorporation of the bridging OH^- ligand to the Ni–Fe cofactor. Under anaerobic conditions, formation of the Ni-B state with a bridging OH^- ligand from the Ni-SI_a state requires not only the transfer of a water molecule into the active site but also the extraction of a proton from a water molecule and oxidation of the Ni ion (Ni^{2+} to Ni^{3+}). The carboxylic group of the glutamate residue may deprotonate the bound water molecule at the active site, producing the bridging OH^- ligand of the Ni–Fe cofactor.[323] Interestingly, the Ni-B state was not produced when the E28Q variant (E34 in *Dv*MF and E25 in *Df*) of the [NiFe]-hydrogenase 1 from *Escherichia coli* (*Ec*Hyd-1) was oxidized on an electrode in the presence of H_2, indicating that the interaction of H_2 with the Ni–Fe cofactor is maintained in the E28Q variant and that the early stages of H_2 activation outpace electrochemical oxidation.[325] It may become much easier to start another cycle by activating H_2 and generating the Ni-R state in the E28Q variant, since protons may not easily leave from the Ni–Fe cofactor in the variant and thus it becomes difficult to produce OH^- from water.

During the catalytic cycle, the Ni–Fe cofactor changes the oxidation states in the following order: from Ni-SI_a (Ni^{2+}), Ni-R (Ni^{2+}), and Ni-C (Ni^{3+}) to the Ni-L (Ni^+) state (Figure 21).[251,293–297,308] These states convert among each other by addition or release of H_2, protons, and/or electrons. In the first step of the cycle, the Ni-SI_a state (with the bridging ligand position vacant) reacts with H_2 (Figure 20E). H_2 is cleaved heterolytically to a proton (H^+) and a hydride (H^-), which initiates the transition of the Ni-SI_a state to the fully reduced Ni-R state. The high-resolution crystal structure of *Dv*MF revealed that the Ni-R state possesses a μ-H^- ligand and a protonated cysteine (C546-SH) at the Ni–Fe cofactor (Figure 20F).[273] The μ-H^- ligand and the protonated cysteine residue in the Ni-R state was also elucidated by nuclear resonance vibrational spectroscopy (NRVS), which is particularly suited to monitor ^{57}Fe ligand vibrations, in combination with DFT calculations.[326–328] The hydride ligand was located closer to the Ni ion in the Ni-R state of the enzyme, whereas a short Fe–H^- bond and a long Ni–H^- bond were found in nearly all synthetic Ni–Fe models.[329–332] The protonated cysteine residue is considered as a part of the proton transfer pathways (see below).

The H_2 binding site at the first step of the cycle is still unclear, and either of the two metal ions may be involved in the formation of a (side-on) H_2 σ-bond complex. Although experimental data on H_2 binding to the Ni–Fe cofactor are not yet available due to the transient nature of intermediate, theoretical studies suggest the Ni ion as the initial site of H_2 binding.[333–337] In addition, complementary studies showed that the competitive inhibitor CO binds to the Ni ion at the Ni–Fe active site (Figure 20D).[274,338] The coordination geometry of the Ni ion is key to the thermodynamically favorable interaction of H_2 with the Ni–Fe cofactor. Theoretical calculations predicted that a peculiar seesaw-shaped geometry in the Ni-SI_a state with *trans* S–Ni–S angles near 120° and 180° is necessary for favorable binding of H_2 to the Ni site.[335] In line with this proposal, the crystal structure of the Ni–Fe

cofactor of F_{420}-reducing [NiFe]-hydrogenase from *Methanosarcina barkeri* (*Mb*) exhibited no ligand at the bridging position with unusual *trans* S–Ni–S angles of 107° and 171° in the Ni-SI_a state (Figure 20E).[339] Similar angles have also been suggested by resonance Raman studies of the O_2-tolerant, membrane-bound [NiFe]-hydrogenase from *Cupriavidus necator*, *Re*MBH (noted by its former name *Ralstonia eutropha*).[340]

One-electron oxidation of the Ni-R state leads to the paramagnetic Ni-C state (Ni^{3+}, $S = 1/2$) with a μH^- ligand and deprotonated C546-S^- at the Ni–Fe active site.[341,342] The Ni-C state is then converted to the paramagnetic Ni-L state (Ni^+), with a vacant bridging position and a (re-)protonated cysteine C546-SH (see below).[296,297,342–345] In the last step of the catalytic cycle, one-electron oxidation coupled with removal of the proton from C546-SH results in conversion of the Ni-L state to the Ni-SIa state.[295,346–351]

3.1.3. Proton Transfer and Proton-Coupled Electron Transfer.—The proton acceptor during the catalytic H_2 oxidation cycle has been proposed by theoretical[352] and Raman spectroscopic studies.[340,353] Apparently, the proton is transferred from the Ni–Fe cofactor to the Ni-coordinating terminal cysteine thiolate (C546 in *Dv*MF), which is the first step in the proton transfer pathway from the Ni–Fe cofactor to the outer coordination sphere (Figure 19).[273,297,346,354–356] The H2 oxidation activity of the E25Q variant (E34 in *Dv*MF) in *Df* [NiFe]-hydrogenase decreased to less than 0.1% compared to the wild-type enzyme.[357] These results indicated that the glutamate residue located close to the C546 ligand plays an important role for the proton transfer during the catalytic reaction, which was supported by theoretical studies.[358,359] Time-resolved infrared spectroscopy addressing the E17Q variant of O_2-tolerant *Pyrococcus furiosus* [NiFe]-hydrogenase (*Pf* SH-1) showed that glutamic acid E17 (E34 in *Dv*MF) is a proton relay for the interconversion between the Ni-C and Ni-SI_a states.[351] The replacement E17Q did not interfere with the μH^- photolysis of the Ni-C state but it disrupted PCET from the Ni-L state to the Ni-SI_a state, preventing formation of the Ni-SI_a state.

Alternatively, the highly conserved arginine (R479 in *Dv*MF and R509 in *Ec*Hyd-1) has been proposed as a proton acceptor, forming a frustrated Lewis pair for the oxidation of H_2 in *Ec*Hyd-1 from studies using variants R509K, D574N, D118A, P508A, and D118N/D574N (R479, D544, D123, P478 and D123/D544 in *Dv*MF, see Figure 19).[360,361] The turnover rate of the R509K variant decreased by a factor of 100 compared to that of the wild-type enzyme. The H_2 oxidation efficiency of the D118A variant, in which aspartate D118 forms a salt bridge to arginine R509, also decreased compared to native *Ec*Hyd-1. In the case of the soluble [NiFe]-hydrogenase 1 from *Pf* SH-1, the R355K (R479 in *Dv*MF) variant altered the ligand binding environment at the Ni–Fe cofactor and destabilized the Ni-C state, resulting in a Ni-C/Ni-L tautomeric equilibrium.[362]

The SH stretching frequency at 2505 cm^{-1} has been detected by highly sensitive Fourier-transform infrared (FTIR) difference spectra utilizing the photoconversion of the Ni-C state to the Ni-L and Ni-SI_a states in *Dv*MF [NiFe]-hydrogenase. The data showed that C546 is protonated in the Ni-L state (Cys-SH) and deprotonated in the Ni-C and Ni-SI_a states (Cys-S^-).[297,346] Glutamic acid E34-COOH was found to be double hydrogen-bonded in the Ni-L state and single hydrogen-bonded in the Ni-C and Ni-SI_a states (Figure 22) according

to the COOH stretching frequency between 1700–1730 cm^{-1}. Additionally, a stretching mode of a "dangling" water molecule was observed in the Ni-L and Ni-C states. These results suggest that the Ni–Fe cofactor and its surrounding amino acids function as an optimized proton transfer system in standard [NiFe]-hydrogenases, and the direction of the proton transfer is regulated by the rearrangement of the hydrogen bond network around C546, E34, and a dangling water molecule (Figure 22).

The Ni-L and Ni-R states of *Dv*MF [NiFe]-hydrogenase are likely to construct a similar hydrogen bond network between C546-SH, E34, T18, a backbone contact including A548-NH, and a dangling water molecule (Figure 22).[346] Several Ni-L states have been identified by light irradiation of the Ni-C state under anaerobic conditions at $T < 100$ K.[342,363–366] From temperature-dependent FTIR studies of *Dv*MF, the ΔH and ΔS values for the equilibrium between the protonated/deprotonated forms (i.e., Cys-SH and Cys-S^-) of two Ni-L states were obtained as 6.4 ± 0.8 kJ mol^{-1} and 25.5 ± 10.3 J mol^{-1} K^{-1}, respectively.[348] The small ΔH and ΔS values indicate efficient proton transfer at the cysteine residue C546 of the Ni–Fe cofactor between the two Ni-L states.

The Ni-SI_a and Ni-C states may form a similar hydrogen bond network between C546-S^-, E34, A548-NH, and a dangling water molecule (Figure 22). Theoretical studies have indicated involvement of a threonine residue in the proton transfer of the transmembrane proton pump bacteriorhodopsin;[367] however, T18 seems to be nonessential for proton transfer in *Df* [NiFe]-hydrogenase and rather stabilizes the local protein structure. This observation was suggested by structural and spectroscopic studies of variants in which threonine was replaced with serine, valine, glutamine, glycine, and asparagine.[368]

3.1.4. Accessory Iron–Sulfur Clusters.—In standard [NiFe]-hydrogenases, three accessory iron–sulfur clusters (denoted proximal $[4Fe\text{-}4S]^{2+/+}$, medial $[3Fe\text{-}4S]^{+/0}$, and distal $[4Fe\text{-}4S]^{2+/+}$) are located almost linearly (each ~12 Å apart) in the small subunit (Figure 23),[273] and mediate electron transfer between the Ni–Fe active site and physiological redox partner, such as cytochrome c_3.[304–307] The proximal $[4Fe\text{-}4S]^{2+/+}$, medial $[3Fe\text{-}4S]^{+/0}$, and distal $[4Fe\text{-}4S]^{2+/+}$ clusters of *Dg* [NiFe]-hydrogenase exhibit redox potentials of −315, −80, and −445 mV versus SHE, respectively.[369]

The accessory iron–sulfur clusters are not only important for electron transfer but may also play a role with respect to hydrogen turnover in the presence of O_2: some [NiFe]-hydrogenases are "O_2-sensitive" (i.e., inhibited by O_2) while the "O_2-tolerant" [NiFe]-hydrogenases maintain activity under aerobic conditions. The latter have been shown to quickly reactivate from the Ni-B state in a process that appears to be very dependent on the nature of the proximal cluster.[370–372] The reactivity toward O_2 clearly distinguishes the bimetallic hydrogenases; as discussed in Section 3.2.2, [FeFe]-hydrogenases are irreversibly destroyed by O_2.

3.1.4.1. Proximal Cluster.: When the proximal $[4Fe\text{-}4S]^{2+/+}$ cluster is reduced in standard [NiFe]-hydrogenases, the $[4Fe\text{-}4S]^{+}$ cluster interacts magnetically with the $Ni^{3+/+}$ center, which causes splitting of the Ni-C/Ni-L EPR signals below 10 K.[373] Spectroscopic studies revealed that the conversion of Ni-C to Ni-SI_a via the Ni-L state is controlled by the redox

state of the proximal $[4Fe\text{-}4S]^{2+/+}$ cluster in *Dv*MF [NiFe]-hydrogenase.[347] The transition of the Ni-L state to the Ni-SI_a state may occur when the proximal $[4Fe\text{-}4S]^{2+/+}$ cluster is oxidized but not when it is reduced. These results suggest that the catalytic cycle is controlled by the redox state of the proximal $[4Fe\text{-}4S]^{2+/+}$ cluster, which may act as a gate for the catalytic electron transfer.

Most of the standard [NiFe]-hydrogenases possess a glutamate near the proximal [4Fe-4S] cluster (Figure 24A), while some [NiFe]-hydrogenases possess an aspartate instead. The crystal structure of membrane-bound *Av* [NiFe]-hydrogenase in the Ni-A state showed that there are two different forms for the proximal [4Fe-4S] cluster; one is a standard cubane, while in the other form the proximal [4Fe-4S] cluster is distorted with one of the Fe ions bound to aspartate D75, which is located nearby the cluster (Figure 24B).[278] It was proposed that the negatively charged side chain of aspartate stabilizes the distorted form of the [4Fe-4S] cluster. A similar coordination was found in the O_2-tolerant [NiFe]-hydrogenase from *Citrobacter* sp. S-77.[285] Additionally, the water molecules near the proximal cluster relocated upon reduction, emphasizing the importance of the water network in this hydrogenase.[285]

Contrary to the standard [NiFe]-hydrogenases, some of the O_2-tolerant, membrane-bound [NiFe]-hydrogenases, such as *Ec*Hyd-1, *Re*MBH, *Hydrogenovibrio marinus* (*Hm*MBH), and *Aquifex aeolicus* (*Ae*MBH), possess a unique proximal $[4Fe\text{-}3S]^{5+/4+/3+}$ cluster ligated by six cysteine residues (Figure 24CD).[286,288–290] This cluster can be oxidized twice within a very small potential range.[374] Its electronic structure has been characterized and debated.[375–378] The importance of the coordination by six cysteines to the proximal iron–sulfur cluster has been shown by site-directed mutagenesis studies in *Re*MBH and *Ec*Hyd-1.[379–382] Replacement of the two supernumerary cysteine residues C19 and C120 in *Re*MBH with glycine residues altered the electronic structure of the proximal cluster, and the double variant was unable to sustain activity under prolonged O_2 exposure.[379] Similar mutagenesis studies in *Ec*Hyd-1 showed that O_2 tolerance depends on C19 and not on the two-electron oxidation at the proximal cluster, which is detected with the O_2-sensitive C19G variant but not with the O_2-tolerant C120G variant.[380] For another example, the O_2-tolerant NAD^+-reducing soluble [NiFe]-hydrogenase from *C. necator*, *Re*SH (noted by its former name *R. eutropha*), can produce trace amounts of superoxide in H_2-driven NAD^+ reduction with O_2.[381] The C41S variant of *Re*SH displayed up to 10% of wild-type activity, suggesting that the coordinating role of C41 at the proximal [4Fe-4S] cluster might be partly substituted by the nearby C39 residue, which is present only in O_2-tolerant pyridine nucleotide-dependent [NiFe]-hydrogenases, whereas the C39G, C39A, and C39S variants increased the O_2 sensitivity compared to wild-type *Re*SH.[382]

EPR and ^{57}Fe Mössbauer spectroscopic studies have shown that the proximal $[4Fe\text{-}3S]^{3+}$ cluster donates two electrons to the Ni–Fe active site, resulting in the “superoxidized” state $[4Fe\text{-}3S]^{5+}$.[374] A charged glutamate near the cluster (COO^-, e.g. in *Hm*MBH and *Ec*Hyd-1) or a deprotonated water molecule (OH^-, e.g. in *Re*MBH) stabilizes the $[4Fe\text{-}3S]^{5+}$ cluster.[286,288,289,307,383] The deprotonated amide nitrogen of the backbone formed by cysteine C26 (in *Hm*MBH) may bind to one of the Fe ions of the cluster, also stabilizing the highly oxidized state. In *Ae*MBH, the proximal $[4Fe\text{-}3S]^{5+/4+/3+}$ and medial [3Fe-4S]

$^{+/0}$ clusters show midpoint potentials that are higher than potential necessary value for the conversion of the Ni-SI_a to Ni-L/Ni-C states in standard [NiFe]-hydrogenase.[345,374,384] Additionally, a kinetic argument favoring the appearance of the Ni-L state in *Ec*Hyd-1 is that the proximal [4Fe-3S]$^{3+}$ cluster is fully reduced at the potentials that are required for both the Ni-C and Ni-L states, impeding the elementary electron transfer step that converts the Ni-L to Ni-SI_a state.

The conserved glutamic acid residue (E34 in *Dv*MF) plays an important role for the mechanism of O_2 protection in the O_2-tolerant NAD^+-reducing [NiFe]-hydrogenase from *H. thermoluteolus* TH-1, which is revealed by the crystal structures (Figure 25).[284] The Ni–Fe cofactor of *Hf*TH-1 in the H_2-reduced state exhibits a similar coordination structure as those of standard [NiFe]-hydrogenases, whereas in the air-oxidized state, an octahedral Ni geometry was found; three bridging thiolate ligands between the Ni and Fe ions, one terminally bound cysteine thiolate, and an unprecedented bidentate ligation of the glutamate side chain (E32 in *Ht* and E34 in *Dv*MF) (Figure 25). The fully occupied octahedral Ni geometry protects the Ni–Fe cofactor from direct attack by O_2. Higuchi, Shomura, and coworkers suggested that the conformational change of the Ni–Fe active site was triggered by the reduction of the proximal [4Fe-4S] cluster (Y1 in Figure 25). The coordination structure of the amino acid residues located in between the Ni–Fe cofactor and the proximal [4Fe-4S] cluster also changed upon reduction. In the reduced state, E32 does not bind to the Ni ion and forms a hydrogen bond network including S464 and E56, notably unrelated to the catalytic proton transfer pathway as discussed above (Figure 22). The side chain of arginine R58 flips between E56 and the proximal [4Fe-4S] cluster (Figure 25), which may affect the efficiency of catalytic electron transfer.

3.1.4.2. Medial and Distal Clusters.: In standard [NiFe]-hydrogenases, the medial [3Fe-4S]$^{+/0}$ cluster possesses a rather high midpoint potential, which may play a role in effectively “trapping” electrons from the Ni–Fe cofactor, facilitating the reaction of the Ni-SI_r state with H_2 via the acid–base equilibrium between the Ni-SI_r and Ni-SI_a states.[373,385,386] Substitution of a proLine, a potential ligand to the [3Fe-4S] cluster, to cysteine (P238C in *Df* [NiFe]-hydrogenase, equivalent P242 in *Dv*MF) triggered the conversion of the medial [3Fe-4S] cluster to a [4Fe-4S] cluster decreasing the midpoint potential from +65 mV to −250 mV versus SHE. This potential decrease caused a 30% reduction in H_2 oxidation activity and a 2-fold increase in H_2 evolution activity without significantly altering the spectroscopic properties of the Ni–Fe active site and the proximal and distal [4Fe-4S] clusters.[387] The distal [4Fe-4S] cluster is located very close to the solvent and interacts with electron acceptors.[251] Three cysteines and one histidine coordinate this cluster (Figure 23). The H184C and H184G variants (distal [4Fe-4S] cluster ligand variants) of *Df* [NiFe]-hydrogenase (H188 in *Dv*MF) showed only 1.5% and 3% oxidative activity compare to the wild-type enzyme, respectively.[388] The activity of the H184G variants decreases or increases upon addition of mercaptoethanol or imidazole to the assay, respectively: these ligands modulate electron transfer rates upon binding to a free coordination site on the distal cluster.[388,389] The affinity of the variants H184G, P238C/H184G, and P238C/H184C for the electron acceptors methyl viologen and cytochrome c_3 was similar or greater than that of the wild-type enzyme, suggesting that H184 does not

govern the partner recognition.[389] DFT calculations demonstrated that substitution of the histidine ligand to a cysteine in *Df* [NiFe]-hydrogenase does not change the reorganization energy of the distal [4Fe-4S] cluster.[390] The calculated rate of electron transfer was, however, reduced by three orders of magnitude, resulting from a change in electronic donor–acceptor coupling including histidine H184 and phenylalanine F193 (F197 in *Dv*MF). These results indicated that the protein environment is tuned for efficient electron transfer. A systematic survey of the substitution of amino acid residues related to the medial and distal iron–sulfur clusters has been reported for the [NiFe]-hydrogenase from *Alteromonas macleodii* (which belongs to Group 1e but shows modest O_2 tolerance).[391–393] For example, the double substitution of P285C at the medial [3Fe-4S] cluster (P242 in *Dv*MF) and H230C at the distal [4Fe-4S] cluster (H188 in *Dv*MF) increased the H_2 evolution activity three- to four-fold compared to the wild-type enzyme.[393] Electrochemistry measurements showed that in the R193L variant of O_2-tolerant *Ec*Hyd-1, in which R193 is located near the histidine ligand (Figure 26, L194 in *Dv*MF), the midpoint potentials of the medial [3Fe-4S]$^{1+/0}$ and distal [4Fe-4S]$^{2+/+}$ clusters are more negative than those of the wild-type enzyme.[394] The R193L variant also enhanced bias toward H_2 evolution and slightly diminished the O_2 tolerance, whereas the catalytic activity of the K189N and Y191E variants (equivalent Q190 and P192 in *Dv*MF) did not change compared to that of wild-type *Ec*Hyd-1.[394]

The electron transfer route between the Ni–Fe cofactor and the protein surface is complicated, and theoretical calculations proposed that multiple routes coexist between the metal centers during catalysis.[395] Thus, enzymatic activity is tuned by not only in the second coordination sphere of the Ni–Fe cofactor but also via the electron transfer trajectory in the outer coordination sphere. Furthermore, in the case of O_2-tolerant [NiFe]-hydrogenases, most variants at the proximal iron–sulfur cluster became O_2 sensitive.[379] In addition to controlling electron transfer, the accessory iron sulfur clusters play an important role in the O_2 tolerance.

3.1.5. Gas Channels in [NiFe]-Hydrogenase.—The Ni–Fe cofactor is deeply buried in the center of the large subunit (Figure 27).[251] Both substrate and inhibitory gas molecules, such as H_2, O_2, and CO, can access the Ni–Fe active site from the solvent region through hydrophobic gas channels predicte from the crystal structure of the protein.[309,354,396–398] Cavity calculations of these cavities using a 1 Å radius probe showed that there are four gas access points at the protein surface, combining into one channel that leads to the Ni–Fe active site.[396,397] In vicinity of the Ni–Fe cofactor, the end of the channel becomes narrower due to a “bottleneck” composed of two hydrophobic amino acid residues, typically valine and leucine (Figure 27).[397,398] Noble gases like Xe and Kr bind to the hydrophobic area of the protein and are well visible in electron density maps; thus, protein crystal structures pressurized with Xe or Kr provide useful information for hydrophobic gas channels.[354,396,399,400] The crystal structures of the Xe-bound standard [NiFe]-hydrogenases from *Df* and *Dv*MF have been determined at 6.0 and 1.8 Å resolution, respectively, where the Xe atoms were observed in the hydrophobic cavities of these enzymes.[354,396] Controversially, molecular dynamics (MD) simulations suggested that gas molecules like H_2 and O_2 could reach the Ni–Fe active site via several pathways.[398,401]

The O_2 transfer pathways of O_2-tolerant *Re*MBH has also been investigated by X-ray crystallography together with computational studies and has been compared with those of O_2-sensitive [NiFe]-hydrogenases.[399,400] The channels of [NiFe]-hydrogenases span distances of 28–76 Å between the protein surface and the Ni–Fe active site, wherein O_2-sensitive [NiFe]-hydrogenases have a wider bottleneck and a more complex channel network than those of their O_2-tolerant counterparts. Several O_2 binding sites have been revealed within the hydrophobic channels that have two entrances and extend to the Ni–Fe active site (Figure 27).

Various site-directed mutagenesis studies have tested the suggestion that the presence of bulky residues at the end of the gas channel in the so-called O_2-tolerant, regulatory hydrogenases (RH) may prevent O_2 access to the active site (e.g., isoleucine and phenylalanine instead of valine and leucine).[397] The H_2 oxidation activity of the I62V and F110L variants of the regulatory [NiFe]-hydrogenase from *C. necator*, *Re*RH (noted by its former name *R. eutropha*), decreased under aerobic conditions 25-fold and 5.5-fold, respectively, compared to the O_2-tolerant wild-type enzyme.[402] These results suggest that *Re* RH exhibits O_2 and CO tolerance owing to interruption of the gas channel at the bottleneck to the Ni–Fe active site with the bulky amino acid residues isoleucine I62 and phenylalanine F110. Furthermore, the double variant I62V/F110L was completely inactive, indicating that the shape of the gas channels may play a key role in O_2 tolerance.[402] The I65V/F113L double variant of the regulatory hydrogenase from *Rhodobacter capsulatus* is also more active and more O_2-sensitive than the native enzyme.[403] The hypothesis is that narrower gas channels and fewer gas entrances limit the mass transport to the catalytic active site, presumably contributing to the net O_2 tolerance of these enzymes. However, site-directed mutagenesis studied aimed at narrowing the end of the gas channel of the O_2-sensitive *Df* [NiFe]-hydrogenase showed that steric hindrance slows down intramolecular diffusion and O_2 inhibition, but without making the variant O_2-tolerant. These gas diffusion processes have been studied intensively using many residue replacements at the bottleneck position, namely V74 and L122 in *Df* [NiFe]-hydrogenase.[309,310,404–406] The rates of intramolecular gas diffusion were measured by using the bimolecular rate constant of inhibition by CO as a proxy of the rate of ligand access to the active site, by analyzing the results of isotope exchange assays, and by measuring the Michaelis constant for H_2.[309–311] The results show that the variations have the same relative effects on the transport of all ligands, CO, O_2, and H_2, and that not only the size but also the charge of the residues in the bottleneck have a very strong effect (up to nearly four orders of magnitude) on the kinetics of ligand access. Slowing down H_2 egress has the direct consequence of selectively slowing H_2 production and increasing the catalytic bias of the enzyme in the direction of H_2 oxidation.[311] Some of the observed effects of the variations on the rates of diffusion could be explained by the results of MD simulations, according to which two distinct gates determine the kinetics, namely V74/R476 and V74/L122.[401,407] Although site-directed mutagenesis slows down the intramolecular diffusion rates, the resulting effect on the kinetics of inhibition by O_2 is 10-fold or less, because the transport toward the active site limits the reaction with O_2 only when it is very slow (e.g., in the V74 M and V74Q variants).[406,408] However, some V74 substitutions (in particular V74C and V74H) have a very beneficial effect on O_2 inhibition that is not related to the kinetics of diffusion: for reasons that have not been clarified,

these variations strongly increase the rate of *reactivation* after O_2 inhibition. The rate of reactivation of *Df* [NiFe]-hydrogenase V74H is close to that observed with the O_2-tolerant enzyme from *A. aeolicus*,[404,409] and mutation to cysteine further increases the O_2 tolerance of *Ec*Hyd-1.[410]

According to the type of [NiFe]-hydrogenase, the gas channels differ in size, shape, and branching, with respect to the physiological requirement of each [NiFe]-hydrogenase. The crystal structure of the *Mb* F_{420}-reducing [NiFe]-hydrogenase in the Xe-bound form revealed an additional gas channel (Figure 28).[339] Interestingly, the [NiFeSe]-hydrogenase from *Desulfovibrio vulgaris* Hildenborough (*Dv*H) has a similar hydrophobic channel,[339,411] although this channel is not observable in the crystal structures of standard [NiFe]-hydrogenases.[354,396,399,400] In the case of *Dv*H [NiFeSe]-hydrogenase site-directed mutagenesis experiments suggest that O_2 reaches the active site through a hydrophilic water channel.[412]

3.2. [FeFe]-Hydrogenase

3.2.1. Structural Features of [FeFe]-Hydrogenase.—

Standard [FeFe]-hydrogenases are in most cases monomeric enzymes with a molecular weight ranging between 50–80 kDa. The [FeFe]-hydrogenase from *Clostridium pasteurianum*, *Cp*I, whose X-ray crystal structure has been published in 1998, shows a mushroom-like shape with four iron–sulfur clusters binding to the “stipe” (Figure 29A).[413–415] Because of the sequence similarity with ferredoxin, this fold is referred to as “F-domain”. The [FeFe]-hydrogenase from *C. acetobutylicum*, *Ca*I, albeit not crystallized, is likely of similar architecture.[416] In both enzymes, the iron–sulfur clusters form a conductive chain that serves in electron exchange between soluble redox partners and the catalytic active site. This chain consists of two buried [4Fe-4S] clusters, one surface-exposed [2Fe-2S] cluster, and one surface-exposed [4Fe-4S] cluster, the later which is bound by a three cysteine and one histidine ligand.[724] From a comparison of *Ca*I variants, it was concluded that the [2Fe-2S] cluster is the main electron transfer conduit, at least when the enzyme is wired to an electrode.[417] On the other hand, docking simulations with *Cp*I suggest that the physiological electron donor, ferredoxin, interacts predominantly with the surface-exposed [4Fe-4S] cluster. According to EPR titrations this cluster has the lowest potential.[418] The authors investigated a catalytically inactive cofactor variant to facilitate steady-state conditions, notably below the H^+/H_2 Nernstian potential, where *Cp*I spontaneously reoxidizes as a result of proton reduction, which prevents equilibrium conditions during the redox titration at low potential.[418,419]

The [FeFe]-hydrogenase from *Desulfovibrio desulfuricans*, *Dd*H, whose X-ray crystal structure was published in 1999, features a smaller F-domain with only two [4Fe-4S] clusters and is surrounded by a peptide “belt” (Figure 29B).[420,421] The [FeFe]-hydrogenase from *Megasphaera elsdenii*, *Me*HydA, lacks this subunit but displays an equally small F-domain.[422] Voltammetry experiments suggested that intramolecular electron transfer in *Me*HydA is rate limiting in H_2 oxidation, which primarily determines the catalytic bias of this enzyme.[423] The electron transfer chain of the recently crystallized hydrogenase from *Clostridium beijeirincki*, *Cb*A5H, consists of only two [4Fe-4S] clusters and an additional *N*-terminal cluster located more than 20 Å away from any other cluster.[424] Because of

significant disorder, these clusters are not visible in PDB entry 6TTL. A crystal structure of the functional [FeFe]-hydrogenase from the green alga *Chlamydomonas reinhardtii*, *Cr*HydA1, has yet to be obtained; however, based on several lines of evidence,[425–430] it can be concluded that *Cr*HydA1 completely lacks the F-domain and any additional metal centers. The homology model shown in Figure 29C highlights an insertion or "loop" that is typical for [FeFe]-hydrogenases of the *Chlorophyta*-type.[26]

The above-mentioned hydrogenases have been crystallized and thoroughly studied using biophysical methods; however, they are not representative of the diversity of the [FeFe]-hydrogenases, some of which are much larger and associated in multienzyme complexes.[266] As an example, the hydrogen-dependent carbon dioxide reductase from *Acetobacterium woodii* has four subunits and 11 predicted iron–sulfur clusters, with an apparent mass around 169 kDa[431,432] while the respiratory formate hydrogen lyase complex (FHL) of *Thermococcus onnurineus* consists of 18 subunits, with a molecular weight of approximately 600 kDa.[433] The coupling of CO_2 and H_2 turnover is discussed in Section 4. The small number of [FeFe]-hydrogenases that have been crystallized so far is certainly an obstacle to learning about how diverse structures and outer sphere effects modulate activity; this is actually true for all GPMs discussed in this review.

Unlike the F-domain, the catalytic "H-domain" shows a high degree of similarity in all [FeFe]-hydrogenases.[246] Four cysteine residues bind a [4Fe-4S] cluster that is part of the active site cofactor and facilitates electron exchange with the accessory iron–sulfur clusters (or soluble redox partners, in case of *Cr*HydA1). These residues are part of at least three protein loops 1–3 (Figure 30).[26] A strictly conserved cysteine residue in loop 3 additionally coordinates the diiron site, which is equipped with CO and CN^- ligands and an azadithiolate group (ADT, compare Figure 17B).[434–436] Together, the [4Fe-4S] cluster and the diiron site form the active site "H-cluster". Figure 30 depicts the H-cluster, including a number of functionally relevant amino acid residues and water molecules in the second and outer coordination sphere.

The standard or group A [FeFe]-hydrogenases *Cp*I, *Ca*I, *Dd*H, and *Cr*HydA1 have been studied intensively and most of what is known about the influence of second and outer coordination sphere is based on the biochemical and biophysical analysis of these enzymes. The diversity of [FeFe]-hydrogenases has been emphasized;[437–439] advances in understanding the second and outer coordination sphere effects in the lesser studied or more complex [FeFe]-hydrogenase groups is currently an emerging area of study. For example, the sensory or bifurcating [FeFe]-hydrogenases from *Thermotoga maritime* (*Tm*HydS, *Tm*HydABC) and *Thermoanaerobacter mathranii* (*Tam*HydS) have been characterized.[440–443] A cryo-EM structure of *Tm*HydABC has recently been published as a preprint.[444] Table 4 shows a comparison of important amino acid residues in the H-domain, highlighting the level of similarity among group A [FeFe]-hydrogenases and the differences to group C and D [FeFe]-hydrogenases. In addition to the above-mentioned enzymes, the table also includes *Cp*II and *Cp*III, *Me*HydA1, and *Cr*HydA2.[424] This comparison is not comprehensive and restricted to experimentally characterized [FeFe]-hydrogenases. As such, Table 4 allows correlating amino acid composition and catalytic function and will serve as a guideline for the analysis of second and outer coordination

sphere effects. Additionally, Table 5 provides a compilation of all amino acid and H-cluster variants that have been published in the last 20 years. We will discuss the influence of natural and artificial variations of the H-domain in Section 3.2.2. Next to the biochemical and electrochemical analysis of turnover activity, the spectroscopic signatures of the active site cofactor have been a major source of information. We define the various H-cluster states hereafter.

3.2.2. H-Cluster, Catalytic Cycle, and Artificial Maturation.

3.2.2.1. Oxidized States.: In the absence of H_2 or other reductants, the H-cluster in standard [FeFe]-hydrogenases adopts the "active-ready", oxidized state, H_{ox}. Moderate spin exchange coupling between [4Fe-4S] cluster and diiron site gives rise to the characteristic, rhombic EPR signal (g = 2.105, 2.044, 2.001, see Figure 31), indicating that the [4Fe-4S] cluster is oxidized (+2 state, a pair of Fe(II)–Fe(III)) while the diiron site adopts a mixed-valence +3 state (Fe(II)–Fe(I)).[481–483] The distribution of charges among Fe_p and Fe_d is debated.[267] [FeFe]-hydrogenase in the H_{ox}-state was analyzed by EPR spectroscopy within cells, isolated in solution, and in crystallized form.[484] X-ray diffraction structures of such crystals indicated a Fe–Fe bridging CO ligand,[413,420] which reflects in a low-frequency IR absorbance band at 1802 cm^{-1}, accompanied by two terminal CO and CN^- bands at higher frequencies (Table 6).[485–487] A small upshift in frequency relative to H_{ox} has been explained by a protonation of a cysteine residue that coordinates the [4Fe-4S] cluster (see below);[488] the EPR signal shifts accordingly (g = 2.106, 2.048, 2.001, see Figure 31).[267] This state is referred to as $H_{ox}H$. In the presence of CO, no H_2 oxidation and proton reduction activity is observed[489] as the oxidized H-cluster reacts with exogenous CO to form the CO-inhibited state, H_{ox}-CO.[414,415] The rhombic EPR signal of H_{ox} converts into an axial signature (g = 2.05, 2.01, see Figure 31), indicative of pronounced spin exchange coupling.[490–492] While the crystal structure of H_{ox} shows an open, apical binding site at Fe_d, the crystal structure of H_{ox}-CO hints at a labile, inhibiting ligand in apical position. Spin polarization favors an apical CO ligand,[492] which contrasts from IR spectroscopy that has suggested ligand rotation and the stabilization of an apical CN^- ligand.[479,493,494] The IR spectrum shows four CO ligands instead of three (Table 6), but due to significant vibrational energy transfer[495–497] the assignment of normal modes is less intuitive than in H_{ox}.[493] Under acidic conditions, $H_{ox}H$-CO is formed.[488] The EPR spectrum of this state has not yet been reported.

3.2.2.2. One-Electron Reduced States.: The H-cluster may adopt two one-electron reduced states, both of which are largely diamagnetic. Reduction of the [4Fe-4S] cluster from +2 to +1 gives rise to the characteristic IR signature of $H_{red'}$ (sometimes referred to as just "H_{red}"), which looks similar to H_{ox} but shifted to lower frequencies (Figure 32A).[470,498,499] In H_{ox} and $H_{red'}$ the H-cluster binds a μCO ligand and maintains the "rotated' structure" with an open, apical biding site at Fe_d (Figure 33A).[500] As such, the H-cluster readily interacts with exogenous CO, forming the reduced, CO-inhibited state $H_{red'}$-CO.[494] As in $H_{ox}H$, protonation of a cysteine has been proposed, stabilizing the excess electron of the [4Fe-4S] cluster in $H_{red'}$.[488,501] This may also explain the small upshift of frequencies under acidic conditions that has been assigned to the $H_{red'}H$ state (Figure 32A).

Reduction of the diiron site from +3 to +2 ((Fe(I)–Fe(I)) gives rise to the characteristic IR signature of H_{red}. Reduction and protonation of the diiron site under ambient conditions triggers the release of the μCO ligand into a terminal position[421] and the formation of a Fe–Fe bridging hydride ligand, μH.[502] Accordingly, H_{red} shows three terminal CO ligands and the apical position is occupied by a CO ligand, most likely (Figure 32A).[479] In variance to H_{ox} and $H_{red'}$, the square-pyramidal geometry of the diiron site is symmetrical (Figure 33B). Under cryogenic conditions, such changes in geometry are precluded and result in an IR signature that clearly shows a μCO ligand.[503–505] The latter is likely to be protonated at the ADT ligand and should be referred to as '$H_{red}H^{+}$'. Whether H_{red} or $H_{red}H^{+}$ are catalytically relevant cofactor intermediates or representative of an H_2-inhbited H-cluster geometry has been debated.[506–509]

3.2.2.3. Two-Electron Reduced States.: Reduction of the [4Fe-4S] cluster starting from H_{red} results in the formation of H_{sred}.[510] This redox state was described for *Cr*HydA1, where it accumulates under H_2, presumably due to the lack of accessory iron–sulfur clusters that distribute reducing equivalents between H-domain and F-domain.[511] The H-cluster is diamagnetic in this "super-reduced" state; however, the assignment of the rhombic EPR spectrum with g = 2.08, 1.94, 1.87 has recently been questioned by Zebger, Horch, and coworkers who assigned an axial signal to H_{sred} (g = 2.15, 1.86).[504] The IR difference between H_{red} and H_{sred} is similar to H_{ox} and $H_{red'}$, that is, a small shift to lower energies (Figure 32B).[512] Just like H_{red}, the rotation of the μCO ligand into terminal position is precluded under cryogenic conditions ('$H_{sred}H^{+}$').[503–505]

A catalytic intermediate with a terminal hydride ligand was first suggested by Krasna and Rittenberg in 1954, based on H_2 and D_2 exchange experiments with the [FeFe]-hydrogenase from *Proteus vulgaris*.[513] 60 years later, the FTIR, Mössbauer, and EPR signatures (g = 2.07, 1.93, 1.88) of the so-called hydride state, H_{hyd}, were identified in protein and cofactor variants (Table 5).[456–458] In wild-type enzyme, accumulation of H_{hyd} was achieved upon H_2 oxidation starting from $H_{ox}H$, which confirmed the hydride state as a "natural", catalytically relevant H-cluster intermediate (Table 6).[446] Subsequent NRVS and NMR studies further established our knowledge about H_{hyd}.[459,474,514] The diiron site resides in a formally "superoxidized" state (Fe(II)–Fe(II)), binding the terminal hydride in apical position at the distal iron ion. This position *trans* to μCO has been exploited to demonstrate the hydride character of the ligand in FTIR H/D exchange experiments.[446,457] Similar to $H_{red'}$, the [4Fe-4S] cluster is reduced (+1) and likely to be protonated.[506] The geometry of H_{hyd} resembles H_{ox} and $H_{red'}$ (Figure 33A).

3.2.2.4. Catalytic Mechanism of Hydrogen Turnover.: The ongoing debate about the catalytic mechanism of [FeFe]-hydrogenase[506,509] is inseparable from questions regarding the influence of second and outer coordination sphere effects that are discussed in Section 3.2.3 and Section 3.2.4. In the following, the two main models will be introduced. The key difference between the models is the assumption of a protonated and reduced diiron site in the "5-step model" or a protonation event at the [4Fe-4S] cluster in the "3-step model".

In the absence of H_2 or other reducing components, all standard [FeFe]-hydrogenases adopt the H_{ox} state,[481–483] which is widely accepted as the starting and end point of a catalytic

cycle that accounts for hydrogen turnover (eq 2). Figure 34 shows a simplified proposal for the succession of redox intermediates in the direction of H_2 evolution. Under the assumption that the H-cluster maintains the μCO geometry upon reduction of the diiron site,[503–505] $H_{red}H^+$ and $H_{sred}H^+$ may be catalytic intermediates. The 5-step model starts with reduction of the [4Fe-4S] cluster and the formation of $H_{red'}$ over H_{ox} (transition A in Figure 34). It is conceivable that the ADT ligand of the diiron site is protonated via the catalytic proton transfer pathway (Section 3.2.5), which may induce intramolecular electron transfer from the [4Fe-4S] cluster to the diiron site, resulting in the formation of $H_{red}H^+$ over $H_{red'}$ (transition B). From here, $H_{sred}H^+$ is formed upon reduction of the [4Fe-4S] cluster (transition C).[510] Although there is no experimental evidence for a protonation of the ADT ligand in any H-cluster state,[506] the formation of a terminal hydride at Fe_d upon intramolecular proton transfer and oxidation of the diiron site seems a reasonable assumption (H_{hyd} over $H_{sred}H^+$, transition D).[498] In the final step of the 5-step model (transition E), protonation of the terminal hydride would lead to H_2 evolution and the recovery of the oxidized resting state, H_{ox}.[514]

On the basis of the observation that the H-cluster undergoes geometry changes upon reduction of the diiron site at ambient temperatures (Figure 32), H_{red} and H_{sred} have been excluded as catalytic intermediates.[505–508] In the alternative “3-step model”, $H_{red'}$ is formed over H_{ox} upon proton-coupled electron transfer to the [4Fe-4S] cluster (transition A*).[501] Here, the protons may reach the H-cluster via the so-called regulatory proton transfer pathway (Section 3.2.4) while in the 5-step model, transition A is a simple reduction process. $H_{red'}$ may convert directly into H_{hyd} in a second step of proton-coupled electron transfer (transition B* in Figure 34) before protonation of the terminal hydride ligand leads to H_2 evolution, analogous to the 5-step model (transition E). It is debated whether H_{ox} or the protonated resting state $H_{ox}H$ is recovered upon H_2 evolution.[488]

Other H-cluster species are also described in the literature. Electrochemistry experiments have shown that various inactive states are formed under *reducing* conditions; whether these forms correspond to any spectroscopically identified species is unclear, although it can be said that not all species that have been isolated and characterized are necessarily catalytic intermediates.[515] Inactive states also accumulate under certain *oxidizing* conditions. H_{inact} (or ‘H_{ox}^{air}’) and H_{trans} represent unready, “superoxidized” H-cluster states that have been observed in some [FeFe]-hydrogenases.[419,516,517] These states differ in the redox state of the [4Fe-4S] cluster, and the IR difference between H_{inact} and H_{trans} is similar to H_{ox} and $H_{red'}$ (Table 6). H_{trans} is paramagnetic and gives a substoichiometric rhombic EPR spectrum with g = 2.06, 1.96, 1.89.[516] Remarkably, [FeFe]-hydrogenases in the H_{inact} state do not react with CO or O_2.[518]

The reductive activation of unready *Dd*H was long believed to be irreversible but it has recently been demonstrated that H_{ox} can be converted into H_{trans} and H_{inact} in the presence of exogenous sulfide, which binds to Fe_d.[519–521] The formation of H_{inact} in the absence of sulfide was considered to cause the reversible high potential inactivation of the enzyme as detected in electrochemistry experiments.[522] Later, it became clear that sulfide-independent oxidative inactivation results from the inhibition of the enzyme by traces of halide ions like chloride or bromide.[523] Recently, the formation of H_{inact} was

observed in the [FeFe]-hydrogenase *Cb*A5H, notably in the absence of either sulfide or halides.[524] The structure of the air-oxidized H-cluster suggests that Fe_d is coordinated by the sulfur atom of the conserved cysteine residue C367 (Figure 35). The formation of H_{inact} in *Cb*A5H and the resulting resistance to O_2 are lost when this cysteine is replaced with aspartate (Table 5).[424] This mechanism explains why the same H_{inact} IR signature is observed in air-oxidized *Cb*A5H,[524] in *Dd*H natively produced in the sulfate-reducing bacterium *D. desulfuricans*,[487] and in certain standard [FeFe]-hydrogenases exposed to sulfide.[520] However, it is unclear why *Cp*I is reportedly insensitive toward exogenous sulfide, unlike other standard [FeFe]-hydrogenases like *Ch*HydA1 and *Dd*H.[521] Moreover, direct coordination of Fe_d by the cysteine side chain was observed exclusively in *Cb*A5H and not in standard [FeFe]-hydrogenases. It has been shown that C367 in *Cb*A5H is located on a loop whose unique flexibility depends on residues up to 13 Å away from the H-cluster (Figure 35).[424] The investigation of how the conversion between active and inactive states depends on the nature of these residues provided a clear demonstration of long-range outer coordination sphere effects on active site reactivity.

Overall, the mechanism of aerobic inactivation is not well understood. While O_2 inhibition of *Dd*H and *Cb*A5H is reminiscent of the reaction of [NiFe]-hydrogenase with O_2 (Section 3.1.4), most [FeFe]-hydrogenases are irreversibly destroyed under aerobic conditions. It is believed that O_2 binds to the H-cluster like a ligand[525–528] and becomes reduced to superoxide, H_2O_2, or other reactive oxygen species (ROS) that subsequently damage the H-cluster.[529–533] Outer coordination sphere effects are likely to play a role, for example, considering O_2 diffusion through the enzyme[465] and the influence of electron transfer[423] or proton transfer[532] on ROS formation. The comparatively sluggish reaction of sensory [FeFe]-hydrogenases with O_2 had been explained with inefficient proton transfer.[443] Additionally, second coordination sphere effects may influence the formation of the H_{ox}-O_2 state where the superoxide ligand is stabilized by hydrogen-bonding interactions with the ADT headgroup, not unlike H_{ox}-CO and H_{hyd}.[479] As the hydride state is a key intermediate in the catalytic cycle (Figure 34) truly O_2-tolerant [FeFe]-hydrogenases may not be feasible.

3.2.2.5. Artificial Maturation of the H-Cluster.: *In vivo*, the iron–sulfur clusters of [FeFe]-hydrogenase are inserted by the regular iron–sulfur machinery, namely the *isc* system.[534] This includes the [4Fe-4S] cluster of the H-domain that serves are “nucleation core” for the synthesis of the H-cluster.[535] This task is performed by three auxiliary enzymes, HydEFG.[536] A precursor of the diiron site is assembled on HydF[537,538,539] by the help of radical *S*-adenosylmethionine (rSAM) enzyme HydG.[540–544] Then, HydF delivers the active site precursor to the hydrogenase apoprotein where it fuses with the bridging cysteine upon CO release to form the H-cluster. A mechanism has been proposed that includes guidance by charged amino acids,[445] not unlike the channel proposal for the maturation of nitrogenase (Section 2.2). It has been suggested that the role of the rSAM enzyme HydE is the synthesis of the ADT ligand.[545–547]

In vitro, the rather intricate maturation process can be hijacked by loading HydF with diiron compounds and mixing HydF with apo-hydrogenase.[468] This allowed for inserting different diiron site mimics into otherwise unaltered enzyme, creating “cofactor variants” or semisynthetic enzymes that are new to nature.[480,548,549] Further, it has been shown that

even HydF can be avoided in the maturation process: incubation of apo-hydrogenase with diiron compounds lead to functional enzyme.[469] The protocol established by Happe and co-workers led to a great variety of cofactor variants, including different dithiolate and diatomic ligands,[418,468–474] chalcogenides,[475,476] and metal ions (Table 5).[478] For example, replacing the central atom X of the dithiolate ligand from nitrogen (ADT) with carbon (PDT), suppresses any redox change at the diiron site.[468–470] This allowed for studying the protonation and redox chemistry of the [4Fe-4S] cluster in detail (Figure 32).[488]

3.2.3. Direct Interactions between H-Cluster and Protein.—The presence of CO and CN^- ligand at the active site cofactor of [FeFe]-hydrogenase was proven by FTIR spectroscopy in 1996.[517] When the H-cluster was modeled into the first electron density of [FeFe]-hydrogenases *Cp*I and *Dd*H, the position of the diatomic ligands was assigned according to second coordination sphere interactions.[413,420] The chemical identity of the CO and CN^- ligands could not be deduced from the electron densities alone. In *Cp*I, the proximal CN^- ligand may accept a hydrogen bond from the side chain of serine S232 and the secondary amine of the backbone formed by S232 and P231 (Figure 36).[26] The latter is strictly conserved in [FeFe]-hydrogenase and most likely is responsible for the correct orientation of the backbone amine toward Fe_p-CN^-; in *Cp*I and *Dd*H the angle between ligand and backbone is ~170°, indicative of a strong hydrogen bond. Serine S232 of *Cp*I is replaced with an alanine in *Dd*H (A109), which cannot form a bond with the H-cluster. Phylogenetically, the low level of conservation (Table 4) suggests a minor role in the second coordination sphere; however, the effect can be demonstrated. Winkler, Happe, Rüdiger, and co-workers identified siteselective shifts of the Fe_p-CN^- IR band by analyzing *Cp*I–S232A and the corresponding variant of *Cr*HydA1, A92S.[464] The authors even introduced an additional hydrogen bond by changing alanine A94 to serine, which doubled the IR shift observed for A92S (Figure 36). Affecting the electron density at Fe_p and the coupling with the [4Fe-4S] cluster, these variants had a clear influence on the directionality of hydrogen turnover,[464] which may explain the difference in catalytic performance between wild-type *Cp*I and *Cr*HydA1.

The hydrogen-bonding environment of the distal CN^- ligand is difficult to characterize experimentally. Early on, the strictly conserved lysine K358 (*Cp*I) and K237 (*Dd*H) was suggested as hydrogen-bonding donor to Fe_d-CN^- (Figure 36).[550] As the chemical nature of the ADT ligand was still unknown in 1999, Fontecilla-Camps and co-workers even proposed a catalytic proton transfer pathway based on K237 in *Dd*H.[420] Site-directed mutagenesis of this lysine, for example, toward alanine[450] or asparagine,[445] precluded any cofactor insertion and hinted at a key role in the activation of apo-hydrogenase.[430] This renders functional studies of hydrogen bonding difficult. Investigating ^{14}N-labeled *Dd*H by hyperfine sublevel correlation spectroscopy (HYSCORE),[483] Lubitz, Silakov, and co-workers assigned the large quadrupole couplings to a hydrogen bond between Fe_d-CN^- and K237.[436] On the contrary, similar experiments on the *Cr*HydA1 cofactor variant PDT by the same group resulted in substantially simplified ^{14}N HYSCORE spectra that showed no coupling with K228 (equivalent K358 or K237).[551] While the role of K358 in hydrogen-bonding remains ambiguous, the sum of weak interactions around Fe_d-CN^- results in a certain level of structural rigidity in the oxidized state;[552] however, this might not preclude ligand rotation

upon H-cluster state transitions. For example, DFT calculations based on 16 different ^{13}CO isotopomers of the H-cluster suggested an apical CN^- ligand in the H_{ox}-CO state,[493] stabilized by an "internal" hydrogen bond with the ADT ligand. While this interpretation is not without controversy,[492] the stability of H_{ox}-CO was found to be largely reduced upon modification of the dithiolate ligand, following a trend, which cannot be explained with an apical CO ligand.[479] In contrast to CN^-, carbonyl ligands are poor hydrogen bond acceptors.[553] A similar concept of internal hydrogen bonding may play a role in the formation and stabilization of H_{hyd}.[458] Moreover, CO/CN^- ligand rotation was discussed in the context of the temperature-dependent interconversion of H_{ox} and H_{red}/H_{sred}.[505,506] While the role of K357 in hydrogen-bonding remains ambiguous, other conserved residues in the vicinity of Fe_d have been proposed to interact with the CN^- ligand, including S323 as well as a backbone contact involving P234 (Figure 36).[26]

Steric or hydrophobic interactions of the protein fold with the terminal CO ligand have not yet been explored experimentally, but the influence of methionine M353 on the bridging carbonyl was subject to dedicated analysis. Triggering the formation of H_{ox} from H_{ox}-CO by visible light irradiation, Lemon and Peters observed an elongation of the distance between μCO and the sulfur atom of the M353 side chain in *Cp*I.[415] Although both H_{ox}-CO and H_{ox} carry a μCO ligand,[485–487] the increased intensity of the μCO band in the CO-inhibited state may be related to the lack of steric pressure and a greater change in dipole moment. Twenty years later, Peters, King, and co-workers revisited *Cp*I by cryogenic XFEL crystallography, assigning similar differences to an oxidized "conformation A" and a reduced "conformation B" (Figure 37).[554] This includes reorientation of both M353 and sereine S357, the latter which is located close to the [4Fe-4S] cluster in *Cp*I (potential effect are discussed in Section 3.2.4). The presence of a μCO ligand has been recognized as a key requirement for hydrogen turnover by various authors.[503,506,555] Precluding the formation of bridging hydride intermediates,[502] the orientation of M353 may play a key role in maintaining the CO-bridged, rotated H-cluster geometry. Note that M353 and K358 are part of Loop 2 (Figure 30), which may indicate coupling between Fe_d-CN^- and μCO. On the contrary, Table 4 indicates that M353 is moderately conserved at best. [FeFe]-hydrogenases with a glycine or serine residues instead of methionine feature altered catalytic properties (*Cp*III or *Tam*HydS) or pronounced downshifts of the μCO frequency (*Cp*II and *Tm*HydS).[440,443,554] No such shift was observed in *Me*HydA, despite the unique variation from methionine to threonine.[422] In the case of the sensory hydrogenases *Tm*HydS and *Tam*HydS, multiple variations seem to contribute to the catalytic phenotype, which makes it difficult to pinpoint individual effects. Replacement of methionine with leucine in the standard hydrogenases *Cp*I and *Ch*HydA1 greatly diminished catalytic activity.[450]

Methionine M353 may interact with the μCO ligand while M497 and cysteine C299 are hydrogen-bonded to the ADT ligand (Figure 37). These residues are strictly conserved in Group A [FeFe]-hydrogenases but replaced with glycine, leucine, or sereine in *Tm*HydS and *Tam*HydS (Table 4). The cysteine plays a key role in proton transfer and will be discussed in the next paragraph. Methionine M497 is part of Loop 3, which also bears C499 and C503 (Figure 30). Its function is unclear; it has been discussed as an alternative proton transfer relay or hydrogen-bonding partner that keeps the ADT ligand in position.[267] Site-directed

mutagenesis of *Cp*I (M497L) and *Cr*HydA1 (M415L) demonstrated the importance of this residue.[450]

3.2.4. Proton Transfer and Proton-Coupled Electron Transfer.—In all hydrogenases, proton transfer is a key determinant of catalytic efficiency.[297] Protons enter the enzyme to be consumed in the evolution of H_2 or leave the enzyme upon H_2 oxidation, following a Grotthuß-type mechanism. This demands a network of hydrogen-bonded amino acid residues, water molecules, or hydrophilic cofactors. Proton transfer across the second and outer coordination sphere has been recognized as one of the major differences between biomimetic catalysts and enzymes.[556–558]

On the basis of the crystal structure of [FeFe]-hydrogenases *Cp*I and *Dd*H various proton transfer pathways have been proposed.[559–562] As an experimental marker for an involvement of individual amino acids, the analysis was initially restricted to catalytic activity.[454,563] However, when it was discovered that the H-cluster accumulates the H_{hyd} in variants specifically impaired in proton transfer (Table 5),[456–458] spectroscopic methods could be used to investigate the minutiae of proton uptake and release. X-ray crystallography[448] and FTIR difference spectra[564] uncovered a tight hydrogen-bonding network in *Cr*HydA1 and *Cp*I, stretching across >20 Å including a small water cluster W1, and C299, the cysteine residue close to the distal iron ion (Figure 38). On the basis of the first crystal structure of *Cp*I, this pathway was proposed early on.[413] The reduction and protonation of the H-cluster upon formation of H_{red} over H_{ox} has been exploited to trigger proton transfer. The changes in protonation and hydrogen bonding gave rise to distinct FTIR difference spectra, suggesting only subtle changes, for example, the formation of a hydrogen bond between E279 and S319 as well as changes with respect to W1. The lack of difference signals in the SH regime hinted toward a largely preserved hydrogen-bonding environment around C299 and did not support protonation of the ADT ligand, that is, in H_{red}.[564] While the residues involved in proton transfer are mostly conserved within Group A, sensory [FeFe]-hydrogenases show drastic variations (Table 4).[440,443] It remains to be understood how protons are transferred in such enzymes; the influence of amino acids replacements on catalytic activity, bias and reversibility[29] certainly emphasize the influence of the outer coordination sphere.

Next to the “catalytic” proton transfer pathway, a comparison of several [FeFe]-hydrogenase crystal structures suggested the existence of a second, water-based proton transfer pathway.[488] Because of the lack of “acidic” moieties in this trajectory (e.g., glutamic acid residues), the difference in apparent pK_a compared the catalytic pathway allows controlling proton transfer to the diiron site and/or the [4Fe-4S] cluster.[512] Figure 39 shows how a chain of water molecules permeates toward the intersection of the F- and H-domains, that is, C193, which coordinates the most proximal [4Fe-4S] cluster and C499, the later which in turn coordinates the H-cluster. Protonation of a cysteine ligand is rather uncommon in nature; however, quantum mechanical calculations of the IR spectra of $H_{ox}H$, H_{red}', and H_{hyd} provided excellent agreement with the experimental CO/CN^- signature when C499 was protonated *in silico*.[565] As demonstrated in Figure 32, redox- and protonation changes in the second coordination sphere of the diiron site (e.g., at the [4Fe-4S] cluster) result in small yet discernible IR band shifts. The spectroscopic characterization is in agreement

with the pH-dependent population of $H_{ox}H$,[488] the pH-dependent transition potential of the $H_{ox}/H_{red'}$ couple,[501] and the observation that H_{hyd} is formed upon H_2 oxidation via $H_{ox}H$ directly.[446]

Influencing the electron density distribution across the H-cluster, the second proton transfer path has been named "regulatory".[488] In general, electrons and protons tend to move in a concerted fashion, minimizing energetic barriers[22–24] and facilitating long-range coupling between electron transfer and proton transfer, an extreme case of outer coordination sphere effects.[447,566,567] In the case of [FeFe]-hydrogenase, PCET shapes the electron density distribution across the H-cluster by locking reducing equivalents at the diiron site upon protonation of the ADT ligand[498] or formation of a bridging hydride (μH).[502] Similar ideas have been put forward to explain the pH-dependence of the [4Fe-4S] cluster,[488,501] although this has been disputed.[568] The existence of two separate proton transfer pathways (Figure 39) complicates the analysis of the pH-dependence and led to conflicting results.[512] These differences have important implications for the understanding of [FeFe]-hydrogenase catalysis, as discussed elsewhere.[506]

3.2.5. Gas Channels in [FeFe]-Hydrogenase.—The mass transport of reactants like H_2, O_2, and CO within [FeFe]-hydrogenase *Cp*I has been studied using molecular dynamics.[465,569–571] Schulten and co-workers calculated how "the protein's natural equilibrium dynamic motion on the nano-second time scale can define predetermined pathways for hydrophobic gas transport", arguing that permanent channels may not be needed.[569] Figure 40A depicts that this applies to small gases like H_2 in particular. But while CO and O_2 may not access the protein as easily as H_2, Mohammadi and Vashisth suggested defining a "network of pathways" that predicts gas diffusion more accurately[570] (Figure 40B). This complexity must be met with a statistical approach to site-directed mutagenesis, therefore automated screening protocols[572,573] were employed understanding the influence of "gas filters", for example, selectively precluding access of O_2 and CO to the active site (Table 5).[452,453] Currently, the role of hydrophobic gas channels in the outer coordination sphere is not well understood. With respect to CO inhibition, there is a remarkable variety that may help identifying certain trends. The rate of CO inhibition among different standard [FeFe]-hydrogenases was found to vary over three orders of magnitude[423,522] while sensory [FeFe]-hydrogenases[440,443] and [FeFe]-hydrogenase complexes show even lower CO affinities.[432] Apparently, nonconserved residues remote from the active site tune the reactivty; however, the identity of the responsible amino acids and the underlying mechanistic contributions have yet to be explored. In the second coordination sphere of the H-cluster, the replacement of the V296 and F290 in *Cr*HydA1 decreased the rate of CO inhibition ten-fold, but the effects on O_2 deactivation were not proportional.[465] The simultaneous variation of two residues located between the H-cluster and the proximal accessory cluster in *Cp*I moderately reduced the rate of inactivation.[452] As the diiron site has been shown to be the initial target of oxidation, this is an interesting observation that may hint at the role of the [4Fe-4S] cluster in the reaction with "activated" O_2.[529,531,533]

4. FORMATE DEHYDROGENASE

Formate dehydrogenases (FDHs) are a diverse group of enzymes in bacteria, archaea, and eukaryotes that catalyze the reversible two electron and one proton abstraction of formate ($HCOO^-$) to produce CO_2 (eq 3).[574,575] In general, these enzymes are involved in diverse metabolic pathways but mostly in the production of CO_2 from formate.[576] On the basis of the low standard potential of formate oxidation ($E°$ = −420 mV vs SHE) prokaryotes derive energy by coupling it to the reduction to one of several terminal electron acceptors.[577] Some enzymes, however, were described to act as CO_2 reductases, with a preference for the reaction of reducing CO_2 to formate.[578]

FDHs are divided into two major classes, into the metal-dependent and metal-independent FDH enzymes.[576] The metal-independent FDHs generally are NAD^+-dependent and distributed from bacteria to yeast, fungi, and plants.[579] These enzymes have no redox-active metal centers involved in catalysis, but instead NAD^+ is used as a cosubstrate and serves as a hydride acceptor for converting formate directly to CO_2.[580] In these proteins, formate is positioned in proximity to the NAD^+ cosubstrate to facilitate the hydride transfer step. Since this review is focused on GPMs, only the metal-dependent FDHs will be described in detail.

The metal-dependent FDH enzymes are restricted to bacteria and archaea and contain either molybdenum (Mo) or tungsten (W) as metal ions in the active site.[575,581,582] They have a higher complexity by being composed of several subunits, which contain in addition to the active site bis-metal-binding pterin (MPT) guanine dinucleotide (bis-MGD) cofactor (Figure 41) various additional cofactors, such as diverse Fe–S clusters, FMN, or hemes (Figure 42).[575]

4.1. Metal-Containing Cofactor of FDH

The metal-containing FDHs are members of the dimethyl sulfoxide (DMSO) reductase family of mononuclear molybdenum (Moco) or tungsten cofactor (Wco)-containing enzymes.[583,584] In these enzymes, the active site in the oxidized state comprises a Mo or W ion present in the bis-MGD, which is coordinated by the two dithiolene groups from the two MGD moieties, a protein derived selenocysteine or cysteine ligand and a sixth ligand that is accepted to be a sulfido ligand (Figure 41B).

Selenocysteine-containing enzymes have generally a higher turnover number than the cysteine-containing ones.[585] The analogous chemical properties of W and Mo, the similar active sites of W- and Mo-containing enzymes, and the fact that W can replace Mo in some enzymes have led to the conclusion that both Mo- and W-containing FDHs have the same reaction mechanism.[581] The question of why in FDH enzymes both metal ions can be found while other enzymes of the DMSO reductase family exclusively function with only one type of metal ion is still not completely understood.[584,586,587] Generally, it was found that W-containing enzymes catalyze reactions with low redox potentials ($E°$ = −420 mV vs SHE), and it was shown that W^{IV} is a more reducing ion than Mo^{IV}.[587] Possibly for these reasons, the conversion of CO_2 to formate was demonstrated to occur preferentially for W-FDH enzymes.[588–590] However, the purified Mo-containing FDHs were also shown

to perform CO_2 reduction in the presence of excess reducing equivalents.[578] In the cell, however, this reaction would thermodynamically not be favored.[577]

4.2. Structural Features of FDH

Overall, there is a great variety in the subunit architecture of metal-containing FDHs. The α-subunit, or the Moco/Wco containing domain, is highly conserved and minimally comprises the Moco/Wco binding site and a [4Fe-4S] cluster proximal to the Moco/Wco cofactor (Figure 42).[575,578] These α-subunits or domains are typically between 80–95 kDa and the overall folds are highly identical. In most cases, the Moco/Wco cofactor and the proximal [4Fe-4S] cluster interface with additional Fe–S clusters, either within the α-subunit or close by in a neighboring subunit.

Metal-dependent FDHs are found either in the cytosol, in the periplasm or are membrane-bound, facing the periplasm (Figure 42).[575,582] The enzymes are generally involved in diverse biochemical pathways and use different electron acceptors/mediators like hemes, ferredoxins, NAD^+, coenzyme F_{420}, or membrane quinols for the reaction of formate oxidation or CO_2 reduction.[591] The formate oxidation activity of FDH is typically followed via the reduction of methyl viologen (MV), benzyl viologen (BV), or NAD^+. Additionally, the analysis of "catalytic" currents can be followed via protein film electrochemistry (Table 7).[592,593]

In organisms that catalyze the oxidation of formate, this reaction is a key process for obtaining energy and reducing equivalents.[577] The CO_2 formed is usually incorporated predominantly into the Calvin-Benson cycle, as in autotrophic organisms.[576] Formate is a key metabolite for bacteria, arising as a metabolic product of bacterial fermentations and functioning as a growth substrate for many microorganisms (e.g., methanogens and sulfate-reducing bacteria).[599–601]

Formate is also an intermediate in the energy metabolism of several prokaryotes, and formate is used as electron donor during anaerobic respiration in these organisms. Because of the low redox potential of the CO_2/formate couple, formate can be oxidized not only through the aerobic respiratory chain, but it also can serve as an electron donor for the anaerobic reduction of fumarate ($E°_{\text{fumarate/succinate}}$ = +30 mV vs SHE) and nitrate ($E°$nitrate/nitrite = +420 mV vs SHE) or nitrite ($E°$nitrite/NO = +375 mV vs SHE).[581]

Some FDHs are in complex with hydrogenases, like the formate-hydrogen-lyase (FHL) systems from *E. coli*, *Pectobacterium atrosepticum*, or *Clostridium carboxidovorans*.[602–605] Physiologically, the *E. coli* FHL is a membrane-bound system involved in formate oxidation and H_2 evolution under fermentative growth conditions.[606] This system contains the formate dehydrogenase subunit FdhF, and a membrane-bound, cytoplasm-faced [NiFe]-hydrogenase (Section 3.1).[607] Similar coupling of FDH and hydrogenase subunits are observed in some CO_2 reductases that catalyze the reduction of CO_2 to formate with the simultaneous and direct oxidation of H_2. For example, the enzyme from *Acetobacter woodii* is a tetramer, with one Moco/[4Fe-4S] cluster subunit, two subunits with four [4Fe-4S] clusters each, and one [FeFe]-hydrogenase subunit (Section 3.2).[431,608] A W-containing homologue has been identified in *Thermoanaerobacter kivui*.[266]

4.2.1. Carbon Dioxide Reduction and Coupled Catalysis.—A distinct class of FDH-associated enzymes are those found in methanogenic archaea that are involved in hydrogenotrophic CO_2 fixation, en route toward the generation of methane (CH_4).[609,610] The first enzyme involved in reductive CO_2 fixation is the enzyme formylmethanofuran dehydrogenase, which is biased toward the reduction of CO_2 and the coupling of the intermediate product formate to the C_1-carrier methanofuran without the requirement of ATP.[611,612] Furthermore, some organisms that undergo methylotrophic or aceticlastic methanogenesis have an ability to produce CO_2 as a final step, also employing a formylmethanofuran dehydrogenase.[613,614] The basis for this biochemical transformation, until recently has been largely speculative. Similar to FDHs described above, formylmethanofuran dehydrogenases are able to coordinate a bis-MGD cofactor with either Mo or W;[597,609,615–620] the enzyme also exhibits a distinct dinuclear Zn amidohydrolase motif that is involved in the condensation of formate and methanofuran.[612] The *Methanothermobacter* strains *M. marburgensis* and *M. wolfeii* harbor distinct operons of formylmethanofuran dehydrogenase that depend on the presence of tungstate (WO_4^{2-}) or molybdate (MoO_4^{2-}).[597,615–618,621] The former is constitutively expressed in both organisms, whereby a Mo-substituted isoenzyme has been also isolated.[620,622,623] Similarly, the genome of the hyperthermophilic methanogen *Methanopyrus kandleri* encodes for two W-containing formylmethanofuran dehydrogenases, with one that is also only expressed in the presence of Se.[624] Interestingly, distinct molybdopterin dinucleotides have been characterized for formylmethanofuran dehydrogenases from *M. marburgensis*, such as coordinating a molybdopterin adenine or hypoxanthine dinucleotide.[625]

4.2.2. Oxygen Sensitivity.—Most FDH enzymes characterized so far are described to be inactivated in the presence of O_2 (referred to as oxygen-sensitive enzymes).[626–629] To prevent damage by O_2 and to stabilize the enzyme, inhibitors like azide (N_3^-) or nitrate (NO_3^-) are added during the purification of the enzyme, inhibitors that are known to significantly increase the stability of most FDH enzymes.[630] FDHs that exhibit activity in the presence of O_2 with inhibitor present (referred to as oxygen-tolerant enzymes) were described for the Mo-containing enzymes from *R. capsulatus* and *C. necator* and the W-containing enzyme from *D. vulgaris* Hildenborough.[595,596,631,632] What contributes to the higher stability of some enzymes (e.g., from various *Desulfovibrio* specimen[590,633–636] and *Methylobacterium extorquens*[609,637]) in the presence of O_2 without inhibitor present, while other enzymes are extremely sensitive to the exposure of O_2 (e.g., *E. coli* FdhF[626]) is not known so far. While hydrogenases act as oxygenases reducing O_2 to reactive oxygen species (Section 3.2) or water (Section 3.1), the O_2 sensitivity of FDH seems to follow other molecular principles. Recently, it was shown the enzyme from *R. capsulatus* is mainly sensitive to O_2 in the absence of N_3^-.[638,639] By extended X-ray absorption fine structure (EXAFS) spectroscopy, it was revealed that the exposure of the enzyme to O_2 results in a heterogeneous ligandation at the Mo ion and to the exchange of the terminal sulfido ligand by an oxo ligand.[638,639] Azide stabilizes the sulfido ligand, suggesting that N_3^- binds in vicinity to the sulfido ligand and hinders thereby the access of O_2 to the active site sulfido group.

4.2.3. Cofactor Biosynthesis and Moco Sulfuration.—The biosynthetic maturation process of FDHs, in conjunction with the number of redox cofactors, is critical to obtain a bis-MGD cofactor with the correct set of ligands at the active site.[640] FDHs, in conjunction with most Mo- and W-containing enzymes coordinate multiple redox centers in addition to the prosthetic Moco or Wco.[575] The maturation of bacterial bis-MGD-containing enzymes is a complex process leading to the insertion of the bulky bis-MGD cofactor into the apoenzyme. Most of these enzymes were shown to contain a specific chaperone for the insertion of the bis-MGD cofactor.[640] FDH together with its molecular chaperone seems to display an exception to this specificity rule, since the *E. coli* chaperone FdhD has been proven to be involved in the maturation of all three FDH enzymes present in the cell.[641–643] For the FDH FdsGBAD from *R. capsulatus* the two proteins FdsC and FdsD were identified to be essential for enzyme activity, but FdsC is not a subunit of the mature enzyme.[596] While FdsD is a subunit of the $(FdsGBAD)_2$ heterodimer,[591] it has only counterparts in some O_2-tolerant FDHs.[575] While an enzyme purified in the absence of FdsD was devoid of Moco, the role of this subunit is not clear so far.[596,644] On the other hand, FdsC shares high amino acid sequence identity to *E. coli* FdhD, the chaperone for the cytosolic *E. coli* formate dehydrogenase FdhF and the two membrane-bound FDHs FdnGHI and FdoGHI from *E. coli*.[644,645] FdhD was reported to be involved in the formation of the essential terminal sulfido ligand at the Mo ion facilitating the reaction between the L-cysteine desulfurase IscS[642] and FdhF-bound bis-MGD, a mechanism which is essential to yield active FdhF.[642] Initially, it was proposed that the two cysteine residues C121 and C124 in FdhD are involved in the sulfur transfer reaction from IscS further onto the bis-MGD in FdhF. For sulfuration of bis-MGD, FdhD specifically interacts with IscS in *E. coli*. It has been suggested that IscS transfers the sulfur from L-cysteine to FdhD in form of a persulfide. Located in a conserved CXXC motif of FdhD, cysteine C121 and C124 were proposed to be involved in the sulfur transfer process from IscS to bis-MGD by Magalon and co-workers[642] as well as Walburger, Arnoux, and co-workers.[643] FdhD was cocrystallized in complex with GDP suggesting direct binding of bis-MGD to FdhD; however, it was not possible to prove that the cofactor is bound in an active form.[643] A study using *R. capsulatus* FdsC provided evidence that the cofactor is indeed bound in the active form containing the terminal sulfido ligand, which was revealed by the insertion of MGD cofactor into TMAO reductase,[644] producing an active enzyme.[645] Further, a phylogenetic study revealed that the CXXC motif is not conserved among FdhD-like chaperones and by site-directed mutagenesis it was proven that the two cysteines in the CXXC motif are not essential, putting the mechanism of the persulfide-transfer involving FdhD as a sulfurtransferase into question.[645] It therefore remains possible that IscS directly transfers the persulfide sulfur to the Mo ion in FdhD-bound bis-MGD, notably without the involvement of additional cysteine residues. The source of electrons for the reductive cleavage of the persulfide is also unknown. Directly comparing the chaperones FdhD from *E. coli* and FdsC from *R. capsulatus* in the same study revealed that their roles in the maturation of FDH enzymes from different subgroups can be exchanged.[645] In summary, the binding of sulfido-containing bis-MGD to the chaperone is a common characteristic of FdhD-like proteins and ensures insertion of a competent active site cofactor for catalysis.

4.3. Role of Sulfido- and Amino Acid Ligands

The first coordination sphere at the active site cofactor of FDHs includes the sulfido ligand and the cysteine or selenocysteine ligand (Figure 41A).[627,646] The sulfido group was shown to act as a hydride acceptor from formate in the reaction of formate oxidation.[647] This reaction step was mainly established by EPR spectroscopy, showing that the C_α hydrogen atom from formate is transferred to a ligand in the first coordination sphere, which resulted in the binding of a strongly coupled and solvent exchangeable proton, with a hyperfine constant of 20–30 MHz in the Mo^V state.[648–650] Similar hyperfine constant values were determined in the Mo-containing enzyme xanthine oxidase, where a hydrogen is transferred from the C_8 hydrogen atom of xanthine to the active site sulfido ligand at the Mo ion.[651] Similar to xanthine oxidase, previous studies showed that FDHs exhibited sensitivity to cyanide (CN^-).[652] In a recent XAS study on *R. capsulatus* FDH it was shown that the sulfido ligand was lost forming thiocyanate (SCN^-), which represents another similarity with xanthine oxidase.[638] The resulting desulfo enzyme harbors an oxo group in place of the sulfido group, which is not able to act as hydride acceptor. However, examples of FDHs that exhibit apparent or partial CN^- insensitivity are known, including W-FDHs from *D. desulfuricans*[648,653] and *D. gigas*,[636] as well as the W-containing isoenzyme of formylmethanofuran dehydrogenase from *M. marburgensis*.[617]

Formate dehydrogenases catalyze formate oxidation and CO_2 reduction at the bis-MGD with the involvement of amino acids in the first and second coordination sphere. Of these, the first amino acid of importance is the cysteine or selenocysteine residue that serves as a covalent linkage between the bis-MGD cofactor and the protein (Figure 41). Given the diversity of FDHs, the preference to encode for a selenocysteine residue has been discussed to reflect an evolutionary advantage. Selenium as being essential for bacteria was discovered by Pinsent in 1954,[654] whereby the activity of FDH was dependent on the presence of Se, and was later discovered to be in the form of a single SeCys residue encoded by the unique codon UGA.[655] Selenocysteine offers a lowered pK_a and improved performance as a nucleophile relative to cysteine that results in enzyme exhibiting an increased catalytic reactivity.[656] These considerations compelled Axley and co-workers in the early 1990s to investigate the essentiality of the residue in *E. coli* FdhF, by performing site-directed mutagenesis.[585] They showed that exchange of the active site selenocysteine to cysteine (U140C) in *E. coli* FdhF resulted in a reduction of k_{cat} by a factor of 300, and a decrease in $K_{M\ formate}$ relative to a constant K_M with BV as an electron acceptor (Tables 7 and 8). While the reduction in k_{cat} is consistent with differences in chemical properties of Se vs S, it also affected the relative affinity of the substrate formate at the active site.[585]

Despite the preliminary studies investigating the role of selenocysteine U140 in *E. coli* FdhF, the role of the amino acid ligand in catalysis is a matter of debate and not clear to date. As discussed in detail below, mainly two models exist, one in which the proteinaceous ligand remains bound to the Mo ion during catalysis and therefore has no direct role in the catalytic mechanism.[632] In the other model, the amino acid ligand is displaced from the Mo ion, thereby providing a coordination site for the substrate and it temporarily serving as a second coordination sphere ligand.[646] While in the Mo^V state of *E. coli* FdhF, it was shown that the Mo ion is hexacoordinated with the amino acid ligand,[629] different data exist on the reduced

Mo^{IV} state. In a reinterpretation of the crystallographic data of the formate-reduced *E. coli* FdhF enzyme it was suggested that the selenocysteine residue is dissociated from the Mo ion and is shifted 12 Å away.[646] However, a recent crystal structure of the formate-reduced *D. vulgaris* Hildenborough W-FDH showed a hexacoordinated metal ion.[599] It needs to be considered that in these structures the oxidation state of the Mo/W ion is speculative (given the presence of multiple redox cofactors) and that none of the structures was solved in a high enough resolution to firmly establish the coordination of the substrate formate. On the contrary, different results have been obtained in XAS studies using different enzyme sources. In a recent study of the *R. capsulatus* enzyme it was suggested that in the Mo^{V} and the Mo^{VI} state the cysteine is a ligand to the Mo ion, while in the formate-reduced Mo^{IV} state (in the absence of N_3^-), the cysteine was displaced from the metal and instead a bond reflecting a Mo–O distance was present.[638] Contrary to this study, EXAFS data of the *E. coli* and *D. desulfuricans* enzymes in the oxidized and reduced states were interpreted with a hexacoordinated Mo ion.[657,658] Here, it needs to be pointed out that the data of the *E. coli* were derived in the presence of high concentrations of the inhibitor N_3^-, which influence the binding of formate (discussed in more detail below). As for the *D. desulfuricans* enzyme the presence of the sulfido ligand is not clear, since it was not assigned by the EXAFS study.

To probe the displacement of the amino acid ligand, inhibition studies with iodoacetamide were performed, an alkylating agent that reacts with “free” thiols. For both the *E. coli* and the *R. capsulatus* enzymes an alkylation of the selenocysteine or cysteine ligand was identified, notably only in the formate-reduced and NO_3^-/N_3^- inhibited enzymes, but not in the oxidized enzyme.[585,598] However, no alkylation of the selenocysteine residue could be identified in the W-containing *D. vulgaris* enzyme.[599] The *E. coli* FdnGHI enzyme likewise is not alkylated when incubated with formate.[630] Heider and Böck speculated that this difference might be correlated to electron transfer from the reduced metal center to the [4Fe-4S] cluster and further to the final electron acceptor, since in some enzymes the Mo^{V} state is more stable than for other enzymes.[659] A fast reoxidation of the enzyme from the Mo^{IV} to the Mo^{VI} state might protect the enzyme from alkylation, while in enzymes with a long-lived reduced state, the amino acid ligand has a higher probability to be alkylated. In conclusion, while hexacoordination of the Mo ion in its Mo^{V} and Mo^{VI} states is established now, the coordination of the Mo^{IV} state needs to be clarified in future studies.

4.3.1. Amino Acids in the Second Coordination Sphere.—

In addition to the active site selenocysteine or cysteine residue, primary components of the second coordination sphere of all metal-containing FDHs include a highly conserved arginine and a histidine residue (Figure 41B) that have been proposed to ensure optimal substrate binding to and proton transfer away from the active site.[575] Site directed mutagenesis studies on *R. capsulatus* FDH revealed that in the H387M variant (equivalent to H141M in Figure 41B), the k_{cat} remained similar to that of wild-type enzyme, suggesting a similar orientation of H387 and M387 (Tables 7 and 8).[598] However, in this variant, the pH optimum was lowered to 7.5 with a 19-fold increase in $K_M^{formate}$. The replacement of H387 with a lysine reduced the activity to 3% of that of the wild-type enzyme, accompanied by an increase in $K_M^{formate}$ and a shift of the pH optimum to 8.0. When R587 (equivalent to R333 in Figure 41B) was replaced by a lysine, retaining the positive charge of the side chain, ~ 30% of wild-type

activity was obtained, however, accompanied by an increase in $K_M^{formate}$ and a shift in the pH optimum to 8.0 (Tables 7 and 8). These results show that H387 influences the pH optimum of the reaction, while the drastic increase in $K_M^{formate}$ reveals a role for R587 in substrate binding at the active site.

4.3.2. Substrate Channels in the Outer Coordination Sphere.—The first FDH structure characterized by X-ray diffraction was the monomeric FdhF protein from *E. coli*, which was solved both in the oxidized (2.8 Å resolution) and formate-reduced (2.3 Å resolution) state (Figure 43A and Figure 44A).[627] The active site Mo ion was initially interpreted to carry a hydroxyl ligand; however, later the Mo–OH bond was reinterpreted as being a Mo-SH one.[646] Two other catalytically important amino acids in the active site were identified to be H141 and R333 (Figure 41B). These two residues are strictly conserved in all Mo- and W-containing FDHs, and their involvement in substrate binding and/or proton abstraction from the substrate has been proposed.[598] After substrate oxidation, electrons are transferred from Mo^{IV} to the nearby [4Fe-4S] cluster. Here, a conserved lysine K44 is located between one pterin ring of bis-MGD and the [4Fe-4S] cluster (Figure 41B), and an involvement of this residue in the electron transfer reaction has been suggested (Figure 43A and Figure 44A).[646]

The second structure of an *E. coli* FDH enzyme is the one of FdnGHI (EcFDH-N) which was solved as a “mushroom shaped” $(\alpha\beta\gamma)_3$ heterotrimer of trimers, with subunits of 113, 32, and 21 kDa, respectively.[660] The crystal structure of FDH-N showed that the catalytic subunit of FdnG, composed of 982 amino acids, has an overall fold similar to the structure of FdhF. The substrate access funnel is opening down to the active site Mo ion, constructed of predominantly positively charged residues thus facilitating substrate binding, and likewise appears similar to FdhF (Figure 44B). The Mo ion of oxidized FdnG binds the bis-MGD cofactor, while additionally coordinated by U196. A sixth ligand in the oxidized enzyme was initially modeled as a hydroxy species (at 2.2 Å), but in light of the reinterpretation of the FdhF structure, the sixth ligand is most likely a terminal sulfido species.[646] Overall the Mo coordination sphere closely resembles that seen in oxidized FdhF (Figure 44A), with an arginine and a histidine present in the active site, thus implying a conserved mechanism involving the same amino acids for formate oxidation.

At the active site of *D. gigas* FDH, the W ion is bound to two MPT moieties, to a selenocysteine, and to an inorganic S or O ligand (Figure 44C).[634,635] The crystallographic data favor a S atom for the sixth ligand, although the resolution of the data did not permit unambiguous discrimination between O and S. As has been shown for other enzymes from the same family, the bis-MGD cofactor is buried in the protein, stabilized by an extensive network of hydrogen bonding interactions. The conserved lysine K56 bridges the pterin of the bis-MGD cofactor and the proximal [4Fe-4S] cluster. In vicinity of the buried W ion H159 and R407 are found (Figure 44C). Formate access to the active site could be facilitated by a channel of charged residues, including H159, R156, H423, H963, H376, K91, K444, K445, A587, and A407. CO_2 release from the active site might be facilitated by a hydrophobic channel, including V412, H159, W730, and Y428.

The crystal structure of the tungsten and SeCys containing FdhAB from *D. vulgaris* Hildenborough was solved in the oxidized and reduced form (Figure 43B and Figure 44D).[599] In the oxidized form, the W ion is hexacoordinated to four S atoms from the two dithiolenes, a Se atom from U192 and an indeterminate sulfur ligand (W-SH or W = S). The catalytic pocket and respective entrance channel are positively charged, and three glycerol molecules haven been modeled in this cleft. In the vicinity of the W ion there are two strictly conserved amino acids: H193, establishing a π-interaction with the Se atom of U192, and R441, which establishes a hydrogen bond with a cocrystallized glycerol molecule. A similar π-interaction is observed in the FDH from *D. gigas*, among respective residues H159, U158, and R407 (Figure 44C).[634] The glycerol closest to the W ion is hydrogen-bonded by S194 and H457, the second glycerol is oriented by R441, T450, and a water molecule oriented by Y462. A third glycerol is found at the channel entrance, oriented by a backbone contact including G207 and water molecules that connect with W492 and R206. These glycerol molecules probably occupy formate binding sites and may shed light on the formate shuttling mechanism.

In the formate-reduced form of FdhAB from *D. vulgaris* Hildenborough, a conformational rearrangement was observed, involving I191, U192, and H193 (Figure 43B).[599] The U192 C_α atom shifts up to 1.00 Å from the position occupied in the oxidized form while the Se atom remains coordinated to the W ion. Further, the catalytically relevant H193 moves away from the active site and a water molecule occupies the position of the imidazole ring, establishing a hydrogen bond with G442. Together, H193 and R441 are oriented in a *cis* conformation, relative to the *trans* orientation observed in the oxidized structure and other FDH structures. This shift also resulted in assignment of a hydrophobic channel distinct from the hydrophilic one identified in the oxidized state (Figure 44D). The U192 loop shift is propagated to neighboring amino acids from different domains that promotes the tilt of the side chains of W533, F537, and F160. Overall, neither formate nor CO_2 were identified in the reduced structure, leaving the possibility that the reduced structure was solved after CO_2 release from the enzyme.

The cryogenic electron microscopy (cryo-EM) structure of *R. capsulatus* FDH revealed a 360 kDa dimer of FdsABGD heterotetramers in which the FdsD subunit is bound to the FdsA subunit (Figure 43C and Figure 44E).[591] In the oxidized structure, the active site structurally resembles that of *E. coli* FdhF with six ligands coordinated to the Mo ion represented by the two dithiolene groups of the bis-MGD molecule, the C386 ligand, and a sulfido ligand that is oriented toward V592 (Figure 44E). Additionally, the NADH-reduced cryo-EM structure was also solved; however, the protocol did not result in a full reduction to the Mo^{IV} state, instead the enzyme was only partially reduced to the Mo^{V} state.[591] In the Mo^{V} state, no structural changes at the bis-MGD pterin and dithiolenes were observed and C386 was present as a ligand to the Mo ion (Figure 43C). The inability of NADH to completely reduce the enzyme might either be dependent on unfavorable redox potentials of the cofactors for the back reaction or is based on the presence of 10 mM N_3^- that prevent complete reduction of the enzyme. Interestingly, in none of the structures clear evidence for stochiometric binding of N_3^- in any particular location of the EM map could be assigned.

Two reactant channel could be assigned in the cryo-EM structures, starting at the Mo ion and separating at the active site residue R587 into different exits (Figure 44E). The pore of the shorter channel is mainly formed by polar and charged residues suggesting channeling of hydrophilic substrate (i.e., formate) from an entry site near FdsD to the active site. The channel-forming residues are similar to those in oxidized FdhF. The second channel bears predominantly hydrophobic residues suggesting the possibility of CO_2 transport to or away from the active site. FdhF contains a similar hydrophobic channel, which is however blocked by V145 and M157 in place of glycine residues in *R. capsulatus* FDH. On the basis of the positioning of R587 at the cross section of both channels, it has been suggested that this residue might control gate opening to each channel thereby facilitating efficient catalysis.[591,598] Intriguingly, the glycine residues are conserved in NAD^+-dependent FDHs while other FDHs display larger hydrophobic residues at this position.

The structural characterization of the W-containing formylmethanofuran dehydrogenase from *M. wolfeii* has provided considerable insight toward the importance of the second and outer coordination spheres in the FDH reaction (Figure 44F).[612] The enzyme, crystallized as a dimer and a tetramer of the FwdABCDFG heterohexamer, respectively, showed a modular composition of the catalytic subunits and 46 iron–sulfur clusters bound in the tetrameric supercomplex. Interestingly, an internal 43 Å-long hydrophilic water cavity separates the bis-MGD and the amidohydrolase active sites (Figure 44F). The interface of the subunits FwdB (housing the bis-MGD) and FwdA (housing the Zn_2-amidohydrolase site) that comprises the hydrophilic channel is distinct from the FdsD–FdsA interface characterized in the cryo-EM structure of *Rc*FDH.[591] However, several of the second coordination sphere residues that constitute this channel are similar, including H119, R288, N113, and N297 (*Mw*FwdA numbering). Interestingly, a H_2O molecule was found in proximity to the active site residue R288 at the interface of the hydrophobic and hydrophilic channels (Figure 44F). The lack of access by which exogenous formate might be expected to bind is consistent with the substantial differences in the substrate affinity among the isoenzymes from *M. wolfeii* and the Mo-containing enzyme from *Methanosarcina barkeri*.[616,617]

Despite being an enzyme that is biased toward the reduction of CO_2, features of the hydrophobic channel associated with CO_2 binding are not so different relative to structurally characterized FDH counterparts (Figure 44). Similar to *Rc*FDH, *Dvh*FDH, and *Dg*FDH, the hydrophobic channel principally begins at the interface of the active site H387 and R587 residues (*Rc*FDH numbering) as an elaborate cavity characterized crystallographically without H_2O molecules bound.[612] While the cryo-EM map of the *Rc*FDH structure[591] does not allow for a direct comparison to assess the hydrophobicity of the channel, the predicted channel is nevertheless similar to that of the crystallographically characterized *Dv*H FDH enzyme.[599]

The hydrophilic channel was proposed to represent a conduit by which protons could be delivered to and from the bis-MGD cofactor in formylmethanofuran dehydrogenase.[612] This is insightful, with respect to clarifying the distinct, requisite pathways to deliver protons, electrons, and substrates. The proton transfer pathway starts at the active site H119 and C118 residue in vicinity of the distal pterin, whereby the protons are aided by numerous H_2O molecules toward H290 and C91 (*Mw*FwdA numbering, Figure 44F).[612] By

comparison, other structurally characterized FDHs also exhibit residues at these positions that could in principle aid in proton shuttling to the active site.[591,599,627]

4.4. Inhibition of FDH in the First and Second Coordination Sphere

Inhibition of different FDH enzymes has been studied intensively using various inhibitors, and among them the most prominent one is N_3^-, which is an isoelectronic molecule to CO_2. Azide has been thought to be a transition analogue for the FDH reaction, and is most often used during the purification of FDHs to protect the enzyme from oxidative damage and loss of the sulfido ligand.[638] Inhibition of FDH using pseudohalides of varying electron donor strengths (e.g., N_3^-, OCN^-, NO_2^-, and NO_3^-) have been precursorily characterized in solution-based, *in vitro* assays.[594,626,652,661–664] While all inhibitors were more potent to inhibit formate oxidation, N_3^- and OCN^- are generally reported to be mixed-type inhibitors, revealing two binding sites with one being competitive and the other binding site being noncompetitive. By comparison, NO_2^- and NO_3^- have been shown to be competitive inhibitors using formate as a substrate.[661] In the crystal structure of *E. coli* FdhF, NO_2^- was proposed to be coordinated to the Mo ion.[627]

Recently, in a chronoamperometry study of *E. coli* FdhF these pseudohalide inhibitors were used to study their binding to the reduced and oxidized enzyme.[665] The inhibition studies revealed that inhibitor binding is oxidation state-dependent, since potential- and formate-dependent results could be ascribed to differences in population of the oxidation state Hirst, Reisner, and co-workers concluded that N_3^-, OCN^-, and NO_3^- bind directly to a vacant coordination site of the Mo ion and that these inhibitors bind more tightly to Mo^{VI} than to Mo^{IV}.[665] In addition, it further was suggested that the selenocysteine residue in *E. coli* FdhF has to dissociate from the Mo ion to generate the vacant position to which the inhibitors can bind.

4.5. Catalytic Mechanism of Formate Oxidation

While metal-dependent FDH enzymes have been studied for several decades and the *E. coli* FdhF enzyme was among the first molybdoenzymes to be crystallized,[627] details of the reaction mechanism, involving the first and second coordination sphere remain poorly understood, and the catalytic mechanism of formate oxidation is still unclear. As will be described below, the numerous mechanisms proposed for FDH reflect a lack in clarity of the coordination environment and oxidation state of the bis-MGD cofactor. Overall, the formate oxidation mechanism is believed to be similar between Mo-containing and W-containing FDHs.

To form CO_2 from formate, FDH enzymes have to catalyze the transfer of one proton and two electrons (eq 3). Currently, it is assumed that this reaction is not an O atom transfer reaction, as characteristic of many Mo/W-bis-MGD family enzymes.[583] It has been proposed that the reaction product is CO_2 rather than bicarbonate (HCO_3^-), the product expected in an O atom transfer mechanism. This assumption was first proposed by Thauer and co-workers in 1975 in the characterization of the FDH from *Clostridium pasteurianum*[666] and has been supported in 1998 by Khangulov and co-workers on *Ec*FDH–H by determining the product formation using of ^{13}C-labeled formate in ^{18}O-enriched water.[647]

A recent study by Fourmond and co-workers applied an electrochemical approach on the *Dvh*FDH enzyme to confirm that the substrate of FDHs for the backreaction of CO_2 reduction is CO_2 rather than HCO_3^-.[592] The method consisted in monitoring the changes in activity that occur during the slow relaxation of the equilibrium between CO_2 and bicarbonate.[592] However, as already pointed out in 1968 by Benedict, Cooper, and co-workers,[667] it still remains possible that these observations are rather a reflection of the binding of the preferred molecule to the active site, rather than what is happening directly at the active site (i.e., catalysis). It therefore might be possible that a charged HCO_3^- molecule is hindered from entering the active site via the hydrophobic channel, while CO_2 could enter easily. At the active site cofactor, CO_2 then could react with H_2O to form HCO_3^-, which would provide the substrate for the reaction of CO_2 reduction. This option has so far been neglected in most studies and should be considered, since in some structures a water molecule has been identified in the active site bound in vicinity to the conserved arginine residue, as discussed above (Figure 44). It also needs to be considered that $H_2{}^{18}O$ exchange in the active site of the enzyme might be slow and therefore the reason why Khangulov and coworkers did not find ^{18}O-labeled CO_2 in their approach.[647] In this respect, approaches that factor second and outer coordination sphere effects regarding CO_2 production or formate diffusion would provide significant insight toward clarifying the formate oxidation/CO_2 reduction mechanism.

Overall, on the basis of different experimental data and theoretical calculations, different catalytic mechanisms for FDHs have been proposed, which we want to describe in more detail (Figure 45). As explained above, a central question is whether the amino acid ligand (selenocysteine or cysteine) remains coordinated to the Mo- or W metal during catalysis or whether it dissociates to provide a vacant site for substrate binding. Further questions relate to the involvement of the second coordination sphere residues that also serve a critical role in the reaction mechanism.

The first mechanism was proposed by Heider and Böck in 1993, before the crystal structure of *E. coli* FdhF was described (Figure 45A).[659] In this mechanism, the binding of only one pterin ligand is proposed (the existence of two dithiolene MPT groups as ligands to the metal ion were first observed in the crystal structure of the *Pyrococcus furiosus* W-containing aldehyde-ferredoxin-oxidoreductase in 1995),[668] one oxo ligand, and the fifth ligand being the selenocysteine residue. The authors suggested that binding of formate to the active site displaces the selenocysteine ligand from the Mo ion and the selenide then initiates formate oxidation by a nucleophilic attack to the Mo-bound formyl group. Carboxyl transfer to the selenocysteine residue would releases CO_2 in the next step. Following the first crystal structure of *E. coli* FdhF solved by Sun and co-workers in 1997[627] and concurrent XAS studies,[657] it was suggested that the Mo ion is coordinated by a hydroxyl group instead of a terminal sulfur atom (Figure 45B). The subsequent identification of a terminal sulfido group in the first coordination sphere of Mo and the observation that the loop containing U140 was shifted away (12 Å) from the Mo ion in the formate-reduced *E. coli* FdhF led to a reformulation of that mechanism (Figure 45C).[646] Romao and Raaijmakers suggested that upon formate binding to the active site, U140 is displaced from the Mo ion. After formate binding to the Mo ion through an O atom, The U140 selenol anion (Se^-, with R333 as counterion) would deprotonate formate at the C_α atom and two electrons are

transferred to the metal center simultaneously to form Mo^{IV}. Subsequently, the proton is transferred to H141, which changes its conformation in the reduced enzyme. After CO_2 release and rebinding of the selenocysteine ligand, the Mo ion is in a hexacoordinated form, with the sulfido group as the axial ligand.[657] The catalytic cycle would be completed with the oxidation of Mo^{IV} to Mo^{VI}, via intramolecular electron transfer to the [4Fe-4S] center. Theoretical calculations of the activation energy for C–H bond cleavage showed that the proton abstraction is much more favored with an unbound selenocysteine (19 kcal/mol compared to 36 kcal/mol for bound selenocysteine). In this mechanistic proposal, the conserved arginine R133 facilitates formate binding and histidine H141 acts as the final proton acceptor.[646] The terminal sulfido ligand of the Mo ion, on the contrary, would have no active role in formate oxidation.

Another mechanism was proposed based on theoretical calculations involving selenocysteine dissociation from the Mo ion through a “sulfur shift” (Figure 45D).[653] In this mechanism, Cerqueira, Gonzales, Moura, and co-workers proposed that the oxidized enzyme is hexacoordinated by the two MGD molecules plus the selenocysteine and the terminal sulfido group. When formate enters the active site, oriented by the positively charged arginine (e.g., R333 in *E. coli* FdhF), the repulsive environment generated would trigger a ligand shift to yield a Mo–S–SeCys moiety. This would create a vacant position to which the formate could bind. Subsequently, the S-SeCys bond is cleaved and the selenol anion abstracts the formate C_α proton (analogous to the model in Figure 45C). Carbon dioxide is subsequently released. The catalytic cycle would be completed with the oxidation of Mo^{IV} to Mo^{VI} via intramolecular electron transfer to the [4Fe-4S] center and deprotonation of the selenocysteine residue. In the absence of formate, the selenocysteine-containing loop (e.g., V139, U140, and H141 in *E. coli* FdhF, see Figure 43A) is reoriented, and the Mo–S–SeCys bond reformed. This proposal[653] is in agreement with the increased acidity of the selenocysteine side chain ($pK_a \approx 5.2$), which allows the existence of a selenol anion at physiological pH values. The alkaline pK_a value of a cysteine side chain ($pK_a \approx 8.2$) would prevent a cysteine residue having such a function. The pK_a values of both amino acids have been evoked to explain why the U140C variant of *E. coli* FdhF shows a 300-fold activity decrease.[585] In addition, the high activation energy calculated for the proton transfer from formate to selenol (SeH) is in agreement with the isotopic effect studies[647] that showed that the formate C–H bond cleavage is the rate-limiting step of the catalytic cycle. The role of the sulfido ligand, however, is also unclear in this mechanism.

An additional mechanism was proposed by Zampella and coworkers in a computational study (Figure 45E).[669] In this mechanism formate first binds to the Mo ion by displacing the selenocysteine group, then Mo abstracts a hydride ion from formate, giving a Mo–H species and releasing CO_2. Upon recovery of the pentacoordinated Mo ion, the sulfido group is protonated at the expense of the hydride species. In this mechanism, also the role of the sulfido group is unclear and a Mo–H bond is very unusual. Following theoretical assumptions, Dong and Ryde recently proposed an additional mechanism (Figure 45F).[670] They proposed that the sulfido ligand abstracts a hydride ion from the substrate, yielding Mo^{IV}–SH; however, distinct from any other mechanism, carboxylate was considered binding to the cysteine ligand, forming a thiocarbonate/cysteine zwitterion. Upon charge compensation, CO_2 leaves the enzyme and the Mo ion is oxidized back to the Mo^{VI} state.

Finally, Hille and Niks proposed a mechanism that is based on experimental data[582,632] and considers binding of formate to the second coordination sphere without contacting the Mo ion (Figure 45G).[671] In their proposal, the sulfido ligand abstracts a hydride ion from formate, resulting in a two electron-reduced intermediate Mo^{IV}–SH, and CO_2 is released. In this mechanism, however, the (seleno-) cysteine would not be involved and the role of the metal ion is only to provide a hydride acceptor by coordinating the sulfido ligand.

4.5.1. Conversion of FDH to a Nitrate Reductase.—The sulfur shift-based mechanism to oxidize formate, described above and depicted in Figure 45A, has also been evoked to explain the nitrate reduction catalyzed by periplasmatic nitrate reductases (NR).[653] The FDH and nitrate reductase active sites are surprisingly superimposable,[598] with the later harboring a Mo ion coordinated by the two characteristic MGD molecules, one terminal sulfido group, and a cysteine sulfur atom.[672] In addition, the nitrate reductase active site also comprises conserved threonine and methionine residues (arginine and histidine, in FDH). In the oxidized active site of both enzymes, the Mo/W ion is hexacoordinated and a sulfur shift is needed to displace the selenocysteine or cysteine residue to create a vacant position for substrate binding (i.e., formate or nitrate).[589,653]

The similarities between FDH and nitrate reductases were highlighted by converting *Rc*FDH to an enzyme with nitrate reductase activity.[598] This was achieved by exchanging the histidine H387 to a methionine residue and the arginine R587 to a threonine residue, both that are conserved in nitrate reductases. In addition, an additional arginine residue was inserted to the active site of *Rc*FDH and this enzyme variant showed bis-MGD dependent nitrate reductase activity. However, the involvement of the sulfido ligand of this enzyme variant for nitrate reductase activity is not clear, since also an enzyme form containing an oxo ligand instead of the sulfido ligand was able to reduce nitrate.[598] Nitrate reductases catalyzes the typical O atom transfer mechanism characteristic for all other molybdoenzymes.[672]

4.5.2. Second and Outer Coordination Sphere Effects on Electron Transfer.—In addition to the active site Mo/W ion, the sulfido ligand, and active site residues involved in CO_2 reduction and formate oxidation of FDH and formylmethanofuran dehydrogenases, additional components are critical toward the catalytic activity. For example, a feature common to all FDHs and formylmethanofuran dehydrogenases is the coordination of a [4Fe-4S] cluster that is within electron channeling distance to the bis-MGD cofactor (Figure 41). For all FDH enzymes identified to date, a [4Fe-4S] cluster is within 12 Å of the Mo/W ion, and within 6 Å of the proximal pterin of the bis-MGD (Figure 44).[591,599,612,627,634,660] This iron–sulfur cluster is proposed to be the entry point of the electron transfer pathway by which electrons that are generated from formate oxidation or are needed for CO_2 reduction are passed along, respectively. Reduction of this $[4Fe\text{-}4S]^{2+/+}$ cluster has been observed by EPR spectroscopy, using either formate or dithionite as a reductant. These are typically conditions by which the bis-MGD cofactor can also become reduced to a Mo^V/W^V oxidation state, which complicated the spectral analysis. Early characterization work of FDH from *Methanobacterium formicicum* to differentiate the [4Fe-4S] cluster from the Mo^V/W^V signal showed that this cluster had *g*-values of 2.047, 1.948, and 1.911;[649,650] however,

it should be noted that this FDH also can bind a [2Fe-2S] cluster whose g-values would overlap.[575] By comparison, reduction of the proximal [4Fe-4S] cluster in *Ec*FDH–H (an FDH that coordinates only one [4Fe-4S] cluster) gave a similar assignment (*g*-values of 2.045, 1.957, and 1.840). Similar assignments have been made for the corresponding iron–sulfur clusters for several FDHs by which EPR spectral data is available.[647]

As a participatory component in the redox events catalyzed by the bis-MGD cofactor, perhaps it is not surprising that communication with the proximal [4Fe-4S] cluster is essential for the catalytic reaction. However, there are few examples of FDHs by which concomitant catalytic activity and loss of the proximal [4Fe-4S] cluster has been shown. For example, a EPR spectral characterization of the FDH from *C. necator* FDH has shown that under conditions by which the [4Fe-4S] cluster is reduced and the bis-MGD is poised in the paramagnetic Mo^V state, electron–electron spin coupling between the two paramagnetic centers occurs, primarily reflected in the loss of sharpness of the Mo(V)-based ^1H hyperfine splitting.[632] As EPR spectroscopy cannot characterize the diamagnetic oxidation states of the bis-MGD cofactor and iron–sulfur cluster, a parallel, multifaceted spectroscopic approach is required to identify all oxidation states.

In addition to participation of the proximal [4Fe-4S] cluster in the catalytic activity of the bis-MGD cofactor, an additional, undercharacterized aspect of FDH catalysis relates to the two molybdopterin guanine dinucleotide ligands that coordinate the Mo/W ion. These relatively large, pterin-based ligands are noninnocent and redox active, meaning that they partake in the electron transfer reactions between the Mo/W ion and the proximal [4Fe-4S] cluster immediately preceding or following catalysis. By comparison, the longer [4Fe-4S] cluster–Mo/W distance (13–16 Å) observed relative to the shorter proximal [4Fe-4S]–(proximal) MGD distance (6–10 Å) supports the presumption that the proximal MGD ligand links the FDH redox events at the Mo/W ion with the iron–sulfur cluster electron conduit.[591,599,612,627,634,660] So far, all bacterial FDHs coordinate two MGD ligands at the active site; however, distinct nucleotides were identified to be bound in place of the guanine in FDH-like enzymes from archaea (e.g., formylmethanofuran dehydrogenase from *M. marburgensis*).[625] The reason for this remains unclear so far.

5. CO DEHYDROGENASE

5.1. Physiological Function and Structure of CODH

CO dehydrogenases (CODHs) are gas-processing metalloenzymes that catalyze the reversible oxidation of CO to CO_2 (eq 4). There are two unrelated classes: one is a Mo-based enzyme exclusively found in aerobic carboxydotrophs.[673,674] These CODHs catalyze the reaction in the direction of CO oxidation (CO_2 release) and will not be discussed here any further. The other is a class of metalloenzymes found mainly in anaerobic bacteria and archaea hosting a Ni- and Fe-containing cofactor, which catalyze both CO oxidation and CO_2 reduction.[675]

Organisms such as *Rhodospirillum rubrum* (*Rr*) and *Carboxydothermus hydrogenoformans* (*Ch*) use the enzyme CODH to oxidize CO to CO_2.[676] The reaction occurs at the so-called “C-cluster”, a unique [Ni-3Fe-4S] cluster with an additional Fe ion. The enzyme

is a homodimer that houses two identical C-clusters and three electron transferring metal centers: two “B-clusters” of the [4Fe-4S] type and one “D-cluster” located at the interface of the two monomers (Figure 46A). The latter is either a [4Fe-4S] cluster (e.g., in *Rr*CODH) or a [2Fe-2S] cluster (e.g., in CODH from *Desulvovibrio vulgaris*, *Dv*).[677] In Figure 46B, the proposed proton transfer pathway toward the C-cluster is shown (see Section 5.3).

In acetogenic bacteria such as *M. thermoacetica* (*Mt*) and methanogenic archaea such as *Methanosarcina barkeri* (*Mb*), a homodimeric CODH is present as part of bifunctional enzyme complexes. This may be in association with the enzyme acetyl-CoA synthase (ACS) in the ACS/CODH complex, which allows acetyl-CoA formation using a CO molecule produced by the reduction of CO_2 as part of the Wood–Ljungdahl carbon fixation pathway,[678] or in an acetyl-CoA decarbonylase/synthase (ACDS) complex that degrades acetyl-CoA to form methane and CO_2.[679] The ACS/CODH complex is a large $\alpha_2\beta_2$ tetramer that associates two β CODH subunits and two α ACS subunits. The CO produced from CO_2 at the C-cluster is combined with a methyl group and coenzyme A (CoA) to form acetyl-CoA at the A-cluster of the ACS (α) subunit; *in vitro*, acetyl-CoA synthesis can also occur using CO as a substrate.[680]

C. hydrogenoformans illustrates the diversity of possible functions of CODHs, since its genome encodes four different isoenzymes:[676] *Ch*CODH I, which is likely involved on respiration on CO; *Ch*CODH II, proposed to provide electrons to form NADPH; *Ch*CODH III, which is incorporated in a bifunctional ACS/CODH complex; and *Ch*CODH IV, proposed to be involved in resistance against O_2.[681] Eisen and co-workers originally proposed that the genome encodes a fifth CODH in *C. hydrogenoformans*,[676] but the latter is more likely to be a hybrid cluster protein.

5.2. Structure and Placidity of the C-Cluster

The structure of the C-cluster has been heavily debated, but the current consensus is that it comprises a [Ni-3Fe-4S] cluster coordinated to a unique fourth iron ion (Fe_u); the latter was also referred to as the “dangling Fe” or “ferrous component II” (Figure 47A).[682] The [Ni-3Fe-4S] cluster is coordinated by four cysteines as in classical [4Fe-4S] clusters including C333, C446, C476, and C526 (*Dv*CODH II numbering). The dangling Fe ion is coordinated by cysteine C295 and histidine H261. The catalytic active site is completed by histidine H93 and lysine K563 that are within hydrogen-bonding distances from the O atoms of the bound reactant, CO_2.[682] Neighboring cysteines C295 and C294 are conserved among CODHs. They are found in all clades except D, C1.3, and A4 of the classification proposed by Sako and co-workers;[683] however, no CODH with verified activity lacks this cysteine residue. Mutating C294 into a serine prevented the assembly of the C cluster in the case of *Mt* ACS/CODH,[684] and yielded a C-cluster devoid of Ni in the case of *Dv*CODH.[685] Exposure to air of *Dv*CODH crystals yielded an alternative form of the C-cluster in which the Ni ion occupies the position of the dangling iron, which moved a little further (Figure 47B). In this configuration, cysteine C295 becomes a bridging ligand between the Fe and Ni ions and C294 coordinates the dangler ion. This state is formed reversibly, as reducing the crystals gives back the “classical” coordination of the C-cluster, and may be involved in the high resistance of *Dv*CODH to O_2 damage.[686,687] Additionally, C294 may be involved in

the insertion of the active site, which would explain the lack of C-cluster when it is mutated into a serine. This hypothesis is also consistent with the fact that mutation of H261 and C295 yield an enzyme devoid of Ni.[688] Histidine H261 and C295 are ligands to the dangling Fe ion in the usual form of the C-cluster (Figure 47B), but bind the Ni ion in the oxidized C-cluster.

The role of the cysteine ligands to the C-cluster was investigated by site-directed mutagenesis on *Rr*CODH. Cysteines C338, C451, C481, and C531 (corresponding to C333, C446, C476, and C526 in *Ch*CODH II) were mutated into serine or alanine residues.[689] None of the mutations affected the incorporation of Ni; however, most of the mutants lost their activity, except the C451S and C531A variant, which retained ~1.4% and 0.1% of CO oxidation activity, respectively. The exact reason for the decreased activity is not known yet, but redox effects may be involved. While the EPR signature of C_{red2} (see below) was observed in the reduced C451S variant, no C_{red1} could be detected under the redox conditions in which the wild-type *Rr*CODH usually gives C_{red1}.[689]

The C-cluster of CODHs may exist in at least three redox states: the fully oxidized, inactive, and EPR-silent "C_{ox}" state, which is reduced at potentials of −100 mV to the paramagnetic "C_{red1}" state (g = 2.01, 1.81, and 1.65). Below approximately −500 mV, the "C_{red2}" state is formed (g = 1.97, 1.87, and 1.75), which is two electrons more reduced than C_{red1}. An EPR-silent, singly reduced state "C_{int}" has been postulated to exist as a transition between C_{red1} and C_{red2}, but it was never isolated.[690] The consensus is that C_{red1}, C_{int}, and C_{red2} are catalytic intermediates.[675,691] The proposed mechanisms all assume that the structure of the CO_2-bound enzyme (Figure 47A) corresponds to a catalytic intermediate and that the binding of CO_2 is followed by the breaking of the bond between the C and the O coordinated to the dangling Fe ion, yielding a CO-bound Ni ion and a hydroxo ligand on the dangling Fe (Figure 48). The main dispute for the time being is the nature of the C_{red2} state. According to the model by Jeoung and Dobbek,[682] C_{red2} corresponds to a Ni^0 state with a hydroxo ligand on the dangling Fe and no extraneous ligand on the nickel (this state is indicated by C_{red2}* in Figure 48).[682] On the basis of DFT computations, Fontecilla-Camps, Amara, and co-workers have proposed instead that the C_{red2} state is a Ni^{2+} hydride (this state is indicated by $C_{red2}^{\dagger}$ in Figure 48), and that the CO_2-bound structure is the result of the unusual insertion of CO_2 into the Ni–H bond,[692] even though insertion of CO_2 into a M-H bond usually results in the production of formate.[693] Bruschi and coworkers have recently used density functional theory (DFT) calculations to investigate the binding of CO_2 to different redox states of the active site C-cluster; their results appear to be incompatible with the presence of a Ni–H species in C_{red2}, thus favoring C_{red2}* over $C_{red2}^{\dagger}$.[694] They calculated that the binding is governed by the protonation states of histidine H93 and lysine K563 (equivalent H93 and K563 in *Ch*CODH II, Figure 47), and opened the possibility that CO_2 may also bind to the C_{int} redox state.

5.3. Substrate Access and Product Egress

The diffusion of CO and CO_2 has been investigated both in monofunctional CODH and in the bifunctional ACS/CODH complex. In ACS/CODH, the site of CO production and the site of CO utilization are over 70 Å apart. As CO does not leak to the solvent when the

ACS/CODH complex produces acetyl-CoA using CO_2 as a substrate, a gastight channel was proposed that would guide the CO molecule from the C-cluster toward the A-cluster, where CO is condensed with a methyl group and coenzyme A.[695,696]

The search for cavities in the X-ray structure of ACS/CODH and the identification of Xe binding sites[680,697,698] defines the long hydrophobic channel that connects the four active sites in the tetrameric ACS/CODH complex (Figure 49). This channel is blocked but the A-cluster is accessible to the solvent for methyl transfer in the so-called open conformation of ACS/CODH.[698,699] Support for these channels transporting CO from the C-cluster to the A-cluster comes from the observation that mutations of the conserved alanine residues that line the putative channel in the ACS subunit of *Mt* ACS/CODH (A110C, A222L, and A265M) only have an effect of the rate of acetyl-CoA production when CO_2 is used as a substrate.[700,701] The mutations have a no significant effect on the CO oxidation activity, and only a moderate effect on the rate of acetyl-CoA production from CO. The acetyl-coA synthesis from CO is strongly inhibited by CO in wild-type ACS/CODH, but not in the three channel variants; this is explained by the possibility that part of the activity in wild-type ACS/CODH is due to CO molecules entering at the C-cluster and crossing the channel toward the A-cluster, combined with CO crowding in the channel regulating the flow of CO from the C-cluster.[700]

The question of how CO_2 reaches the C-cluster of ACS/CODH is less clear. It has been suggested that CO_2 may enter the enzyme at the level of the A-cluster (which would involve transport against the opposite flux of CO),[699] or via the water channel along the $\beta\beta$ subunit interface,[703] or along dynamically formed pathways that are not detected as clear cavities in the crystal structure.[704] The latter hypothesis has been investigated in molecular dynamics (MD) calculations, according to which CO_2 transport is controlled by two strictly conserved histidine residues, H113 and H116 (H93 and H96 in *Ch*CODH II, Figure 47). Upon reduction of CO_2, a hydrogen-bond network in the active site pocket becomes rigid enough to prevent CO from exiting the protein via the CO_2 access pathway, and directs CO from the C-cluster to the A-cluster.[704]

In the CODH subunit of Mt ACS/CODH, histidines H113 and H116, along with H119 and H122, asparagine N284 and lysine K587 were proposed to be involved in proton transfer between the solvent and the C-cluster (H93, H96, H99, H102, N262, and K563 in *Ch*CODH II, see Figure 46B). Variants H116A and H122A did not show catalytic turnover but activity could be restored by introducing a histidine as a neighboring amino acid.[684] On the basis of a series of single and multiple site-directed mutagenesis replacements, Kim and co-workers proposed that protons first go to histidine H113 or lysine K587, then necessarily H116, then either H119, asparagine N284 or a water molecule, and finally to the solvent-exposed histidine H122.

Additional hydrophobic cavities have been identified through calculations in the monofunctional CODH from *C. hydrogenoformans* and *R. rubrum*.[705,706] Structure comparison suggests that bulky residues that are present in ACS/CODH block some of the pathways that are functional in reactant diffusion in *Ch*CODH and *Rr*CODH, and whose

presence in the ACS/CODH complex would prevent effective channeling of CO from the C-cluster to the A-cluster.[698]

5.4. Diversity of CO Dehydrogenase

Figure 50 represents a sequence alignment of the main CODHs that have been studied so far, with the exception of the ACS/CODH from *M. barkeri*. All amino acid residues that have been modified by mutagenesis so far are indicated using red backgrounds, and the amino acids within 8 Å of the Ni ion of the active site are framed in red. Figure 50 shows that the environment of the active site is highly conserved, with only a few positions with nonconserved amino acids, and a few more with small variations, notably at position 293 (with isoleucine, leucine, or methionine), 311 (with asparagine, histidine, or serine), 312 (with tyrosine, serine, histidine or phenylalanine), 331 (with valine or tyrosine), 444 (with valine, alanine, or cysteine), 478 (with alanine, serine, or threonine), 529 (with asparagine or cysteine), 560 (with methionine, glutamine, or tyrosine), 561 (with histidine, serine, or threonine), and 561 with serine, histidine, or threonine). Positions 477, 479, and 559 are not conserved.

In spite of this high sequence identity, the properties of the CODH appear to change greatly from one CODH to another. Regarding the K_m for CO, the values range from 20 nM for *Ch*CODH IV to 30 μM for *Rr* CODH, with other values between 0.5–3 μM for *Dv*CODH, *Ch*CODH I, and *Tc*CODH I and II from *Thermococcus sp. AM4* (*Tc*).[681,707–710] To date, no clear pattern has been noticed relating the sequence and the values of K_m, and no mutation has been published that affects the K_m for CO. K_m values for CO_2 reduction are much higher than those for CO oxidation, and in some cases they could not be determined because it was not possible to saturate the enzyme with CO_2. They range from 0.2 mM for *Rr*, 0.47 mM for *Tc*CODH I, to values undetermined but larger than 2 mM (*Ch*CODH I) or 7 mM (*Tc*CODH II).[709–711] Similarly to CO, no mutation yet is known to affect the K_m for CO_2.

CODHs have been said to be highly O_2-sensitive,[675] but in fact the reactivity of CODHs with O_2 varies greatly, from *Rr*CODH being entirely destroyed by a 10 s exposure to O_2[712] to *Dv*CODH, losing only 70% of its activity upon aerobic purification,[687] and reactivating almost fully upon reduction after exposure to O_2,[686] a property that is reminiscent of the well-known reductive activation of [NiFe]-hydrogenases (Section 3.1) and certain [FeFe]-hydrogenases (Section 3.2). *Ch*CODH IV requires much higher concentrations of O_2 than the other CODHs to lose 50% of its activity, but unlike *Dv*CODH it does not reactivate upon reduction.[681] This has been attributed to the presence of a bulky phenylalanine residue on the backside of the C-cluster (F307), in the position corresponding to S312 in *Ch*CODH II (Figure 50). However, *Tc*CODH I and II, which also feature a phenylalanine in the same position (F346 and F322, respectively), do not share the exceptionally high resistance of *Ch*CODH IV against O_2.[709]

Perhaps the best understood reactivity with O_2 is that of *Dv*CODH, which harbors a [2Fe-2S] cluster as the D-cluster, unlike the other CODHs characterized so far, which hold a [4Fe-4S] cluster. The [2Fe-2S] type D-cluster of *Dv*CODH is at least partially responsible for the high O_2 resistance of *Dv*CODH, since upon mutation to a “classical” [4Fe-4S] cluster, the enzyme loses the ability to be purified aerobically.[687] Deletion of the D-cluster

also prevents C-cluster assembly,[685] which shows that the maturation of the active site is also sensitive to either long-distance effects, or long-range electron transfer.

6. CONCLUDING REMARKS

Throughout Sections 2–5, we have seen how the activity of gas-processing metalloenzymes (GPMs) is defined by second and outer coordination sphere effects. As noted in Section 1, the optimized catalysis of GPMs has been afforded through tailored evolution of the active site cofactors from abiotic minerals and peptide "nests" coordinating these inorganic microcompartments.[15–20] Several factors that drive second and outer coordination sphere effects in nitrogenase, hydrogenase, FDH and CODH have been described herein. It will be difficult to understand GPMs without knowledge about the structure and electronic properties of the metallic cofactors; however, we emphasize that bioinorganic chemistry must explore beyond the first coordination sphere. Concluding this article, we will highlight a number of common motifs including mass transport (Section 6.1), redox leveling (Section 6.2), and the stabilization of reactive geometries (Section 6.3). The developed concepts may inspire the design of biomimetic catalysts for the transformation of N_2, H_2, CO_2, and CO as critical feedstock in "green" energy conversion.

6.1. Mass Transport

Under ambient conditions, N_2, H_2, CO_2, and CO are small volatile molecules with mostly hydrophobic properties. Such reactants approach the active site cofactor by molecular diffusion. Wolfenden and co-workers discussed how enzymatic catalysis is occasionally limited by mass transport, demonstrating the efficiency of GPMs like superoxide dismutase and carbonic anhydrase.[713] At the example of hydrogenase, FDH, and CODH we saw that proteinaceous "gas filters" influence the catalytic rates and substrate selectivity (Sections 3–5). While hydrophobic channels and pockets are routinely identified in xenon- or krypton-pressurized protein crystals,[714] the collective motion of the protein fold and packing defects[715] complicate the identification of individual "gate keepers", that is, amino acid residues of key importance. From the viewpoint of synthetic chemistry, we note that it may not be necessary to install molecular gas filters. In recent years, redox hydrogels have been demonstrated to facilitate enzymatic turnover in the presence of gaseous inhibitors, for example, by reducing O_2 before it reaches the enzyme.[716–718]

Proton transfer is another mass transport phenomenon critical to the performance of GPMs. In Section 1, we compared the basic reactions catalyzed by nitrogenase, hydrogenase, FDH and CODH (eq 1–4). Each reaction includes at least one proton. Protons are transferred via water molecules and the hydrophilic groups of a protein when hydrogen-bonded or in hydrogen-bonding distance (2.7–3.3 Å).[719] These criteria make proton transfer pathways extremely reliant on protein structural dynamics. In *Av*NifDK of the Mo-nitrogenase, second coordination sphere residues R96, Q191, and H195 (analogous to K83, Q176, and H180 in *Av*VnfDGK of the V-nitrogenase) are potentially involved in proton transfer and hydrogen bonding to catalytic intermediates that replace the bridging sulfide ligand S2B (Figure 14). Additionally, the homocitrate ligand may be involved,[232] but any outer coordination sphere effects on proton transfer have yet to be unraveled. The cysteine residue that coordinates

the active site cofactor of nitrogenase (C275 in *Av*NifDK, C257 in *Av*VnfDGK) is not involved in proton transfer, which is a marked difference from hydrogenase where cysteines of the first and second coordination sphere play key roles in proton transfer.[297] In [NiFe]-hydrogenase *Dv*MF, nickel-coordinating C546 accepts a proton after heterolytic H_2 splitting. Glutamic acid residue E34 represents a proton relay before the proton is released into bulk water (Figure 22). In [FeFe]-hydrogenase *Cp*1, cysteine C299 close to the distal iron ion (Fe_d) of the H-cluster functions as a relay site between cofactor and a ~ 20 Å proton transfer pathway including two glutamic acid residues (E279, E282), a serine residue (S319), and a small water cluster (Figure 39). In the primary sequence, C299 is followed by C300, which binds to the [4Fe-4S] part of the H-cluster. A similar motif can be found in *Ec*FDH where Mo-binding selenocysteine U140 is followed by histidine H141 (Figure 42), the later which has been suggested to play a key role in proton transfer. In the outer coordination sphere, R333 may be involved in proton transfer, but the molecular details of this event are yet to be understood.[575] Similar to FDH and nitrogenase, histidines are the most likely proton relay sites in CODH. On the basis of biochemical experiments with various amino acid variants of *Ch*CODH II, a trajectory between the catalytic C-cluster and bulk solvent including H93, H96, H99, H102, N262, and K563 has been proposed (Figure 48). Hydrogenases, on the contrary, rely on cysteine and glutamic acid residues primarily,[297] resulting in an overall pK_a decrease of 2–3 compared to histidine-based proton transfer pathways. This may reflect the necessity for a tightly controlled proton transfer in systems that exclusively catalyze H_2 oxidation and proton reduction.

6.2. Redox Leveling

While proton transfer demands short distances, the probability for electrons to tunnel across distances as far as 18 Å is high enough to enable electron transfer within biologically relevant time scales.[720] Conductive wires are formed by iron–sulfur clusters in nitrogenase, hydrogenase, FDH, and CODH, guiding electrons back and forth between the active site cofactor and redox proteins like ferredoxin, flavodoxin, or cytochrome. The “accessory” clusters of GPMs are determined by first and second coordination sphere effects to ensure directional electron transfer. For example, the replacement of a cysteine by a histidine ligand at the distal [4Fe-4S] cluster in [FeFe]-hydrogenase has a strong effect on activity.[418] In special cases, the electronic properties are flexible and controlled by the enzyme. Examples include the P-cluster in nitrogenase that changes its geometry upon reduction (Figure 3) or the proximal iron–sulfur cluster in O_2-tolerant [NiFe]-hydrogenases (Figure 24). In [FeFe]-hydrogenase, a protonation event at the backend of the H-cluster has been shown to affect the redox potential (Figure 39). These special cases demonstrate how enzymes modulate electron transfer in a flexible way.

Compared to the branching chains of metal clusters found in electron bifurcating/confurcating enzymes,[265,266,721] the GPMs discussed in this review are wired in a straightforward fashion. The sophistication, however, lies in the spatiotemporal coupling of redox and protonation events at the active site cofactor, which allows for an accumulation of charges at mild potentials (“redox leveling”). This is clearly illustrated in the Lowe-Thorneley model for N_2 reduction (Figure 6) and holds true for H_2 turnover as well (Figure 21 and Figure 34). The mechanistic details in FDH and CODH are less well understood,

but similar proposals have been considered (Figure 45 and Figure 48). How do GPMs facilitate proton-coupled electron transfer? While the electron transfer chains are hard-wired, the distance constraints of proton transfer allow for flexible fine-tuning, for example, by small changes in protein structure as demonstrated in [NiFe]- and [FeFe]-hydrogenase.[297] The data discussed in this review now suggest that metalloenzymes initiate PCET by guiding protons to the cofactor. Here, the catalytic redox reaction is induced only upon arrival of the proton (and other reactants like N_2, CO_2, or CO). As tunneling is a quantum mechanical phenomenon, the formal requirements of PCET are fulfilled.[22–24] From the viewpoint of synthetic chemistry, we note that molecular wiring may not be necessary. For example, when biomimetic Ni-complexes were deposited in a conductive hydrogel, redox events could be triggered by external electric fields.[722] At variance, the design of proton transfer pathways seems to be imperative for efficient electron transfer and catalysis.[556]

6.3. Stabilization of Reactive Geometries

Second coordination sphere effects are not limited to mass transport and redox leveling. In nitrogenase, hydrogen-bonding between H195 and R96 with bridging ligands in position S2B or between Q191 and terminal ligands (Figure 14) stabilizes the reactive geometry of the active site cofactor. Ligands include N_2, CO, or H. Positions S3A and S5A could be catalytically relevant as well; in *Av*NifDK of the Mo-nitrogenase, ligands likely derived from the bound N_2 entities have been identified as being hydrogen-bonded to backbone amines of G356 and G357 at position S3A, and the side chain of R96 at position S5A (Figure 12). In hydrogenases, potential hydrogen-bonding contacts inspired the assignment of CO and CN^- ligands. This includes S502, P478 and R479 in [NiFe]-hydrogenase *Dv*MF (Figure 19). Arginine 479 may also form a frustrated Lewis pair (FLP) with the Ni–Fe cofactor and has been suggested to be part of the “outer-shell canopy”, an alternative proton transfer pathway.[360] The mechanism shown in Figure 22 favors C546 as FLP but the role of R479 in polarizing the bridging ligand cannot be excluded.[361] Arginine 96 and H195 at the nitrogenase cofactor may have a similar function (Figure 14). In [FeFe]-hydrogenase, the ADT ligand serves as “internal” FLP; however, hydrogen-bonding with the adjacent C299 and M497 residues (Figure 38) was found to be of key importance for efficient proton transfer and catalysis. Another methionine, M353, may destabilize the μCO ligand and contribute to the flexible geometry of the diiron site (Figure 37). Around the proximal CN^- ligand, strong hydrogen bonding with P231 and S232 was confirmed whereas any contacts around the distal CN^- ligand remain speculation (Figure 36). The catalytic mechanism of FDH is controversial and various proposals coexist (Figure 45). The involvement of R333 and H141 seems to be accepted, which represents a similar mechanistic element to those employed by [NiFe]-hydrogenase and nitrogenase. Histidines play important roles in CODH, across all coordination spheres. In the reduced, CO_2-bound state of *Ch*CODH II, H93 and K563 are in hydrogen-bonding distance to the substrate, stabilizing the reactive geometry (Figure 47). Lysine K563 is turned into a nickel ligand in the oxidized state, switching between the first and second coordination sphere.[677] This behavior is reminiscent of C367 in [FeFe]-hydrogenase *Cb*A5H (C299 in *Cp*I) binding to Fe_d in the O_2-inhibited state (Figure 35). From the viewpoint of synthetic chemistry, hydrophilic groups in the second coordination sphere should have dual functions. Our data emphasize that histidines, arginines, and cysteines serve as hydrogen-bonding partners to substrates like N_2, H, CO_2,

and CO, stabilizing reactive geometries. However, without contact to residues involved in proton transfer in the outer coordination sphere (Section 6.1), efficient catalysis cannot be achieved.

ACKNOWLEDGMENTS

S.T.S. was supported by the Deutsche Forschungsgemeinschaft (DFG) via the SPP 1927 priority program "Iron–Sulfur for Life" Grant No. STR1554/5-1. Jifu Duan is acknowledged for helpful comments on Table 5. Guodong Rao is acknowledged for the simulation of EPR spectra in Figure 32. The work of C.L. and V.F. was supported by Centre National de la Recherche Scientifique (CNRS), Aix Marseille Université, Agence Nationale de la Recherche (ANR-11-BSV5-0005, ANR-12-BS08-0014, ANR-14-CE05-0010, ANR-15-CE05-0020, ANR-16-CE29-0010, ANR-17-CE11-0027, ANR-18-CE05-0029), and the Excellence Initiative of Aix-Marseille University – A*MIDEX, a French "Investissements d'Avenir" programme (ANR-11-IDEX-0001-02). The work of S.L. was supported by the Deutsche Forschungsgemeinschaft (DFG) via the SPP 1927 priority program "Iron–Sulfur for Life" Grant No. E1171-15-2 and by the EXC 2008/1 (UniSysCat), funded by Germany ´s Excellence Strategy – EXC 2008-390540038 – UniSysCat. The work of S.H. and H.O. was supported by the Grant-in-Aid from the Japan Society for the Promotion of Science (JSPS Category B, No. JP21H02060 to S.H. and No. JP20H03215 to H.O.). M.W.R. and Y.H. were supported by NIH-NIGMS grants GM67626 (to M.W.R. and Y.H.) and GM141046 (to Y.H. and M.W.R.), which funded research related to nitrogenase assembly and catalysis, respectively. The authors were also supported by the Department of Energy grants DOE (BES) DE-SC0016510 (to Y.H. and M.W.R.) and DE-SC0014470 (to M.W.R. and Y.H.), which funded work related to the mechanistic investigation of ammonia formation by nitrogenase engineering and hydrocarbon formation by nitrogenase hybrid systems, respectively. In addition, the authors were supported by NSF grants CHE-1904131 (to M.W.R. and Y.H.) and CHE-1651398 (to Y.H.) that supported work related to CO activation by nitrogenase and CO_2 reduction by nitrogenase Fe proteins, respectively.

Biographies

Sven T. Stripp graduated in Biology and Biotechnology and received his Ph.D. degree from Ruhr-Universität Bochum, Germany. Afterwards, he moved to Freie Universität Berlin for postdoctoral studies on surface-enhanced vibrational spectroscopy. Since 2015 he has been a group leader in the Department of Physics where he develops *in situ* FTIR, Raman, and UV–vis spectroscopic approaches to investigate metalloenzymes under biologically relevant conditions. He habilitated in Physical Chemistry in 2021.

Benjamin R. Duffus received his B.A. in chemistry (*cum laude*) from Concordia College (Moorhead, MN) in 2005. Following postgraduate study in synthetic inorganic chemistry at Texas A&M University, he completed his Ph.D. at Montana State University in 2014, focusing on the biosynthesis of complex iron–sulfur clusters. Since 2014, he is a postdoctoral research associate in Molecular Enzymology at the University of Potsdam, Germany. His interests blend biochemical and spectroscopic approaches toward mechanistic and biosynthetic studies of metalloenzymes, with a focus toward complex, iron–sulfur cluster molybdoenzymes.

Vincent Fourmond received his Ph.D. at the Université Paris Descartes in 2007. After two postdocs in the groups of Christophe Léger and Vincent Artero, he became permanent CNRS research associate in 2011. His interests lie in using kinetics to understand the mechanism of redox metalloenzymes and in the development of the general purpose data analysis software QSoas.

Christophe Léger received his Ph.D. from the University of Bordeaux and was a postdoc in the group of Fraser Armstrong from 1999 to 2002. He is “Directeur de Recherche” at CNRS. His interests lie in kinetic and mechanistic studies of complex metalloenzymes.

Silke Leimkühler received her Ph.D. in 1998 from Ruhr-Universität Bochum, Germany. After postdoctoral studies at Duke University, USA, she returned to Germany as a research group leader to the Technical-University of Braunschweig. In 2004 she accepted a Junior-Professor position at the University of Potsdam, Germany, and since 2009 she is a full professor in Molecular Enzymology at the same institute. Her research interests focus on molybdenum cofactor biosynthesis, molybdoenzyme enzymology, and iron–sulfur cluster assembly.

Shun Hirota received his Ph.D. from the Graduate University for Advanced Studies in Japan. After postdoctoral studies in Japan and the US, he joined Nagoya University as an assistant professor in 1996 and became an associate professor at Kyoto Pharmaceutical University in 2002. He was invited to Nara Institute of Science and Technology as a full professor in 2007. His research interests include structures, functions, and reaction mechanisms of metalloproteins.

Yilin Hu received her Ph.D. in Biochemistry from Loma Linda University, USA. She was a postdoctoral fellow at the University of California, Irvine, and is currently Professor at the same institute. She focuses on studies related to nitrogenase mechanism and assembly, with an emphasis on the genetic manipulation of nitrogenase systems.

Andrew J. Jasniewski received his B.S. degree from the University of Wisconsin—Madison working with Thomas Brunold on functional models of the Mn-dependent superoxide dismutase. He then moved to the University of Minnesota to study the structures and spectroscopy of nonheme diiron enzymes and related model complexes with Lawrence Que Jr., receiving his Ph.D. degree in 2017. He currently works at the University of California, Irvine with Markus Ribbe and Yilin Hu on the biochemistry and spectroscopy of nitrogenase.

Hideaki Ogata received his Ph.D. from Kyoto University, Japan in 2003. After a short period of the postdoctoral research at Himeji Institute of Technology, he joined the Max Planck Institute for Chemical Energy Conversion, Mülheim an der Ruhr, Germany where he worked as a group leader until 2017. He then moved to Hokkaido University and later to Nara Institute of Science and Technology. He is now a professor at University of Hyogo, Japan. His research interests are structural and spectroscopic studies of metalloenzymes.

Markus W. Ribbe received his Ph.D. in Microbiology from the University of Bayreuth, Germany. He was a postdoctoral fellow at the University of California, Irvine, and is now Chancellor’s Professor at the same institute. He focuses on the mechanistic investigation of nitrogenase catalysis and assembly by combined biochemical, spectroscopic, and structural approaches.

REFERENCES

(1). Holm RH; Solomon EI Preface: Bioinorganic Enzymology. Chem. Rev 1996, 96, 2237–2238. [PubMed: 11848827]

(2). Holm RH; Solomon EI Preface: Biomimetic Inorganic Chemistry. Chem. Rev 2004, 104, 347–348. [PubMed: 14871127]

(3). Holm RH; Solomon EI Introduction: Bioinorganic Enzymology II. Chem. Rev 2014, 114, 4039–4040. [PubMed: 24758378]

(4). McEvoy JP; Brudvig GW Water-Splitting Chemistry of Photosystem II. Chem. Rev 2006, 106, 4455–4483. [PubMed: 17091926]

(5). Vinyard DJ; Ananyev GM; Charles Dismukes G Photosystem II: The Reaction Center of Oxygenic Photosynthesis. Annu. Rev. Biochem 2013, 82, 577–606. [PubMed: 23527694]

(6). Vinyard DJ; Brudvig GW Progress Toward a Molecular Mechanism of Water Oxidation in Photosystem II. Annu. Rev. Phys. Chem 2017, 68, 101–116. [PubMed: 28226223]

(7). Babcock GT; Wikström M Oxygen Activation and the Conversation of Energy in Cell Respiration. Nature 1992, 356, 301–308. [PubMed: 1312679]

(8). Yoshikawa S; Muramoto K; Shinzawa-Itoh K Proton-Pumping Mechanism of Cytochrome c Oxidase. Annu. Rev. Biophys 2011, 40, 205–223. [PubMed: 21545285]

(9). Wikström M; Krab K; Sharma V Oxygen Activation and Energy Conservation by Cytochrome c Oxidase. Chem. Rev 2018, 118, 2469–2490. [PubMed: 29350917]

(10). Fontecilla-Camps JC; Amara P; Cavazza C; Nicolet Y; Volbeda A Structure-Function Relationships of Anaerobic Gas-Processing Metalloenzymes. Nature 2009, 460, 814–822. [PubMed: 19675641]

(11). Brandes JA; Boctor NZ; Cody GD; Cooper BA; Hazen RM; Yoder HS Abiotic Nitrogen Reduction on the Early Earth. Nature 1998, 395, 365–367. [PubMed: 9759725]

(12). Russell MJ The Alkaline Solution to the Emergence of Life: Energy, Entropy and Early Evolution. Acta Biotheor. 2007, 55, 133–179. [PubMed: 17704896]

(13). Konkena B; junge Puring K; Sinev I; Piontek S; Khavryuchenko O; Dürholt JP; Schmid R; Tüysüz H; Muhler M; Schuhmann W; et al. Pentlandite Rocks as Sustainable and Stable Efficient Electrocatalysts for Hydrogen Generation. Nat. Commun 2016, 7, 12269. [PubMed: 27461840]

(14). McGlynn SE; Mulder DW; Shepard EM; Broderick JB; Peters JW Hydrogenase Cluster Biosynthesis: Organometallic Chemistry Nature's Way. Dalt. Trans 2009, No. 22, 4274–4285.

(15). Nitschke W; McGlynn SE; Milner-White EJ; Russell MJ On the Antiquity of Metalloenzymes and Their Substrates in Bioenergetics. Biochim. Biophys. Acta - Bioenerg 2013, 1827, 871–881.

(16). Russell MJ; Nitschke W; Branscomb E The Inevitable Journey to Being. Philos. Trans. R. Soc. B Biol. Sci 2013, 368, 20120254.

(17). Sousa FL; Thiergart T; Landan G; Nelson-Sathi S; Pereira IAC; Allen JF; Lane N; Martin WF Early Bioenergetic Evolution. Philos. Trans. R. Soc. B Biol. Sci 2013, 368, 20130088.

(18). Milner-White EJ; Russell MJ Sites for Phosphates and Iron-Sulfur Thiolates in the First Membranes: 3 to 6 Residue Anion-Binding Motifs (Nests). Orig. Life Evol. Biosph 2005, 35, 19–27. [PubMed: 15889648]

(19). Milner-White EJ; Russell MJ Predicting the Conformations of Peptides and Proteins in Early Evolution. Biol. Direct 2008, 3, 3. [PubMed: 18226248]

(20). Hanscam R; Shepard EM; Broderick JB; Copié V; Szilagyi RK Secondary Structure Analysis of Peptides with Relevance to Iron-Sulfur Cluster Nesting. J. Comput. Chem 2019, 40, 515–526. [PubMed: 30548652]

(21). Beinert H; Holm RH; Münck E Iron-Sulfur Clusters: Nature's Modular, Multipurpose Structures. Science 1997, 277, 653–659. [PubMed: 9235882]

(22). Dempsey JL; Winkler JR; Gray HB Proton-Coupled Electron Flow in Protein Redox Machines. Chem. Rev 2010, 110, 7024–7039. [PubMed: 21082865]

(23). Warren JJ; Tronic TA; Mayer JM Thermochemistry of Proton-Coupled Electron Transfer Reagents and Its Implications. Chem. Rev 2010, 110, 6961–7001. [PubMed: 20925411]

(24). Hammes-Schiffer S Proton-Coupled Electron Transfer: Moving Together and Charging Forward. J. Am. Chem. Soc 2015, 137, 8860–8871. [PubMed: 26110700]

(25). Banerjee R; Lipscomb JD Small-Molecule Tunnels in Metalloenzymes Viewed as Extensions of the Active Site. Acc. Chem. Res 2021, 54, 2185–2195. [PubMed: 33886257]

(26). Winkler M; Esselborn J; Happe T Molecular Basis of [FeFe]-Hydrogenase Function: An Insight into the Complex Interplay between Protein and Catalytic Cofactor. Biochim. Biophys. Acta 2013, 1827, 974–985. [PubMed: 23507618]

(27). Gray HB; Winkler JR Electron Transfer in Proteins. Annu. Rev. Biochem 1996, 65, 537–561. [PubMed: 8811189]

(28). Mulder DW; Peters JW; Raugei S Catalytic Bias in Oxidation-Reduction Catalysis. Chem. Commun 2021, 57, 713–720.

(29). Fourmond V; Plumeré N; Léger C Reversible Catalysis. Nat. Rev. Chem 2021, 5, 348–360.

(30). Zhang X; Ward BB; Sigman DM Global Nitrogen Cycle: Critical Enzymes, Organisms, and Processes for Nitrogen Budgets and Dynamics. Chem. Rev 2020, 120, 5308–5351. [PubMed: 32530264]

(31). Logan JA Nitrogen Oxides in the Troposphere: Global and Regional Budgets. J. Geophys. Res. Ocean 1983, 88, 10785–10807.

(32). Liaw YP; Sisterson DL; Miller NL Comparison of Field, Laboratory, and Theoretical Estimates of Global Nitrogen Fixation by Lightning. J. Geophys. Res. Atmos 1990, 95, 22489–22494.

(33). Cleveland CC; Townsend AR; Schimel DS; Fisher H; Howarth RW; Hedin LO; Perakis SS; Latty EF; Von Fischer JC; Elseroad A; et al. Global Patterns of Terrestrial Biological Nitrogen (N2) Fixation in Natural Ecosystems. Global Biogeochem. Cycles 1999, 13, 623–645.

(34). Noxon JF Atmospheric Nitrogen Fixation by Lightning. Geophys. Res. Lett 1976, 3, 463–465.

(35). Noxon JF Tropospheric NO2. J. Geophys. Res. Ocean 1978, 83, 3051–3057.

(36). Darwent BB Bond Dissociation Energies in Simple Molecules; U.S. National Bureau of Standards, 1970.

(37). Raymond J; Siefert JL; Staples CR; Blankenship RE The Natural History of Nitrogen Fixation. Mol. Biol. Evol 2004, 21, 541–554. [PubMed: 14694078]

(38). Boyd ES; Hamilton TL; Peters JW An Alternative Path for the Evolution of Biological Nitrogen Fixation. Front. Microbiol 2011, 2, 205. [PubMed: 22065963]

(39). Mus F; Colman DR; Peters JW; Boyd ES Geobiological Feedbacks, Oxygen, and the Evolution of Nitrogenase. Free Radic. Biol. Med 2019, 140, 250–259. [PubMed: 30735835]

(40). Zehr JP; Capone DG Changing Perspectives in Marine Nitrogen Fixation. Science 2020, 368, No. eaay9514. [PubMed: 32409447]

(41). Fan K; Weisenhorn P; Gilbert JA; Shi Y; Bai Y; Chu H Soil PH Correlates with the Co-Occurrence and Assemblage Process of Diazotrophic Communities in Rhizosphere and Bulk Soils of Wheat Fields. Soil Biol. Biochem 2018, 121, 185–192.

(42). Wang C; Zheng M; Song W; Wen S; Wang B; Zhu C; Shen R Impact of 25 Years of Inorganic Fertilization on Diazotrophic Abundance and Community Structure in an Acidic Soil in Southern China. Soil Biol. Biochem 2017, 113, 240–249.

(43). Gaby JC; Buckley DH Assessment of Nitrogenase Diversity in the Environment. In Biological Nitrogen Fixation; Wiley, 2015; pp 209–216.

(44). Noar JD; Bruno-Bárcena JM Azotobacter Vinelandii: The Source of 100 Years of Discoveries and Many More to Come. Microbiology 2018, 164, 421–436. [PubMed: 29533747]

(45). Huber H; Thomm M; König H; Thies G; Stetter KO Methanococcus Thermolithotrophicus, a Novel Thermophilic Lithotrophic Methanogen. Arch. Microbiol 1982, 132, 47–50.

(46). Belay N; Sparling R; Daniels L Dinitrogen Fixation by a Thermophilic Methanogenic Bacterium. Nature 1984, 312, 286–288. [PubMed: 6504143]

(47). Weidner S; Pühler A; Küster H Genomics Insights into Symbiotic Nitrogen Fixation. Curr. Opin. Biotechnol 2003, 14, 200–205. [PubMed: 12732321]

(48). Stougaard J Genetics and Genomics of Root Symbiosis. Curr. Opin. Plant Biol 2001, 4, 328–335. [PubMed: 11418343]

(49). Ribbe MW; Hu Y; Hodgson KO; Hedman B Biosynthesis of Nitrogenase Metalloclusters. Chem. Rev 2014, 114, 4063–4080. [PubMed: 24328215]

(50). Buren S; Jimenez-Vicente E; Echavarri-Erasun C; Rubio LM Biosynthesis of Nitrogenase Cofactors. Chem. Rev 2020, 120, 4921–4968. [PubMed: 31975585]

(51). Jasniewski AJ; Lee CC; Ribbe MW; Hu Y Reactivity, Mechanism, and Assembly of the Alternative Nitrogenases. Chem. Rev 2020, 120, 5107–5157. [PubMed: 32129988]

(52). Seefeldt LC; Yang Z-Y; Lukoyanov DA; Harris DF; Dean DR; Raugei S; Hoffman BM Reduction of Substrates by Nitrogenases. Chem. Rev 2020, 120, 5082–5106. [PubMed: 32176472]

(53). Seefeldt LC; Yang Z-Y; Duval S; Dean DR Nitrogenase Reduction of Carbon-Containing Compounds. Biochim. Biophys. Acta, Bioenerg 2013, 1827, 1102–1111.

(54). Schlögl R Catalytic Synthesis of Ammonia—A “Never-Ending Story”? Angew. Chemie Int. Ed 2003, 42, 2004–2008.

(55). Burgess BK Substrate Reactions of Nitrogenase. In Molybdenum Enzymes; Spiro TG, Ed.; Metal Ions In Biology; Wiley: New York, 1985; pp 161–219.

(56). Thorneley RNF; Lowe DJ Kinetics and Mechanism of the Nitrogenase Enzyme System. In Molybdenum Enzymes; Spiro TG, Ed.; Metal Ions In Biology; Wiley: New York, 1985; pp 221–284.

(57). Burgess BK; Wherland S; Newton WE; Stiefel EI Nitrogenase Reactivity: Insight into the Nitrogen-Fixing Process through Hydrogen-Inhibition and HD-Forming Reactions. Biochemistry 1981, 20, 5140–5146. [PubMed: 6945872]

(58). Jensen BB; Burris RH Effect of High PN2 and High PD2 on Ammonia Production, Hydrogen Evolution, and Hydrogen Deuteride Formation by Nitrogenases. Biochemistry 1985, 24, 1141–1147. [PubMed: 3913463]

(59). Burgess BK; Corbin JL; Rubinson JF; Li JG; Dilworth MJ; Newton WE Nitrogenase Reactivity. In Advances in Nitrogen Fixation Research: Proceedings of the 5th International Symposium on Nitrogen Fixation, Noordwijkerhout, The Netherlands, August 28 - September 3, 1983; Veeger C, Newton WE, Eds.; Springer Netherlands: Dordrecht, 1984; p 146.

(60). Hoffman BM; Lukoyanov D; Yang Z-Y; Dean DR; Seefeldt LC Mechanism of Nitrogen Fixation by Nitrogenase: The Next Stage. Chem. Rev 2014, 114, 4041–4062. [PubMed: 24467365]

(61). Einsle O; Rees DC Structural Enzymology of Nitrogenase Enzymes. Chem. Rev 2020, 120, 4969–5004. [PubMed: 32538623]

(62). Van Stappen C; Decamps L; Cutsail GE; Bjornsson R; Henthorn JT; Birrell JA; Debeer S The Spectroscopy of Nitrogenases. Chem. Rev 2020, 120, 5005–5081. [PubMed: 32237739]

(63). Rutledge HL; Tezcan FA Electron Transfer in Nitrogenase. Chem. Rev 2020, 120, 5158–5193. [PubMed: 31999100]

(64). Dingler C; Kuhla J; Wassink H; Oelze J Levels and Activities of Nitrogenase Proteins in Azotobacter Vinelandii Grown at Different Dissolved Oxygen Concentrations. J. Bacteriol 1988, 170, 2148–2152. [PubMed: 3162907]

(65). Kirn J; Rees DC Crystallographic Structure and Functional Implications of the Nitrogenase Molybdenum-Iron Protein from Azotobacter Vinelandii. Nature 1992, 360, 553–560. [PubMed: 25989647]

(66). Spatzal T; Aksoyoglu M; Zhang L; Andrade SLA; Schleicher E; Weber S; Rees DC; Einsle O Evidence for Interstitial Carbon in Nitrogenase FeMo Cofactor. Science 2011, 334, 940. [PubMed: 22096190]

(67). Georgiadis MM; Komiya H; Chakrabarti P; Woo D; Kornuc JJ; Rees DC Crystallographic Structure of the Nitrogenase Iron Protein from Azotobacter Vinelandii. Science 1992, 257, 1653–1659. [PubMed: 1529353]

(68). Jasniewski A; Sickerman N; Hu Y; Ribbe M The Fe Protein: An Unsung Hero of Nitrogenase. Inorganics 2018, 6, 25.

(69). Schindelin H; Kisker C; Schlessman JL; Howard JB; Rees DC Structure of ADP·AlF4-Stabilized Nitrogenase Complex and Its Implications for Signal Transduction. Nature 1997, 387, 370–376. [PubMed: 9163420]

(70). Tezcan FA; Kaiser JT; Mustafi D; Walton MY; Howard JB; Rees DC Nitrogenase Complexes: Multiple Docking Sites for a Nucleotide Switch Protein. Science 2005, 309, 1377–1380. [PubMed: 16123301]

(71). Peters JW; Fisher K; Newton WE; Dean DR Involvement of the P Cluster in Intramolecular Electron Transfer within the Nitrogenase MoFe Protein. J. Biol. Chem 1995, 270, 27007–27013. [PubMed: 7592949]

(72). Chan MK; Kim J; Rees DC The Nitrogenase FeMo-Cofactor and P-Cluster Pair: 2.2 Å Resolution Structures. Science 1993, 260, 792–794. [PubMed: 8484118]

(73). Pierik AJ; Wassink H; Haaker H; Hagen WR Redox Properties and EPR Spectroscopy of the P Clusters of Azotobacter Vinelandii MoFe Protein. Eur. J. Biochem 1993, 212, 51–61. [PubMed: 8383042]

(74). Smith BE; Lang G Mössbauer Spectroscopy of the Nitrogenase Proteins from Klebsiella Pneumoniae. Structural Assignments and Mechanistic Conclusions. Biochem. J 1974, 137, 169–180. [PubMed: 4596139]

(75). Huynh BH; Henzl MT; Christner JA; Zimmermann R; Orme-Johnson WH; Münck E Nitrogenase XII. Mössbauer Studies of the MoFe Protein from Clostridium Pasteurianum W5. Biochim. Biophys. Acta, Protein Struct 1980, 623, 124–138.

(76). Zimmermann R; Münck E; Brill WJ; Shah VK; Henzl MT; Rawlings J; Orme-Johnson WH Nitrogenase X: Mössbauer and EPR Studies on Reversibly Oxidized MoFe Protein from Azotobacter Vinelandii OP Nature of the Iron Centers. Biochim. Biophys. Acta - Protein Struct 1978, 537, 185–207.

(77). McLean PA; Papaefthymiou V; Orme-Johnson WH; Münck E Isotopic Hybrids of Nitrogenase. Mössbauer Study of MoFe Protein with Selective 57Fe Enrichment of the P-Cluster. J. Biol. Chem 1987, 262, 12900–12903. [PubMed: 2820958]

(78). Peters JW; Stowell MHB; Soltis SM; Finnegan MG; Johnson MK; Rees DC Redox-Dependent Structural Changes in the Nitrogenase P-Cluster. Biochemistry 1997, 36, 1181–1187. [PubMed: 9063865]

(79). Keable SM; Vertemara J; Zadvornyy OA; Eilers BJ; Danyal K; Rasmussen AJ; De Gioia L; Zampella G; Seefeldt LC; Peters JW Structural Characterization of the Nitrogenase Molybdenum-Iron Protein with the Substrate Acetylene Trapped near the Active Site. J. Inorg. Biochem 2018, 180, 129–134. [PubMed: 29275221]

(80). Mayer SM; Lawson DM; Gormal CA; Roe SM; Smith BE New Insights into Structure-Function Relationships in Nitrogenase: A 1.6 Å Resolution X-Ray Crystallographic Study of Klebsiella Pneumoniae MoFe-Protein. J. Mol. Biol 1999, 292, 871–891. [PubMed: 10525412]

(81). Danyal K; Dean DR; Hoffman BM; Seefeldt LC Electron Transfer within Nitrogenase: Evidence for a Deficit-Spending Mechanism. Biochemistry 2011, 50, 9255–9263. [PubMed: 21939270]

(82). Danyal K; Mayweather D; Dean DR; Seefeldt LC; Hoffman BM Conformational Gating of Electron Transfer from the Nitrogenase Fe Protein to MoFe Protein. J. Am. Chem. Soc 2010, 132, 6894–6895. [PubMed: 20429505]

(83). Seefeldt LC; Hoffman BM; Peters JW; Raugei S; Beratan DN; Antony E; Dean DR Energy Transduction in Nitrogenase. Acc. Chem. Res 2018, 51, 2179–2186. [PubMed: 30095253]

(84). Rupnik K; Lee CC; Wiig JA; Hu Y; Ribbe MW; Hales BJ Nonenzymatic Synthesis of the P-Cluster in the Nitrogenase MoFe Protein: Evidence of the Involvement of All-Ferrous [Fe4S4] 0 Intermediates. Biochemistry 2014, 53, 1108–1116. [PubMed: 24520862]

(85). Kim J; Rees DC Structural Models for the Metal Centers in the Nitrogenase Molybdenum-Iron Protein. Science 1992, 257, 1677–1682. [PubMed: 1529354]

(86). Lancaster KM; Roemelt M; Ettenhuber P; Hu Y; Ribbe MW; Neese F; Bergmann U; DeBeer S X-Ray Emission Spectroscopy Evidences a Central Carbon in the Nitrogenase Iron-Molybdenum Cofactor. Science 2011, 334, 974–977. [PubMed: 22096198]

(87). Wiig JA; Hu Y; Lee CC; Ribbe MW Radical SAM-Dependent Carbon Insertion into the Nitrogenase M-Cluster. Science 2012, 337, 1672–1675. [PubMed: 23019652]

(88). Wiig JA; Hu Y; Ribbe MW Refining the Pathway of Carbide Insertion into the Nitrogenase M-Cluster. Nat. Commun 2015, 6, 8034. [PubMed: 26259825]

(89). Spatzal T; Perez KA; Einsle O; Howard JB; Rees DC Ligand Binding to the FeMo-Cofactor: Structures of CO-Bound and Reactivated Nitrogenase. Science 2014, 345, 1620–1623. [PubMed: 25258081]

(90). Spatzal T; Perez KA; Howard JB; Rees DC Catalysis-Dependent Selenium Incorporation and Migration in the Nitrogenase Active Site Iron-Molybdenum Cofactor. Elife 2015, 4, No. e11620. [PubMed: 26673079]

(91). Kang W; Lee CC; Jasniewski AJ; Ribbe MW; Hu Y Structural Evidence for a Dynamic Metallocofactor during N 2 Reduction by Mo-Nitrogenase. Science 2020, 368, 1381–1385. [PubMed: 32554596]

(92). Sippel D; Einsle O The Structure of Vanadium Nitrogenase Reveals an Unusual Bridging Ligand. Nat. Chem. Biol 2017, 13, 956–960. [PubMed: 28692069]

(93). Sippel D; Rohde M; Netzer J; Trncik C; Gies J; Grunau K; Djurdjevic I; Decamps L; Andrade SLA; Einsle O A Bound Reaction Intermediate Sheds Light on the Mechanism of Nitrogenase. Science 2018, 359, 1484–1489. [PubMed: 29599235]

(94). Rohde M; Grunau K; Einsle O CO Binding to the FeV Cofactor of CO-Reducing Vanadium Nitrogenase at Atomic Resolution. Angew. Chemie Int. Ed 2020, 59, 23626–23630.

(95). Rohde M; Laun K; Zebger I; Stripp ST; Einsle O Two Ligand-Binding Sites in CO-Reducing V Nitrogenase Reveal a General Mechanistic Principle. Sci. Adv 2021, 7, No. eabg4474. [PubMed: 34049880]

(96). Orme-Johnson WH; Hamilton WD; Jones TL; Tso MYW; Burris RH; Shah VK; Brill WJ Electron Paramagnetic Resonance of Nitrogenase and Nitrogenase Components from Clostridium Pasteurianum W5 and Azotobacter Vinelandii OP. Proc. Natl. Acad. Sci. U. S. A 1972, 69, 3142–3145. [PubMed: 4343957]

(97). Yoo SJ; Angove HC; Papaefthymiou V; Burgess BK; Münck E Mössbauer Study of the MoFe Protein of Nitrogenase from Azotobacter Vinelandii Using Selective 57Fe Enrichment of the M-Centers. J. Am. Chem. Soc 2000, 122, 4926–4936.

(98). Bjornsson R; Lima FA; Spatzal T; Weyhermuller T; Glatzel P; Bill E; Einsle O; Neese F; DeBeer S Identification of a Spin-Coupled Mo(III) in the Nitrogenase Iron-Molybdenum Cofactor. Chem. Sci 2014, 5, 3096–3103.

(99). Morgan TV; Mortenson LE; McDonald JW; Watt GD Comparison of Redox and EPR Properties of the Molybdenum Iron Proteins of Clostridium Pasteurianum and Azotobacter Vinelandii Nitrogenases. J. Inorg. Biochem 1988, 33, 111–120. [PubMed: 2842451]

(100). Burgess BK; Lowe DJ Mechanism of Molybdenum Nitrogenase. Chem. Rev 1996, 96, 2983–3012. [PubMed: 11848849]

(101). Bjornsson R; Neese F; DeBeer S Revisiting the Mössbauer Isomer Shifts of the FeMoco Cluster of Nitrogenase and the Cofactor Charge. Inorg. Chem 2017, 56, 1470–1477. [PubMed: 28071903]

(102). Benediktsson B; Bjornsson R QM/MM Study of the Nitrogenase MoFe Protein Resting State: Broken-Symmetry States, Protonation States, and QM Region Convergence in the FeMoco Active Site. Inorg. Chem 2017, 56, 13417–13429. [PubMed: 29053260]

(103). Spatzal T; Schlesier J; Burger E-M; Sippel D; Zhang L; Andrade SLA; Rees DC; Einsle O Nitrogenase FeMoco Investigated by Spatially Resolved Anomalous Dispersion Refinement. Nat. Commun 2016, 7, 10902. [PubMed: 26973151]

(104). O'Donnell MJ; Smith BE Electron-Paramagnetic-Resonance Studies on the Redox Properties of the Molybdenum-Iron Protein of Nitrogenase between + 50 and −450 MV. Biochem. J 1978, 173, 831–838. [PubMed: 30448]

(105). Watt GD; Burns A; Lough S; Tennent DL Redox and Spectroscopic Properties of Oxidized MoFe Protein from Azotobacter Vinelandii. Biochemistry 1980, 19, 4926–4932. [PubMed: 6252962]

(106). Walker JE; Saraste M; Runswick MJ; Gay NJ Distantly Related Sequences in the Alpha- and Beta-Subunits of ATP Synthase, Myosin, Kinases and Other ATP-Requiring Enzymes and a Common Nucleotide Binding Fold. EMBO J 1982, 1, 945–951. [PubMed: 6329717]

(107). Howard JB; Rees DC Structural Basis of Biological Nitrogen Fixation. Chem. Rev 1996, 96, 2965–2982. [PubMed: 11848848]

(108). Jang SB; Seefeldt LC; Peters JW Insights into Nucleotide Signal Transduction in Nitrogenase: Structure of an Iron Protein with MgADP Bound. Biochemistry 2000, 39, 14745–14752. [PubMed: 11101289]

(109). Chen L; Gavini N; Tsuruta H; Eliezer D; Burgess BK; Doniach S; Hodgson KO MgATP-Induced Conformational Changes in the Iron Protein from Azotobacter Vinelandii, as Studied by Small-Angle X-Ray Scattering. J. Biol. Chem 1994, 269, 3290–3294. [PubMed: 8106367]

(110). Ryle MJ; Seefeldt LC Elucidation of a MgATP Signal Transduction Pathway in the Nitrogenase Iron Protein: Formation of a Conformation Resembling the MgATP-Bound State by Protein Engineering. Biochemistry 1996, 35, 4766–4775. [PubMed: 8664266]

(111). Ryle MJ; Lanzilotta WN; Seefeldt LC; Scarrow RC; Jensen GM Circular Dichroism and X-Ray Spectroscopies of Azotobacter Vinelandii Nitrogenase Iron Protein: MgATP and MgADP Induced Protein Conformation Changes Affecting the [4Fe-4S] Cluster and Characterization of a [2Fe-2S] Form. J. Biol. Chem 1996, 271, 1551–1557. [PubMed: 8576152]

(112). Stephens PJ; McKenna CE; Smith BE; Nguyen HT; McKenna M-C; Thomson AJ; Devlin F; Jones JB Circular Dichroism and Magnetic Circular Dichroism of Nitrogenase Proteins. Proc. Natl. Acad. Sci. U. S. A 1979, 76, 2585–2589. [PubMed: 379860]

(113). Liu J; Chakraborty S; Hosseinzadeh P; Yu Y; Tian S; Petrik I; Bhagi A; Lu Y Metalloproteins Containing Cytochrome, Iron-Sulfur, or Copper Redox Centers. Chem. Rev 2014, 114, 4366–4369. [PubMed: 24758379]

(114). Lindahl PA; Day EP; Kent TA; Orme-Johnson WH; Münck E Mössbauer, EPR, and Magnetization Studies of the Azotobacter Vinelandii Fe Protein. Evidence for a [4Fe-4S]1+ Cluster with Spin S = 3/2. J. Biol. Chem 1985, 260, 11160–11173. [PubMed: 2993304]

(115). Yates MG Electron Transport to Nitrogenase in Azotobacter Chroococcum: Azotobacter Flavodoxin Hydroquinone as an Electron Donor. FEBS Lett 1972, 27, 63–67. [PubMed: 11946808]

(116). Thorneley RN; Deistung J Electron-Transfer Studies Involving Flavodoxin and a Natural Redox Partner, the Iron Protein of Nitrogenase. Conformational Constraints on Protein-Protein Interactions and the Kinetics of Electron Transfer within the Protein Complex. Biochem. J 1988, 253, 587–595. [PubMed: 3140782]

(117). Bennett LT; Jacobson MR; Dean DR Isolation, Sequencing, and Mutagenesis of the NifF Gene Encoding Flavodoxin from Azotobacter Vinelandii. J. Biol. Chem 1988, 263, 1364–1369. [PubMed: 3121629]

(118). Duyvis MG; Wassink H; Haaker H Nitrogenase of Azotobacter Vinelandii: Kinetic Analysis of the Fe Protein Redox Cycle. Biochemistry 1998, 37, 17345–17354. [PubMed: 9860849]

(119). Setubal JC; dos Santos P; Goldman BS; Ertesvåg H; Espin G; Rubio LM; Valla S; Almeida NF; Balasubramanian D; Cromes L; et al. Genome Sequence of *Azotobacter Vinelandii*, an Obligate Aerobe Specialized To Support Diverse Anaerobic Metabolic Processes. J. Bacteriol 2009, 191, 4534–4545. [PubMed: 19429624]

(120). Sickerman NS; Rettberg LA; Lee CC; Hu Y; Ribbe MW Cluster Assembly in Nitrogenase. Essays Biochem 2017, 61, 271–279. [PubMed: 28487403]

(121). Hu Y; Corbett MC; Fay AW; Webber JA; Hedman B; Hodgson KO; Ribbe MW Nitrogenase Reactivity with P-Cluster Variants. Proc. Natl. Acad. Sci. U. S. A 2005, 102, 13825–13830. [PubMed: 16166259]

(122). Hu Y; Fay AW; Lee CC; Ribbe MW P-Cluster Maturation on Nitrogenase MoFe Protein. Proc. Natl. Acad. Sci. U. S. A 2007, 104, 10424–10429. [PubMed: 17563349]

(123). Lee CC; Blank MA; Fay AW; Yoshizawa JM; Hu Y; Hodgson KO; Hedman B; Ribbe MW Stepwise Formation of P-Cluster in Nitrogenase MoFe Protein. Proc. Natl. Acad. Sci. U. S. A 2009, 106, 18474–18478. [PubMed: 19828444]

(124). Rupnik K; Hu Y; Lee CC; Wiig JA; Ribbe MW; Hales BJ P+ State of Nitrogenase P-Cluster Exhibits Electronic Structure of a [Fe4S4]+ Cluster. J. Am. Chem. Soc 2012, 134, 13749–13754. [PubMed: 22839751]

(125). Kennedy C; Dean D The NifU, NifS and NifV Gene Products Are Required for Activity of All Three Nitrogenases of Azotobacter Vinelandii. Mol. Gen. Genet 1992, 231, 494–498. [PubMed: 1538703]

(126). Zheng L; Dean DR Catalytic Formation of a Nitrogenase Iron-Sulfur Cluster. J. Biol. Chem 1994, 269, 18723–18726. [PubMed: 8034623]

(127). Shah VK; Allen JR; Spangler NJ; Ludden PW In Vitro Synthesis of the Iron-Molybdenum Cofactor of Nitrogenase. Purification and Characterization of NifB Cofactor, the Product of NIFB Protein. J. Biol. Chem 1994, 269, 1154–1158. [PubMed: 8288575]

(128). Sickerman NS; Ribbe MW; Hu Y Nitrogenase Cofactor Assembly: An Elemental Inventory. Acc. Chem. Res 2017, 50, 2834–2841. [PubMed: 29064664]

(129). Wiig JA; Hu Y; Ribbe MW NifEN-B Complex of Azotobacter Vinelandii Is Fully Functional in Nitrogenase FeMo Cofactor Assembly. Proc. Natl. Acad. Sci. U. S. A 2011, 108, 8623–8627. [PubMed: 21551100]

(130). Kang W; Rettberg LA; Stiebritz MT; Jasniewski AJ; Tanifuji K; Lee CC; Ribbe MW; Hu Y X-Ray Crystallographic Analysis of NifB with a Full Complement of Clusters: Structural Insights into the Radical SAM-Dependent Carbide Insertion During Nitrogenase Cofactor Assembly. Angew. Chemie Int. Ed 2021, 60, 2364–2370.

(131). Rettberg LA; Wilcoxen J; Lee CC; Stiebritz MT; Tanifuji K; Britt RD; Hu Y Probing the Coordination and Function of Fe4S4Modules in Nitrogenase Assembly Protein NifB. Nat. Commun 2018, 9, 2824. [PubMed: 30026506]

(132). Jasniewski AJ; Wilcoxen J; Tanifuji K; Hedman B; Hodgson KO; Britt RD; Hu Y; Ribbe MW Spectroscopic Characterization of an Eight-Iron Nitrogenase Cofactor Precursor That Lacks the “9th Sulfur. Angew. Chemie Int. Ed 2019, 58, 14703–14707.

(133). Tanifuji K; Lee CC; Sickerman NS; Tatsumi K; Ohki Y; Hu Y; Ribbe MW Tracing the ‘Ninth Sulfur’ of the Nitrogenase Cofactor via a Semi-Synthetic Approach. Nat. Chem 2018, 10, 568–572. [PubMed: 29662207]

(134). Hu Y; Corbett MC; Fay AW; Webber JA; Hodgson KO; Hedman B; Ribbe MW FeMo Cofactor Maturation on NifEN. Proc. Natl. Acad. Sci. U. S. A 2006, 103, 17119–17124. [PubMed: 17050696]

(135). Yoshizawa JM; Blank MA; Fay AW; Lee CC; Wiig JA; Hu Y; Hodgson KO; Hedman B; Ribbe MW Optimization of FeMoco Maturation on NifEN. J. Am. Chem. Soc 2009, 131, 9321–9325. [PubMed: 19514721]

(136). Hu Y; Corbett MC; Fay AW; Webber JA; Hodgson KO; Hedman B; Ribbe MW Nitrogenase Fe Protein: A Molybdate/Homocitrate Insertase. Proc. Natl. Acad. Sci. U. S. A 2006, 103, 17125–17130. [PubMed: 17062756]

(137). Fay AW; Blank MA; Rebelein JG; Lee CC; Ribbe MW; Hedman B; Hodgson KO; Hu Y Assembly Scaffold NifEN: A Structural and Functional Homolog of the Nitrogenase Catalytic Component. Proc. Natl. Acad. Sci. U. S. A 2016, 113, 9504–9508. [PubMed: 27506795]

(138). Tezcan FA; Kaiser JT; Howard JB; Rees DC Structural Evidence for Asymmetrical Nucleotide Interactions in Nitrogenase. J. Am. Chem. Soc 2015, 137, 146–149. [PubMed: 25522159]

(139). Fisher K; Dilworth MJ; Newton WE Differential Effects on N2 Binding and Reduction, HD Formation, and Azide Reduction with α-195His- and α-191Gln-Substituted MoFe Proteins of Azotobacter Vinelandii Nitrogenase. Biochemistry 2000, 39, 15570–15577. [PubMed: 11112544]

(140). Yang Z-Y; Khadka N; Lukoyanov D; Hoffman BM; Dean DR; Seefeldt LC On Reversible H2 Loss upon N2 Binding to FeMo-Cofactor of Nitrogenase. Proc. Natl. Acad. Sci. U. S. A 2013, 110, 16327–16332. [PubMed: 24062454]

(141). Chatt J; Pearman AJ; Richards RL The Reduction of Mono-Coordinated Molecular Nitrogen to Ammonia in a Protic Environment. Nature 1975, 253, 39–40.

(142). Chatt J; Pearman AJ; Richards RL Relevance of Oxygen Ligands to Reduction of Ligating Dinitrogen. Nature 1976, 259, 204.

(143). Chatt J; Pearman AJ; Richards RL Conversion of Dinitrogen in Its Molybdenum and Tungsten Complexes into Ammonia and Possible Relevance to the Nitrogenase Reaction. J. Chem. Soc. Dalt. Trans 1977, No. 19, 1852–1860.

(144). Chatt J; Pearman AJ; Richards RL Diazenido (Iminonitrosyl) (N2H), Hydrazido(2-) (N2H2, and Hydrazido(1-) (N2H3) Ligands as Intermediates in the Reduction of Ligating Dinitrogen to Ammonia. J. Organomet. Chem 1975, 101, C45–C47.

(145). Yandulov DV; Schrock RR Reduction of Dinitrogen to Ammonia at a Well-Protected Reaction Site in a Molybdenum Triamidoamine Complex. J. Am. Chem. Soc 2002, 124, 6252–6253. [PubMed: 12033849]

(146). Yandulov DV; Schrock RR Catalytic Reduction of Dinitrogen to Ammonia at a Single Molybdenum Center. Science 2003, 301, 76–78. [PubMed: 12843387]

(147). Hinnemann B; Nørskov JK Catalysis by Enzymes: The Biological Ammonia Synthesis. Top. Catal 2006, 37, 55–70.

(148). Tanabe Y; Nishibayashi Y Developing More Sustainable Processes for Ammonia Synthesis. Coord. Chem. Rev 2013, 257, 2551–2564.

(149). Harris DF; Lukoyanov DA; Kallas H; Trncik C; Yang Z-Y; Compton P; Kelleher N; Einsle O; Dean DR; Hoffman BM; et al. Mo-, V-, and Fe-Nitrogenases Use a Universal Eight-Electron Reductive-Elimination Mechanism To Achieve N2 Reduction. Biochemistry 2019, 58, 3293–3301. [PubMed: 31283201]

(150). Harris DF; Yang Z-Y; Dean DR; Seefeldt LC; Hoffman BM Kinetic Understanding of N2 Reduction versus H2 Evolution at the E4(4H) Janus State in the Three Nitrogenases. Biochemistry 2018, 57, 5706–5714. [PubMed: 30183278]

(151). Einsle O; Tezcan FA; Andrade SLA; Schmid B; Yoshida M; Howard JB; Rees DC Nitrogenase MoFe-Protein at 1.16 Å Resolution: A Central Ligand in the FeMo-Cofactor. Science 2002, 297, 1696–1700. [PubMed: 12215645]

(152). Thomann H; Bernardo M; Newton WE; Dean DR N Coordination of FeMo Cofactor Requires His-195 of the MoFe Protein Alpha Subunit and Is Essential for Biological Nitrogen Fixation. Proc. Natl. Acad. Sci. U. S. A 1991, 88, 6620–6623. [PubMed: 11607203]

(153). DeRose VJ; Kim C-H; Newton WE; Dean DR; Hoffman BM Electron Spin Echo Envelope Modulation Spectroscopic Analysis of Altered Nitrogenase MoFe Proteins from Azotobacter Vinelandii. Biochemistry 1995, 34, 2809–2814. [PubMed: 7893692]

(154). Lee H-I; Thrasher KS; Dean DR; Newton WE; Hoffman BM 14N Electron Spin-Echo Envelope Modulation of the S = 3/2 Spin System of the Azotobacter Vinelandii Nitrogenase Iron-Molybdenum Cofactor. Biochemistry 1998, 37, 13370–13378. [PubMed: 9748344]

(155). Schmid B; Ribbe MW; Einsle O; Yoshida M; Thomas LM; Dean DR; Rees DC; Burgess BK Structure of a Cofactor-Deficient Nitrogenase MoFe Protein. Science 2002, 296, 352–356. [PubMed: 11951047]

(156). Fay AW; Hu Y; Schmid B; Ribbe MW Molecular Insights into Nitrogenase FeMoco Insertion - The Role of His 274 and His 451 of MoFe Protein α Subunit. J. Inorg. Biochem 2007, 101, 1630–1641. [PubMed: 17521738]

(157). Hu Y; Fay AW; Ribbe MW Molecular Insights into Nitrogenase FeMo Cofactor Insertion: The Role of His 362 of the MoFe Protein α Subunit in FeMo Cofactor Incorporation. *JBIC* J. Biol. Inorg. Chem 2007, 12, 449–460. [PubMed: 17203313]

(158). Hu Y; Fay AW; Schmid B; Makar B; Ribbe MW Molecular Insights into Nitrogenase FeMoco Insertion: Trp-444 of MoFe Protein α-Subunit Locks FeMoco in its Binding Site. J. Biol. Chem 2006, 281, 30534–30541. [PubMed: 16893897]

(159). Kim J; Woo D; Rees DC X-Ray Crystal Structure of the Nitrogenase Molybdenum-Iron Protein from Clostridium Pasteurianum at 3.0-Å Resolution. Biochemistry 1993, 32, 7104–7115. [PubMed: 8393705]

(160). Shah VK; Brill WJ Isolation of an Iron-Molybdenum Cofactor from Nitrogenase. Proc. Natl. Acad. Sci. U. S. A 1977, 74, 3249–3253. [PubMed: 410019]

(161). Burgess BK The Iron-Molybdenum Cofactor of Nitrogenase. Chem. Rev 1990, 90, 1377–1406.

(162). Tanifuji K; Ohki Y Metal-Sulfur Compounds in N2 Reduction and Nitrogenase-Related Chemistry. Chem. Rev 2020, 120, 5194–5251. [PubMed: 32459087]

(163). Lundell DJ; Howard JB Isolation and Partial Characterization of Two Different Subunits from the Molybdenum-Iron Protein of Azotobacter Vinelandii Nitrogenase. J. Biol. Chem 1978, 253, 3422–3426. [PubMed: 649581]

(164). Hausinger RP; Howard JB The Amino Acid Sequence of the Nitrogenase Iron Protein from Azotobacter Vinelandii. J. Biol. Chem 1982, 257, 2483–2490. [PubMed: 6801032]

(165). Brigle KE; Newton WE; Dean DR Complete Nucleotide Sequence of the Azotobacter Vinelandii Nitrogenase Structural Gene Cluster. Gene 1985, 37, 37–44. [PubMed: 3863780]

(166). Wang SZ; Chen JS; Johnson JL Distinct Structural Features of the α and β Subunits of Nitrogenase Molybdenum-Iron Protein of Clostridium Pasteurianum: An Analysis of Amino Acid Sequences. Biochemistry 1988, 27, 2800–2810. [PubMed: 2840948]

(167). Holland D; Zilberstein A; Zamir A; Sussman JL A Quantitative Approach to Sequence Comparisons of Nitrogenase MoFe Protein α- and β-Subunits Including the Newly Sequenced NifK Gene from Klebsiella Pneumoniae. Biochem. J 1987, 247, 277–285. [PubMed: 3322261]

(168). Ioannidis I; Buck M Nucleotide Sequence of the Klebsiella Pneumoniae NifD Gene and Predicted Amino Acid Sequence of the α-Subunit of Nitrogenase MoFe Protein. Biochem. J 1987, 247, 287–291. [PubMed: 3322262]

(169). Brigle KE; Setterquist RA; Dean DR; Cantwell JS; Weiss MC; Newton WE Site-Directed Mutagenesis of the Nitrogenase MoFe Protein of Azotobacter Vinelandii. Proc. Natl. Acad. Sci. U. S. A 1987, 84, 7066–7069. [PubMed: 16593879]

(170). Dean DR; Brigle KE; May HD; Newton WE Site-Directed Mutagenesis of the Nitrogenase MoFe Protein. In Nitrogen fixation: hundred years after; Bothe H, de Bruijn FJ, Newton WE, Eds.; Gustav Fischer: Stuttgart; New York, 1988; pp 107–113.

(171). Kent HM; Baines M; Gormal C; Smith BE; Buck M Analysis of Site-Directed Mutations in the α-and β-Subunits of Klebsiella Pneumoniae Nitrogenase. Mol. Microbiol 1990, 4, 1497–1504.

(172). Kent HM; Ioannidis I; Gormal C; Smith BE; Buck M Site-Directed Mutagenesis of the Klebsiella Pneumoniae Nitrogenase. Effects of Modifying Conserved Cysteine Residues in the α- and β-Subunits. Biochem. J 1989, 264, 257–264. [PubMed: 2557830]

(173). Meyer J Iron-Sulfur Protein Folds, Iron-Sulfur Chemistry, and Evolution. JBIC J. Biol. Inorg. Chem 2008, 13, 157–170. [PubMed: 17992543]

(174). Christiansen J; Cash VL; Seefeldt LC; Dean DR Isolation and Characterization of an Acetylene-Resistant Nitrogenase. J. Biol. Chem 2000, 275, 11459–11464. [PubMed: 10753963]

(175). Christiansen J; Seefeldt LC; Dean DR Competitive Substrate and Inhibitor Interactions at the Physiologically Relevant Active Site of Nitrogenase*. J. Biol. Chem 2000, 275, 36104–36107. [PubMed: 10948195]

(176). Mayer SM; Niehaus WG; Dean DR Reduction of Short Chain Alkynes by a Nitrogenase α-70Ala-Substituted MoFe Protein. J. Chem. Soc. Dalt. Trans 2002, No. 5, 802–807.

(177). Barney BM; Igarashi RY; Dos Santos PC; Dean DR; Seefeldt LC Substrate Interaction at an Iron-Sulfur Face of the FeMo-Cofactor during Nitrogenase Catalysis. J. Biol. Chem 2004, 279, 53621–53624. [PubMed: 15465817]

(178). Dos Santos PC; Mayer SM; Barney BM; Seefeldt LC; Dean DR Alkyne Substrate Interaction within the Nitrogenase MoFe Protein. J. Inorg. Biochem 2007, 101, 1642–1648. [PubMed: 17610955]

(179). Yang Z-Y; Dean DR; Seefeldt LC Molybdenum Nitrogenase Catalyzes the Reduction and Coupling of CO to Form Hydrocarbons. J. Biol. Chem 2011, 286, 19417–19421. [PubMed: 21454640]

(180). Benton PMC; Mayer SM; Shao J; Hoffman BM; Dean DR; Seefeldt LC Interaction of Acetylene and Cyanide with the Resting State of Nitrogenase α-96-Substituted MoFe Proteins. Biochemistry 2001, 40, 13816–13825. [PubMed: 11705370]

(181). Maskos Z; Fisher K; Sørlie M; Newton WE; Hales BJ Variant MoFe Proteins of Azotobacter Vinelandii: Effects of Carbon Monoxide on Electron Paramagnetic Resonance Spectra Generated during Enzyme Turnover. JBIC, J. Biol. Inorg. Chem 2005, 10, 394–406. [PubMed: 15887041]

(182). Scott DJ; May HD; Newton WE; Brigle KE; Dean DR Role for the Nitrogenase MoFe Protein α-Subunit in FeMo-Cofactor Binding and Catalysis. Nature 1990, 343, 188–190. [PubMed: 2153269]

(183). Fisher K; Dilworth MJ; Kim C-H; Newton WE Azotobacter Vinelandii Nitrogenases Containing Altered MoFe Proteins with Substitutions in the FeMo-Cofactor Environment: Effects on the Catalyzed Reduction of Acetylene and Ethylene. Biochemistry 2000, 39, 2970–2979. [PubMed: 10715117]

(184). Sørlie M; Christiansen J; Lemon BJ; Peters JW; Dean DR; Hales BJ Mechanistic Features and Structure of the Nitrogenase α-Gln195 MoFe Protein. Biochemistry 2001, 40, 1540–1549. [PubMed: 11327812]

(185). Scott DJ; Dean DR; Newton WE Nitrogenase-Catalyzed Ethane Production and CO-Sensitive Hydrogen Evolution from MoFe Proteins Having Amino Acid Substitutions in an Alpha-Subunit FeMo Cofactor-Binding Domain. J. Biol. Chem 1992, 267, 20002–20010. [PubMed: 1328190]

(186). Fisher K; Hare ND; Newton WE Another Role for CO with Nitrogenase? CO Stimulates Hydrogen Evolution Catalyzed by Variant Azotobacter Vinelandii Mo-Nitrogenases. Biochemistry 2014, 53, 6151–6160. [PubMed: 25203280]

(187). Kim C-H; Newton WE; Dean DR Role of the MoFe Protein α-Subunit Histidine-195 Residue in FeMo-Cofactor Binding and Nitrogenase Catalysis. Biochemistry 1995, 34, 2798–2808. [PubMed: 7893691]

(188). Dilworth MJ; Fisher K; Kim C-H; Newton WE Effects on Substrate Reduction of Substitution of Histidine-195 by Glutamine in the α-Subunit of the MoFe Protein of Azotobacter Vinelandii Nitrogenase. Biochemistry 1998, 37, 17495–17505. [PubMed: 9860864]

(189). Lee H-I; Sørlie M; Christiansen J; Yang T-C; Shao J; Dean DR; Hales BJ; Hoffman BM Electron Inventory, Kinetic Assignment (En), Structure, and Bonding of Nitrogenase Turnover Intermediates with C2H2 and CO. J. Am. Chem. Soc 2005, 127, 15880–15890. [PubMed: 16277531]

(190). Shen J; Dean DR; Newton WE Evidence for Multiple Substrate-Reduction Sites and Distinct Inhibitor-Binding Sites from an Altered Azotobacter Vinelandii Nitrogenase MoFe Protein. Biochemistry 1997, 36, 4884–4894. [PubMed: 9125509]

(191). Fisher K; Dilworth MJ; Kim C-H; Newton WE Azotobacter Vinelandii Nitrogenases with Substitutions in the FeMo-Cofactor Environment of the MoFe Protein: Effects of Acetylene or Ethylene on Interactions with H+, HCN, and CN-. Biochemistry 2000, 39, 10855–10865. [PubMed: 10978172]

(192). Simpson FB; Burris RH A Nitrogen Pressure of 50 atm Does Not Prevent Evolution of Hydrogen by Nitrogenase. Science 1984, 224, 1095–1097. [PubMed: 6585956]

(193). Dilworth MJ Acetylene Reduction by Nitrogen-Fixing Preparations from Clostridium Pasteurianum. Biochim. Biophys. Acta, Gen. Subj 1966, 127, 285–294.

(194). Seefeldt LC; Hoffman BM; Dean DR Mechanism of Mo-Dependent Nitrogenase. Annu. Rev. Biochem 2009, 78, 701–722. [PubMed: 19489731]

(195). Lowe DJ; Fisher K; Thorneley RN Klebsiella Pneumoniae Nitrogenase. Mechanism of Acetylene Reduction and Its Inhibition by Carbon Monoxide. Biochem. J 1990, 272, 621–625. [PubMed: 2268290]

(196). McLean PA; Dixon RA Requirement of NifV Gene for Production of Wild-Type Nitrogenase Enzyme in Klebsiella Pneumoniae. Nature 1981, 292, 655–656. [PubMed: 7019729]

(197). Liang J; Madden M; Shah VK; Burris RH Citrate Substitutes for Homocitrate in Nitrogenase of a NifV Mutant of Klebsiella Pneumoniae. Biochemistry 1990, 29, 8577–8581. [PubMed: 2271541]

(198). Dilworth MJ; Eady RR Hydrazine Is a Product of Dinitrogen Reduction by the Vanadium-Nitrogenase from Azotobacter Chroococcum. Biochem. J 1991, 277, 465–468. [PubMed: 1859374]

(199). Thorneley RNF; Eady RR; Lowe DJ Biological Nitrogen Fixation by Way of an Enzyme-Bound Dinitrogen-Hydride Intermediate. Nature 1978, 272, 557–558.

(200). Rivera-Ortiz JM; Burris RH Interactions among Substrates and Inhibitors of Nitrogenase. J. Bacteriol 1975, 123, 537–545. [PubMed: 1150625]

(201). Hwang JC; Chen CH; Burris RH Inhibition of Nitrogenase-Catalyzed Reductions. Biochim. Biophys. Acta - Bioenerg 1973, 292, 256–270.

(202). Davis LC; Henzl MT; Burris RH; Orme-Johnson WH Iron-Sulfur Clusters in the Molybdenum-Iron Protein Component of Nitrogenase. Electron Paramagnetic Resonance of the Carbon Monoxide Inhibited State. Biochemistry 1979, 18, 4860–4869. [PubMed: 228701]

(203). Lowe DJ; Eady RR; Thorneley RNF Electron-Paramagnetic-Resonance Studies on Nitrogenase of Klebsiella Pneumoniae. Evidence for Acetylene- and Ethylene-Nitrogenase Transient Complexes. Biochem. J 1978, 173, 277–290. [PubMed: 210766]

(204). Davis LC; Shah VK; Brill WJ Nitrogenase: VII. Effect of Component Ratio, ATP and H2, on the Distribution of Electrons to Alternative Substrates. Biochim. Biophys. Acta - Enzymol 1975, 403, 67–78.

(205). Benton PMC; Christiansen J; Dean DR; Seefeldt LC Stereospecificity of Acetylene Reduction Catalyzed by Nitrogenase. J. Am. Chem. Soc 2001, 123, 1822–1827. [PubMed: 11456800]

(206). Hoffman BM; Lukoyanov D; Dean DR; Seefeldt LC Nitrogenase: A Draft Mechanism. Acc. Chem. Res 2013, 46, 587–595. [PubMed: 23289741]

(207). Bergmann J; Oksanen E; Ryde U Critical Evaluation of a Crystal Structure of Nitrogenase with Bound N2 Ligands. JBIC J. Biol. Inorg. Chem 2021, 26, 341–353. [PubMed: 33713183]

(208). Kang W; Lee CC; Jasniewski AJ; Ribbe MW; Hu Y Response to Comment on “Structural Evidence for a Dynamic Metallocofactor during N2 Reduction by Mo-Nitrogenase. Science 2021, 371, No. eabe5856. [PubMed: 33574184]

(209). Peters JW; Einsle O; Dean DR; DeBeer S; Hoffman BM; Holland PL; Seefeldt LC Comment on “Structural Evidence for a Dynamic Metallocofactor during N2 Reduction by Mo-Nitrogenase. Science 2021, 371, No. eabe5481. [PubMed: 33574183]

(210). Lockshin A; Burris RH Inhibitors of Nitrogen Fixation in Extracts from Clostridium Pasteurianum. Biochim. Biophys. Acta - Gen. Subj 1965, 111, 1–10.

(211). Cameron LM; Hales BJ Investigation of CO Binding and Release from Mo-Nitrogenase during Catalytic Turnover. Biochemistry 1998, 37, 9449–9456. [PubMed: 9649328]

(212). Yates MG; Lowe DJ Nitrogenase of Azotobacter Chroococcum: A New Electronparamagnetic-Resonance Signal Associated with a Transient Species of the MoFe Protein during Catalysis. FEBS Lett 1976, 72, 121–126.

(213). Christie PD; Lee H-I; Cameron LM; Hales BJ; Orme-Johnson WH; Hoffman BM Identification of the CO-Binding Cluster in Nitrogenase MoFe Protein by ENDOR of 57Fe Isotopomers. J. Am. Chem. Soc 1996, 118, 8707–8709.

(214). Lee CC; Fay AW; Weng T-C; Krest CM; Hedman B; Hodgson KO; Hu Y; Ribbe MW Uncoupling Binding of Substrate CO from Turnover by Vanadium Nitrogenase. Proc. Natl. Acad. Sci. U. S. A 2015, 112, 13845–13849. [PubMed: 26515097]

(215). Lee CC; Wilcoxen J; Hiller CJ; Britt RD; Hu Y Evaluation of the Catalytic Relevance of the CO-Bound States of V-Nitrogenase. Angew. Chemie Int. Ed 2018, 57, 3411–3414.

(216). Hiller CJ; Lee CC; Stiebritz MT; Rettberg LA; Hu Y Strategies Towards Capturing Nitrogenase Substrates and Intermediates via Controlled Alteration of Electron Fluxes. Chem. Eur. J 2019, 25, 2389–2395. [PubMed: 30225894]

(217). Lee HI; Cameron LM; Hales BJ; Hoffman BM CO Binding to the FeMo Cofactor of CO-Inhibited Nitrogenase: 13CO and 1H Q-Band ENDOR Investigation. J. Am. Chem. Soc 1997, 119, 10121–10126.

(218). George SJ; Ashby GA; Wharton CW; Thorneley RNF Time-Resolved Binding of Carbon Monoxide to Nitrogenase Monitored by Stopped-Flow Infrared Spectroscopy. J. Am. Chem. Soc 1997, 119, 6450–6451.

(219). Pollock RC; Lee H-I; Cameron LM; DeRose VJ; Hales BJ; Orme-Johnson WH; Hoffman BM Investigation of CO Bound to Inhibited Forms of Nitrogenase MoFe Protein by 13C ENDOR. J. Am. Chem. Soc 1995, 117, 8686–8687.

(220). Maskos Z; Hales BJ Photo-Lability of CO Bound to Mo-Nitrogenase from Azotobacter Vinelandii. J. Inorg. Biochem 2003, 93, 11–17. [PubMed: 12538048]

(221). Yan L; Dapper CH; George SJ; Wang H; Mitra D; Dong W; Newton WE; Cramer SP Photolysis of Hi-CO Nitrogenase - Observation of a Plethora of Distinct CO Species Using Infrared Spectroscopy. Eur. J. Inorg. Chem 2011, 2011, 2064–2074. [PubMed: 27630531]

(222). Moore VG; Tittsworth RC; Hales BJ Construction and Characterization of Hybrid Component 1 from V-Nitrogenase Containing FeMo Cofactor. J. Am. Chem. Soc 1994, 116, 12101–12102.

(223). Hu Y; Lee CC; Ribbe MW Extending the Carbon Chain: Hydrocarbon Formation Catalyzed by Vanadium/Molybdenum Nitrogenases. Science 2011, 333, 753–755. [PubMed: 21817053]

(224). Lee CC; Hu Y; Ribbe MW Vanadium Nitrogenase Reduces CO. Science 2010, 329, 642. [PubMed: 20689010]

(225). Lee CC; Hu Y; Ribbe MW Unique Features of the Nitrogenase VFe Protein from Azotobacter Vinelandii. Proc. Natl. Acad. Sci. U. S. A 2009, 106, 9209–9214. [PubMed: 19478062]

(226). Buscagan TM; Perez KA; Maggiolo AO; Rees DC; Spatzal T Structural Characterization of Two CO Molecules Bound to the Nitrogenase Active Site. Angew. Chemie Int. Ed 2021, 60, 5704–5707.

(227). Dance I How Does Vanadium Nitrogenase Reduce CO to Hydrocarbons? Dalt. Trans 2011, 40, 5516–5527.

(228). Dance I The Pathway for Serial Proton Supply to the Active Site of Nitrogenase: Enhanced Density Functional Modeling of the Grotthuss Mechanism. Dalt. Trans 2015, 44, 18167–18186.

(229). Dance I Computational Investigations of the Chemical Mechanism of the Enzyme Nitrogenase. ChemBioChem 2020, 21, 1671–1709. [PubMed: 31803989]

(230). Cao L; Caldararu O; Ryde U Protonation States of Homocitrate and Nearby Residues in Nitrogenase Studied by Computational Methods and Quantum Refinement. J. Phys. Chem. B 2017, 121, 8242–8262. [PubMed: 28783353]

(231). Imperial J; Hoover TR; Madden MS; Ludden PW; Shah VK Substrate Reduction Properties of Dinitrogenase Activated in Vitro Are Dependent upon the Presence of Homocitrate or Its Analogs during Iron-Molybdenum Cofactor Synthesis. Biochemistry 1989, 28, 7796–7799. [PubMed: 2514794]

(232). Siegbahn PEM A Major Structural Change of the Homocitrate Ligand of Probable Importance for the Nitrogenase Mechanism. Inorg. Chem 2018, 57, 1090–1095. [PubMed: 29303565]

(233). McLean PA; Smith BE; Dixon RA Nitrogenase of Klebsiella Pneumoniae NifV Mutants. Investigation of the Novel Carbon Monoxide-Sensitivity of Hydrogen Evolution by the Mutant Enzyme. Biochem. J 1983, 211, 589–597. [PubMed: 6349611]

(234). Newton WE; Vichitphan K; Fisher K Substrate Reduction and CO Susceptibility of the ΔnifV and α-Q191K MoFe Proteins of Azotobacter Vinelandii Nitrogenase. In 13th International Congress on Nitrogen Fixation; Finan TM, O'Brian MR, Layzell DB, Vassey JK, Newton WE, Eds.; CABI Publishing: Hamilton, Ontario, Canada, 2001; p 370.

(235). Liedtke J; Lee CC; Tanifuji K; Jasniewski AJ; Ribbe MW; Hu Y Characterization of a Mo-Nitrogenase Variant Containing a Citrate-Substituted Cofactor. ChemBioChem 2021, 22, 151–155. [PubMed: 32918851]

(236). Newcomb MP; Lee CC; Tanifuji K; Jasniewski AJ; Liedtke J; Ribbe MW; Hu Y A V-Nitrogenase Variant Containing a Citrate-Substituted Cofactor. ChemBioChem 2020, 21, 1742–1748. [PubMed: 31747483]

(237). Mayer SM; Gormal CA; Smith BE; Lawson DM Crystallographic Analysis of the MoFe Protein of Nitrogenase from a NifV Mutant of Klebsiella Pneumoniae Identifies Citrate as a Ligand to the Molybdenum of Iron Molybdenum Cofactor (FeMoco)*. J. Biol. Chem 2002, 277, 35263–35266. [PubMed: 12133839]

(238). Seefeldt LC; Rasche ME; Ensign SA Carbonyl Sulfide and Carbon Dioxide as New Substrates, and Carbon Disulfide as a New Inhibitor, of Nitrogenase. Biochemistry 1995, 34, 5382–5389. [PubMed: 7727396]

(239). Rebelein JG; Hu Y; Ribbe MW Differential Reduction of CO2 by Molybdenum and Vanadium Nitrogenases. Angew. Chemie Int. Ed 2014, 53, 11543–11546.

(240). Yang Z-Y; Moure VR; Dean DR; Seefeldt LC Carbon Dioxide Reduction to Methane and Coupling with Acetylene to Form Propylene Catalyzed by Remodeled Nitrogenase. Proc. Natl. Acad. Sci. U. S. A 2012, 109, 19644–19648. [PubMed: 23150564]

(241). Zheng Y; Harris DF; Yu Z; Fu Y; Poudel S; Ledbetter RN; Fixen KR; Yang Z-Y; Boyd ES; Lidstrom ME; et al. A Pathway for Biological Methane Production Using Bacterial Iron-Only Nitrogenase. Nat. Microbiol 2018, 3, 281–286. [PubMed: 29335552]

(242). Gaffron H Reduction of Carbon Dioxide with Molecular Hydrogen in Green Algae. Nature 1939, 3614, 204–205.

(243). Kluyver AJ; Manten A Some Observations on the Metabolism of Bacteria Oxidizing Molecular Hydrogen. Antonie Van Leeuwenhoek 1942, 8, 71–85.

(244). Gest H Oxidation and Evolution of Molecular Hydrogen by Microorganisms. Bacteriol. Rev 1954, 18, 43–73. [PubMed: 13140082]

(245). Schwartz E; Friedrich B The H2-Metabolizing Prokaryotes. In The Prokaryotes; Dworkin M, Falkow S, Rosenberg E, Schleifer K-H, Stackebrandt E, Eds.; Springer: New York, 2006; pp 496–563.

(246). Greening C; Biswas A; Carere CR; Jackson CJ; Taylor MC; Stott MB; Cook GM; Morales SE Genomic and Metagenomic Surveys of Hydrogenase Distribution Indicate H2 Is a Widely Utilised Energy Source for Microbial Growth and Survival. ISME J 2016, 10, 761–777. [PubMed: 26405831]

(247). Benoit SL; Maier RJ; Sawers RG; Greening C Molecular Hydrogen Metabolism: A Widespread Trait of Pathogenic Bacteria and Protists. Microbiol. Mol. Biol. Rev 2020, 84, No. e00092–19. [PubMed: 31996394]

(248). Das D; Veziroglu TN Hydrogen Production by Biological Processes: A Survey of Literature. Int. J. Hydrogen Energy 2001, 26, 13–28.

(249). Tamagnini P; Axelsson R; Lindberg P; Oxelfelt F; Wünschiers R; Lindblad P Hydrogenases and Hydrogen Metabolism of Cyanobacteria. Microbiol. Mol. Biol. Rev 2002, 66, 1–20. [PubMed: 11875125]

(250). Melis A; Happe T Trails of Green Alga Hydrogen Research - from Hans Gaffron to New Frontiers. Photosynth. Res 2004, 80, 401–409. [PubMed: 16328836]

(251). Lubitz W; Ogata H; Rüdiger O; Reijerse E Hydrogenases. Chem. Rev 2014, 114, 4081–4148. [PubMed: 24655035]

(252). Vignais PM; Billoud B Occurrence, Classification, and Biological Function of Hydrogenases: An Overview. Chem. Rev 2007, 107, 4206–4272. [PubMed: 17927159]

(253). Shima S; Pilak O; Vogt S; Schick M; Stagni MS; Meyer-Klaucke W; Warkentin E; Thauer RK; Ermler U The Crystal Structure of [Fe]-Hydrogenase Reveals the Geometry of the Active Site. Science 2008, 321, 572–575. [PubMed: 18653896]

(254). Thauer RK; Kaster A-K; Goenrich M; Schick M; Hiromoto T; Shima S Hydrogenases from Methanogenic Archaea, Nickel, a Novel Cofactor, and H2 Storage. Annu. Rev. Biochem 2010, 79, 507–536. [PubMed: 20235826]

(255). Huang G; Wagner T; Ermler U; Shima S Methanogenesis Involves Direct Hydride Transfer from H2 to an Organic Substrate. Nat. Rev. Chem 2020, 4, 213–221.

(256). Bothe H; Schmitz O; Yates MG; Newton WE Nitrogen Fixation and Hydrogen Metabolism in Cyanobacteria. Microbiol. Mol. Biol. Rev 2010, 74, 529–551. [PubMed: 21119016]

(257). Fritsch J; Lenz O; Friedrich B Structure, Function and Biosynthesis of O2-Tolerant Hydrogenases. Nat. Rev. Microbiol 2013, 11, 106–114. [PubMed: 23321533]

(258). Parkin A; Sargent F The Hows and Whys of Aerobic H2 Metabolism. Curr. Opin. Chem. Biol 2012, 16, 26–34. [PubMed: 22366384]

(259). Shafaat HS; Rüdiger O; Ogata H; Lubitz W [NiFe] Hydrogenases: A Common Active Site for Hydrogen Metabolism under Diverse Conditions. Biochim. Biophys. Acta 2013, 1827, 986–1002. [PubMed: 23399489]

(260). Armstrong FA; Fontecilla-Camps JC A Natural Choice for Activating Hydrogen. Science 2008, 321, 498–499. [PubMed: 18653870]

(261). Horner DS; Foster PG; Embley TM Iron Hydrogenases and the Evolution of Anaerobic Eukaryotes. Mol. Biol. Evol 2000, 17, 1695–1709. [PubMed: 11070057]

(262). Meyer J [FeFe] Hydrogenases and Their Evolution: A Genomic Perspective. Cell. Mol. Life Sci 2007, 64, 1063–1084. [PubMed: 17353991]

(263). Hemschemeier A; Happe T Alternative Photosynthetic Electron Transport Pathways during Anaerobiosis in the Green Alga Chlamydomonas Reinhardtii. Biochim. Biophys. Acta - Bioenerg 2011, 1807, 919–926.

(264). Melis A; Zhang L; Forestier M; Ghirardi ML; Seibert M Sustained Photobiological Hydrogen Gas Production upon Reversible Inactivation of Oxygen Evolution in the Green Alga Chlamydomonas Reinhardtii. Plant Physiol 2000, 122, 127–136. [PubMed: 10631256]

(265). Buckel W; Thauer RK Flavin-Based Electron Bifurcation, A New Mechanism of Biological Energy Coupling. Chem. Rev 2018, 118, 3862–3886. [PubMed: 29561602]

(266). Schuchmann K; Chowdhury NP; Müller V Complex Multimeric [FeFe] Hydrogenases: Biochemistry, Physiology and New Opportunities for the Hydrogen Economy. Front. Microbiol 2018, 9, 2911. [PubMed: 30564206]

(267). Land H; Senger M; Berggren G; Stripp ST Current State of [FeFe]-Hydrogenase Research - Biodiversity and Spectroscopic Investigations. ACS Catal 2020, 10, 7069–7086.

(268). Fasano A; Land H; Fourmond V; Berggren G; Léger C Reversible or Irreversible Catalysis of H+/H2 Conversion by FeFe Hydrogenases. J. Am. Chem. Soc 2021, 143, 20320–20325. [PubMed: 34813699]

(269). Søndergaard D; Pedersen CNS; Greening C HydDB: A Web Tool for Hydrogenase Classification and Analysis. Sci. Rep 2016, 6, 34212. [PubMed: 27670643]

(270). Nishikawa K; Ogata H; Higuchi Y Structural Basis of the Function of [NiFe]-Hydrogenases. Chem. Lett 2020, 49, 164–173.

(271). Volbeda A; Charon M; Piras C; Hatchikian EC; Frey M; Fontecilla-Camps JC Crystal Structure of the Nickel-Iron Hydrogenase from Desulfovibrio Gigas. Nature 1995, 373, 580–587. [PubMed: 7854413]

(272). Higuchi Y; Yagi T; Yasuoka N Unusual Ligand Structure in Ni-Fe Active Center and an Additional Mg Site in Hydrogenase Revealed by High Resolution X-Ray Structure Analysis. Structure 1997, 5, 1671–1680. [PubMed: 9438867]

(273). Ogata H; Nishikawa K; Lubitz W Hydrogens Detected by Subatomic Resolution Protein Crystallography in a [NiFe] Hydrogenase. Nature 2015, 520, 571–574. [PubMed: 25624102]

(274). Ogata H; Mizoguchi Y; Mizuno N; Miki K; Adachi S; Yasuoka N; Yagi T; Yamauchi O; Hirota S; Higuchi Y Structural Studies of the Carbon Monoxide Complex of [NiFe] Hydrogenase from Desulfovibrio Vulgaris Miyazaki F: Suggestion for the Initial Activation Site for Dihydrogen. J. Am. Chem. Soc 2002, 124, 11628–11635. [PubMed: 12296727]

(275). Ogata H; Hirota S; Nakahara A; Komori H; Shibata N; Kato T; Kano K; Higuchi Y Activation Process of [NiFe] Hydrogenase Elucidated by High-Resolution X-Ray Analyses: Conversion of the Ready to the Unready State. Structure 2005, 13, 1635–1642. [PubMed: 16271886]

(276). Higuchi Y; Ogata H; Miki K; Yasuoka N; Yagi T Removal of the Bridging Ligand Atom at the Ni-Fe Active Site of [NiFe] Hydrogenase upon Reduction with H2, as Revealed by X-Ray Structure Analysis at 1.4 Å Resolution. Structure 1999, 7, 549–556. [PubMed: 10378274]

(277). Volbeda A; Martin L; Cavazza C; Matho M; Faber BW; Roseboom W; Albracht SPJ; Garcin E; Rousset M; Fontecilla-Camps JC Structural Differences between the Ready and Unready Oxidized States of [NiFe] Hydrogenases. J. Biol. Inorg. Chem 2005, 10, 239–249. [PubMed: 15803334]

(278). Ogata H; Kellers P; Lubitz W The Crystal Structure of the [NiFe] Hydrogenase from the Photosynthetic Bacterium Allochromatium Vinosum: Characterization of the Oxidized Enzyme (Ni-A State). J. Mol. Biol 2010, 402, 428–444. [PubMed: 20673834]

(279). Mills DJ; Vitt S; Strauss M; Shima S; Vonck J De Novo Modeling of the F420-Reducing [NiFe]-Hydrogenase from a Methanogenic Archaeon by Cryo-Electron Microscopy. Elife 2013, 2, No. e00218. [PubMed: 23483797]

(280). Vitt S; Ma K; Warkentin E; Moll J; Pierik AJ; Shima S; Ermler U The F-420-Reducing [NiFe]-Hydrogenase Complex from Methanothermobacter Marburgensis, the First X-Ray Structure of a Group 3 Family Member. J. Mol. Biol 2014, 426, 2813–2826. [PubMed: 24887099]

(281). Schafer C; Bommer M; Hennig SE; Jeoung JH; Dobbek H; Lenz O Structure of an Actinobacterial-Type [NiFe]-Hydrogenase Reveals Insight into O-2-Tolerant H-2 Oxidation. Structure 2016, 24, 285–292. [PubMed: 26749450]

(282). Matias PM; Soares CM; Saraiva LM; Coelho R; Morais J; Le Gall J; Carrondo MA [NiFe] Hydrogenase from Desulfovibrio Desulfuricans ATCC 27774: Gene Sequencing, Three-Dimensional Structure Determination and Refinement at 1.8 Å and Modelling Studies of Its Interaction with the Tetrahaem Cytochrome c 3. J. Biol. Inorg. Chem 2001, 6, 63–81. [PubMed: 11191224]

(283). Bowman L; Flanagan L; Fyfe PK; Parkin A; Hunter WN; Sargent F How the Structure of the Large Subunit Controls Function in an Oxygen-Tolerant [NiFe]-Hydrogenase. Biochem. J 2014, 458, 449–458. [PubMed: 24428762]

(284). Shomura Y; Taketa M; Nakashima H; Tai H; Nakagawa H; Ikeda Y; Ishii M; Igarashi Y; Nishihara H; Yoon KS; et al. Structural Basis of the Redox Switches in the NAD+-Reducing Soluble [NiFe]-Hydrogenase. Science 2017, 357, 928–932. [PubMed: 28860386]

(285). Noor NDM; Matsuura H; Nishikawa K; Tai HL; Hirota S; Kim J; Kang JY; Tateno M; Yoon KS; Ogo S; et al. Redox-Dependent Conformational Changes of a Proximal [4Fe-4S] Cluster in Hyb-Type [NiFe]-Hydrogenase to Protect the Active Site from O2. Chem. Commun 2018, 54, 12385–12388.

(286). Volbeda A; Amara P; Darnault C; Mouesca J-M; Parkin A; Roessler MM; Armstrong FA; Fontecilla-Camps JC X-Ray Crystallographic and Computational Studies of the O2-Tolerant [NiFe]-Hydrogenase 1 from Escherichia Coli. Proc. Natl. Acad. Sci. U. S. A 2012, 109, 5305–5310. [PubMed: 22431599]

(287). Beaton SE; Evans RM; Finney AJ; Lamont CM; Armstrong FA; Sargent F; Carr SB The Structure of Hydrogenase-2 from Escherichia Coli : Implications for H2-Driven Proton Pumping. Biochem. J 2018, 475, 1353–1370. [PubMed: 29555844]

(288). Fritsch J; Scheerer P; Frielingsdorf S; Kroschinsky S; Friedrich B; Lenz O; Spahn CMT The Crystal Structure of an Oxygen-Tolerant Hydrogenase Uncovers a Novel Iron-Sulphur Centre. Nature 2011, 479, 249–252. [PubMed: 22002606]

(289). Shomura Y; Yoon KS; Nishihara H; Higuchi Y Structural Basis for a [4Fe-3S] Cluster in the Oxygen-Tolerant Membrane-Bound [NiFe]-Hydrogenase. Nature 2011, 479, 253–256. [PubMed: 22002607]

(290). Frielingsdorf S; Fritsch J; Schmidt A; Hammer M; Löwenstein J; Siebert E; Pelmenschikov V; Jaenicke T; Kalms J; Rippers Y; et al. Reversible [4Fe-3S] Cluster Morphing in an O2-Tolerant [NiFe] Hydrogenase. Nat. Chem. Biol 2014, 10, 378–385. [PubMed: 24705592]

(291). Happe RP; Roseboom W; Pierik AJ; Albracht SPJ; Bagley KA Biological Activition of Hydrogen. Nature 1997, 385, 126. [PubMed: 8990114]

(292). Pierik AJ; Roseboom W; Happe RP; Bagley KA; Albracht PJ Carbon Monoxide and Cyanide as Intrinsic Ligands to Iron in the Active Site of [NiFe]-Hydrogenases. J. Biol. Chem 1999, 274, 3331–3337. [PubMed: 9920874]

(293). Armstrong FA; Evans RM; Hexter SV; Murphy BJ; Roessler MM; Wulff P Guiding Principles of Hydrogenase Catalysis Instigated and Clarified by Protein Film Electrochemistry. Acc. Chem. Res 2016, 49, 884–892. [PubMed: 27104487]

(294). Ash PA; Hidalgo R; Vincent KA Proton Transfer in the Catalytic Cycle of [NiFe] Hydrogenases: Insight from Vibrational Spectroscopy. ACS Catal 2017, 7, 2471–2485. [PubMed: 28413691]

(295). Greene BL; Vansuch GE; Chica BC; Adams MWW; Dyer RB Applications of Photogating and Time Resolved Spectroscopy to Mechanistic Studies of Hydrogenases. Acc. Chem. Res 2017, 50, 2718–2726. [PubMed: 29083854]

(296). Tai H; Higuchi Y; Hirota S Comprehensive Reaction Mechanisms at and near the Ni-Fe Active Sites of [NiFe] Hydrogenases. Dalt. Trans 2018, 47, 4408–4423.

(297). Tai H; Hirota S; Stripp ST Proton Transfer Mechanisms in Bimetallic Hydrogenases. Acc. Chem. Res 2021, 54, 232–241. [PubMed: 33326230]

(298). Ogata H; Lubitz W; Higuchi Y Structure and Function of [NiFe] Hydrogenases. J. Biochem 2016, 160, 251–258. [PubMed: 27493211]

(299). Baltazar CSA; Marques MC; Soares CM; DeLacey AM; Pereira IAC; Matias PM Nickel-Iron-Selenium Hydrogenases - An Overview. Eur. J. Inorg. Chem 2011, 948–962.

(300). Garcin E; Vernede X; Hatchikian EC; Volbeda A; Frey M; Fontecilla-Camps JC The Crystal Structure of a Reduced [NiFeSe] Hydrogenase Provides an Image of the Activated Catalytic Center. Structure 1999, 7, 557–566. [PubMed: 10378275]

(301). Marques MC; Tapia C; Gutiérrez-Sanz O; Ramos AR; Keller KL; Wall JD; De Lacey AL; Matias PM; Pereira IAC The Direct Role of Selenocysteine in [NiFeSe] Hydrogenase Maturation and Catalysis. Nat. Chem. Biol 2017, 13, 544–550. [PubMed: 28319099]

(302). Ceccaldi P; Marques MC; Fourmond V; Pereira IC; Léger C Oxidative Inactivation of NiFeSe Hydrogenase. Chem. Commun 2015, 51, 14223–14226.

(303). Volbeda A; Amara P; Iannello M; De Lacey AL; Cavazza C; Fontecilla-Camps JC Structural Foundations for the O2 Resistance of Desulfomicrobium Baculatum [NiFeSe]-Hydrogenase. Chem. Commun 2013, 49, 7061–7063.

(304). Yagi T; Kimura K; Daidoji H; Sakai F; Tamura S; et al. Properties of Purified Hydrogenase from the Particulate Fraction of Desulfovibrio Vulgaris, Miyazaki. J. Biochem 1976, 79, 661–671. [PubMed: 181372]

(305). Yahata N; Saitoh T; Takayama Y; Ozawa K; Ogata H; Higuchi Y; Akutsu H Redox Interaction of Cytochrome C3 with [NiFe] Hydrogenase from Desulfovibrio Vulgaris Miyazaki F. Biochemistry 2006, 45, 1653–1662. [PubMed: 16460012]

(306). Yagi T; Higuchi Y Studies on Hydrogenase. Proc. Japan Acad. Ser. B-Physical Biol. Sci 2013, 89, 16–33.

(307). Volbeda A; Darnault C; Parkin A; Sargent F; Armstrong FA; Fontecilla-Camps JC Crystal Structure of the O(2)-Tolerant Membrane-Bound Hydrogenase 1 from Escherichia Coli in Complex with Its Cognate Cytochrome B. Structure 2013, 21, 184–190. [PubMed: 23260654]

(308). Tai H; Hirota S Mechanism and Application of the Catalytic Reaction of [NiFe] Hydrogenase: Recent Developments. Chembiochem 2020, 21, 1573–1581. [PubMed: 32180334]

(309). Leroux F; Dementin S; Burlat B; Cournac L; Volbeda A; Champ S; Martin L; Guigliarelli B; Bertrand P; Fontecilla-Camps J; et al. Experimental Approaches to Kinetics of Gas Diffusion in Hydrogenase. Proc. Natl. Acad. Sci. U. S. A 2008, 105, 11188–11193. [PubMed: 18685111]

(310). Liebgott P-P; de Lacey AL; Burlat B; Cournac L; Richaud P; Brugna M; Fernandez VM; Guigliarelli B; Rousset M; Léger C; et al. Original Design of an Oxygen-Tolerant [NiFe] Hydrogenase: Major Effect of a Valine-to-Cysteine Mutation near the Active Site. J. Am. Chem. Soc 2011, 133, 986–997. [PubMed: 21175174]

(311). Abou Hamdan A; Dementin S; Liebgott PP; Gutierrez-Sanz O; Richaud P; De Lacey AL; Roussett M; Bertrand P; Cournac L; Léger C Understanding and Tuning the Catalytic Bias of Hydrogenase. J. Am. Chem. Soc 2012, 134, 8368–8371. [PubMed: 22540997]

(312). van Gastel M; Stein M; Brecht M; Schroder O; Lendzian F; Bittl R; Ogata H; Higuchi Y; Lubitz W A Single-Crystal ENDOR and Density Functional Theory Study of the Oxidized States of the [NiFe] Hydrogenase from Desulfovibrio Vulgaris Miyazaki F. J. Biol. Inorg. Chem 2006, 11, 41–51. [PubMed: 16292669]

(313). Pandelia M-E; Ogata H; Lubitz W Intermediates in the Catalytic Cycle of [NiFe] Hydrogenase: Functional Spectroscopy of the Active Site. ChemPhysChem 2010, 11, 1127–1140. [PubMed: 20301175]

(314). Fernandez VM; Hatchikian EC; Patil DS; Cammack R ESR-Detectable Nickel and Iron-Sulphur Centres in Relation to the Reversible Activation of Desulfovibrio Gigas Hydrogenase. Biochim. Biophys. Acta - Gen. Subj 1986, 883, 145–154.

(315). Barilone JL; Ogata H; Lubitz W; Van Gastel M Structural Differences between the Active Sites of the Ni-A and Ni-B States of the [NiFe] Hydrogenase: An Approach by Quantum Chemistry and Single Crystal ENDOR Spectroscopy. Phys. Chem. Chem. Phys 2015, 17, 16204–16212. [PubMed: 26035632]

(316). Maroney MJ Nailing down Hydrogenase. Nat. Chem. Biol 2013, 9, 11–12. [PubMed: 23238681]

(317). Pandelia ME; Ogata H; Currell LJ; Flores M; Lubitz W Probing Intermediates in the Activation Cycle of [NiFe] Hydrogenase by Infrared Spectroscopy: The Ni-SIr State and Its Light Sensitivity. J. Biol. Inorg. Chem 2009, 14, 1227–1241. [PubMed: 19626348]

(318). Fichtner C; Laurich C; Bothe E; Lubitz W Spectroelectrochemical Characterization of the [NiFe] Hydrogenase of Desulfovibrio Vulgaris Miyazaki F. Biochemistry 2006, 45, 9706–9716. [PubMed: 16893172]

(319). Bleijlevens B; van Broekhuizen F. a; De Lacey AL; Roseboom W; Fernandez VM; Albracht SPJ The Activation of the [NiFe]-Hydrogenase from Allochromatium Vinosum. An Infrared Spectro-Electrochemical Study. J. Biol. Inorg. Chem 2004, 9, 743–752. [PubMed: 15243788]

(320). De Lacey AL; Hatchikian EC; Volbeda A; Frey M; Fontecilla-Camps JC; Fernandez VM Infrared-Spectroelectrochemical Characterization of the [NiFe] Hydrogenase of Desulfovibrio Gigas. J. Am. Chem. Soc 1997, 119, 7181–7189.

(321). Millo D; Pandelia M-E; Utesch T; Wisitruangsakul N; Mroginski MA; Lubitz W; Hildebrandt P; Zebger I Spectroelectrochemical Study of the [NiFe] Hydrogenase from Desulfovibrio Vulgaris Miyazaki F in Solution and Immobilized on Biocompatible Gold Surfaces. J. Phys. Chem. B 2009, 113, 15344–15351. [PubMed: 19845323]

(322). Breglia R; Greco C; Fantucci P; De Gioia L; Bruschi M Reactivation of the Ready and Unready Oxidized States of [NiFe]-Hydrogenases: Mechanistic Insights from DFT Calculations. Inorg. Chem 2019, 58, 279–293. [PubMed: 30576127]

(323). De Lacey AL; Pardo A; Fernández VM; Dementin S; Adryanczyk-Perrier G; Hatchikian CE; Rousset M FTIR Spectroelectrochemical Study of the Activation and Inactivation Processes of [NiFe] Hydrogenases: Effects of Solvent Isotope Replacement and Site-Directed Mutagenesis. J. Biol. Inorg. Chem 2004, 9, 636–642. [PubMed: 15175937]

(324). DeLacey AL; Fernandez VM; Rousset M; Cavazza C; Hatchikian EC Spectroscopic and Kinetic Characterization of Active Site Mutants of Desulfovibrio Fructosovorans Ni-Fe Hydrogenase. J. Biol. Inorg. Chem 2003, 8, 129–134. [PubMed: 12459907]

(325). Evans RM; Ash PA; Beaton SE; Brooke EJ; Vincent KA; Carr SB; Armstrong FA Mechanistic Exploitation of a Self-Repairing, Blocked Proton Transfer Pathway in an O2-Tolerant [NiFe]-Hydrogenase. J. Am. Chem. Soc 2018, 140, 10208–10220. [PubMed: 30070475]

(326). Ogata H; Kramer T; Wang H; Schilter D; Pelmenschikov V; van Gastel M; Neese F; Rauchfuss TB; Gee LB; Scott AD; et al. Hydride Bridge in [NiFe]-Hydrogenase Observed by Nuclear Resonance Vibrational Spectroscopy. Nat. Commun 2015, 6, 7890. [PubMed: 26259066]

(327). Wang HX; Yoda Y; Ogata H; Tanaka Y; Lubitz W A Strenuous Experimental Journey Searching for Spectroscopic Evidence of a Bridging Nickel-Iron-Hydride in [NiFe] Hydrogenase. J. Synchrotron Radiat 2015, 22, 1334–1344. [PubMed: 26524296]

(328). Kamali S; Wang HX; Mitra D; Ogata H; Lubitz W; Manor BC; Rauchfuss TB; Byrne D; Bonnefoy V; Jenney FE; et al. Observation of the Fe-CN and Fe-CO Vibrations in the Active Site of [NiFe] Hydrogenase by Nuclear Resonance Vibrational Spectroscopy. Angew. Chem. Int. Ed 2013, 52, 724–728.

(329). Ogo S; Ichikawa K; Kishima T; Matsumoto T; Nakai H; Kusaka K; Ohhara T A Functional [NiFe]-hydrogenase Mimic That Catalyzes Electron and Hydride Transfer from H2. Science 2013, 339, 682–684. [PubMed: 23393260]

(330). Manor BC; Rauchfuss TB Hydrogen Activation by Biomimetic [NiFe]-Hydrogenase Model Containing Protected Cyanide Cofactors. J. Am. Chem. Soc 2013, 135, 11895–11900. [PubMed: 23899049]

(331). Chambers GM; Huynh MT; Li Y; Hammes-Schiffer S; Rauchfuss TB; Reijerse E; Lubitz W Models of the Ni-L and Ni-SIa States of the [NiFe]-Hydrogenase Active Site. Inorg. Chem 2016, 55, 419–431. [PubMed: 26421729]

(332). Ulloa OA; Huynh MT; Richers CP; Bertke JA; Nilges MJ; Hammes-Schiffer S; Rauchfuss TB Mechanism of H2 Production by Models for the [NiFe]-Hydrogenases: Role of Reduced Hydrides. J. Am. Chem. Soc 2016, 138, 9234–9245. [PubMed: 27328053]

(333). Dong G; Phung QM; Hallaert SD; Pierloot K; Ryde U H2 Binding to the Active Site of [NiFe] Hydrogenase Studied by Multiconfigurational and Coupled-Cluster Methods. Phys. Chem. Chem. Phys 2017, 19, 10590–10601. [PubMed: 28397891]

(334). Dong G; Ryde U; Aa Jensen HJ; Hedegard ED Exploration of H2 Binding to the [NiFe]-Hydrogenase Active Site with Multiconfigurational Density Functional Theory. Phys. Chem. Chem. Phys 2018, 20, 794–801. [PubMed: 29205241]

(335). Bruschi M; Tiberti M; Guerra A; De Gioia L Disclosure of Key Stereoelectronic Factors for Efficient H2 Binding and Cleavage in the Active Site of [NiFe]-Hydrogenases. J. Am. Chem. Soc 2014, 136, 1803–1814. [PubMed: 24392667]

(336). Brazzolotto D; Gennari M; Queyriaux N; Simmons TR; Pécaut J; Demeshko S; Meyer F; Orio M; Artero V; Duboc C Nickel-Centred Proton Reduction Catalysis in a Model of [NiFe] Hydrogenase. Nat. Chem 2016, 8, 1054–1060. [PubMed: 27768098]

(337). Dong G; Phung QM; Pierloot K; Ryde U Reaction Mechanism of [NiFe] Hydrogenase Studied by Computational Methods. Inorg. Chem 2018, 57, 15289–15298. [PubMed: 30500163]

(338). Pandelia ME; Ogata H; Currell LJ; Flores M; Lubitz W Inhibition of the [NiFe] Hydrogenase from Desulfovibrio Vulgaris Miyazaki F by Carbon Monoxide: An FTIR and EPR Spectroscopic Study. Biochim. Biophys. Acta - Bioenerg 2010, 1797, 304–313.

(339). Ilina Y; Lorent C; Katz S; Jeoung J; Shima S; Horch M; Zebger I; Dobbek H X-ray Crystallography and Vibrational Spectroscopy Reveal the Key Determinants of Biocatalytic Dihydrogen Cycling by [NiFe] Hydrogenases. Angew. Chem. Int. Ed 2019, 58, 18710–18714.

(340). Horch M; Schoknecht J; Mroginski MA; Lenz O; Hildebrandt P; Zebger I Resonance Raman Spectroscopy on [NiFe] Hydrogenase Provides Structural Insights into Catalytic Intermediates and Reactions. J. Am. Chem. Soc 2014, 136, 9870–9873. [PubMed: 24956459]

(341). Stein M; van Lenthe E; Baerends EJ; Lubitz W Relativistic DFT Calculations of the Paramagnetic Intermediates of [NiFe] Hydrogenase. Implications for the Enzymatic Mechanism. J. Am. Chem. Soc 2001, 123, 5839–5840. [PubMed: 11403633]

(342). Brecht M; Van Gastel M; Buhrke T; Friedrich B; Lubitz W Direct Detection of a Hydrogen Ligand in the [NiFe] Center of the Regulatory H2-Sensing Hydrogenase from Ralstonia Eutropha in Its Reduced State by HYSCORE and ENDOR Spectroscopy. J. Am. Chem. Soc 2003, 125, 13075–13083. [PubMed: 14570480]

(343). Foerster S; Stein M; Brecht M; Ogata H; Higuchi Y; Lubitz W Single Crystal EPR Studies of the Reduced Active Site of [NiFe] Hydrogenase from Desulfovibrio Vulgaris Miyazaki F. J. Am. Chem. Soc 2003, 125, 83–93. [PubMed: 12515509]

(344). Hidalgo R; Ash PA; Healy AJ; Vincent KA Infrared Spectroscopy during Electrocatalytic Turnover Reveals the Ni-L Active Site State during H2 Oxidation by a NiFe Hydrogenase. Angew. Chem. Int. Ed 2015, 54, 7110–7113.

(345). Murphy BJ; Hidalgo R; Roessler MM; Evans RM; Ash PA; Myers WK; Vincent KA; Armstrong FA Discovery of Dark PH-Dependent H+ Migration in a [NiFe]-Hydrogenase and Its Mechanistic Relevance: Mobilizing the Hydrido Ligand of the Ni-C Intermediate. J. Am. Chem. Soc 2015, 137, 8484–8489. [PubMed: 26103582]

(346). Tai H; Nishikawa K; Higuchi Y; Mao Z-W; Hirota S Cysteine SH and Glutamate COOH Contributions to [NiFe] Hydrogenase Proton Transfer Revealed by Highly Sensitive FTIR Spectroscopy. Angew. Chem. Int. Ed 2019, 58, 13285–13290.

(347). Tai H; Nishikawa K; Suzuki M; Higuchi Y; Hirota S Control of the Transition between Ni-C and Ni-SIastates by the Redox State of the Proximal Fe-S Cluster in the Catalytic Cycle of [NiFe] Hydrogenase. Angew. Chem. Int. Ed 2014, 53, 13817–13820.

(348). Tai H; Nishikawa K; Inoue S; Higuchi Y; Hirota S FT-IR Characterization of the Light-Induced Ni-L2 and Ni-L3 States of [NiFe] Hydrogenase from Desulfovibrio Vulgaris Miyazaki F. J. Phys. Chem. B 2015, 119, 13688–13674.

(349). Greene BL; Wu CH; McTernan PM; Adams MWW; Dyer RB Proton-Coupled Electron Transfer Dynamics in the Catalytic Mechanism of a [NiFe]-Hydrogenase. J. Am. Chem. Soc 2015, 137, 4558–4566. [PubMed: 25790178]

(350). Greene BL; Wu C; Vansuch GE; Adams MWW; Dyer RB Proton Inventory and Dynamics in the Nia-S to Nia-C Transition of a [NiFe] Hydrogenase. Biochemistry 2016, 55, 1813–1825. [PubMed: 26956769]

(351). Greene BL; Vansuch GE; Wu CH; Adams MWW; Dyer RB Glutamate Gated Proton-Coupled Electron Transfer Activity of a [NiFe]-Hydrogenase. J. Am. Chem. Soc 2016, 138, 13013–13021. [PubMed: 27617712]

(352). Kampa M; Pandelia ME; Lubitz W; Van Gastel M; Neese F A Metal-Metal Bond in the Light-Induced State of [Nife] Hydrogenases with Relevance to Hydrogen Evolution. J. Am. Chem. Soc 2013, 135, 3915–3925. [PubMed: 23402569]

(353). Siebert E; Horch M; Rippers Y; Fritsch J; Frielingsdorf S; Lenz O; Velazquez Escobar F; Siebert F; Paasche L; Kuhlmann U; et al. Resonance Raman Spectroscopy as a Tool to Monitor the Active Site of Hydrogenases. Angew. Chem. Int. Ed 2013, 52, 5162–5165.

(354). Ogata H; Lubitz W; Higuchi Y [NiFe] Hydrogenases: Structural and Spectroscopic Studies of the Reaction Mechanism. Dalton Trans 2009, 9226, 7577–7587.

(355). Teixeira VH; Soares CM; Baptista AM Proton Pathways in a [NiFe]-Hydrogenase: A Theoretical Study. Proteins 2008, 70, 1010–1022. [PubMed: 17847093]

(356). Galván IF; Volbeda A; Fontecilla-Camps JC; Field MJ A QM/MM Study of Proton Transport Pathways in a [NiFe] Hydrogenase. Proteins Struct. Funct. Genet 2008, 73, 195–203. [PubMed: 18412257]

(357). Dementin S; Burlat B; De Lacey AL; Pardo A; Adryanczyk-Perrier G; Guigliarelli B; Fernandez VM; Rousset M A Glutamate Is the Essential Proton Transfer Gate during the Catalytic Cycle of the [NiFe] Hydrogenase. J. Biol. Chem 2004, 279, 10508–10513. [PubMed: 14688251]

(358). Oteri F; Baaden M; Lojou E; Sacquin-Mora S Multiscale Simulations Give Insight into the Hydrogen in and out Pathways of [NiFe]-Hydrogenases from Aquifex Aeolicus and Desulfovibrio Fructosovorans. J. Phys. Chem. B 2014, 118, 13800–13811. [PubMed: 25399809]

(359). Dong G; Ryde U Protonation States of Intermediates in the Reaction Mechanism of [NiFe] Hydrogenase Studied by Computational Methods. J. Biol. Inorg. Chem 2016, 21, 383–394. [PubMed: 26940957]

(360). Evans RM; Brooke EJ; Wehlin SAM; Nomerotskaia E; Sargent F; Carr SB; Phillips SEV; Armstrong FA Mechanism of Hydrogen Activation by [NiFe] Hydrogenases. Nat. Chem. Biol 2016, 12, 46–50. [PubMed: 26619250]

(361). Brooke EJ; Evans RM; Islam STA; Roberts GM; Wehlin SAM; Carr SB; Phillips SEV; Armstrong FA Importance of the Active Site “Canopy” Residues in an O2-Tolerant [NiFe]-Hydrogenase. Biochemistry 2017, 56, 132–142. [PubMed: 28001048]

(362). Vansuch GE; Wu C-H; Haja DK; Blair SA; Chica B; Johnson MK; Adams MWW; Dyer RB Metal-Ligand Cooperativity in the Soluble Hydrogenase-1 from Pyrococcus Furiosus. Chem. Sci 2020, 11, 8572–8581. [PubMed: 34123117]

(363). Fichtner C; van Gastel M; Lubitz W Wavelength Dependence of the Photo-Induced Conversion of the Ni-C to the Ni-L Redox State in the [NiFe] Hydrogenase of Desulfovibrio Vulgaris Miyazaki F. Phys. Chem. Chem. Phys 2003, 5, 5507–5513.

(364). van der Zwaan JW; Albracht SPJ; Fontijn RD; Slater EC Monovalent Nickel in Hydrogenase from Chromatium Vinosum. Light Sensitivity and Evidence for Direct Interaction with Hydrogen. FEBS Lett 1985, 179, 271–277. [PubMed: 2981705]

(365). Medina M; Williams R; Cammack R; Hatchikian EC Studies of Light-Induced Nickel EPR Signals in Desulfovibrio Gigas Hydrogenase. J. Chem. Soc. Faraday Trans 1994, 90, 2921–2924.

(366). Medina M; Hatchikian EC; Cammack R Studies of Light-Induced Nickel EPR Signals in Hydrogenase: Comparison of Enzymes with and without Selenium. Biochim. Biophys. Acta - Bioenerg 1996, 1275, 227–236.

(367). Bondar AN; Elstner M; Suhai S; Smith JC; Fischer S Mechanism of Primary Proton Transfer in Bacteriorhodopsin. Structure 2004, 12, 1281–1288. [PubMed: 15242604]

(368). Abou-Hamdan A; Ceccaldi P; Lebrette H; Gutierrez-Sanz O; Richaud P; Cournac L; Guigliarelli B; de Lacey AL; Léger C; Volbeda A; et al. A Threonine Stabilizes the NiC and NiR Catalytic Intermediates of [NiFe]-Hydrogenase. J. Biol. Chem 2015, 290, 8550–8558. [PubMed: 25666617]

(369). Roberts LM; Lindahl PA Analysis of Oxidative Titrations of Desulfovibrio Gigas Hydrogenase; Implications for the Catalytic Mechanism. Biochemistry 1994, 33, 14339–14350. [PubMed: 7947844]

(370). Radu V; Frielingsdorf S; Lenz O; Jeuken LJC Reactivation from the Ni-B State in [NiFe] Hydrogenase of Ralstonia Eutropha Is Controlled by Reduction of the Superoxidised Proximal Cluster. Chem. Commun 2016, 52, 2632–2635.

(371). Evans RM; Parkin A; Roessler MM; Murphy BJ; Adamson H; Lukey MJ; Sargent F; Volbeda A; Fontecilla-Camps JC; Armstrong FA a. Principles of Sustained Enzymatic Hydrogen Oxidation in the Presence of Oxygen - The Crucial Influence of High Potential Fe-S Clusters in the Electron Relay of [NiFe]-Hydrogenases. J. Am. Chem. Soc 2013, 135, 2694–2707. [PubMed: 23398301]

(372). Pandelia ME; Fourmond V; Tron-Infossi P; Lojou E; Bertrand P; Léger C; Giudici-Orticoni MT; Lubitz W Membrane-Bound Hydrogenase I from the Hyperthermophilic Bacterium Aquifex Aeolicus: Enzyme Activation, Redox Intermediates and Oxygen Tolerance. J. Am. Chem. Soc 2010, 132, 6991–7004. [PubMed: 20441192]

(373). Lubitz W; Reijerse E; van Gastel M [NiFe] and [FeFe] Hydrogenases Studied by Advanced Magnetic Resonance Techniques. Chem. Rev 2007, 107, 4331–4365. [PubMed: 17845059]

(374). Pandelia ME; Nitschke W; Infossi P; Giudici-Orticoni MT; Bill E; Lubitz W Characterization of a Unique [FeS] Cluster in the Electron Transfer Chain of the Oxygen Tolerant [NiFe] Hydrogenase from Aquifex Aeolicus. Proc. Natl. Acad. Sci. U. S. A 2011, 108, 6097–6102. [PubMed: 21444783]

(375). Pandelia ME; Bykov D; Izsak R; Infossi P; Giudici-Orticoni MT; Bill E; Neese F; Lubitz W Electronic Structure of the Unique [4Fe-3S] Cluster in O 2-Tolerant Hydrogenases Characterized by 57Fe Mössbauer and EPR Spectroscopy. Proc. Natl. Acad. Sci. U. S. A 2013, 110, 483–488. [PubMed: 23267108]

(376). Mouesca J-M; Amara P; Fontecilla-Camps JC Electronic States of the O2-Tolerant [NiFe] Hydrogenase Proximal Cluster. Proc. Natl. Acad. Sci. U. S. A 2013, 110, No. E2538. [PubMed: 23716706]

(377). Pandelia M-E; Bykov D; Izsak R; Infossi P; Giudici-Orticoni M-T; Bill E; Neese F; Lubitz W Reply to Mouesca et al. : Electronic Structure of the Proximal [4Fe-3S] Cluster of O2-Tolerant [NiFe] Hydrogenases. Proc. Natl. Acad. Sci. U. S. A 2013, 110, No. E2539. [PubMed: 24003456]

(378). Mouesca JM; Fontecilla-Camps JC; Amara P The Structural Plasticity of the Proximal [4Fe3S] Cluster Is Responsible for the O2 Tolerance of Membrane-Bound [NiFe] Hydrogenases. Angew. Chem. Int. Ed 2013, 52, 2002–2006.

(379). Goris T; Wait AF; Saggu M; Fritsch J; Heidary N; Stein M; Zebger I; Lendzian F; Armstrong FA; Friedrich B; et al. A Unique Iron-Sulfur Cluster Is Crucial for Oxygen Tolerance of a [NiFe]-Hydrogenase. Nat. Chem. Biol 2011, 7, 310–318. [PubMed: 21390036]

(380). Lukey MJ; Roessler MM; Parkin A; Evans RM; Davies RA; Lenz O; Friedrich B; Sargent F; Armstrong FA Oxygen-Tolerant [NiFe]-Hydrogenases: The Individual and Collective Importance of Supernumerary Cysteines at the Proximal Fe-S Cluster. J. Am. Chem. Soc 2011, 133, 16881–16892. [PubMed: 21916508]

(381). Lauterbach L; Lenz O Catalytic Production of Hydrogen Peroxide and Water by Oxygen-Tolerant [NiFe]-Hydrogenase during H-2 Cycling in the Presence of O-2. J. Am. Chem. Soc 2013, 135, 17897–17905. [PubMed: 24180286]

(382). Karstens K; Wahlefeld S; Horch M; Grunzel M; Lauterbach L; Lendzian F; Zebger I; Lenz O Impact of the Iron-Sulfur Cluster Proximal to the Active Site on the Catalytic Function of an O-2-Tolerant NAD(+)-Reducing [NiFe]-Hydrogenase. Biochemistry 2015, 54, 389–403. [PubMed: 25517969]

(383). Dance I What Is the Trigger Mechanism for the Reversal of Electron Flow in Oxygen-Tolerant [NiFe] Hydrogenases? Chem. Sci 2015, 6, 1433–1443. [PubMed: 29560232]

(384). Roessler MM; Evans RM; Davies RA; Harmer J; Armstrong FA EPR Spectroscopic Studies of the Fe-S Clusters in the O-2-Tolerant [NiFe]-Hydrogenase Hyd-1 from Escherichia Coli and Characterization of the Unique [4Fe-3S] Cluster by HYSCORE. J. Am. Chem. Soc 2012, 134, 15581–15594. [PubMed: 22900997]

(385). Tai H; Xu L; Inoue S; Nishikawa K; Higuchi Y; Hirota S Photoactivation of the Ni-SIr State to the Ni-SIa State in [NiFe] Hydrogenase: FT-IR Study on the Light Reactivity of the Ready Ni-SIr State and as-Isolated Enzyme Revisited. Phys. Chem. Chem. Phys 2016, 18, 22025–22030. [PubMed: 27456760]

(386). Tai H; Xu L; Nishikawa K; Higuchi Y; Hirota S Equilibrium between Inactive Ready Ni-SIr and Active Ni-SIa States of [NiFe] Hydrogenase Studied by Utilizing Ni-SIr-to-Ni-SIa Photoactivation. Chem. Commun 2017, 53, 10444–10447.

(387). Rousset M; Montet Y; Guigliarelli B; Forget N; Asso M; Bertrand P; Fontecilla-Camps JC; Hatchikian EC [3Fe-4S] to [4Fe-4S] Cluster Conversion in Desulfovibrio Fructosovorans [NiFe] Hydrogenase by Site-Directed Mutagenesis. Proc. Natl. Acad. Sci. U. S. A 1998, 95, 11625–11630. [PubMed: 9751716]

(388). Dementin S; Belle V; Bertrand P; Guigliarelli B; Adryanczyk-Perrier G; De Lacey AL; Fernandez VM; Rousset M; Léger C Changing the Ligation of the Distal [4Fe4S] Cluster in NiFe Hydrogenase Impairs Inter- and Intramolecular Electron Transfers. J. Am. Chem. Soc 2006, 128, 5209–5218. [PubMed: 16608357]

(389). Dementin S; Burlat B; Fourmond V; Leroux F; Liebgott P-P; Abou Hamdan A; Léger C; Rousset M; Guigliarelli B; Bertrand P Rates of Intra- and Intermolecular Electron Transfers in Hydrogenase Deduced from Steady-State Activity Measurements. J. Am. Chem. Soc 2011, 133, 10211–10221. [PubMed: 21615141]

(390). Petrenko A; Stein M Distal [FeS]-Cluster Coordination in [NiFe]-Hydrogenase Facilitates Intermolecular Electron Transfer. Int. J. Mol. Sci 2017, 18, 100.

(391). Yonemoto IT; Smith HO; Weyman PD Designed Surface Residue Substitutions in [NiFe] Hydrogenase That Improve Electron Transfer Characteristics. Int. J. Mol. Sci 2015, 16, 2020–2033. [PubMed: 25603181]

(392). Yonemoto IT; Clarkson BR; Smith HO; Weyman PD A Broad Survey Reveals Substitution Tolerance of Residues Ligating FeS Clusters in [NiFe] Hydrogenase. BMC Biochem 2014, 15, 10. [PubMed: 24934472]

(393). Yonemoto IT; Matteri CW; Nguyen TA; Smith HO; Weyman PD Dual Organism Design Cycle Reveals Small Subunit Substitutions That Improve [NiFe] Hydrogenase Hydrogen Evolution. J. Biol. Eng 2013, 7, 17. [PubMed: 23819621]

(394). Adamson H; Robinson M; Wright JJ; Flanagan LA; Walton J; Elton D; Gavaghan DJ; Bond AM; Roessler MM; Parkin A Retuning the Catalytic Bias and Overpotential of a [NiFe]-Hydrogenase via a Single Amino Acid Exchange at the Electron Entry/Exit Site. J. Am. Chem. Soc 2017, 139, 10677–10686. [PubMed: 28697596]

(395). Vidal-Limon AM; Tafoya P; Santini BL; Contreras OE; Aguila SA Electron Transfer Pathways Analysis of Oxygen Tolerant [NiFe]-Hydrogenases for Hydrogen Production: A Quantum Mechanics/Molecular Mechanics - Statistical Coupled Analysis. Int. J. Hydrog. Energy 2017, 42, 20494–20502.

(396). Montet Y; Amara P; Volbeda A; et al. Gas Access to the Active Site of Ni-Fe Hydrogenases Probed by X-Ray Crystallography and Molecular Dynamics. Nat. Struct. Biol 1997, 4, 523–526. [PubMed: 9228943]

(397). Volbeda A High-Resolution Crystallographic Analysis of Desulfovibrio Fructosovorans [NiFe] Hydrogenase. Int. J. Hydrogen Energy 2002, 27, 1449–1461.

(398). Topin J; Rousset M; Antonczak S; Golebiowski J Kinetics and Thermodynamics of Gas Diffusion in a NiFe Hydrogenase. Proteins-Structure Funct. Bioinforma 2012, 80, 677–682.

(399). Kalms J; Schmidt A; Frielingsdorf S; van der Linden P; von Stetten D; Lenz O; Carpentier P; Scheerer P Krypton Derivatization of an O2 -Tolerant Membrane-Bound [NiFe] Hydrogenase Reveals a Hydrophobic Tunnel Network for Gas Transport. Angew. Chem. Int. Ed 2016, 55, 5586–5590.

(400). Kalms J; Schmidt A; Frielingsdorf S; Utesch T; Gotthard G; von Stetten D; van der Linden P; Royant A; Mroginski MA; Carpentier P; et al. Tracking the Route of Molecular Oxygen in O2-Tolerant Membrane-Bound [NiFe] Hydrogenase. Proc. Natl. Acad. Sci. U.S.A 2018, 115, E2229–E2237. [PubMed: 29463722]

(401). Wang PH; Best RB; Blumberger J Multiscale Simulation Reveals Multiple Pathways for H2 and O2 Transport in a [NiFe]-Hydrogenase. J. Am. Chem. Soc 2011, 133, 3548–3556. [PubMed: 21341658]

(402). Buhrke T; Lenz O; Krauss N; Friedrich B Oxygen Tolerance of the H2-Sensing [NiFe] Hydrogenase from Ralstonia Eutropha H16 Is Based on Limited Access of Oxygen to the Active Site. J. Biol. Chem 2005, 280, 23791–23796. [PubMed: 15849358]

(403). Duché O; Elsen S; Cournac L; Colbeau A Enlarging the Gas Access Channel to the Active Site Renders the Regulatory Hydrogenase HupUV of Rhodobacter Capsulatus O2 Sensitive without Affecting Its Transductory Activity. FEBS J 2005, 272, 3899–3908. [PubMed: 16045760]

(404). Abou Hamdan A; Liebgott P-P; Fourmond V; Gutierrez-Sanz O; De Lacey AL; Infossi P; Rousset M; Dementin S; Léger C Relation between Anaerobic Inactivation and Oxygen Tolerance in a Large Series of NiFe Hydrogenase Mutants. Proc. Natl. Acad. Sci. U. S. A 2012, 109, 19916–19921. [PubMed: 23169623]

(405). Liebgott P; Leroux F; Burlat B; Dementin S; et al. Relating Diffusion along the Substrate Tunnel and Oxygen Sensitivity in Hydrogenase. Nat. Chem. Biol 2010, 6, 63–70. [PubMed: 19966788]

(406). Dementin S; Leroux F; Cournac L; de Lacey AL; Volbeda A; Léger C; Burlat B; Martinez N; Champ S; Martin L; et al. Introduction of Methionines in the Gas Channel Makes [NiFe] Hydrogenase Aero-Tolerant. J. Am. Chem. Soc 2009, 131, 10156–10164. [PubMed: 19580279]

(407). Wang PH; Blumberger J Mechanistic Insight into the Blocking of CO Diffusion in [NiFe]-Hydrogenase Mutants through Multiscale Simulation. Proc. Natl. Acad. Sci. U. S. A 2012, 109, 6399–6404. [PubMed: 22493222]

(408). Liebgott PP; Leroux F; Burlat B; Dementin S; Baffert C; Lautier T; Fourmond V; Ceccaldi P; Cavazza C; Meynial-Salles I; et al. Relating Diffusion along the Substrate Tunnel and Oxygen Sensitivity in Hydrogenase. Nat. Chem. Biol 2010, 6, 63–70. [PubMed: 19966788]

(409). Fourmond V; Infossi P; Giudici-Orticoni M-T; Bertrand P; Léger C Two-Step" Chronoamperometric Method for Studying the Anaerobic Inactivation of an Oxygen Tolerant NiFe Hydrogenase. J. Am. Chem. Soc 2010, 132, 4848–4857. [PubMed: 20230028]

(410). del Barrio M; Guendon C; Kpebe A; Baffert C; Fourmond V; Brugna M; Léger C Valine-to-Cysteine Mutation Further Increases the Oxygen Tolerance of Escherichia Coli NiFe Hydrogenase Hyd-1. ACS Catal 2019, 9, 4084–4088.

(411). Marques MC; Coelho R; Pereira IAC; Matias PM Redox State-Dependent Changes in the Crystal Structure of [NiFeSe] Hydrogenase from Desulfovibrio Vulgaris Hildenborough. Int. J. Hydrog. Energy 2013, 38, 8664–8682.

(412). Zacarias S; Temporao A; del Barrio M; Fourmond V; Léger C; Matias PM; Pereira IAC A Hydrophilic Channel Is Involved in Oxidative Inactivation of a [NiFeSe] Hydrogenase. ACS Catal 2019, 9, 8509–8519.

(413). Peters JW; Lanzilotta WN; Lemon BJ; Seefeldt LC X-Ray Crystal Structure of the Fe-Only Hydrogenase (CpI) from Clostridium Pasteurianum to 1.8 Angstrom Resolution. Science 1998, 282, 1853–1858. [PubMed: 9836629]

(414). Lemon BJ; Peters JW Binding of Exogenously Added Carbon Monoxide at the Active Site of the Iron-Only Hydrogenase (CpI) from Clostridium Pasteurianum. Biochemistry 1999, 38, 12969–12973. [PubMed: 10529166]

(415). Lemon BJ; Peters JW Photochemistry at the Active Site of the Carbon Monoxide Inhibited Form of the Iron-Only Hydrogenase (CpI). J. Am. Chem. Soc 2000, 122, 3793–3794.

(416). Gorwa MF; Croux C; Soucaille P Molecular Characterization and Transcriptional Analysis of the Putative Hydrogenase Gene of Clostridium Acetobutylicum ATCC 824. J. Bacteriol 1996, 178, 2668–2675. [PubMed: 8626337]

(417). Gauquelin C; Baffert C; Richaud P; Kamionka E; Etienne E; Guieysse D; Girbal L; Fourmond V; André I; Guigliarelli B; et al. Roles of the F-Domain in [FeFe] Hydrogenase. Biochim. Biophys. Acta - Bioenerg 2018, 1859, 69–77. [PubMed: 28842179]

(418). Artz JH; Mulder DW; Ratzloff MW; Lubner CE; Zadvornyy OA; LeVan AX; Williams SG; Adams MWW; Jones AK; King PW; et al. Reduction Potentials of [FeFe]-Hydrogenase Accessory Iron-Sulfur Clusters Provide Insights into the Energetics of Proton Reduction Catalysis. J. Am. Chem. Soc 2017, 139, 9544–9550. [PubMed: 28635269]

(419). Pierik AJ; Hagen WR; Redeker JS; Wolbert RBG; Boersma M; Verhagen MFJM; Grande HJ; Veeger C; Mutsaers PH; Sands RH; et al. Redox Properties of the Iron-Sulfur Clusters in Activated Fe-Hydrogenase from Desulfovibrio Vulgaris (Hildenborough). Eur. J. Biochem 1992, 209, 63–72. [PubMed: 1396719]

(420). Nicolet Y; Piras C; Legrand P; Hatchikian CE; Fontecilla-Camps JC Desulfovibrio Desulfuricans Iron Hydrogenase: The Structure Shows Unusual Coordination to an Active Site Fe Binuclear Center. Structure 1999, 7, 13–23. [PubMed: 10368269]

(421). Nicolet Y; de Lacey AL; Vernède X; Fernandez VM; Hatchikian EC; Fontecilla-Camps JC Crystallographic and FTIR Spectroscopic Evidence of Changes in Fe Coordination Upon Reduction of the Active Site of the Fe-Only Hydrogenase from Desulfovibrio d Esulfuricans. J. Am. Chem. Soc 2001, 123, 1596–1601. [PubMed: 11456758]

(422). Caserta G; Adamska-Venkatesh A; Pecqueur L; Atta M; Artero V; Roy S; Reijerse E; Lubitz W; Fontecave M Chemical Assembly of Multiple Metal Cofactors: The Heterologously Expressed Multidomain [FeFe]-Hydrogenase from Megasphaera Elsdenii. Biochim. Biophys. Acta - Bioenerg 2016, 1857, 1734–1740.

(423). Caserta G; Papini C; Adamska-Venkatesh A; Pecqueur L; Sommer C; Reijerse E; Lubitz W; Gauquelin C; Meynial-Salles I; Pramanik D; et al. Engineering an [FeFe]-Hydrogenase: Do Accessory Clusters Influence O2 Resistance and Catalytic Bias? J. Am. Chem. Soc 2018, 140, 5516–5526. [PubMed: 29595965]

(424). Winkler M; Duan J; Rutz A; Felbek C; Scholtysek L; Lampret O; Jaenecke J; Apfel U-P; Gilardi G; Valetti F; et al. A Safety Cap Protects Hydrogenase from Oxygen Attack. Nat. Commun 2021, 12, 756. [PubMed: 33531463]

(425). Happe T; Naber JD Isolation, Characterization and N-terminal Amino Acid Sequence of Hydrogenase from the Green Alga Chlamydomonas Reinhardtii. Eur. J. Biochem 1993, 214, 475–481. [PubMed: 8513797]

(426). Winkler M; Hemschemeier A; Gotor C; Melis A; Happe T [FeFe]-Hydrogenases in Green Algae: Photo-Fermentation and Hydrogen Evolution under Sulfur Deprivation. Int. J. Hydrogen Energy 2002, 27, 1431–1439.

(427). Kamp C; Silakov A; Winkler M; Reijerse EJ; Lubitz W; Happe T Isolation and First EPR Characterization of the [FeFe]-Hydrogenases from Green Algae. Biochim. Biophys. Acta 2008, 1777, 410–416. [PubMed: 18355437]

(428). Sybirna K; Antoine T; Lindberg P; Fourmond V; Rousset M; Méjean V; Bottin H Shewanella Oneidensis: A New and Efficient System for Expression and Maturation of Heterologous [Fe-Fe] Hydrogenase from Chlamydomonas Reinhardtii. BMC Biotechnol 2008, 8, 73. [PubMed: 18801156]

(429). Stripp ST; Sanganas O; Happe T; Haumann M The Structure of the Active Site H-Cluster of [FeFe] Hydrogenase from the Green Alga Chlamydomonas Reinhardtii Studied by X-Ray Absorption Spectroscopy. Biochemistry 2009, 48, 5042–5049. [PubMed: 19397274]

(430). Mulder DW; Boyd ES; Sarma R; Lange RK; Endrizzi JA; Broderick JB; Peters JW Stepwise [FeFe]-Hydrogenase H-Cluster Assembly Revealed in the Structure of HydAΔEFG. Nature 2010, 465, 248–251. [PubMed: 20418861]

(431). Schuchmann K; Müller V Direct and Reversible Hydrogenation of CO2 to Formate by a Bacterial Carbon Dioxide Reductase. Science 2013, 342, 1382–1386. [PubMed: 24337298]

(432). Ceccaldi P; Schuchmann K; Müller V; Elliott SJ The Hydrogen Dependent CO2 Reductase: The First Completely Co Tolerant FeFe-Hydrogenase. Energy Environ. Sci 2017, 10, 503–508.

(433). Lipscomb GL; Schut GJ; Thorgersen MP; Nixon WJ; Kelly RM; Adams MWW Engineering Hydrogen Gas Production from Formate in a Hyperthermophile by Heterologous Production of an 18-Subunit Membrane-Bound Complex. J. Biol. Chem 2014, 289, 2873–2879. [PubMed: 24318960]

(434). Pierik AJ; Hulstein M; Hagen WR; Albracht SPJ A Low-Spin Iron with CN and CO as Intrinsic Ligands Forms the Core of the Active Site in [Fe]-Hydrogenases. Eur. J. Biochem 1998, 258, 572–578. [PubMed: 9874225]

(435). Pandey AS; Harris TV; Giles LJ; Peters JW; Szilagyi RK Dithiomethylether as a Ligand in the Hydrogenase H-Cluster. J. Am. Chem. Soc 2008, 130, 4533–4540. [PubMed: 18324814]

(436). Silakov A; Wenk B; Reijerse E; Lubitz W 14N HYSCORE Investigation of the H-Cluster of [FeFe] Hydrogenase: Evidence for a Nitrogen in the Dithiol Bridge. Phys. Chem. Chem. Phys 2009, 11, 6592–6599. [PubMed: 19639134]

(437). Vignais PM; Billoud B; Meyer J Classification and Phylogeny of Hydrogenases. FEMS Microbiol. Rev 2001, 25, 455–501. [PubMed: 11524134]

(438). Horner DS; Heil B; Happe T; Embley TM Iron Hydrogenases - Ancient Enzymes in Modern Eukaryotes. Trends Biochem. Sci 2002, 27, 148–153. [PubMed: 11893512]

(439). Calusinska M; Happe T; Joris B; Wilmotte A The Surprising Diversity of Clostridial Hydrogenases: A Comparative Genomic Perspective. Microbiology 2010, 156, 1575–1588. [PubMed: 20395274]

(440). Chongdar N; Birrell JA; Pawlak K; Sommer C; Reijerse EJ; Rüdiger O; Lubitz W; Ogata H Unique Spectroscopic Properties of the H-Cluster in a Putative Sensory [FeFe] Hydrogenase. J. Am. Chem. Soc 2018, 140, 1057–1068. [PubMed: 29251926]

(441). Chongdar N; Pawlak K; Rüdiger O; Reijerse EJ; Rodríguez-Maciá P; Lubitz W; Birrell JA; Ogata H Spectroscopic and Biochemical Insight into an Electron-Bifurcating [FeFe] Hydrogenase. J. Biol. Inorg. Chem 2020, 25, 135–149. [PubMed: 31823008]

(442). Land H; Ceccaldi P; Mészáros LS; Lorenzi M; Redman HJ; Senger M; Stripp ST; Berggren G Discovery of Novel [FeFe]-Hydrogenases for Biocatalytic H2-Production. Chem. Sci 2019, 10, 9941–9948. [PubMed: 32055351]

(443). Land H; Sekretareva A; Huang P; Redman HJ; Nemeth B; Polidori N; Meszaros LS; Senger M; Stripp ST; Berggren G Characterization of a Putative Sensory [FeFe]-Hydrogenase Provides New Insight into the Role of the Active Site Architecture. Chem. Sci 2020, 11, 12789–12801. [PubMed: 34094474]

(444). Furlan C; Chongdar N; Gupta P; Lubitz W; Ogata H; James N; Birrell JA Structural Insight on the Mechanism of an Electron-Bifurcating [FeFe] Hydrogenase. ChemRxiv 2021, 1–13.

(445). Lampret O; Esselborn J; Haas R; Rutz A; Booth RL; Kertess L; Wittkamp F; Megarity CF; Armstrong FA; Winkler M; et al. The Final Steps of [FeFe]-Hydrogenase Maturation. Proc. Natl. Acad. Sci. U. S. A 2019, 116, 15802–15810. [PubMed: 31337676]

(446). Winkler M; Senger M; Duan J; Esselborn J; Wittkamp F; Hofmann E; Apfel U-P; Stripp ST; Happe T Accumulating the Hydride State in the Catalytic Cycle of [FeFe]-Hydrogenases. Nat. Commun 2017, 8, 16115. [PubMed: 28722011]

(447). Lampret O; Duan J; Hofmann E; Winkler M; Armstrong FA; Happe T The Roles of Long-Range Proton-Coupled Electron Transfer in the Directionality and Efficiency of [FeFe]-Hydrogenases. Proc. Natl. Acad. Sci. U. S. A 2020, 117, 20520–20529. [PubMed: 32796105]

(448). Duan J; Senger M; Esselborn J; Engelbrecht V; Wittkamp F; Apfel U-P; Hofmann E; Stripp ST; Happe T; Winkler M Crystallographic and Spectroscopic Assignment of the Proton Transfer Pathway in [FeFe]-Hydrogenases. Nat. Commun 2018, 9, 4726. [PubMed: 30413719]

(449). Cornish AJ; Ginovska B; Thelen A; Da Silva JCS; Soares TA; Raugei S; Dupuis M; Shaw WJ; Hegg EL Single-Amino Acid Modifications Reveal Additional Controls on the Proton Pathway of [FeFe]-Hydrogenase. Biochemistry 2016, 55, 3165–3173. [PubMed: 27186945]

(450). Knörzer P; Silakov A; Foster CE; Armstrong FA; Lubitz W; Happe T Importance of the Protein Framework for Catalytic Activity of [FeFe]-Hydrogenases. J. Biol. Chem 2012, 287, 1489–1499. [PubMed: 22110126]

(451). Bingham AS; Smith PR; Swartz JR Evolution of an [FeFe] Hydrogenase with Decreased Oxygen Sensitivity. Int. J. Hydrogen Energy 2012, 37, 2965–2976.

(452). Koo J; Swartz JR System Analysis and Improved [FeFe] Hydrogenase O2 Tolerance Suggest Feasibility for Photosynthetic H2 Production. Metab. Eng 2018, 49, 21–27. [PubMed: 30057338]

(453). Koo J Enhanced Aerobic H2 Production by Engineering an [FeFe] Hydrogenase from Clostridium Pasteurianum. Int. J. Hydrogen Energy 2020, 45, 10673–10679.

(454). Morra S; Giraudo A; Di Nardo G; King PW; Gilardi G; Valetti F Site Saturation Mutagenesis Demonstrates a Central Role for Cysteine 298 as Proton Donor to the Catalytic Site in CaHydA [FeFe]-Hydrogenase. PLoS One 2012, 7, No. e48400. [PubMed: 23133586]

(455). Morra S; Maurelli S; Chiesa M; Mulder DW; Ratzloff MW; Giamello E; King PW; Gilardi G; Valetti F The Effect of a C298D Mutation in CaHydA [FeFe]-Hydrogenase: Insights into the Protein-Metal Cluster Interaction by EPR and FTIR Spectroscopic Investigation. Biochim. Biophys. Acta - Bioenerg 2016, 1857, 98–106.

(456). Mulder DW; Guo Y; Ratzloff MW; King PW Identification of a Catalytic Iron-Hydride at the H-Cluster of [FeFe]-Hydrogenase. J. Am. Chem. Soc 2017, 139, 83–86. [PubMed: 27973768]

(457). Mulder DW; Ratzloff MW; Bruschi M; Greco C; Koonce E; Peters JW; King PW Investigations on the Role of Proton-Coupled Electron Transfer in Hydrogen Activation by [FeFe]-Hydrogenase. J. Am. Chem. Soc 2014, 136, 15394–15402. [PubMed: 25286239]

(458). Pham CC; Mulder DW; Pelmenschikov V; King PW; Ratzloff MW; Wang H; Mishra N; Alp EE; Zhao J; Hu MY; et al. Terminal Hydride Species in [FeFe]-Hydrogenases Are Vibrationally Coupled to the Active Site Environment. Angew. Chemie Int. Ed 2018, 57, 10605–10609.

(459). Rumpel S; Sommer C; Reijerse E; Farès C; Lubitz W Direct Detection of the Terminal Hydride Intermediate in [FeFe] Hydrogenase by NMR Spectroscopy. J. Am. Chem. Soc 2018, 140, 3863–3866. [PubMed: 29521088]

(460). Rodríguez-Maciá P; Kertess L; Burnik J; Birrell JA; Hofmann E; Lubitz W; Happe T; Rüdiger O His-Ligation to the [4Fe-4S] Subcluster Tunes the Catalytic Bias of [FeFe] Hydrogenase. J. Am. Chem. Soc 2019, 141, 472–481. [PubMed: 30545220]

(461). Kertess L; Adamska-Venkatesh A; Rodríguez-Maciá P; Rüdiger O; Lubitz W; Happe T Influence of the [4Fe-4S] Cluster Coordinating Cysteines on Active Site Maturation and Catalytic Properties of C. Reinhardtii [FeFe]-Hydrogenase. Chem. Sci 2017, 8, 8127–8137. [PubMed: 29568461]

(462). Orain C; Saujet L; Gauquelin C; Soucaille P; Meynial-Salles I; Baffert C; Fourmond V; Bottin H; Léger C Electrochemical Measurements of the Kinetics of Inhibition of Two FeFe Hydrogenases by O 2 Demonstrate That the Reaction Is Partly Reversible. J. Am. Chem. Soc 2015, 137, 12580–12587. [PubMed: 26352172]

(463). Sybirna K; Ezanno P; Baffert C; Léger C; Bottin H Arginine171 of Chlamydomonas Reinhardtii [Fe-Fe] Hydrogenase HydA1 Plays a Crucial Role in Electron Transfer to Its Catalytic Center. Int. J. Hydrogen Energy 2013, 38, 2998–3002.

(464). Lampret O; Adamska-Venkatesh A; Konegger H; Wittkamp F; Apfel U-P; Reijerse EJ; Lubitz W; Rüdiger O; Happe T; Winkler M Interplay between CN - Ligands and the Secondary Coordination Sphere of the H-Cluster in [FeFe]-Hydrogenases. J. Am. Chem. Soc 2017, 139, 18222–18230. [PubMed: 29179539]

(465). Kubas A; Orain C; De Sancho D; Saujet L; Sensi M; Gauquelin C; Meynial-Salles I; Soucaille P; Bottin H; Baffert C; Fourmond V; Best RB; Blumberger J; Léger C Mechanism of O2 Diffusion and Reduction in FeFe Hydrogenases. Nat. Chem 2017, 9, 88–95. [PubMed: 27995927]

(466). Winkler M; Kuhlgert S; Hippler M; Happe T Characterization of the Key Step for Light-Driven Hydrogen Evolution in Green Algae. J. Biol. Chem 2009, 284, 36620–36627. [PubMed: 19846550]

(467). Engelbrecht V; Liedtke K; Rutz A; Yadav S; Günzel A; Happe T One Isoform for One Task? The Second Hydrogenase of Chlamydomonas Reinhardtii Prefers Hydrogen Uptake. Int. J. Hydrogen Energy 2021, 46, 7165–7175.

(468). Berggren G; Adamska A; Lambertz C; Simmons TR; Esselborn J; Atta M; Gambarelli S; Mouesca J-M; Reijerse E; Lubitz W; et al. Biomimetic Assembly and Activation of [FeFe]-Hydrogenases. Nature 2013, 499, 66–69. [PubMed: 23803769]

(469). Esselborn J; Lambertz C; Adamska-Venkatesh A; Simmons T; Berggren G; Noth J; Siebel J; Hemschemeier A; Artero V; Reijerse E; et al. Spontaneous Activation of [FeFe]-Hydrogenases by an Inorganic [2Fe] Active Site Mimic. Nat. Chem. Biol 2013, 9, 607–609. [PubMed: 23934246]

(470). Adamska-Venkatesh A; Krawietz D; Siebel JF; Weber K; Happe T; Reijerse E; Lubitz W New Redox States Observed in [FeFe] Hydrogenases Reveal Redox Coupling within the H-Cluster. J. Am. Chem. Soc 2014, 136, 11339–11346. [PubMed: 25025613]

(471). Siebel JF; Adamska-Venkatesh A; Weber K; Rumpel S; Reijerse E; Lubitz W Hybrid [FeFe]-Hydrogenases with Modified Active Sites Show Remarkable Residual Enzymatic Activity. Biochemistry 2015, 54, 1474–1483. [PubMed: 25633077]

(472). Adamska-Venkatesh A; Simmons TR; Siebel JF; Artero V; Fontecave M; Reijerse E; Lubitz W Artificially Maturated [FeFe] Hydrogenase from Chlamydomonas Reinhardtii: A HYSCORE and ENDOR Study of a Non-Natural H-Cluster. Phys. Chem. Chem. Phys 2015, 17, 5421–5430. [PubMed: 25613229]

(473). Adamska-Venkatesh A; Roy S; Siebel JF; Simmons TR; Fontecave M; Artero V; Reijerse E; Lubitz W Spectroscopic Characterization of the Bridging Amine in the Active Site of [FeFe] Hydrogenase Using Isotopologues of the H-Cluster. J. Am. Chem. Soc 2015, 137, 12744–12747. [PubMed: 26393426]

(474). Reijerse EJ; Pham CC; Pelmenschikov V; Gilbert-Wilson R; Adamska-Venkatesh A; Siebel JF; Gee LB; Yoda Y; Tamasaku K; Lubitz W; et al. Direct Observation of an Iron-Bound Terminal Hydride in [FeFe]-Hydrogenase by Nuclear Resonance Vibrational Spectroscopy. J. Am. Chem. Soc 2017, 139, 4306–4309. [PubMed: 28291336]

(475). Noth J; Esselborn J; Güldenhaupt J; Brünje A; Sawyer A; Apfel U-P; Gerwert K; Hofmann E; Winkler M; Happe T [FeFe]-Hydrogenase with Chalcogenide Substitutions at the H-Cluster Maintains Full H2 Evolution Activity. Angew. Chemie Int. Ed 2016, 55, 8396–8400.

(476). Kertess L; Wittkamp F; Sommer C; Esselborn J; Rüdiger O; Reijerse EJ; Hofmann E; Lubitz W; Winkler M; Happe T; et al. Chalcogenide Substitution in the [2Fe] Cluster of [FeFe]-Hydrogenases Conserves High Enzymatic Activity. Dalt. Trans 2017, 46, 16947–16958.

(477). Sommer C; Rumpel S; Roy S; Farès C; Artero V; Fontecave M; Reijerse E; Lubitz W Spectroscopic Investigations of a Semi-Synthetic [FeFe] Hydrogenase with Propane Di-Selenol as Bridging Ligand in the Binuclear Subsite: Comparison to the Wild Type and Propane Di-Thiol Variants. JBIC, J. Biol. Inorg. Chem 2018, 23, 481–491. [PubMed: 29627860]

(478). Sommer C; Richers CP; Lubitz W; Rauchfuss TB; Reijerse EJA [RuRu] Analogue of an [FeFe]-Hydrogenase Traps the Key Hydride Intermediate of the Catalytic Cycle. Angew. Chemie Int. Ed 2018, 57, 5429–5432.

(479). Duan J; Mebs S; Laun K; Wittkamp F; Heberle J; Hofmann E; Apfel U-P; Winkler M; Senger M; Haumann M; et al. Geometry of the Catalytic Active Site in [FeFe]-Hydrogenase Is Determined by Hydrogen Bonding and Proton Transfer. ACS Catal 2019, 9, 9140–9149.

(480). Esselborn J; Muraki N; Klein K; Engelbrecht V; Metzler-Nolte N; Apfel U-P; Hofmann E; Kurisu G; Happe T A Structural View of Synthetic Cofactor Integration into [FeFe]-Hydrogenases. Chem. Sci 2016, 7, 959–968. [PubMed: 29896366]

(481). Popescu C; Münck E Electronic Structure of the H Cluster in [FeFe]-Hydrogenases. J. Am. Chem. Soc 1999, 121 (34), 7877–7884.

(482). Pereira ASS; Tavares P; Moura I; Moura JJGJ; Huynh BHH Mössbauer Characterization of the Iron-Sulfur Clusters in Desulfovibrio v Ulgaris Hydrogenase. J. Am. Chem. Soc 2001, 123, 2771–2782. [PubMed: 11456963]

(483). Silakov A; Reijerse EJ; Albracht SPJ; Hatchikian EC; Lubitz W The Electronic Structure of the H-Cluster in the [FeFe]-Hydrogenase from Desulfovibrio Desulfuricans: A Q-Band 57Fe-ENDOR and HYSCORE Study. J. Am. Chem. Soc 2007, 129, 11447–11458. [PubMed: 17722921]

(484). Sidabras JW; Duan J; Winkler M; Happe T; Hussein R; Zouni A; Suter D; Schnegg A; Lubitz W; Reijerse EJ Extending Electron Paramagnetic Resonance to Nanoliter Volume Protein Single Crystals Using a Self-Resonant Microhelix. Sci. Adv 2019, 5, No. eaay1394. [PubMed: 31620561]

(485). De Lacey AL; Stadler C; Cavazza C; Hatchikian EC; Fernandez VM FTIR Characterization of the Active Site of the Fe-Hydrogenase from Desulfovibrio Desulfuricans. J. Am. Chem. Soc 2000, 122, 11232–11233.

(486). Chen Z; Lemon BJ; Huang S; Swartz DJ; Peters JW; Bagley KA Infrared Studies of the CO-Inhibited Form of the Fe-Only Hydrogenase from Clostridium Pasteurianum I: Examination of Its Light Sensitivity at Cryogenic Temperatures. Biochemistry 2002, 41, 2036–2043. [PubMed: 11827551]

(487). Roseboom W; De Lacey AL; Fernandez VM; Hatchikian EC; Albracht SPJ The Active Site of the [FeFe]-Hydrogenase from Desulfovibrio Desulfuricans. II. Redox Properties, Light Sensitivity and CO-Ligand Exchange as Observed by Infrared Spectroscopy. J. Biol. Inorg. Chem 2006, 11, 102–118. [PubMed: 16323019]

(488). Senger M; Mebs S; Duan J; Shulenina O; Laun K; Kertess L; Wittkamp F; Apfel U-P; Happe T; Winkler M; et al. Protonation/Reduction Dynamics at the [4Fe-4S] Cluster of the Hydrogen-Forming Cofactor in [FeFe]-Hydrogenases. Phys. Chem. Chem. Phys 2018, 20, 3128–3140. [PubMed: 28884175]

(489). Goldet G; Brandmayr C; Stripp ST; Happe T; Cavazza C; Fontecilla-Camps JC; Armstrong FA Electrochemical Kinetic Investigations of the Reactions of [FeFe]-Hydrogenases with Carbon Monoxide and Oxygen: Comparing the Importance of Gas Tunnels and Active-Site Electronic/Redox Effects. J. Am. Chem. Soc 2009, 131, 14979–14989. [PubMed: 19824734]

(490). Telser J; Benecky MJ; Adams MWW; Mortenson LE; Hoffman BM An EPR and Electron Nuclear Double Resonance Investigation of Carbon Monoxide Binding to Hydrogenase I (Bidirectional) from Clostridium Pasteurianum W5. J. Biol. Chem 1986, 261, 13536–13541. [PubMed: 3020036]

(491). Telser J; Benecky MJ; Adams MWW; Mortenson LE; Hoffman BM EPR and Electron Nuclear Double Resonance Investigation of Oxidized Hydrogenase II (Uptake) from Clostridium Pasteurianum W5. Effects of Carbon Monoxide Binding. J. Biol. Chem 1987, 262, 6589–6594. [PubMed: 3032973]

(492). Reijerse E; Birrell JA; Lubitz W Spin Polarization Reveals the Coordination Geometry of the [FeFe] Hydrogenase Active Site in Its CO-Inhibited State. J. Phys. Chem. Lett 2020, 11, 4597–4602. [PubMed: 32420744]

(493). Senger M; Mebs S; Duan J; Wittkamp F; Apfel U-P; Heberle J; Haumann M; Stripp ST Stepwise Isotope Editing of [FeFe]-Hydrogenases Exposes Cofactor Dynamics. Proc. Natl. Acad. Sci. U. S. A 2016, 113, 8454–8459. [PubMed: 27432985]

(494). Laun K; Mebs S; Duan J; Wittkamp F; Apfel U-P; Happe T; Winkler M; Haumann M; Stripp ST Spectroscopical Investigations on the Redox Chemistry of [FeFe]-Hydrogenases in the Presence of Carbon Monoxide. Molecules 2018, 23, 1669.

(495). Zilberman S; Stiefel EI; Cohen MH; Car R Resolving the CO/CN Ligand Arrangement in CO-Inactivated [FeFe] Hydrogenase by First Principles Density Functional Theory Calculations. Inorg. Chem 2006, 45, 5715–5717. [PubMed: 16841968]

(496). Greco C; Bruschi M; Heimdal J; Fantucci P; De Gioia L; Ryde U Structural Insights into the Active-Ready Form of [FeFe]-Hydrogenase and Mechanistic Details of Its Inhibition by Carbon Monoxide. Inorg. Chem 2007, 46, 7256–7258. [PubMed: 17676838]

(497). Yu L; Greco C; Bruschi M; Ryde U; De Gioia L; Reiher M Targeting Intermediates of [FeFe]-Hydrogenase by CO and CN Vibrational Signatures. Inorg. Chem 2011, 50, 3888–3900. [PubMed: 21443182]

(498). Sommer C; Adamska-Venkatesh A; Pawlak K; Birrell JA; Rüdiger O; Reijerse EJ; Lubitz W Proton Coupled Electronic Rearrangement within the H-Cluster as an Essential Step in the Catalytic Cycle of [FeFe] Hydrogenases. J. Am. Chem. Soc 2017, 139, 1440–1443. [PubMed: 28075576]

(499). Katz S; Noth J; Horch M; Shafaat HS; Happe T; Hildebrandt P; Zebger I Vibrational Spectroscopy Reveals the Initial Steps of Biological Hydrogen Evolution. Chem. Sci 2016, 7, 6746–6752. [PubMed: 28451119]

(500). Singleton ML; Bhuvanesh N; Reibenspies JH; Darensbourg MY Synthetic Support of De Novo Design: Sterically Bulky [FeFe]-Hydrogenase Models. Angew. Chemie Int. Ed 2008, 47, 9492–9495.

(501). Senger M; Laun K; Wittkamp F; Duan J; Haumann M; Happe T; Winkler M; Apfel U-P; Stripp ST Proton-Coupled Reduction of the Catalytic [4Fe-4S] Cluster in [FeFe]-Hydrogenases. Angew. Chemie Int. Ed 2017, 56, 16503–16506.

(502). Mebs S; Senger M; Duan J; Wittkamp F; Apfel U-P; Happe T; Winkler M; Stripp ST; Haumann M Bridging Hydride at Reduced H-Cluster Species in [FeFe]-Hydrogenases Revealed by Infrared Spectroscopy, Isotope Editing, and Quantum Chemistry. J. Am. Chem. Soc 2017, 139, 12157–12160. [PubMed: 28825810]

(503). Birrell JA; Pelmenschikov V; Mishra N; Wang H; Yoda Y; Rauchfuss TB; Cramer SP; Lubitz W; Debeer S; et al. Spectroscopic and Computational Evidence That [FeFe] Hydrogenases Operate Exclusively with CO-Bridged Intermediates. J. Am. Chem. Soc 2020, 142, 222–232. [PubMed: 31820961]

(504). Lorent C; Katz S; Duan J; Kulka CJ; Caserta G; Teutloff C; Yadav S; Apfel U-P; Winkler M; Happe T; et al. Shedding Light on Proton and Electron Dynamics in [FeFe] Hydrogenases. J. Am. Chem. Soc 2020, 142, 5493–5497. [PubMed: 32125830]

(505). Stripp ST; Mebs S; Haumann M Temperature Dependence of Structural Dynamics at the Catalytic Cofactor of [FeFe]-Hydrogenase. Inorg. Chem 2020, 59, 16474–16488. [PubMed: 33147959]

(506). Haumann M; Stripp ST The Molecular Proceedings of Biological Hydrogen Turnover. Acc. Chem. Res 2018, 51, 1755–1763. [PubMed: 30001117]

(507). Siegbahn PEM; Liao RZ Energetics for Proton Reduction in FeFe Hydrogenase. J. Phys. Chem. A 2020, 124, 10540–10549. [PubMed: 33275428]

(508). Kleinhaus JT; Wittkamp F; Yadav S; Siegmund D; Apfel U-P [FeFe]-Hydrogenases: Maturation and Reactivity of Enzymatic Systems and Overview of Biomimetic Models. Chem. Soc. Rev 2021, 50 (50), 1668–1784. [PubMed: 33305760]

(509). Birrell JA; Rodríguez-Maciá P; Reijerse EJ; Martini MA; Lubitz W The Catalytic Cycle of [FeFe] Hydrogenase: A Tale of Two Sites. Coord. Chem. Rev 2021, 449, 214191.

(510). Albracht SPJ; Roseboom W; Hatchikian EC The Active Site of the [FeFe]-Hydrogenase from Desulfovibrio Desulfuricans. I. Light Sensitivity and Magnetic Hyperfine Interactions as Observed by Electron Paramagnetic Resonance. J. Biol. Inorg. Chem 2006, 11, 88–101. [PubMed: 16323020]

(511). Adamska-Venkatesh A; Silakov A; Lambertz C; Rüdiger O; Happe T; Reijerse E; Lubitz W Identification and Characterization of the “Super-Reduced” State of the H-Cluster in [FeFe] Hydrogenase: A New Building Block for the Catalytic Cycle? Angew. Chemie Int. Ed 2012, 51, 11458–11462.

(512). Laun K; Baranova I; Duan J; Kertess L; Wittkamp F; Apfel U-P; Happe T; Senger M; Stripp ST Site-Selective Protonation of the One-Electron Reduced Cofactor in [FeFe]-Hydrogenase. Dalt. Trans 2021, 50, 3641–3650.

(513). Krasna AI; Rittenberg D The Mechanism of Action of the Enzyme Hydrogenase. J. Am. Chem. Soc 1954, 76, 3015–3020.

(514). Pelmenschikov V; Birrell JA; Pham CC; Mishra N; Wang H; Sommer C; Reijerse E; Richers CP; Tamasaku K; Yoda Y; et al. Reaction Coordinate Leading to H2 Production in [FeFe]-Hydrogenase Identified by Nuclear Resonance Vibrational Spectroscopy and Density Functional Theory. J. Am. Chem. Soc 2017, 139, 16894–16902. [PubMed: 29054130]

(515). Hajj V; Baffert C; Sybirna K; Meynial-Salles I; Soucaille P; Bottin H; Fourmond V; Léger C FeFe Hydrogenase Reductive Inactivation and Implication for Catalysis. Energy Environ. Sci 2014, 7, 715–719.

(516). Patil DS; Moura JJ; He SH; Teixeira M; Prickril BC; DerVartanian DV; Peck HD; LeGall J; Huynh BH EPR-Detectable Redox Centers of the Periplasmic Hydrogenase from Desulfovibrio Vulgaris. J. Biol. Chem 1988, 263, 18732–18738. [PubMed: 2848804]

(517). van der Spek TM; Arendsen AF; Happe RP; Yun S; Bagley KA; Stufkens DJ; Hagen WR; Albracht SPJ; Spek TM; Arendsen AF; et al. Similarities in the Architecture of the Active Sites of Ni-Hydrogenases and Fe-Hydrogenases Detected by Means of Infrared Spectroscopy. Eur. J. Biochem 1996, 237, 629–634. [PubMed: 8647106]

(518). van der Westen HM; Mayhew SG; Veeger C Separation of Hydrogenase from Intact Cells of Desulfovibrio Vulgaris Purification and Properties. FEBS Lett 1978, 86, 122–126. [PubMed: 620819]

(519). Rodríguez-Maciá P; Reijerse EJ; Van Gastel M; Debeer S; Lubitz W; Rüdiger O; Birrell JA Sulfide Protects [FeFe] Hydrogenases from O2. J. Am. Chem. Soc 2018, 140, 9346–9350. [PubMed: 30008217]

(520). Rodríguez-Maciá P; Galle LM; Bjornsson R; Lorent C; Zebger I; Yoda Y; Cramer SP; DeBeer S; Span I; Birrell JA Caught in the Hinact: Crystal Structure and Spectroscopy Reveal a Sulfur Bound to the Active Site of an O2-Stable State of [FeFe] Hydrogenase. Angew. Chem. Int. Ed 2020, 59, 16786–16794.

(521). Felbek C; Arrigoni F; de Sancho D; Jacq-Bailly A; Best RB; Fourmond V; Bertini L; Léger C Mechanism of Hydrogen Sulfide-Dependent Inhibition of FeFe Hydrogenase. ACS Catal 2021, 11, 15162–15176.

(522). Parkin A; Cavazza C; Fontecilla-Camps JC; Armstrong F. a. Electrochemical Investigations of the Interconversions between Catalytic and Inhibited States of the [FeFe]-Hydrogenase from Desulfovibrio Desulfuricans. J. Am. Chem. Soc 2006, 128, 16808–16815. [PubMed: 17177431]

(523). del Barrio M; Sensi M; Fradale L; Bruschi M; Greco C; de Gioia L; Bertini L; Fourmond V; Léger C Interaction of the H-Cluster of FeFe Hydrogenase with Halides. J. Am. Chem. Soc 2018, 140, 5485–5492. [PubMed: 29590528]

(524). Morra S; Arizzi M; Valetti F; Gilardi G Oxygen Stability in the New [FeFe]-Hydrogenase from Clostridium Beijerinckii SM10 (CbA5H). Biochemistry 2016, 55, 5897–5900. [PubMed: 27749036]

(525). Bruska MK; Stiebritz MT; Reiher M Regioselectivity of H-Cluster Oxidation. J. Am. Chem. Soc 2011, 133, 20588–20603. [PubMed: 22106822]

(526). Stiebritz MT; Reiher M Hydrogenases and Oxygen. Chem. Sci 2012, 3, 1739–1751.

(527). Finkelmann AR; Stiebritz MT; Reiher M Activation Barriers of Oxygen Transformation at the Active Site of [FeFe] Hydrogenases. Inorg. Chem 2014, 53, 11890–11902. [PubMed: 25345467]

(528). Kubas A; De Sancho D; Best RB; Blumberger J Aerobic Damage to [FeFe]-Hydrogenases: Activation Barriers for the Chemical Attachment of O2. Angew. Chem. Int. Ed 2014, 53, 4081–4084.

(529). Stripp ST; Goldet G; Brandmayr C; Sanganas O; Vincent KA; Haumann M; Armstrong FA; Happe T How Oxygen Attacks [FeFe] Hydrogenases from Photosynthetic Organisms. Proc. Natl. Acad. Sci. U. S. A 2009, 106, 17331–17336. [PubMed: 19805068]

(530). Lambertz C; Leidel N; Havelius KGV; Noth J; Chernev P; Winkler M; Happe T; Haumann M O2 Reactions at the Six-Iron Active Site (H-Cluster) in [FeFe]-Hydrogenase. J. Biol. Chem 2011, 286, 40614–40623. [PubMed: 21930709]

(531). Swanson KD; Ratzloff MW; Mulder DW; Artz JH; Ghose S; Hoffman A; White S; Zadvornyy OA; Broderick JB; Bothner B; et al. [FeFe]-Hydrogenase Oxygen Inactivation Is Initiated at the H Cluster 2Fe Subcluster. J. Am. Chem. Soc 2015, 137, 1809–1816. [PubMed: 25579778]

(532). Mebs S; Kositzki R; Duan J; Kertess L; Senger M; Wittkamp F; Apfel U-P; Happe T; Stripp ST; Winkler M; et al. Hydrogen and Oxygen Trapping at the H-Cluster of [FeFe]-Hydrogenase Revealed by Site-Selective Spectroscopy and QM/MM Calculations. BBA - Bioenerg 2018, 1859, 28–41.

(533). Esselborn J; Kertess L; Apfel U-P; Hofmann E; Happe T Loss of Specific Active-Site Iron Atoms in Oxygen-Exposed [FeFe]-Hydrogenase Determined by Detailed X-Ray Structure Analyses. J. Am. Chem. Soc 2019, 141, 17721–17728. [PubMed: 31609603]

(534). Kuchenreuther JM; Britt RD; Swartz JR New Insights into [FeFe] Hydrogenase Activation and Maturase Function. PLoS One 2012, 7, No. e45850. [PubMed: 23049878]

(535). Mulder DW; Ortillo DO; Gardenghi DJ; Naumov AV; Ruebush SS; Szilagyi RK; Huynh B; Broderick JB; Peters JW Activation of HydA(DeltaEFG) Requires a Preformed [4Fe-4S] Cluster. Biochemistry 2009, 48, 6240–6248. [PubMed: 19435321]

(536). Böck A; King PW; Blokesch M; Posewitz MC Maturation of Hydrogenases. Advances In Microbial Physiology 2006, 51, 1–71. [PubMed: 17091562]

(537). McGlynn SE; Shepard EM; Winslow MA; Naumov AV; Duschene KS; Posewitz MC; Broderick WE; Broderick JB; Peters JW HydF as a Scaffold Protein in [FeFe] Hydrogenase H-Cluster Biosynthesis. FEBS Lett 2008, 582, 2183–2187. [PubMed: 18501709]

(538). Caserta G; Pecqueur L; Adamska-Venkatesh A; Papini C; Roy S; Artero V; Atta M; Reijerse E; Lubitz W; Fontecave M Structural and Functional Characterization of the Hydrogenase-Maturation HydF Protein. Nat. Chem. Biol 2017, 13, 779–784. [PubMed: 28553946]

(539). Scott AG; Szilagyi RK; Mulder DW; Ratzloff MW; Byer AS; King PW; Broderick WE; Shepard EM; Broderick JB Compositional and Structural Insights into the Nature of the H-Cluster Precursor on HydF. Dalt. Trans 2018, 47, 9521–9535.

(540). Shepard EM; Duffus BR; George SJ; McGlynn SE; Challand MR; Swanson KD; Roach PL; Cramer SP; Peters JW; Broderick JB [FeFe]-Hydrogenase Maturation: HydG-Catalyzed Synthesis of Carbon Monoxide. J. Am. Chem. Soc 2010, 132, 9247–9249. [PubMed: 20565074]

(541). Driesener RC; Challand MR; McGlynn SE; Shepard EM; Boyd ES; Broderick JB; Peters JW; Roach PL [FeFe]-Hydrogenase Cyanide Ligands Derived from S-Adenosylmethionine-Dependent Cleavage of Tyrosine. Angew. Chemie Int. Ed 2010, 49, 1687–1690.

(542). Kuchenreuther JM; Myers WK; Suess DLM; Stich TA; Pelmenschikov V; Shiigi S. a; Cramer SP; Swartz JR; Britt RD; George SJ The HydG Enzyme Generates an Fe(CO)2(CN) Synthon in Assembly of the FeFe Hydrogenase H-Cluster. Science 2014, 343, 424–427. [PubMed: 24458644]

(543). Nicolet Y; Pagnier A; Zeppieri L; Martin L; Amara P; Fontecilla-Camps JC Crystal Structure of HydG from Carboxydothermus Hydrogenoformans: A Trifunctional [FeFe]-Hydrogenase Maturase. ChemBioChem 2015, 16, 397–402. [PubMed: 25504963]

(544). Rao G; Tao L; Suess DLM; Britt RD A [4Fe-4S]-Fe(CO)(CN)-l-Cysteine Intermediate Is the First Organometallic Precursor in [FeFe] Hydrogenase H-Cluster Bioassembly. Nat. Chem 2018, 10, 555–560. [PubMed: 29632334]

(545). Betz JN; Boswell NW; Fugate CJ; Holliday GL; Akiva E; Scott AG; Babbitt PC; Peters JW; Shepard EM; Broderick JB Hydrogenase Maturation: Insights into the Role Hyde Plays in Dithiomethylamine Biosynthesis. Biochemistry 2015, 54, 1807–1818. [PubMed: 25654171]

(546). Rohac R; Amara P; Benjdia A; Martin L; Ruffié P; Favier A; Berteau O; Mouesca JM; Fontecilla-Camps JC; Nicolet Y Carbon-Sulfur Bond-Forming Reaction Catalysed by the Radical SAM Enzyme HydE. Nat. Chem 2016, 8, 491–500. [PubMed: 27102684]

(547). Rao G; Tao L; Britt RD Serine Is the Molecular Source of the NH(CH2)2 Bridgehead Moiety of the in Vitro Assembled [FeFe] Hydrogenase H-Cluster Guodong. Chem. Sci 2020, 11, 1241–1247.

(548). Simmons TR; Berggren G; Bacchi M; Fontecave M; Artero V Mimicking Hydrogenases: From Biomimetics to Artificial Enzymes. Coord. Chem. Rev 2014, 270–271, 127–150.

(549). Artero V; Berggren G; Atta M; Caserta G; Roy S; Pecqueur L; Fontecave M From Enzyme Maturation to Synthetic Chemistry: The Case of Hydrogenases. Acc. Chem. Res 2015, 48, 2380–2387. [PubMed: 26165393]

(550). Peters JW Structure and Mechanism of Iron-Only Hydrogenases. Curr. Opin. Struct. Biol 1999, 9, 670–676. [PubMed: 10607666]

(551). Adamska-Venkatesh A; Simmons TR; Siebel JF; Artero V; Fontecave M; Reijerse E; Lubitz W Artificially Maturated [FeFe] Hydrogenase from Chlamydomonas Reinhardtii: A HYSCORE and ENDOR Study of a Non-Natural H-Cluster. Phys. Chem. Chem. Phys 2015, 17, 5421–5430. [PubMed: 25613229]

(552). Bruschi M; Greco C; Kaukonen M; Fantucci P; Ryde U; De Gioia L Influence of the [2Fe]H Subcluster Environment on the Properties of Key Intermediates in the Catalytic Cycle of [FeFe] Hydrogenases: Hints for the Rational Design of Synthetic Catalysts. Angew. Chemie Int. Ed 2009, 48, 3503–3506.

(553). Braga D; Grepioni F Hydrogen-Bonding Interactions with the CO Ligand in the Solid State. Acc. Chem. Res 1997, 30, 81–87.

(554). Artz JH; Zadvornyy OA; Mulder DW; Keable SM; Cohen AE; Ratzloff MW; Williams SG; Ginovska B; Kumar N; Song J; et al. Tuning Catalytic Bias of Hydrogen Gas Producing Hydrogenases. J. Am. Chem. Soc 2020, 142, 1227–1235. [PubMed: 31816235]

(555). Ratzloff MW; Artz JH; Mulder DW; Collins RT; Furtak TE; King PW CO-Bridged H-Cluster Intermediates in the Catalytic Mechanism of [FeFe]-Hydrogenase CaI. J. Am. Chem. Soc 2018, 140, 7623–7628. [PubMed: 29792026]

(556). Ginovska-Pangovska B; Dutta A; Reback ML; Linehan JC; Shaw WJ Beyond the Active Site: The Impact of the Outer Coordination Sphere on Electrocatalysts for Hydrogen Production and Oxidation. Acc. Chem. Res 2014, 47, 2621–2630. [PubMed: 24945095]

(557). Esmieu C; Raleiras P; Berggren G From Protein Engineering to Artificial Enzymes-Biological and Biomimetic Approaches towards Sustainable Hydrogen Production. Sustain. Energy Fuels 2018, 2, 724–750. [PubMed: 31497651]

(558). Amanullah S; Saha P; Nayek A; Ahmed ME; Dey A Biochemical and Artificial Pathways for the Reduction of Carbon Dioxide, Nitrite and the Competing Proton Reduction: Effect of 2nd sphere Interactions in Catalysis. Chem. Soc. Rev 2021, 50, 3755–3823. [PubMed: 33514959]

(559). Hong G; Cornish AJ; Hegg EL; Pachter R On Understanding Proton Transfer to the Biocatalytic [Fe-Fe](H) Sub-Cluster in [Fe-Fe]H(2)Ases: QM/MM MD Simulations. Biochim. Biophys. Acta 2011, 1807, 510–517. [PubMed: 21296047]

(560). Sode O; Voth GA Electron Transfer Activation of a Second Water Channel for Proton Transport in [FeFe]-Hydrogenase. J. Chem. Phys 2014, 141, 22D527.

(561). Ginovska-Pangovska B; Ho M-H; Linehan JC; Cheng Y; Dupuis M; Raugei S; Shaw WJ Molecular Dynamics Study of the Proposed Proton Transport Pathways in [FeFe]-Hydrogenase. Biochim. Biophys. Acta 2014, 1837, 131–138. [PubMed: 23981729]

(562). Long H; King PW; Chang CH Proton Transport in Clostridium Pasteurianum [FeFe] Hydrogenase I: A Computational Study. J. Phys. Chem. B 2014, 118, 890–900. [PubMed: 24405487]

(563). Cornish AJ; Gärtner K; Yang H; Peters JW; Hegg EL Mechanism of Proton Transfer in [FeFe]-Hydrogenase from Clostridium Pasteurianum. J. Biol. Chem 2011, 19, 38341–38347.

(564). Senger M; Eichmann V; Laun K; Duan J; Wittkamp F; Knör G; Apfel U-P; Happe T; Winkler M; Heberle J; et al. How [FeFe]-Hydrogenase Facilitates Bidirectional Proton Transfer. J. Am. Chem. Soc 2019, 141, 17394–17403. [PubMed: 31580662]

(565). Mebs S; Duan J; Wittkamp F; Stripp ST; Happe T; Apfel U-P; Winkler M; Haumann M Differential Protonation at the Catalytic Six-Iron Cofactor of [FeFe]-Hydrogenases Revealed by 57 Fe Nuclear Resonance X-Ray Scattering and Quantum Mechanics/Molecular Mechanics Analyses. Inorg. Chem 2019, 58, 4000–4013. [PubMed: 30802044]

(566). Gray HB; Winkler JR Long-Range Electron Transfer. Proc. Natl. Acad. Sci. U. S. A 2005, 102, 3534–3539. [PubMed: 15738403]

(567). Kaila VRI Long-Range Proton-Coupled Electron Transfer in Biological Energy Conversion: Towards Mechanistic Understanding of Respiratory Complex I. J. R. Soc. Interface 2018, 15, 20170916. [PubMed: 29643224]

(568). Rodríguez-Maciá P; Breuer N; DeBeer S; Birrell JA Insight into the Redox Behavior of the [4Fe-4S] Subcluster in [FeFe] Hydrogenases. ACS Catal 2020, 10, 13084–13095.

(569). Cohen J; Kim K; King P; Seibert M; Schulten K Finding Gas Diffusion Pathways in Proteins: Application to O2 and H2 Transport in CpI [FeFe]-Hydrogenase and the Role of Packing Defects. Structure 2005, 13, 1321–1329. [PubMed: 16154089]

(570). Mohammadi M; Vashisth H Pathways and Thermodynamics of Oxygen Diffusion in [FeFe]-Hydrogenase. J. Phys. Chem. B 2017, 121, 10007. [PubMed: 28975788]

(571). Liu Y; Mohammadi M; Vashisth H Diffusion Network of CO in FeFe-Hydrogenase. J. Chem. Phys 2018, 149, 204108. [PubMed: 30501239]

(572). Stapleton JA; Swartz JR A Cell-Free Microtiter Plate Screen for Improved [FeFe] Hydrogenases. PLoS One 2010, 5, No. e10554. [PubMed: 20479937]

(573). Stapleton JA; Swartz JR Development of an in Vitro Compartmentalization Screen for High-Throughput Directed Evolution of [FeFe] Hydrogenases. PLoS One 2010, 5, No. e15275 [PubMed: 21151915]

(574). Appel AM; Bercaw JE; Bocarsly AB; Dobbek H; Dubois DL; Dupuis M; Ferry JG; Fujita E; Hille R; Kenis PJA; et al. Frontiers, Opportunities, and Challenges in Biochemical and Chemical Catalysis of CO2 Fixation. Chem. Rev 2013, 113, 6621–6658. [PubMed: 23767781]

(575). Hartmann T; Schwanhold N; Leimkühler S Assembly and Catalysis of Molybdenum or Tungsten-Containing Formate Dehydrogenases from Bacteria. BBA - Proteins Proteomics 2015, 1854, 1090–1100. [PubMed: 25514355]

(576). Maia LB; Moura I; Moura JJG Carbon Dioxide UtilisationThe Formate Route. In Enzymes for Solving Humankind's Problems; Moura JJG, Moura I, Maia LB, Eds.; Springer Nature Switzerland: Cham, Switzerland, 2021; pp 29–81.

(577). Thauer RK; Jungermann K; Decker K Energy Conservation in Chemotrophic Anaerobic Bacteria. Bacteriol. Rev 1977, 41, 100–180. [PubMed: 860983]

(578). Nielsen CF; Lange L; Meyer AS Classification and Enzyme Kinetics of Formate Dehydrogenases for Biomanufacturing via CO2 Utilization. Biotechnol. Adv 2019, 37, 107408. [PubMed: 31200015]

(579). Popov VO; Lamzin VS NAD+-Dependent Formate Dehydrogenase. Biochem. J 1994, 301, 625–643. [PubMed: 8053888]

(580). Schirwitz K; Schmidt A; Lamzin VS High-Resolution Structures of Formate Dehydrogenase from Candida Boidinii. Protein Sci 2007, 16, 1146–1156. [PubMed: 17525463]

(581). Maia LB; Moura JJ; Moura I Molybdenum and Tungsten-Dependent Formate Dehydrogenases. J. Biol. Inorg. Chem 2015, 20, 287–309. [PubMed: 25476858]

(582). Niks D; Hille R Molybdenum- and Tungsten-Containing Formate Dehydrogenases and Formylmethanofuran Dehydrogenases: Structure, Mechanism, and Cofactor Insertion. Protein Sci 2019, 28, 111–122. [PubMed: 30120799]

(583). Hille R The Mononuclear Molybdenum Enzymes. Chem. Rev 1996, 96, 2757–2816. [PubMed: 11848841]

(584). Hille R; Hall J; Basu P The Mononuclear Molybdenum Enzymes. Chem. Rev 2014, 114, 3963–4038. [PubMed: 24467397]

(585). Axley MJ; Böck A; Stadtman TC Catalytic Properties of an Escherichia Coli Formate Dehydrogenase Mutant in Which Sulfur Replaces Selenium. Proc. Natl. Acad. Sci. U. S. A 1991, 88, 8450–8454. [PubMed: 1924303]

(586). Kletzin A; Adams MW Tungsten in Biological Systems. FEMS Microbiol. Rev 1996, 18, 5–63. [PubMed: 8672295]

(587). Johnson MK; Rees DC; Adams MW Tungstoenzymes. Chem. Rev 1996, 96, 2817–2840. [PubMed: 11848842]

(588). Brondino CD; Passeggi MC; Caldeira J; Almendra MJ; Feio MJ; Moura JJ; Moura I Incorporation of Either Molybdenum or Tungsten into Formate Dehydrogenase from Desulfovibrio Alaskensis NCIMB 13491; EPR Assignment of the Proximal Iron-Sulfur Cluster to the Pterin Cofactor in Formate Dehydrogenases from Sulfate-Reducing Bacteria. J. Biol. Inorg. Chem 2004, 9, 145–151. [PubMed: 14669076]

(589). Moura JJ; Brondino CD; Trincao J; Romao MJ Mo and W Bis-MGD Enzymes: Nitrate Reductases and Formate Dehydrogenases. J. Biol. Inorg. Chem 2004, 9, 791–799. [PubMed: 15311335]

(590). Almendra MJ; Brondino CD; Gavel O; Pereira AS; Tavares P; Bursakov S; Duarte R; Caldeira J; Moura JJG; Moura I Purification and Characterization of a Tungsten-Containing Formate Dehydrogenase from Desulfovibrio Gigas. Biochemistry 1999, 38, 16366–16372. [PubMed: 10587462]

(591). Radon C; Mittelstädt G; Duffus BR; Bürger J; Hartmann T; Mielke T; Teutloff C; Leimkühler S; Wendler P Cryo-EM Structures Reveal Intricate Fe-S Cluster Arrangement and Charging in Rhodobacter Capsulatus Formate Dehydrogenase. Nat. Commun 2020, 11, 1912. [PubMed: 32313256]

(592). Meneghello M; Oliveira AR; Jacq-Bailly A; Pereira IAC; Léger C; Fourmond V Formate Dehydrogenases Reduce CO2 Rather than HCO3-: An Electrochemical Demonstration. Angew. Chemie Int. Ed 2021, 60, 9964–9967.

(593). Meneghello M; Léger C; Fourmond V Electrochemical Studies of CO 2 -Reducing Metalloenzymes. Chem. - A Eur. J 2021, 27, 17542–17553.

(594). Axley MJ; Grahame DA Kinetics for Formate Dehydrogenase of Escherichia Coli Formate-Hydrogenlyase. J. Biol. Chem 1991, 266, 13731–13736. [PubMed: 1906883]

(595). da Silva SM; Pimentel C; Valente FMA; Rodrigues-Pousada C; Pereira IAC Tungsten and Molybdenum Regulation of Formate Dehydrogenase Expression in Desulfovibrio Vulgaris Hildenborough. J. Bacteriol 2011, 193, 2909–2916. [PubMed: 21498650]

(596). Hartmann T; Leimkühler S The Oxygen-Tolerant and NAD +-Dependent Formate Dehydrogenase from Rhodobacter Capsulatus Is Able to Catalyze the Reduction of CO2 to Formate. FEBS J 2013, 280, 6083–6096. [PubMed: 24034888]

(597). Schmitz RA; Richter M; Linder D; Thauer RK A Tungsten-Containing Active Formylmethanofuran Dehydrogenase in the Thermophilic Archaeon Methanobacterium Wolfei. Eur. J. Biochem 1992, 207, 559–565. [PubMed: 1633810]

(598). Hartmann T; Schrapers P; Utesch T; Nimtz M; Rippers Y; Dau H; Mroginski MA; Haumann M; Leimkühler S The Molybdenum Active Site of Formate Dehydrogenase Is Capable of Catalyzing C-H Bond Cleavage and Oxygen Atom Transfer Reactions. Biochemistry 2016, 55, 2381–2389. [PubMed: 27054466]

(599). Oliveira AR; Mota C; Mourato C; Domingos RM; Santos MFA; Gesto D; Guigliarelli B; Santos-Silva T; Romao MJ; Pereira IAC Toward the Mechanistic Understanding of Enzymatic CO2 Reduction. ACS Catal 2020, 10, 3844–3856.

(600). Plugge CM; Zhang W; Scholten JC; Stams AJ Metabolic Flexibility of Sulfate-Reducing Bacteria. Front. Microbiol 2011, 2, 81. [PubMed: 21734907]

(601). Stams AJ; Plugge CM Electron Transfer in Syntrophic Communities of Anaerobic Bacteria and Archaea. Nat. Rev. Microbiol 2009, 7, 568–577. [PubMed: 19609258]

(602). Rossmann R; Sawers G; Böck A Mechanism of Regulation of the Formate-Hydrogenlyase Pathway by Oxygen, Nitrate, and PH: Definition of the Formate Regulon. Mol. Microbiol 1991, 5, 2807–2814. [PubMed: 1779767]

(603). Lamont CM; Kelly CL; Pinske C; Buchanan G; Palmer T; Sargent F Expanding the Substrates for a Bacterial Hydrogenlyase Reaction. Microbiology 2017, 163, 649–653. [PubMed: 28488566]

(604). Finney AJ; Lowden R; Fleszar M; Albareda M; Coulthurst SJ; Sargent F The Plant Pathogen Pectobacterium Atrosepticum Contains a Functional Formate Hydrogenlyase-2 Complex. Mol. Microbiol 2019, 112, 1440–1452. [PubMed: 31420965]

(605). Ramio-Pujol S; Ganigue R; Baneras L; Colprim J Impact of Formate on the Growth and Productivity of Clostridium Ljungdahlii PETC and Clostridium Carboxidivorans P7 Grown on Syngas. Int. Microbiol 2014, 17, 195–204. [PubMed: 26421736]

(606). Sawers G; Suppmann B Anaerobic Induction of Pyruvate Formate-Lyase Gene Expression Is Mediated by the ArcA and FNR Proteins. J. Bacteriol 1992, 174, 3474–3478. [PubMed: 1592804]

(607). Sawers G The Hydrogenases and Formate Dehydrogenases of Escherichia Coli. Antonie Van Leeuwenhoek 1994, 66, 57–88. [PubMed: 7747941]

(608). Schwarz FM; Schuchmann K; Müller V Hydrogenation of CO2 at Ambient Pressure Catalyzed by a Highly Active Thermostable Biocatalyst. Biotechnol. Biofuels 2018, 11, 237. [PubMed: 30186365]

(609). Vorholt JA; Thauer RK Molybdenum and Tungsten Enzymes in C1 Metabolism. In Metals Ions in Biological System: Vol. 39: Molybdenum and Tungsten: Their Roles in Biological Processes; Sigel A, Sigel H, Eds.; CRC Press: Boca Raton, FL, 2002; Vol. 39, pp 571–619.

(610). Thauer RK Biochemistry of Methanogenesis: A Tribute to Marjory Stephenson:1998 Marjory Stephenson Prize Lecture. Microbiology 1998, 144, 2377–2406. [PubMed: 9782487]

(611). Börner G; Karrasch M; Thauer RK Formylmethanofuran Dehydrogenase-Activity in Cell-Extracts of Methanobacterium-Thermoautotrophicum and of Methanosarcina-Barkeri. Febs Lett 1989, 244, 21–25.

(612). Wagner T; Ermler U; Shima S The Methanogenic CO2 Reducing-and-Fixing Enzyme Is Bifunctional and Contains 46 [4Fe-4S] Clusters. Science 2016, 354, 114–117. [PubMed: 27846502]

(613). Welte C; Kröninger L; Deppenmeier U Experimental Evidence of an Acetate Transporter Protein and Characterization of Acetate Activation in Aceticlastic Methanogenesis of Methanosarcina Mazei. FEMS Microbiol. Lett 2014, 359, 147–153. [PubMed: 25088360]

(614). Kurth JM; Op den Camp HJM; Welte CU Several Ways One Goal—Methanogenesis from Unconventional Substrates. Appl. Microbiol. Biotechnol 2020, 104, 6839–6854. [PubMed: 32542472]

(615). Schmitz RA; Albracht SP; Thauer RK A Molybdenum and a Tungsten Isoenzyme of Formylmethanofuran Dehydrogenase in the Thermophilic Archaeon Methanobacterium Wolfei. Eur. J. Biochem 1992, 209, 1013–1018. [PubMed: 1330558]

(616). Schmitz RA; Albracht SPJ; Thauer RK Properties of the Tungsten-Substituted Molybdenum Formylmethanofuran Dehydrogenase from Methanobacterium Wolfei. Febs Lett 1992, 309, 78–81. [PubMed: 1324851]

(617). Bertram PA; Karrasch M; Schmitz RA; Bocher R; Albracht SPJ; Thauer RK Formylmethanofuran Dehydrogenases from Methanogenic Archaea: Substrate Specificity, EPR Properties and Reversible Inactivation by Cyanide of the Molybdenum or Tungsten Iron-Sulfur Proteins. Eur. J. Biochem 1994, 220, 477–484. [PubMed: 8125106]

(618). Bertram PA; Schmitz RA; Linder D; Thauer RK Tungstate Can Substitute for Molybdate in Sustaining Growth of Methanobacterium Thermoautotrophicum. Identification and Characterization of a Tungsten Isoenzyme of Formylmethanofuran Dehydrogenase. Arch. Microbiol 1994, 161, 220–228. [PubMed: 8161283]

(619). Schmitz RA; Bertram PA; Thauer RK Tungstate Does Not Support Synthesis of Active Formylmethanofuran Dehydrogenase in Methanosarcina Barkeri. Arch. Microbiol 1994, 161, 528–530.

(620). Hochheimer I; Schmitz RA; Thauer RK; Hedderich R The Tungsten Formylmethanofuran Dehydrogenase from Methanobacterium Thermoautotrophicum Contains Sequence Motifs Characteristic for Enzymes Containing Molybdopterin Dinucleotide. Eur. J. Biochem 1995, 234, 910–920. [PubMed: 8575452]

(621). Bertram PA; Thauer RK Thermodynamics of the Formylmethanofuran Dehydrogenase Reaction in Methanobacterium Thermoautotrophicum. Eur. J. Biochem 1994, 226, 811–818. [PubMed: 7813470]

(622). Hochheimer A; Hedderich R; Thauer RK The Formylmethanofuran Dehydrogenase Isoenzymes in Methanobacterium Wolfei and Methanobacterium Thermoautotrophicum: Induction of the Molybdenum Isoenzyme by Molybdate and Constitutive Synthesis of the Tungsten Isoenzyme. Arch. Microbiol 1998, 170, 389–393. [PubMed: 9818358]

(623). Hochheimer A; Linder D; Thauer RK; Hedderich R The Molybdenum Formylmethanofuran Dehydrogenase Operon and the Tungsten Formylmethanofuran Dehydrogenase Operon from Methanobacterium Thermoautotrophicum - Structures and Transcriptional Regulation. Eur. J. Biochem 1996, 242, 156–162. [PubMed: 8954165]

(624). Vorholt JA; Vaupel M; Thauer RK A Selenium-Dependent and a Selenium-Independent Formylmethanofuran Dehydrogenase and Their Transcriptional Regulation in the Hyperthermophilic Methanopyrus Kandleri. Mol. Microbiol 1997, 23, 1033–1042. [PubMed: 9076739]

(625). Börner G; Karrasch M; Thauer RK Molybdopterin Adenine Dinucleotide and Molybdopterin Hypoxanthine Dinucleotide in Formylmethanofuran Dehydrogenase from Methanobacterium Thermoautotrophicum (Marburg). FEBS Lett 1991, 290, 31–34. [PubMed: 1915887]

(626). Axley MJ; Grahame DA; Stadtman TC Escherichia Coli Formate-Hydrogen Lyase. Purification and Properties of the Selenium-Dependent Formate Dehydrogenase Component. J. Biol. Chem 1990, 265, 18213–18218. [PubMed: 2211698]

(627). Boyington JC; Gladyshev VN; Khangulov SV; Stadtman TC; Sun PD Crystal Structure of Formate Dehydrogenase H: Catalysis Involving Mo, Molybdopterin, Selenocysteine, and an Fe4S4 Cluster. Science 1997, 275, 1305–1308. [PubMed: 9036855]

(628). Gladyshev VN; Boyington JC; Khangulov SV; Grahame DA; Stadtman TC; Sun PD Characterization of Crystalline Formate Dehydrogenase H from Escherichia Coli. Stabilization, EPR Spectroscopy, and Preliminary Crystallographic Analysis. J. Biol. Chem 1996, 271, 8095–8100. [PubMed: 8626495]

(629). Gladyshev VN; Khangulov SV; Axley MJ; Stadtman TC Coordination of Selenium to Molybdenum in Formate Dehydrogenase H from Escherichia Coli. Proc. Natl. Acad. Sci. U. S. A 1994, 91, 7708–7711. [PubMed: 8052647]

(630). Enoch HG; Lester RL The Purification and Properties of Formate Dehydrogenase and Nitrate Reductase from Escherichia Coli. J. Biol. Chem 1975, 250, 6693–6705. [PubMed: 1099093]

(631). Oh JI; Bowien B Structural Analysis of the Fds Operon Encoding the NAD+-Linked Formate Dehydrogenase of Ralstonia Eutropha. J. Biol. Chem 1998, 273, 26349–26360. [PubMed: 9756865]

(632). Niks D; Duvvuru J; Escalona M; Hille R Spectroscopic and Kinetic Properties of the Molybdenum-Containing, NAD+-Dependent Formate Dehydrogenase from Ralstonia Eutropha. J. Biol. Chem 2016, 291, 1162–1174. [PubMed: 26553877]

(633). Riederer-Henderson MA; Peck HD In Vitro Requirements for Formate Dehydrogenase Activity from Desulfovibrio. Can. J. Microbiol 1986, 32, 425–429.

(634). Raaijmakers H; Macieira S; Dias JM; Teixeira S; Bursakov S; Huber R; Moura JJG; Moura I; Romao MJ Gene Sequence and the 1.8 A Crystal Structure of the Tungsten-Containing Formate Dehydrogenase from Desulfovibrio Gigas. Structure 2002, 10, 1261–1272. [PubMed: 12220497]

(635). Raaijmakers H; Teixeira S; Dias JM; Almendra MJ; Brondino CD; Moura I; Moura JJ; Romao MJ Tungsten-Containing Formate Dehydrogenase from Desulfovibrio Gigas: Metal Identification and Preliminary Structural Data by Multi-Wavelength Crystallography. J. Biol. Chem 2001, 6, 398–404.

(636). Riederer-Henderson MA; Peck HD Properties of Formate Dehydrogenase from Desulfovibrio Gigas. Can. J. Microbiol 1986, 32, 430–435.

(637). Laukel M; Chistoserdova L; Lidstrom ME; Vorholt JA The Tungsten-Containing Formate Dehydrogenase from Methylobacterium Extorquens AM1: Purification and Properties. Eur. J. Biochem 2003, 270, 325–333. [PubMed: 12605683]

(638). Duffus BR; Schrapers P; Schuth N; Mebs S; Dau H; Leimkühler S; Haumann M Anion Binding and Oxidative Modification at the Molybdenum Cofactor of Formate Dehydrogenase from Rhodobacter Capsulatus Studied by X-Ray Absorption Spectroscopy. Inorg. Chem 2020, 59, 214–225. [PubMed: 31814403]

(639). Schrapers P; Hartmann T; Kositzki R; Dau H; Reschke S; Schulzke C; Leimkühler S; Haumann M Sulfido and Cysteine Ligation Changes at the Molybdenum Cofactor during Substrate Conversion by Formate Dehydrogenase (FDH) from Rhodobacter Capsulatus. Inorg. Chem 2015, 54, 3260–3271. [PubMed: 25803130]

(640). Iobbi-Nivol C; Leimkühler S Molybdenum Enzymes, Their Maturation and Molybdenum Cofactor Biosynthesis in Escherichia Coli. Biochim. Biophys. Acta 2013, 1827, 1086–1101. [PubMed: 23201473]

(641). Abaibou H; Pommier J; Benoit S; Giordano G; Mandrand-Berthelot MA Expression and Characterization of the Escherichia Coli Fdo Locus and a Possible Physiological Role for Aerobic Formate Dehydrogenase. J. Bacteriol 1995, 177, 7141–7149. [PubMed: 8522521]

(642). Thomé R; Gust A; Toci R; Mendel R; Bittner F; Magalon A; Walburger A A Sulfurtransferase Is Essential for Activity of Formate Dehydrogenases in Escherichia Coli. J. Biol. Chem 2012, 287, 4671–4678. [PubMed: 22194618]

(643). Arnoux P; Ruppelt C; Oudouhou F; Lavergne J; Siponen MI; Toci R; Mendel RR; Bittner F; Pignol D; Magalon A; et al. Sulphur Shuttling across a Chaperone during Molybdenum Cofactor Maturation. Nat. Commun 2015, 6, 6148. [PubMed: 25649206]

(644). Böhmer N; Hartmann T; Leimkühler S The Chaperone FdsC for Rhodobacter Capsulatus Formate Dehydrogenase Binds the Bis-Molybdopterin Guanine Dinucleotide Cofactor. FEBS Lett 2014, 588, 531–537. [PubMed: 24444607]

(645). Schwanhold N; Iobbi-Nivol C; Lehmann A; Leimkühler S Same but Different: Comparison of Two System-Specific Molecular Chaperones for the Maturation of Formate Dehydrogenases. PLoS One 2018, 13, No. e0201935. [PubMed: 30444874]

(646). Raaijmakers HC; Romao MJ Formate-Reduced E. Coli Formate Dehydrogenase H: The Reinterpretation of the Crystal Structure Suggests a New Reaction Mechanism. J. Biol. Inorg. Chem 2006, 11, 849–854. [PubMed: 16830149]

(647). Khangulov SV; Gladyshev VN; Dismukes GC; Stadtman TC Selenium-Containing Formate Dehydrogenase H from Escherichia Coli: A Molybdopterin Enzyme That Catalyzes Formate Oxidation without Oxygen Transfer. Biochemistry 1998, 37, 3518–3528. [PubMed: 9521673]

(648). Rivas MG; Gonzalez PJ; Brondino CD; Moura JJ; Moura I EPR Characterization of the Molybdenum(V) Forms of Formate Dehydrogenase from Desulfovibrio Desulfuricans ATCC 27774 upon Formate Reduction. J. Inorg. Biochem 2007, 101, 1617–1622. [PubMed: 17574676]

(649). Barber MJ; Siegel LM; Schauer NL; May HD; Ferry JG Formate Dehydrogenase from Methanobacterium Formicicum: Electron Paramagnetic Resonance Spectroscopy of the Molybdenum and Iron-Sulfur Centers. J. Biol. Chem 1983, 258, 839–845.

(650). Barber MJ; May HD; Ferry JG Inactivation of Formate Dehydrogenase from Methanobacterium Formicicum by Cyanide. Biochemistry 1986, 25, 8150–8155.

(651). Malthouse JP; Gutteridge S; Bray RC Rapid Type 2 Molybdenum(V) Electron-Paramagnetic Resonance Signals from Xanthine Oxidase and the Structure of the Active Centre of the Enzyme. Biochem. J 1980, 185, 767–770. [PubMed: 6248034]

(652). Thauer RK; Fuchs G; Käufer B Reduced Ferredoxin: CO2 Oxidoreductase from Clostridium Pasteurianum. Effect of Ligands to Transition Metals on the Activity and the Stability of the Enzyme. Hoppe Seylers Zeitschrift für Physiol. Chemie 1975, 356, 653–662.

(653). Mota CS; Rivas MG; Brondino CD; Moura I; Moura JJ; Gonzalez PJ; Cerqueira NM The Mechanism of Formate Oxidation by Metal-Dependent Formate Dehydrogenases. J. Biol. Inorg. Chem 2011, 16, 1255–1268. [PubMed: 21773834]

(654). Pinsent J The Need for Selenite and Molybdate in the Formation of Formic Dehydrogenase by Members of the Coli-Aerogenes Group of Bacteria. Biochem. J 1954, 57, 10–16. [PubMed: 13159942]

(655). Zinoni F; Birkmann A; Leinfelder W; Böck A Cotranslational Insertion of Selenocysteine into Formate Dehydrogenase from Escherichia-Coli Directed by a Uga Codon. Proc. Natl. Acad. Sci. U. S. A 1987, 84, 3156–3160. [PubMed: 3033637]

(656). Reich HJ; Hondal RJ Why Nature Chose Selenium. ACS Chem. Biol 2016, 11, 821–841. [PubMed: 26949981]

(657). George GN; Colangelo CM; Dong J; Scott RA; Khangulov SV; Gladyshev VN; Stadtman TC X-Ray Absorption Spectroscopy of the Molybdenum Site of Escherichia Coli Formate Dehydrogenase. J. Am. Chem. Soc 1998, 120, 1267–1273.

(658). George GN; Costa C; Moura JG; Moura I Observation of Ligand-Based Redox Chemistry at the Active Site of a Molybdenum Enzyme. J. Am. Chem. Soc 1999, 121, 2625–2626.

(659). Heider J; Bock A Selenium Metabolism in Micro-Organisms. Adv. Microb. Physiol 1993, 35, 71–109. [PubMed: 8310883]

(660). Jormakka M; Törnroth S; Byrne B; Iwata S Molecular Basis of Proton Motive Force Generation: Structure of Formate Dehydrogenase-N. Science 2002, 295, 1863–1868. [PubMed: 11884747]

(661). Jollie DR; Lipscomb JD Formate Dehydrogenase from Methylosinus Trichosporium Ob3b: Purification and Spectroscopic Characterization of the Cofactors. J. Biol. Chem 1991, 266, 21853–21863. [PubMed: 1657982]

(662). Friedebold J; Bowien B Physiological and Biochemical Characterization of the Soluble Formate Dehydrogenase, a Molybdoenzyme from Alcaligenes Eutrophus. J. Bacteriol 1993, 175, 4719–4728. [PubMed: 8335630]

(663). Yamamoto I; Saiki T; Liu S-M; Ljungdahl LG Purification and Properties of NADP-Dependent Formate Dehydrogenase from Clostridium Thermoaceticum, a Tungsten-Selenium-Iron Protein. J. Biol. Chem 1983, 258, 1826–1832. [PubMed: 6822536]

(664). Schauer NL; Ferry JG Properties of Formate Dehydrogenase in Methanobacterium Formicicum. J. Bacteriol 1982, 150, 1–7. [PubMed: 7061389]

(665). Robinson WE; Bassegoda A; Reisner E; Hirst J Oxidation-State-Dependent Binding Properties of the Active Site in a Mo-Containing Formate Dehydrogenase. J. Am. Chem. Soc 2017, 139, 9927–9936. [PubMed: 28635274]

(666). Thauer RK; Käufer B; Fuchs G The Active Species of “CO2” Utilized by Reduced Ferredoxin: CO2 Oxidoreductase from Clostridium Pasteurianum. Eur. J. Biochem 1975, 55, 111–117. [PubMed: 240689]

(667). Cooper TG; Tchen TT; Wood HG; Benedict CR The Carboxylation of Phosphoenolpyruvate and Pyruvate. I. The Active Species of “CO2” Utilized by Phosphoenolpyruvate Carboxykinase, Carboxytransphosphorylase, and Pyruvate Carboxylase. J. Biol. Chem 1968, 243, 3857–3863. [PubMed: 5661712]

(668). Chan MK; Mukund S; Kletzin A; Adams MWW; Rees DC Structure of a Hyperthermophilic Tungstopterin Enzyme, Aldehyde Ferredoxin Oxidoreductase. Science 1995, 267, 1463–1469. [PubMed: 7878465]

(669). Tiberti M; Papaleo E; Russo N; De Gioia L; Zampella G Evidence for the Formation of a Mo - H Intermediate in the Catalytic Cycle of Formate Dehydrogenase. Inorg. Chem 2012, 51, 8331–8339. [PubMed: 22800191]

(670). Dong G; Ryde U Reaction Mechanism of Formate Dehydrogenase Studied by Computational Methods. J. Biol. Inorg. Chem 2018, 23, 1243–1254. [PubMed: 30173398]

(671). Niks D; Hille R Reductive Activation of CO2 by Formate Dehydrogenases. Methods Enzymol 2018, 613, 277–295. [PubMed: 30509470]

(672). Najmudin S; Gonzalez PJ; Trincao J; Coelho C; Mukhopadhyay A; Cerqueira NM; Romao CC; Moura I; Moura JJ; Brondino CD; et al. Periplasmic Nitrate Reductase Revisited: A Sulfur Atom Completes the Sixth Coordination of the Catalytic Molybdenum. J. Biol. Inorg. Chem 2008, 13, 737–753. [PubMed: 18327621]

(673). Hille R; Dingwall S; Wilcoxen J The Aerobic CO Dehydrogenase from Oligotropha Carboxidovorans. J. Biol. Inorg. Chem 2015, 20, 243–251. [PubMed: 25156151]

(674). Kaufmann P; Duffus BR; Teutloff C; Leimkühler S Functional Studies on Oligotropha Carboxidovorans Molybdenum-Copper CO Dehydrogenase Produced in Escherichia Coli. Biochemistry 2018, 57, 2889–2901. [PubMed: 29676148]

(675). Can M; Armstrong FA; Ragsdale SW Structure, Function, and Mechanism of the Nickel Metalloenzymes, CO Dehydrogenase, and Acetyl-CoA Synthase. Chem. Rev 2014, 114, 4149–4174. [PubMed: 24521136]

(676). Wu M; Ren Q; Durkin AS; Daugherty SC; Brinkac LM; Dodson RJ; Madupu R; Sullivan SA; Kolonay JF; Nelson WC; et al. Life in Hot Carbon Monoxide: The Complete Genome Sequence of Carboxydothermus Hydrogenoformans Z-2901. PLoS Genet 2005, 1, No. e65. [PubMed: 16311624]

(677). Wittenborn EC; Merrouch M; Ueda C; Fradale L; Léger C; Fourmond V; Pandelia M-E; Dementin S; Drennan CL Redox-Dependent Rearrangements of the NiFeS Cluster of Carbon Monoxide Dehydrogenase. Elife 2018, 7, No. e39451. [PubMed: 30277213]

(678). Ragsdale SW; Pierce E Acetogenesis and the Wood-Ljungdahl Pathway of CO2 Fixation. Biochim. Biophys. Acta - Proteins Proteomics 2008, 1784, 1873–1898.

(679). Gong W; Hao B; Wei Z; Ferguson DJ; Tallant T; Krzycki JA; Chan MK Structure of the A2ε2 Ni-Dependent CO Dehydrogenase Component of the Methanosarcina Barkeri Acetyl-CoA Decarbonylase/Synthase Complex. Proc. Natl. Acad. Sci. U. S. A 2008, 105, 9558–9563. [PubMed: 18621675]

(680). Doukov TI; Iverson TM; Seravalli J; Ragsdale SW; Drennan CL A Ni-Fe-Cu Center in a Bifunctional Carbon Monoxide Dehydrogenase/Acetyl-CoA Synthase. Science 2002, 298, 567–572. [PubMed: 12386327]

(681). Domnik L; Merrouch M; Goetzl S; Jeoung JH; Léger C; Dementin S; Fourmond V; Dobbek H CODH-IV: A High-Efficiency CO-Scavenging CO Dehydrogenase with Resistance to O2. Angew. Chem. Int. Ed 2017, 56, 15466–15469.

(682). Jeoung J-H; Dobbek H Carbon Dioxide Activation at the Ni,Fe-Cluster of Anaerobic Carbon Monoxide Dehydrogenase. Science 2007, 318, 1461–1464. [PubMed: 18048691]

(683). Inoue M; Nakamoto I; Omae K; Oguro T; Ogata H; Yoshida T; Sako Y Structural and Phylogenetic Diversity of Anaerobic Carbon-Monoxide Dehydrogenases. Front. Microbiol 2019, 9, 3353. [PubMed: 30705673]

(684). Kim EJ; Feng J; Bramlett MR; Lindahl PA Evidence for a Proton Transfer Network and a Required Persulfide-Bond-Forming Cysteine Residue in Ni-Containing Carbon Monoxide Dehydrogenases. Biochemistry 2004, 43, 5728–5734. [PubMed: 15134447]

(685). Wittenborn EC; Cohen SE; Merrouch M; Léger C; Fourmond V; Dementin S; Drennan CL Structural Insight into Metallocofactor Maturation in Carbon Monoxide Dehydrogenase. J. Biol. Chem 2019, 294, 13017–13026. [PubMed: 31296570]

(686). Merrouch M; Hadj-Saïd J; Domnik L; Dobbek H; Léger C; Dementin S; Fourmond V O2 Inhibition of Ni-Containing CO Dehydrogenase Is Partly Reversible. Chem. - A Eur. J 2015, 21, 18934–18938.

(687). Wittenborn EC; Guendon C; Merrouch M; Benvenuti M; Fourmond V; Léger C; Drennan CL; Dementin S The Solvent-Exposed Fe-S D-Cluster Contributes to Oxygen-Resistance in Desulfovibrio Vulgaris Ni-Fe Carbon Monoxide Dehydrogenase. ACS Catal 2020, 10, 7328–7335. [PubMed: 32655979]

(688). Inoue T; Takao K; Yoshida T; Wada K; Daifuku T; Yoneda Y; Fukuyama K; Sako Y Cysteine 295 Indirectly Affects Ni Coordination of Carbon Monoxide Dehydrogenase-II C-Cluster. Biochem. Biophys. Res. Commun 2013, 441, 13–17. [PubMed: 24120497]

(689). Jeon WB; Singer SW; Ludden PW; Rubio LM New Insights into the Mechanism of Nickel Insertion into Carbon Monoxide Dehydrogenase: Analysis of Rhodospirillum Rubrum Carbon Monoxide Dehydrogenase Variants with Substituted Ligands to the [Fe3S4] Portion of the Active-Site C-Cluster. J. Biol. Inorg. Chem 2005, 10, 903–912. [PubMed: 16283394]

(690). Fraser DM; Lindahl PA Evidence for a Proposed Intermediate Redox State in the CO/CO2 Active Site of Acetyl-CoA Synthase (Carbon Monoxide Dehydrogenase) from Clostridium Thermoaceticum. Biochemistry 1999, 38, 15706–15711. [PubMed: 10625436]

(691). Lindahl PA Implications of a Carboxylate-Bound C-Cluster Structure of Carbon Monoxide Dehydrogenase. Angew. Chem. Int. Ed 2008, 47, 4054–4056.

(692). Amara P; Mouesca J-M; Volbeda A; Fontecilla-Camps JC Carbon Monoxide Dehydrogenase Reaction Mechanism: A Likely Case of Abnormal CO 2 Insertion to a Ni-H - Bond. Inorg. Chem 2011, 50, 1868–1878. [PubMed: 21247090]

(693). Yang JY; Kerr TA; Wang XS; Barlow JM Reducing CO2 to HCO2- at Mild Potentials: Lessons from Formate Dehydrogenase. J. Am. Chem. Soc 2020, 142, 19438–19445. [PubMed: 33141560]

(694). Breglia R; Arrigoni F; Sensi M; Greco C; Fantucci P; De Gioia L; Bruschi M First-Principles Calculations on Ni,Fe-Containing Carbon Monoxide Dehydrogenases Reveal Key Stereoelectronic Features for Binding and Release of CO2to/from the C-Cluster. Inorg. Chem 2021, 60, 387–402. [PubMed: 33321036]

(695). Maynard EL; Lindahl PA Evidence of a Molecular Tunnel Connecting the Active Sites for CO2 Reduction and Acetyl-CoA Synthesis in Acetyl-CoA Synthase from Clostridium Thermoaceticum. J. Am. Chem. Soc 1999, 121, 9221–9222.

(696). Seravalli J; Ragsdale SW Channeling of Carbon Monoxide during Anaerobic Carbon Dioxide Fixation. Biochemistry 2000, 39, 1274–1277. [PubMed: 10684606]

(697). Darnault C; Volbeda A; Kim EJ; Legrand P; Vernède X; Lindahl PA; Fontecilla-Camps JC Ni-Zn-[Fe4-S4] and Ni-Ni-[Fe4-S4] Clusters in Closed and Open α Subunits of Acetyl-CoA Synthase/Carbon Monoxide Dehydrogenase. Nat. Struct. Biol 2003, 10, 271–279. [PubMed: 12627225]

(698). Doukov TI; Blasiak LC; Seravalli J; Ragsdale SW; Drennan CL Xenon in and at the End of the Tunnel of Bifunctional Carbon Monoxide Dehydrogenase/Acetyl-CoA Synthase. Biochemistry 2008, 47, 3474–3483. [PubMed: 18293927]

(699). Volbeda A; Fontecilla-Camps JC Crystallographic Evidence for a CO/CO2 Tunnel Gating Mechanism in the Bifunctional Carbon Monoxide Dehydrogenase/Acetyl Coenzyme A Synthase from Moorella Thermoacetica. J. Biol. Inorg. Chem 2004, 9, 525–532. [PubMed: 15221479]

(700). Tan X; Loke HK; Fitch S; Lindahl PA The Tunnel of Acetyl-Coenzyme A Synthase/Carbon Monoxide Dehydrogenase Regulates Delivery of CO to the Active Site. J. Am. Chem. Soc 2005, 127, 5833–5839. [PubMed: 15839681]

(701). Tan X; Lindahl PA Tunnel Mutagenesis and Ni-Dependent Reduction and Methylation of the α Subunit of Acetyl Coenzyme A Synthase/Carbon Monoxide Dehydrogenase. J. Biol. Inorg. Chem 2008, 13, 771–778. [PubMed: 18365259]

(702). Biester A; Dementin S; Drennan CL Visualizing the Gas Channel of a Monofunctional Carbon Monoxide Dehydrogenase. J. Inorg. Biochem 2022, 230, 111774. [PubMed: 35278753]

(703). Tan X; Volbeda A; Fontecilla-Camps JC; Lindahl PA Function of the Tunnel in Acetylcoenzyme A Synthase/Carbon Monoxide Dehydrogenase. J. Biol. Inorg. Chem 2006, 11, 371–378. [PubMed: 16502006]

(704). Wang PH; Bruschi M; De Gioia L; Blumberger J Uncovering a Dynamically Formed Substrate Access Tunnel in Carbon Monoxide Dehydrogenase/Acetyl-CoA Synthase. J. Am. Chem. Soc 2013, 135, 9493–9502. [PubMed: 23713976]

(705). Dobbek H; Svetlitchnyi V; Gremer L; Huber R; Meyer O Crystal Structure of a Carbon Monoxide Dehydrogenase Reveals a [Ni-4Fe-5S] Cluster. Science 2001, 293, 1281–1285. [PubMed: 11509720]

(706). Drennan CL; Heo J; Sintchak MD; Schreiter E; Ludden PW Life on Carbon Monoxide: X-Ray Structure of Rhodospirillum Rubrum Ni-Fe-S Carbon Monoxide Dehydrogenase. Proc. Natl. Acad. Sci. U. S. A 2001, 98, 11973–11978. [PubMed: 11593006]

(707). Ensign SA; Hyman MR; Ludden PW Nickel-Specific, Slow-Binding Inhibition of Carbon Monoxide Dehydrogenase from Rhodospirillum Rubrum by Cyanide. Biochemistry 1989, 28, 4973–4979. [PubMed: 2504285]

(708). Hadj-Saïd J; Pandelia ME; Léger C; Fourmond V; Dementin S The Carbon Monoxide Dehydrogenase from Desulfovibrio Vulgaris. Biochim. Biophys. Acta - Bioenerg 2015, 1847, 1574–1583.

(709). Benvenuti M; Meneghello M; Guendon C; Jacq-Bailly A; Jeoung J-H; Dobbek H; Léger C; Fourmond V; Dementin S The Two CO-Dehydrogenases of Thermococcus Sp. AM4. Biochim. Biophys. Acta - Bioenerg 2020, 1861, 148188. [PubMed: 32209322]

(710). Parkin A; Seravalli J; Vincent KA; Ragsdale SW; Armstrong FA Rapid and Efficient Electrocatalytic CO2/CO Interconversions by Carboxydothermus Hydrogenoformans CO Dehydrogenase I on an Electrode. J. Am. Chem. Soc 2007, 129, 10328–10329. [PubMed: 17672466]

(711). Ensign SA Reactivity of Carbon Monoxide Dehydrogenase from Rhodospirillum Rubrum with Carbon Dioxide, Carbonyl Sulfide, and Carbon Disulfide. Biochemistry 1995, 34, 5372–5381. [PubMed: 7727395]

(712). Bonam D; Murrell SA; Ludden PW Carbon Monoxide Dehydrogenase from Rhodospirillum Rubrum. J. Bacteriol 1984, 159, 693–699. [PubMed: 6430875]

(713). Snider MG; Temple BS; Wolfenden R The Path to the Transition State in Enzyme Reactions: A Survey of Catalytic Efficiencies. J. Phys. Org. Chem 2004, 17, 586–591.

(714). Prangé T; Schiltz M; Pernot L; Colloc'h N; Longhi S; Bourguet W; Fourme R Exploring Hydrophobic Sites in Proteins With Xenon or Krypton. Proteins Struct. Funct. Genet 1998, 30, 61–73. [PubMed: 9443341]

(715). Richards FM Areas, Volumes, Packing and Protein Structure. Annu. Rev. Biophys. Bioeng 1977, 6, 151–176 June. [PubMed: 326146]

(716). Plumeré N; Rüdiger O; Oughli AA; Williams R; Vivekananthan J; Pöller S; Schuhmann W; Lubitz W A Redox Hydrogel Protects Hydrogenase from High-Potential Deactivation and Oxygen Damage. Nat. Chem 2014, 6, 822–827. [PubMed: 25143219]

(717). Li H; Buesen D; Dementin S; Léger C; Fourmond V; Plumeré N Complete Protection of O2-Sensitive Catalysts in Thin Films. J. Am. Chem. Soc 2019, 141, 16734–16742. [PubMed: 31525046]

(718). Hardt S; Stapf S; Filmon DT; Birrell JA; Rüdiger O; Fourmond V; Léger C; Plumeré N Reversible H2 Oxidation and Evolution by Hydrogenase Embedded in a Redox Polymer Film. Nat. Catal 2021, 4, 251–258. [PubMed: 33842839]

(719). Wraight CA Chance and Design-Proton Transfer in Water, Channels and Bioenergetic Proteins. Biochim. Biophys. Acta - Bioenerg 2006, 1757, 886–912.

(720). Gray HB; Winkler JR Electron Tunneling through Proteins. Q. Rev. Biophys 2003, 36, 341–372. [PubMed: 15029828]

(721). Feng X; Schut GJ; Haja DK; Adams MWW; Li H Structure and Electron Transfer Pathways of an Electron-Bifurcating NiFe-Hydrogenase. Sci. Adv 2022, 8, 1–14.

(722). Oughli AA; Ruff A; Boralugodage NP; Rodríguez-Maciá P; Plumeré N; Lubitz W; Shaw WJ; Schuhmann W; Rüdiger O Dual Properties of a Hydrogen Oxidation Ni-Catalyst Entrapped within a Polymer Promote Self-Defense against Oxygen. Nat. Commun 2018, 9, 864. [PubMed: 29491416]

(723). Lee CC; Kang W; Jasniewski AJ; Stiebritz MT; Tanifuji K; Ribbe MW; Hu Y Evidence of Substrate Binding and Product Release via Belt-Sulfur Mobilization of the Nitrogenase Cofactor. Nat. Catal 2022, 5, 443–454.

(724). Zuchan K; Baymann F; Baffert C; Brugna M; Nitschke W The dyad of the Y-junction- and a flavin module unites diverse redox enzymes. Biochimica et Biophysica Acta (BBA) - Bioenergetics 2021, 1862 (6), 148401. [PubMed: 33684340]

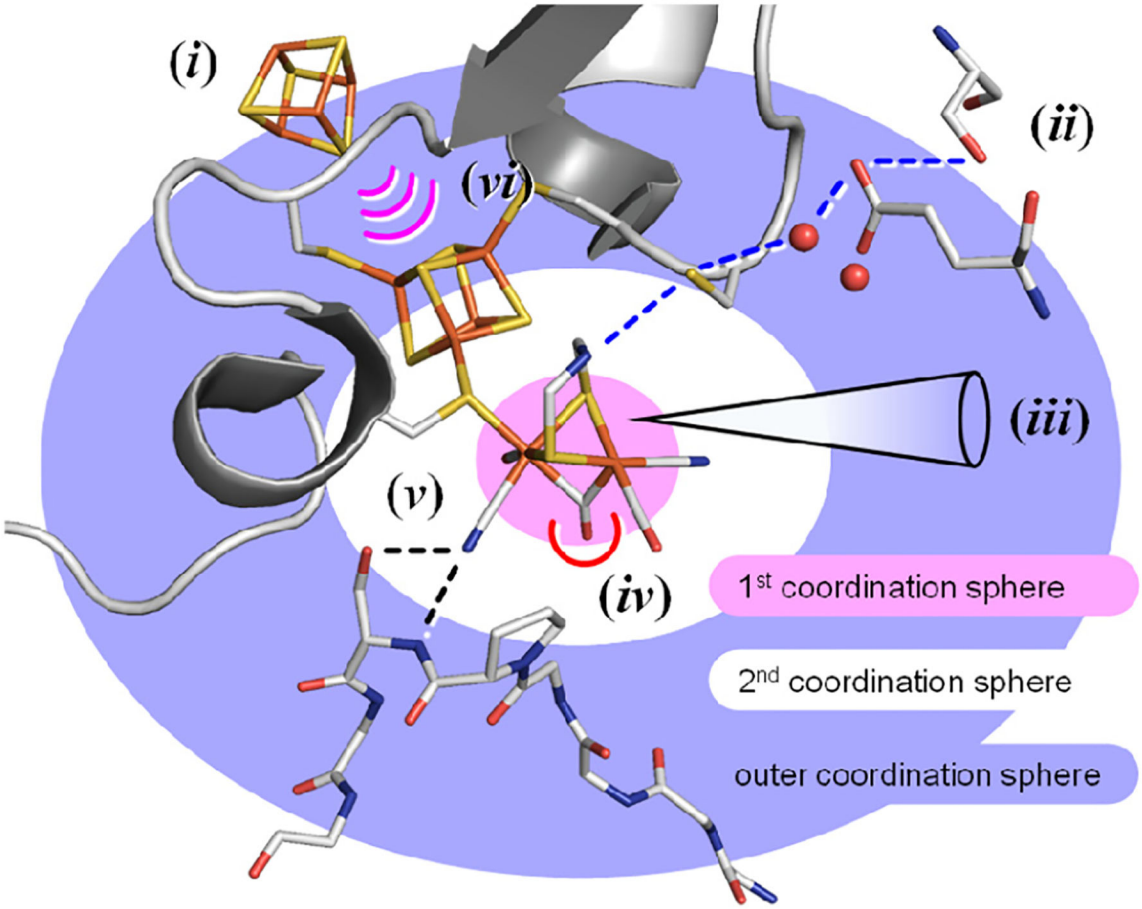

Figure 1.

Definitions. The figure shows the active site of [FeFe]-hydrogenase (PDB ID 4XDC). For this enzyme, the first coordination sphere (light magenta) is defined by the two iron ions of the catalytic cofactor and its ligands. The second coordination sphere (white) comprises a [4Fe-4S] cluster as well as (*iv*) hydrophobic interactions and (*v*) hydrogen-bonding contacts with the protein fold. Outer coordination sphere effects include (*i*) electron transfer, (*ii*) proton transfer, (*iii*) hydrophobic gas channels, and (*vi*) electric field effects.

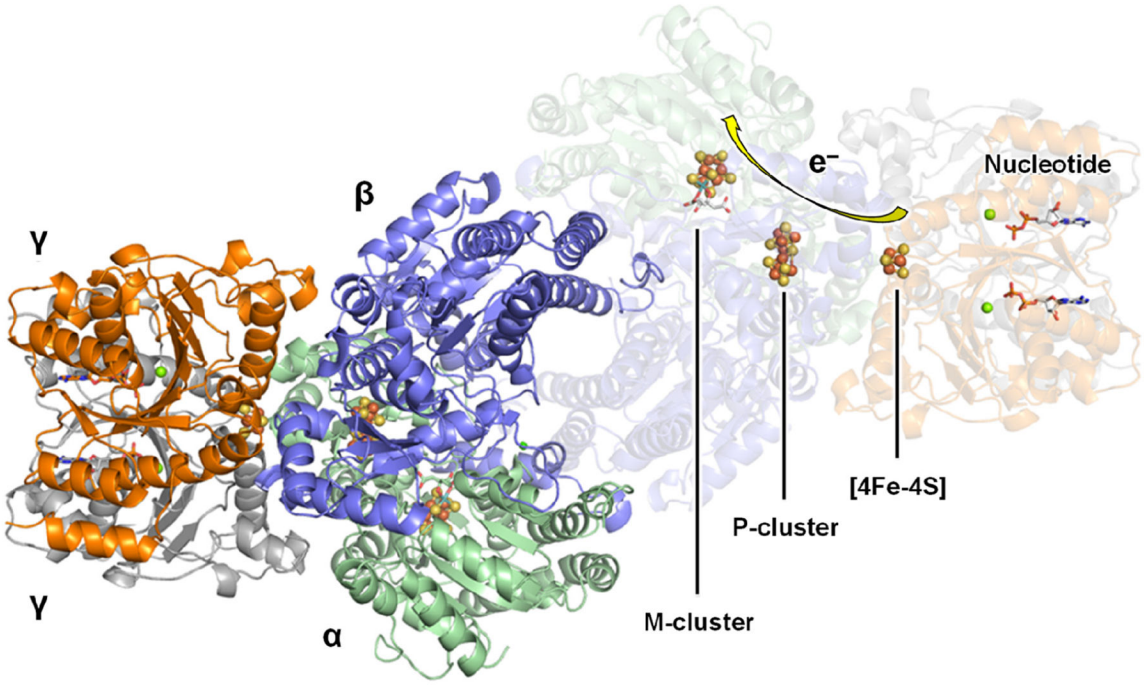

Figure 2.

Crystal structure of the NifH:NifDK complex (PDB ID 1N2C). The relevant metalloclusters are highlighted and the proposed direction of electron flow through the enzyme is depicted as a yellow arrow. The coloring scheme is as follows: NifD (green cartoon), NifK (blue cartoon), NifH (orange and gray cartoon), Fe, orange; S, yellow; C, gray. Reprinted (adapted or reprinted in part) with permission from ref 50. Copyright 2020 American Chemical Society.

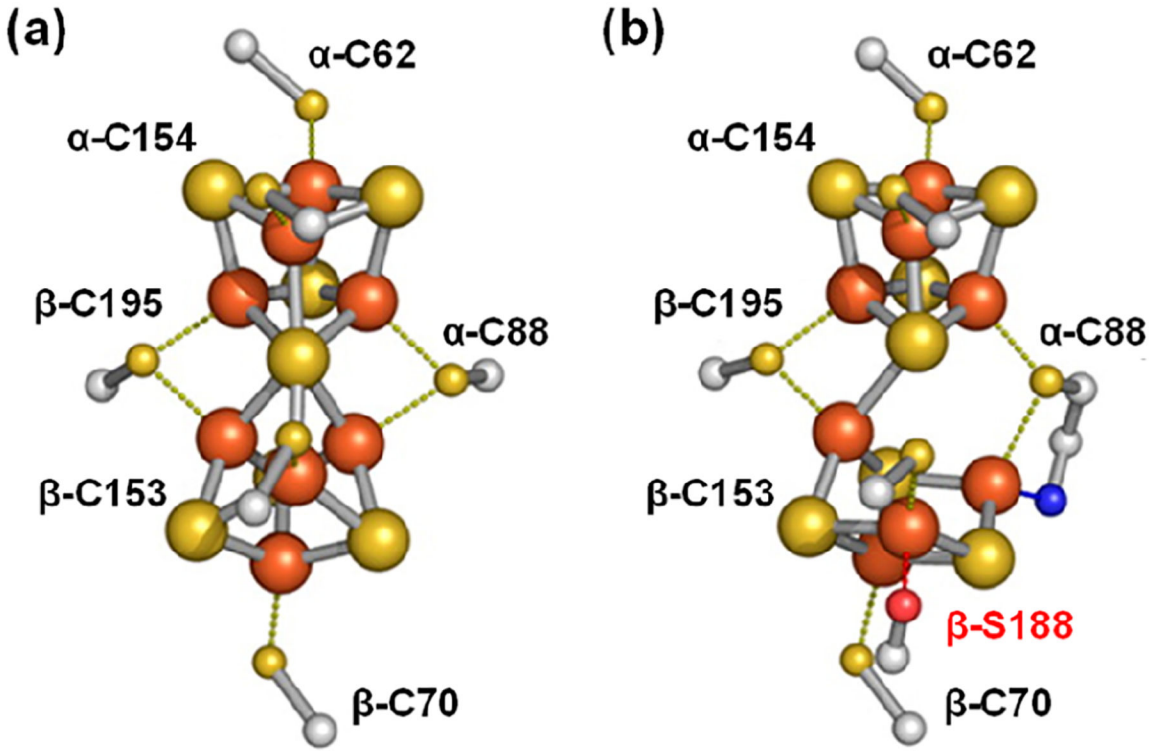

Figure 3.

Structure of the P-cluster. (a) Dithionite-reduced state (P^N, PDB ID 3U7Q) and (b) indigo disulfonate-oxidized state (P^{OX}, PDB ID 3MIN). Atomic coloring: Fe, orange; S, yellow; C, gray; N, blue. Reprinted (adapted or reprinted in part) with permission from ref 84. Copyright 2014 American Chemical Society.

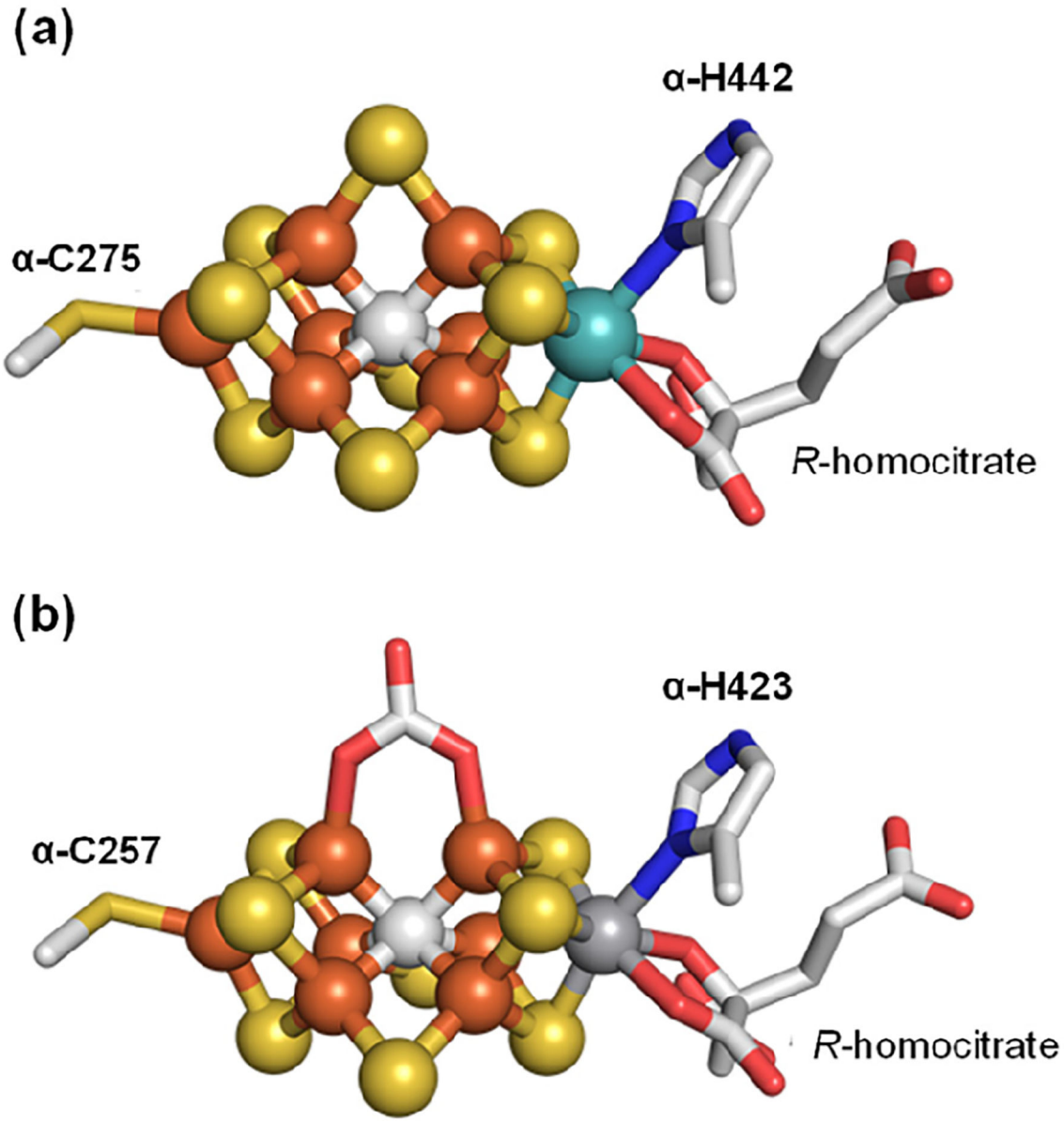

Figure 4.

Catalytic cofactors from the crystal structures of (a) NifDK and (b) VnfDGK. The atoms of the clusters are shown as ball-and-stick models with the amino acid residues, *R*-homocitrate and carbonate presented as sticks. Atomic coloring: Fe, orange; S, yellow; Mo, teal; V, dark gray; C, light gray; N, blue; O, red (PDB ID 3U7Q, NifDK; 5N6Y, VnfDGK).

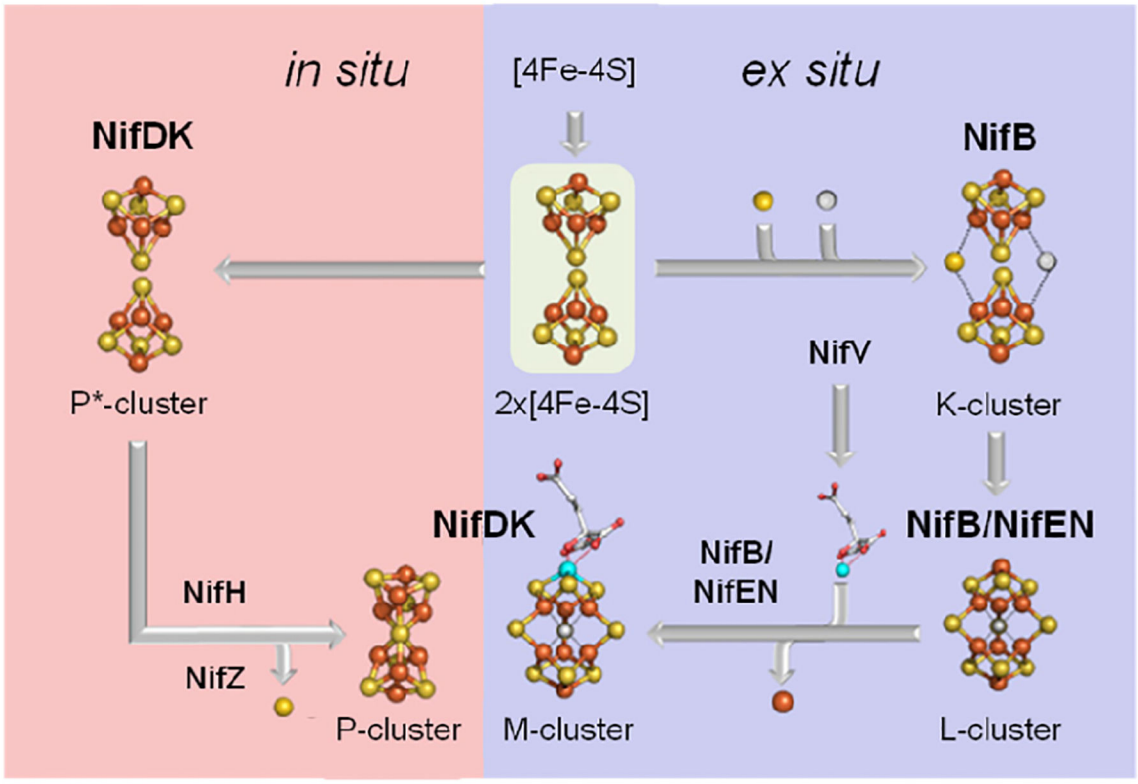

Figure 5.

Biosynthetic diagram for the assembly of nitrogenase metalloclusters. The red portion represents the *in situ* pathway for the synthesis of the P-cluster on NifDK. The blue portion reflects the *ex situ* synthesis of the M-cluster. Proteins and cluster species are labeled accordingly. Atoms are represented as ball-and-stick models and with atomic coloring as follows: Fe, orange; S, yellow; C, gray; O, red; Mo, teal. Reprinted (adapted or reprinted in part) with permission from ref 51. Copyright 2020 American Chemical Society.

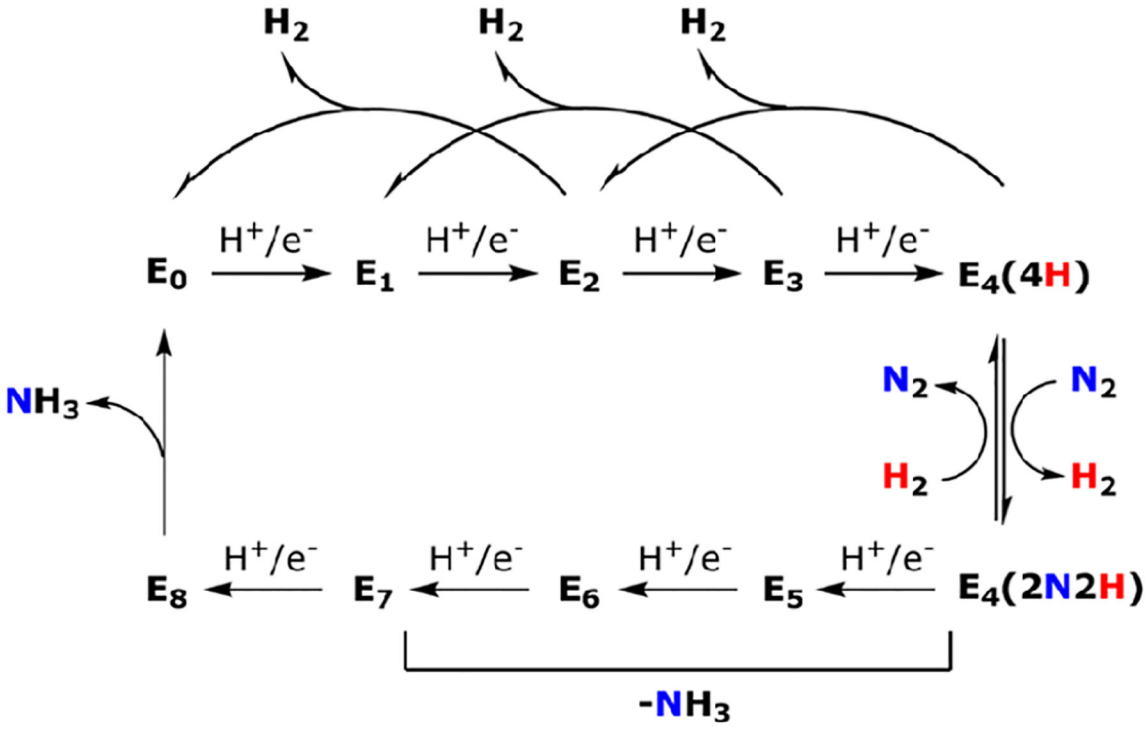

Figure 6.

Modified Lowe-Thorneley model for N_2 reduction by Mo-dependent nitrogenase. The E_n labeling indicates *n* number of proton and electron pairs that have been loaded on one of the $\alpha\beta$-dimers of NifDK. Reprinted (adapted or reprinted in part) with permission from ref 51. Copyright 2020 American Chemical Society.

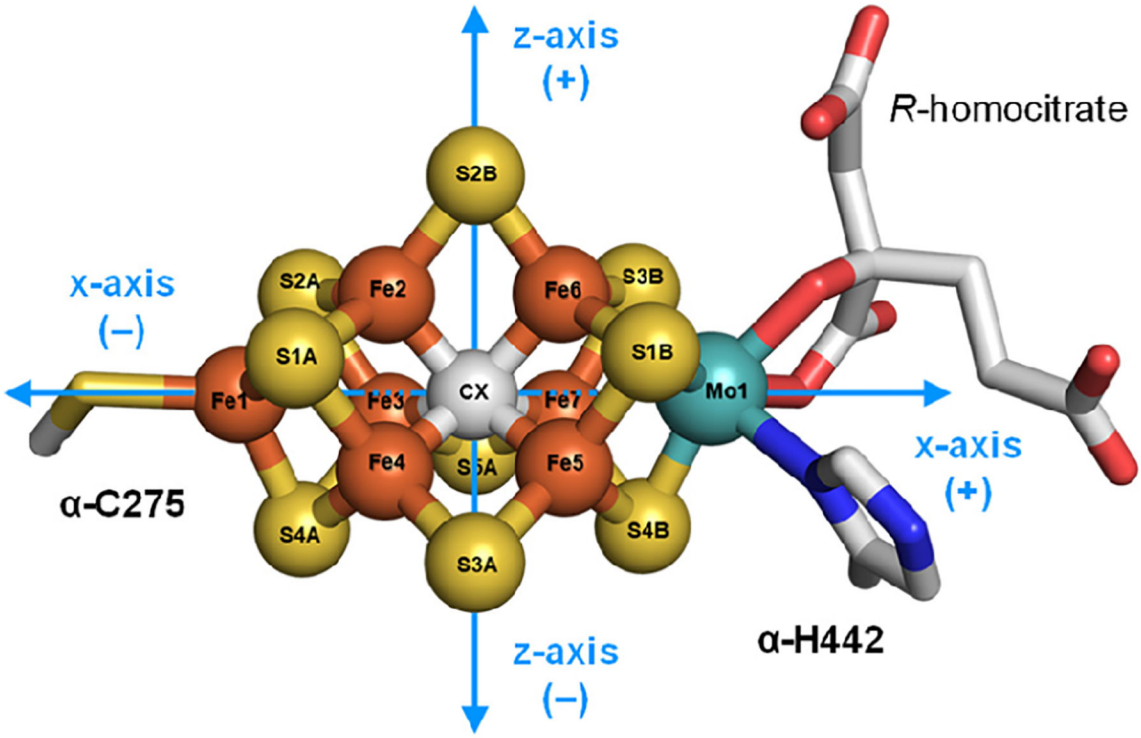

Figure 7.

A relative coordinate system is (blue arrows) overlaid with the crystal structure of M-cluster. The coordinate system assumes CX as the origin (0, 0, 0), the *x*-axis passes through Fe1, CX and Mo1 with positive values toward Mo1, the *y*-axis passes through CX into the page with positive values pointing out of the page, and the *z*-axis passes through S2B and CX with positive values toward S2B. The cluster is presented as a ball-and-stick model with atomic coloring: Fe, orange; S, yellow; C, gray; O, red; N, blue.

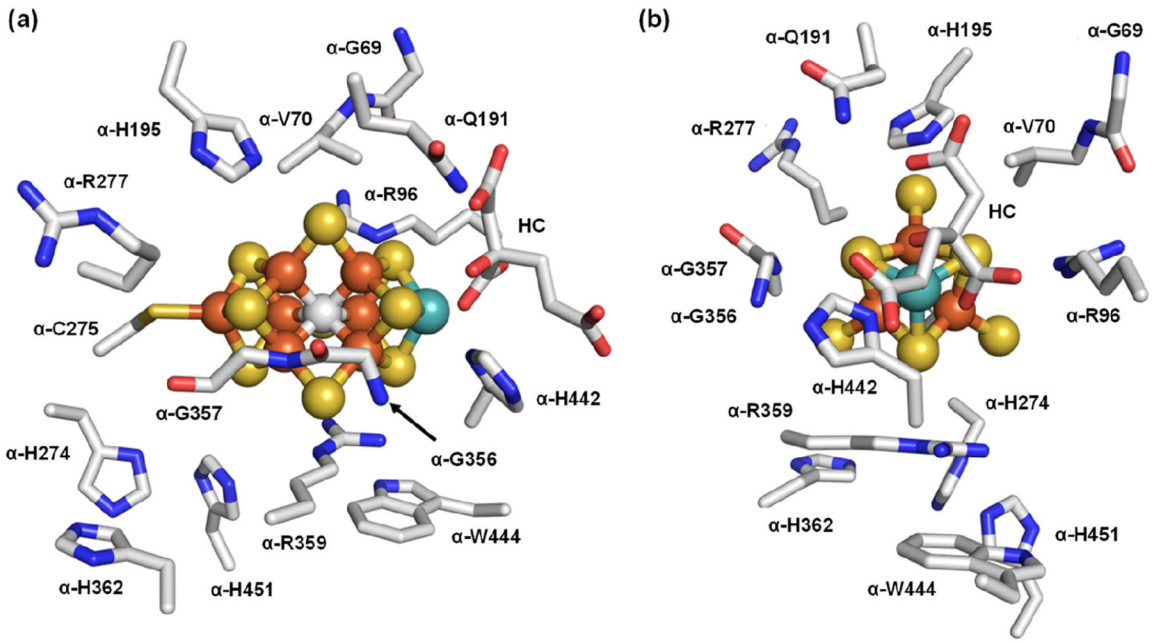

Figure 8.

Display of amino acid residues targeted for mutagenesis within the active site M-cluster of NifDK from *A. vinelandii*. (a) Side view and (b) view along the Mo-C-Fe1 axis of the M-cluster site are shown (PDB ID 3U7Q). The cluster is presented as a ball-and-stick model while the homocitrate ligand (HC) and amino acid side chains are shown as sticks. Atomic coloring: Fe, orange; S, yellow; C, gray; O, red; N, blue.

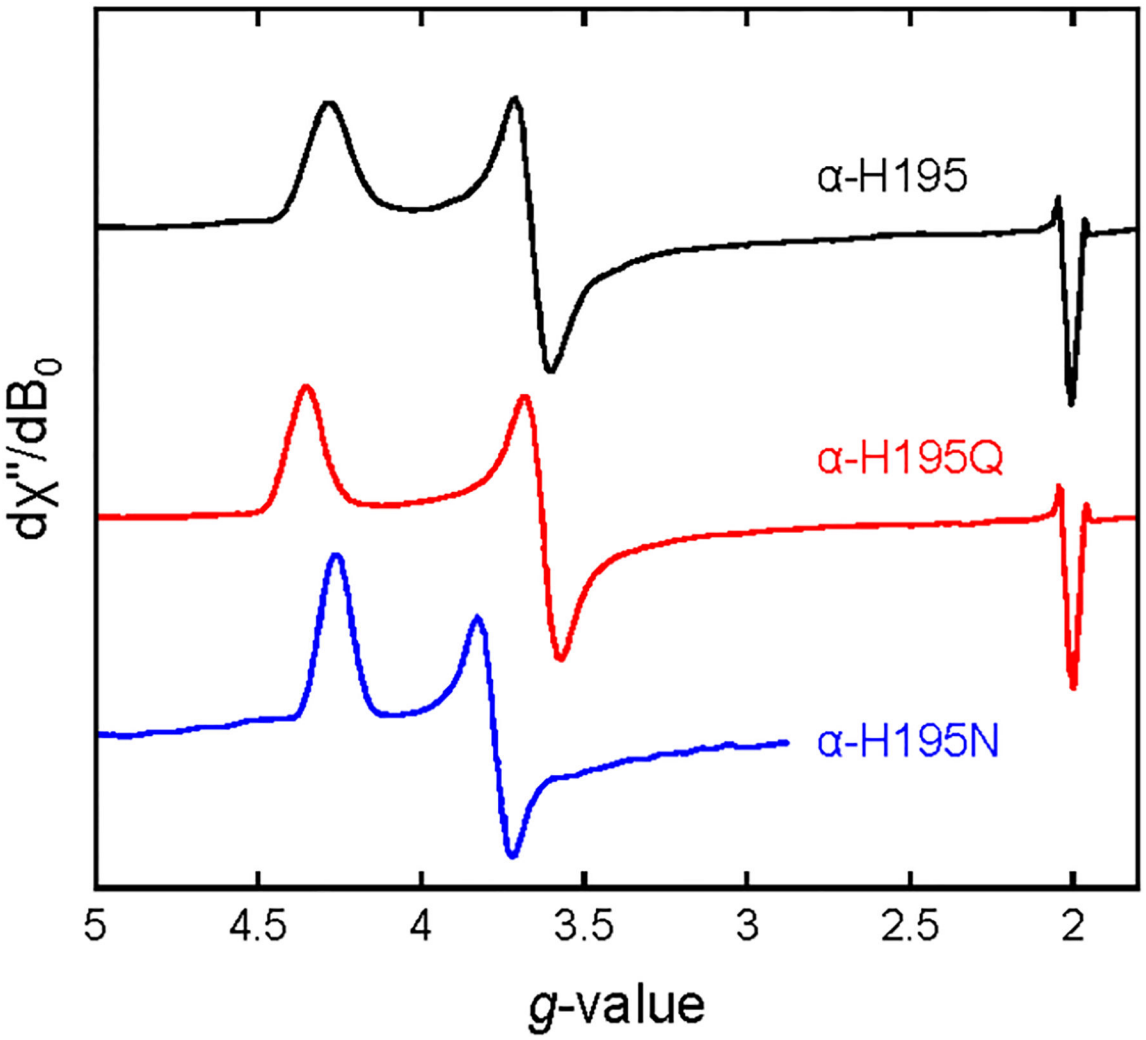

Figure 9.

EPR characterization of the M-cluster. The figure depicts wild-type (black), α-H195Q (red), and α-H195N (blue) NifDK proteins from *A. vinelandii*. The $g \approx 2$ region is not shown for α-H195N due to contamination. Adapted with permission from ref 153. Copyright 1995 American Chemical Society. Data digitalized via WebPlotDigitizer v4.5.

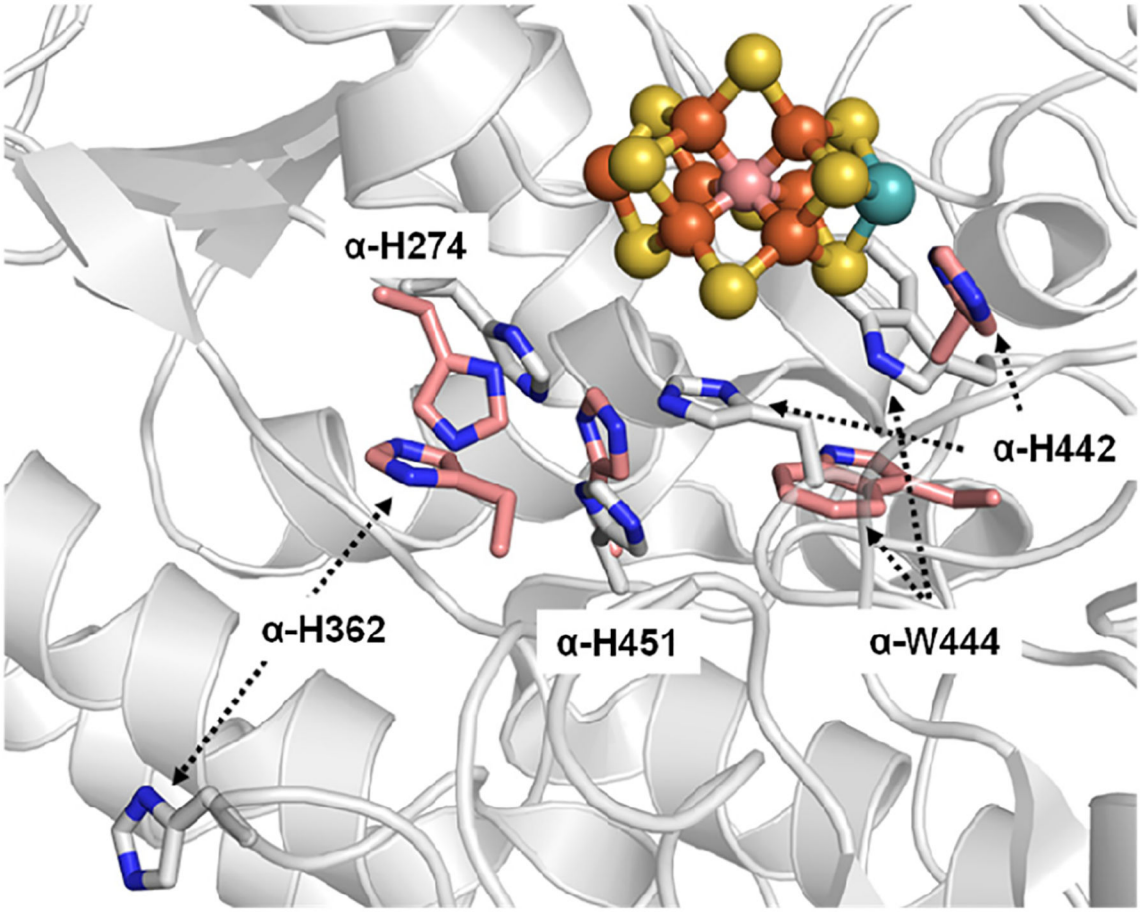

Figure 10.

Crystal structure of Δ*nif B* NifDK (in gray; PDB ID 1L5H), overlaid with the M-cluster and selected residues from the crystal structure of wild-type *Av*NifDK (in pink; PDB ID 3U7Q). The two structures were aligned, and the M-cluster and specific residues from the wild-type protein were superimposed on top of the Δ*nif B* NifDK structure. The residues α-H274, α-H442, and α-H451 represent the identified "histidine triad". The cluster atoms are shown as ball-and-stick models, and the amino acid residues are presented as sticks. Atomic coloring: Fe, orange; S, yellow; C, gray (in DnifB NifDK) or pink (in wild-type NfDK); O, red; N, blue.

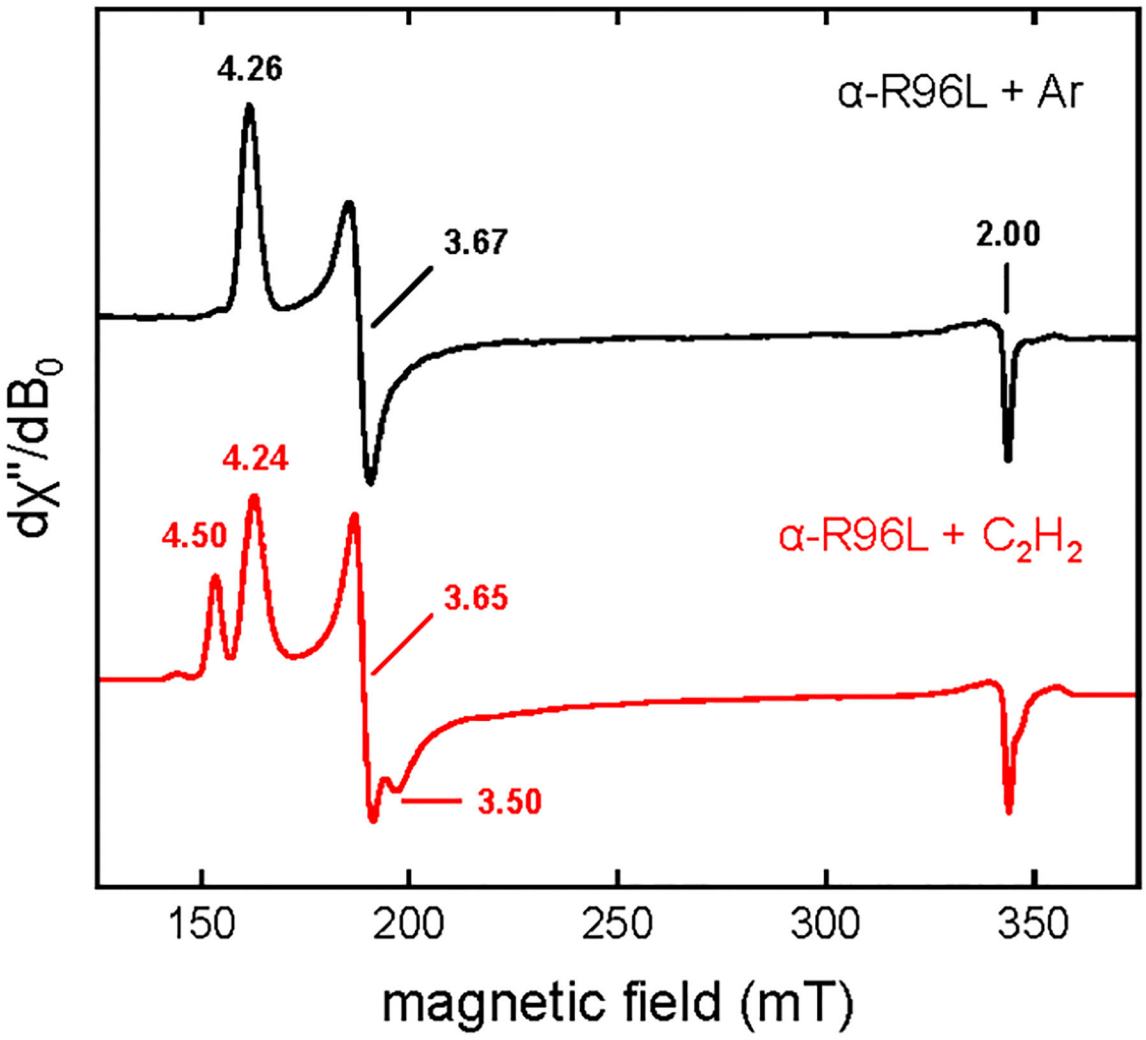

Figure 11.

EPR spectra of α-R96L NifDK under nonturnover conditions with acetylene. The α-R96L NifDK protein was prepared under 1 atm of Ar (top spectrum, black) or under 1 atm of acetylene (bottom spectrum, red). Reprinted (adapted or reprinted in part) with permission from ref 180. Copyright 2001 American Chemical Society. Data digitalized via WebPlotDigitizer v4.5.

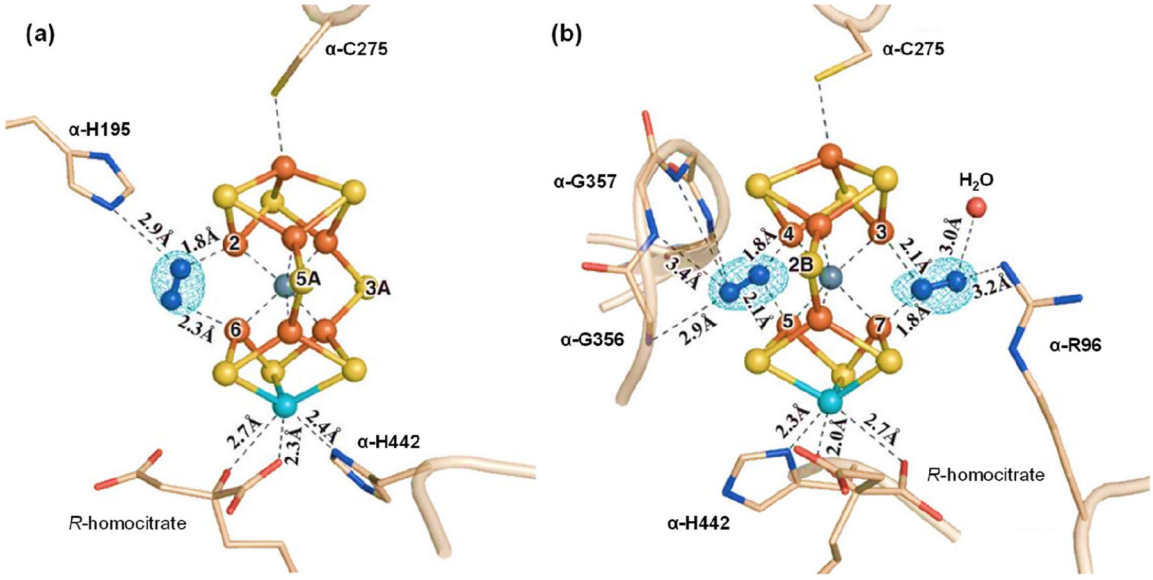

Figure 12.

Crystal structure of NifDK*. The M-cluster and key interacting residues at Site 1 (a) and Site 2 (b) are depicted (PDB ID 6UGO). The cluster and N molecules are presented as ball-and-stick models while the residues are shown as sticks. The M-clusters are superimposed with the $F_0 - F_c$ omit map of the N_2 ligands contoured at 10σ (mesh). Atomic coloring: Fe, orange; S, yellow; C, gray; O, red; N, blue. Reprinted (adapted or reprinted in part) with permission from ref 91. Copyright 2020 American Association for the Advancement of Science.

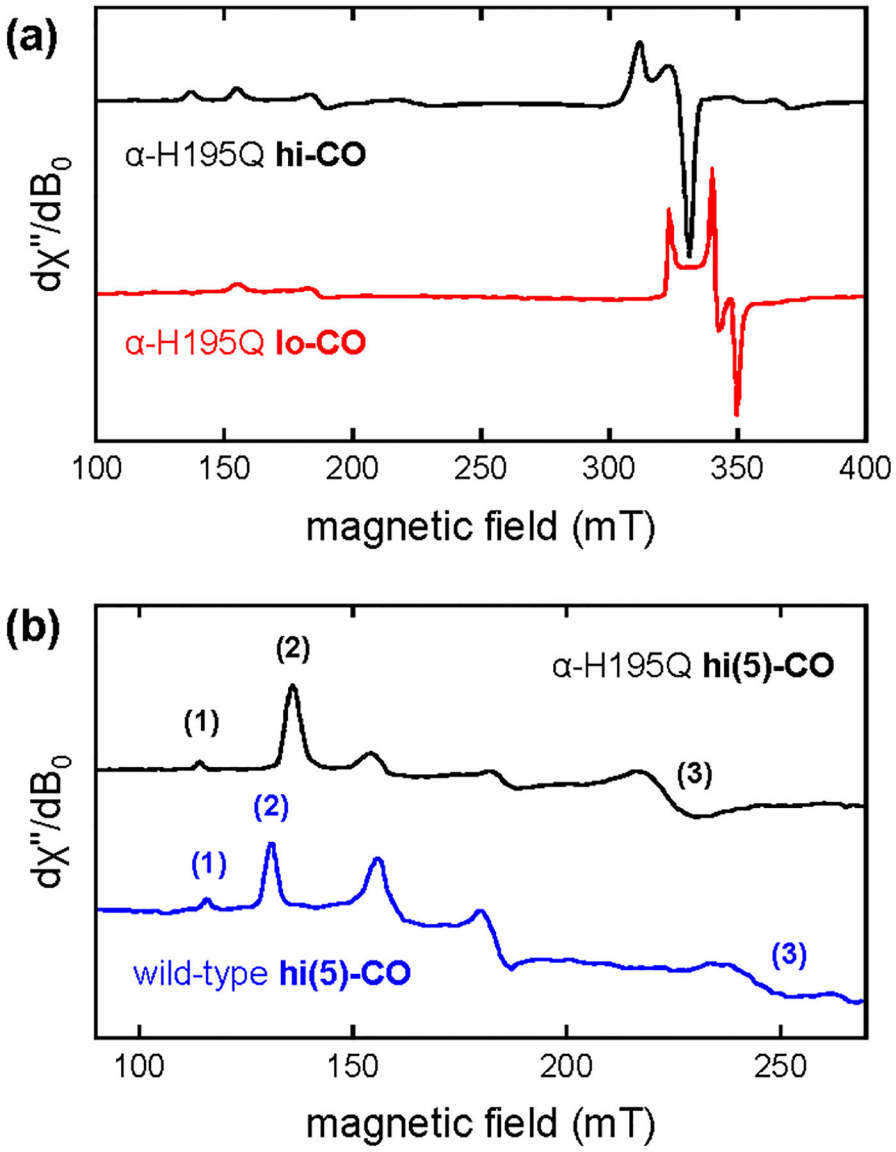

Figure 13.

EPR characterization of *A. vinelandii* NifDK during enzymatic turnover in the presence of CO. (a) α-H195Q NifDK in the presence of 1.0 atm CO (top, black) and 0.001 atm CO (bottom, red) showing the hi-CO and lo-CO signals, respectively. The small inflections are associated with the $S = 3/2$ signal of the resting state of the M-cluster. (b) EPR spectra of α-H195Q NifDK (top, black) and wild-type NifDK (bottom, blue) during turnover with 1 atm of CO, with the three lowest inflections (1)–(3) of the hi(5)-CO signal. The CO-related spectra of α-H195Q and wild-type NifDK are nearly identical. Reprinted (adapted or reprinted in part) with permission from ref 184. Copyright 2001 American Chemical Society. Data digitalized via WebPlotDigitizer v4.5.

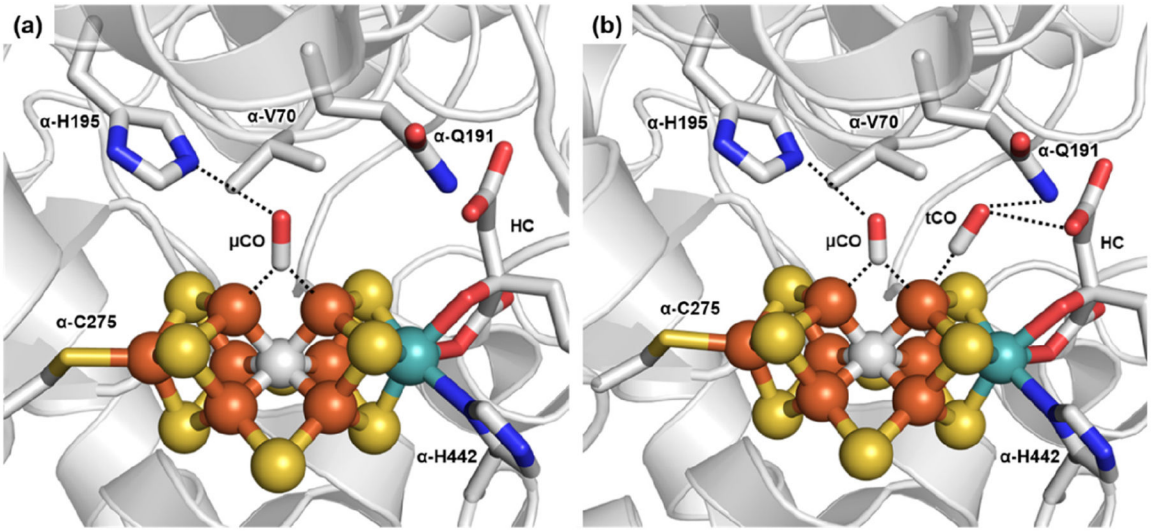

Figure 14.

Crystal structure of NifDK-CO (a) and NifDK-(2CO) (b) from *A. vinelandii*. The cluster atoms are shown as ball-and-stick models, the CO, *R*-homoctirate (HC), and amino acid residues are presented as sticks. Black dotted lines represent a bonding interaction, blue dotted lines represent potential hydrogen bonding interactions. Atomic coloring: Fe, orange; S, yellow; C, gray; O, red; N, blue. PDB IDs: NifDK-CO, 4TKV; NifDH-(2CO), 7JRF.

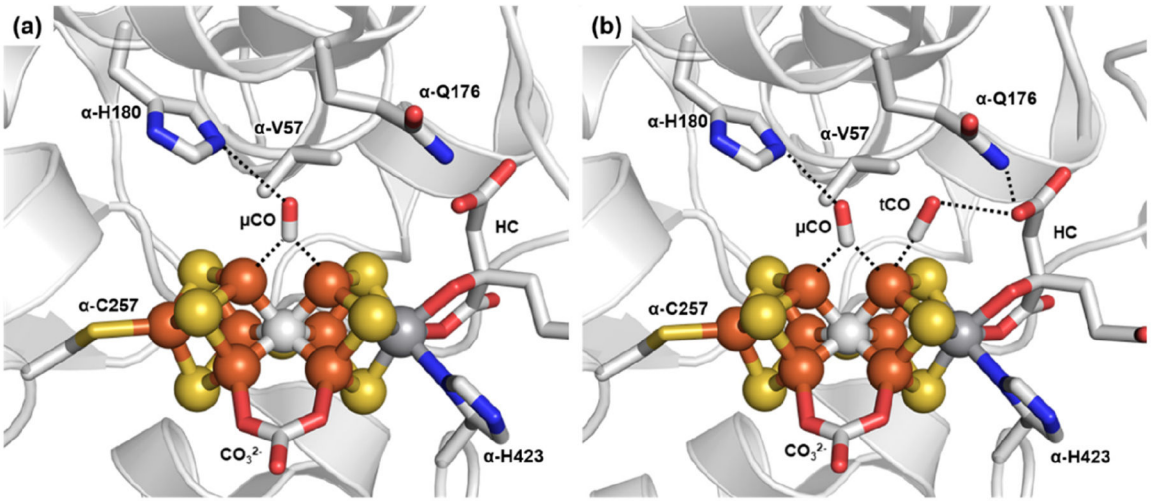

Figure 15.

Crystal structure of VnfDGK-CO (a) and VnfDGK-(2CO) (b) from *A. vinelandii*. The cluster atoms are shown as ball-and-stick models, the CO, *R*-homoctirate (HC), carbonate, and amino acid residues are presented as sticks. Black dotted lines represent a bonding interaction, blue dotted lines represent potential hydrogen bonding interactions. Atomic coloring: Fe, orange; S, yellow; C, gray; O, red; N, blue. PDB IDs: VnfDGK-CO, 7ADR; VnfGDH-(2CO), 7AIZ.

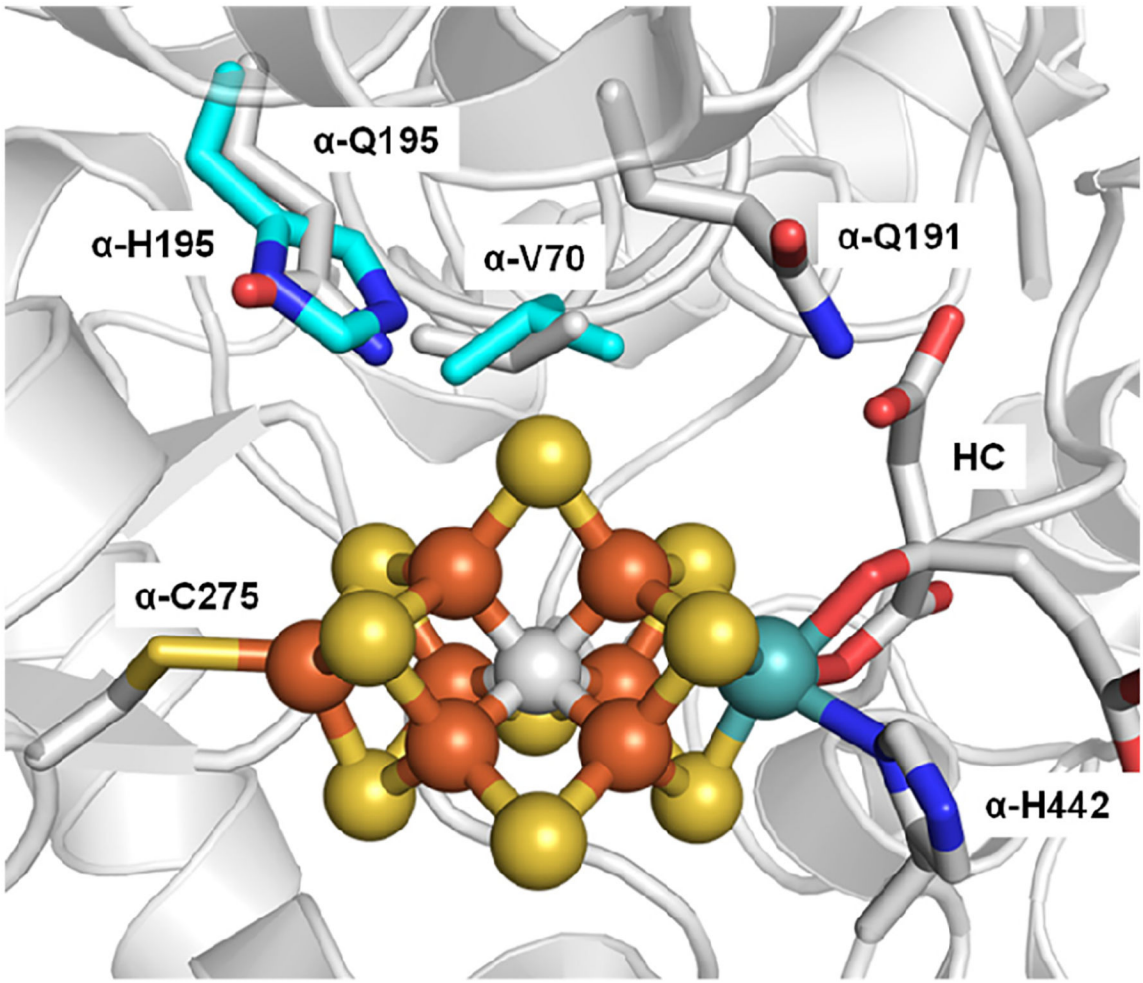

Figure 16.

Crystal structure of α-H195Q NifDK (in gray; PDB ID 1FP4), overlaid with the crystal structure of wild-type NifDK (in cyan; PDB ID 3U7Q) from *A. vinelandii*. The cluster atoms are shown as ball-and-stick models, the *R*-homocitrate (HC), and amino acid residues are presented as sticks. Atomic coloring: Fe, orange; S, yellow; C, gray; O, red; N, blue.

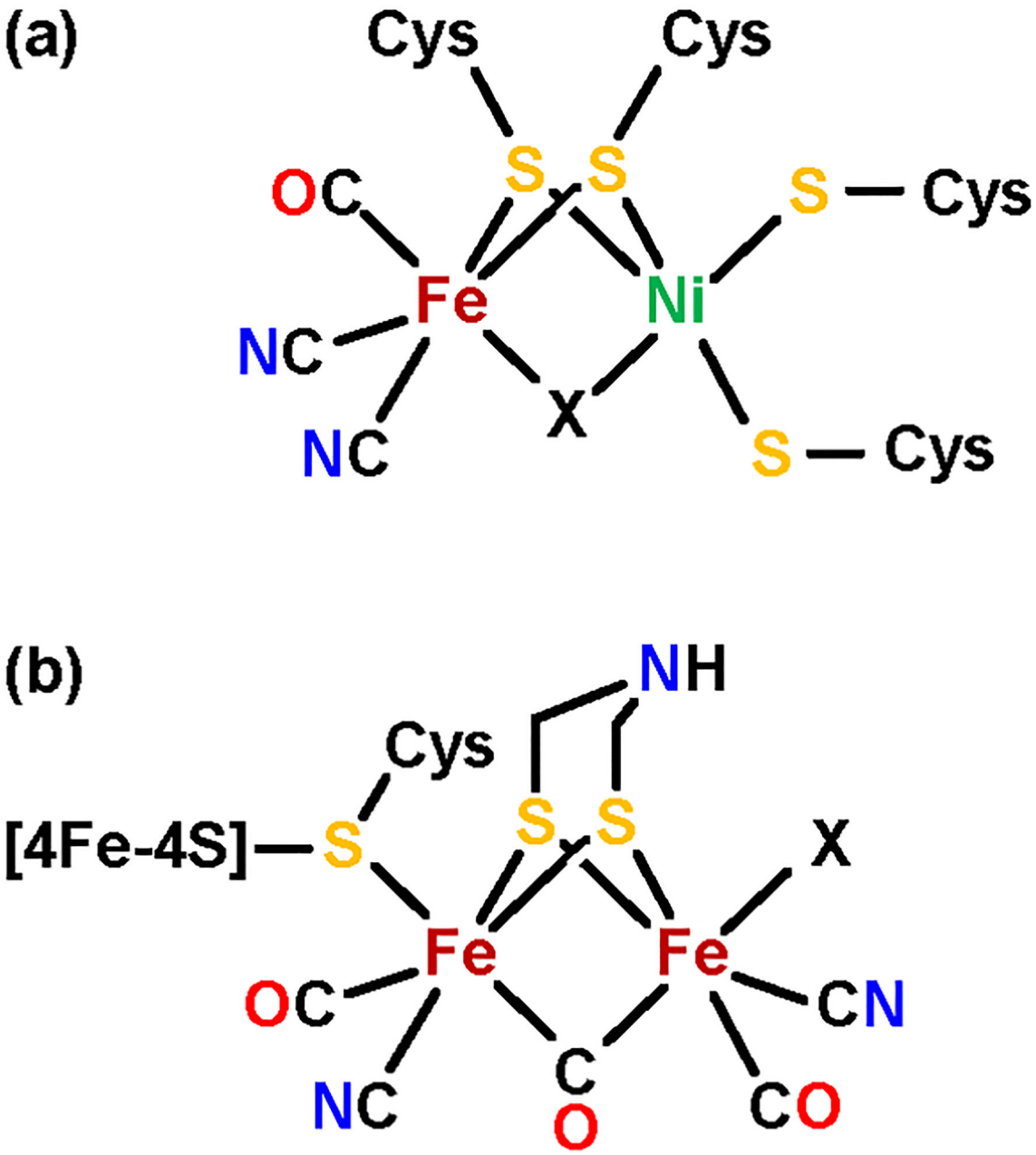

Figure 17.

Schematic representation of hydrogenase cofactors. (a) [NiFe]-hydrogenase active site cofactor and (b) [FeFe]-hydrogenase active site cofactor. The [4Fe-4S] cluster is coordinated by three further cysteines (not shown). Note the presence of an azadithiolate ligand (ADT, $S_2(CH_2)_2NH$) at the diiron site. 'X' marks the catalytic binding site in both cofactors.

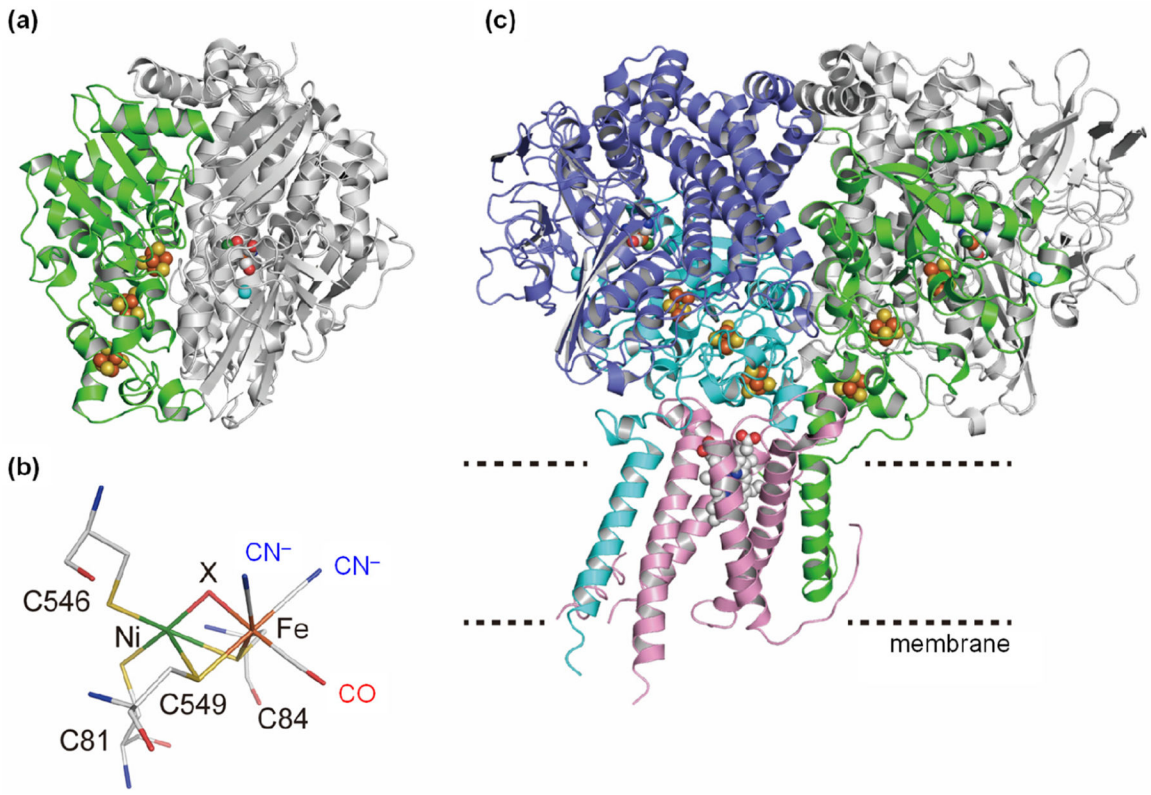

Figure 18.

Crystal structures of [NiFe]-hydrogenase. (a) Crystal structure of the standard [NiFe]-hydrogenase from *D. vulgaris* Miyazaki F (PDB ID 1WUJ). (b) Stick representation of the Ni–Fe active site with two CN^-, one CO, and a bridging ligand X that may be μOH^-, μOOH^-, or μH^- (PDB ID 1WUJ shows the Ni-B state). The Ni–Fe active site cofactor is located inside the large subunit, whereas three iron–sulfur clusters are located almost linearly (each ~12 Å apart) in the small subunit. (c) Crystal structure of O_2-tolerant membrane-bound [NiFe]-hydrogenase from *E. coli* (PDB ID 4GD3). Atomic coloring: Ni, green; Fe, orange; S, yellow; C, gray; O, red; N, blue.

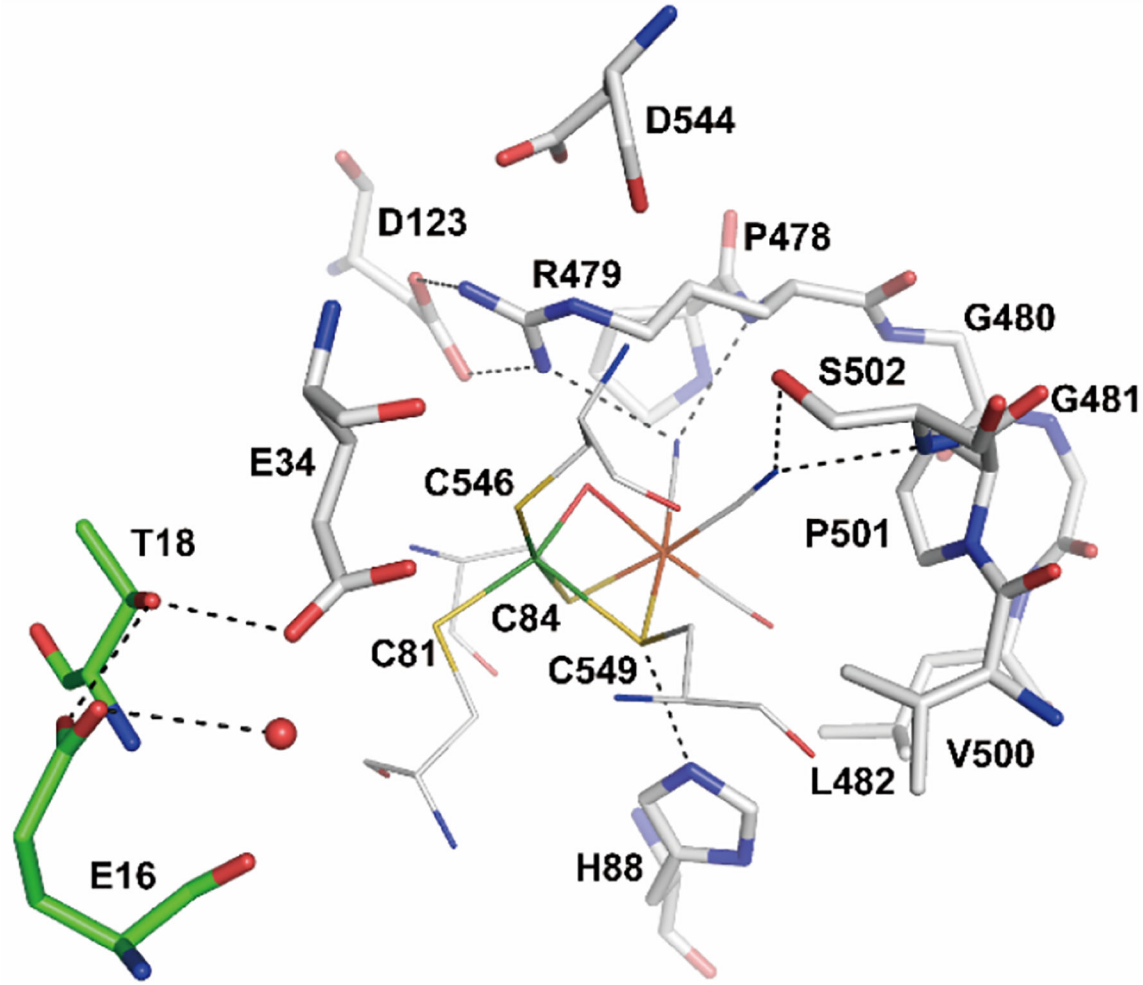

Figure 19.

Second and outer coordination spheres of the Ni–Fe active site. Crystal structure of the standard [NiFe]-hydrogenase from *D. vulgaris* Miyazaki F in the Ni-B state (PDB ID 1WUJ). Glutamate E34, histidine H88, arginine R479, and serine S502 are important residues located in the second coordination sphere of the Ni–Fe active site. The dotted lines indicate the hydrogen bond network. Atomic coloring: Ni, green; Fe, orange; S, yellow; C, gray; O, red; N, blue.

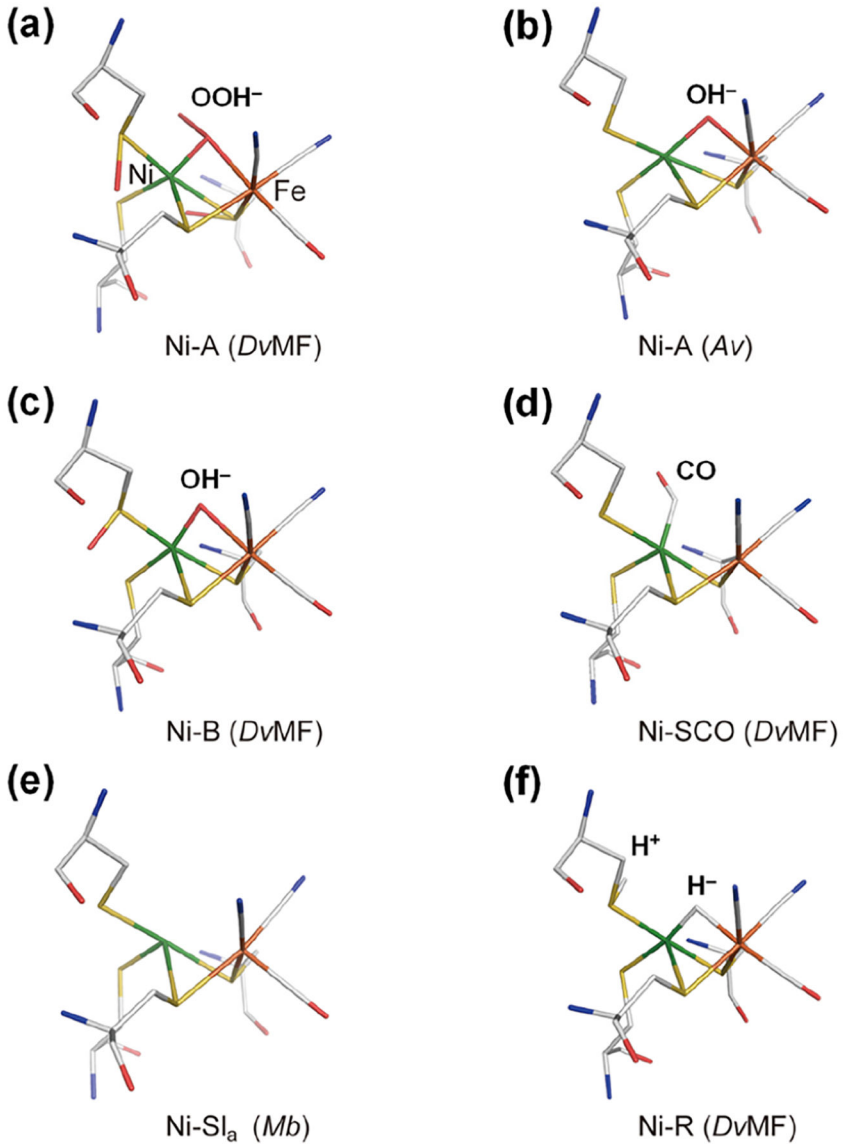

Figure 20.

Crystal structures of the Ni–Fe active site in various oxidation states. (a) The Ni-A state of *Dv*MF hydrogenase (PDB ID 1WUI) and (b) of *Av* hydrogenase (PDB ID 3MYR). (c) Ni-B state (PDB ID 1WUJ). (d) CO-inhibited Ni-SCO state (PDB ID 1UBH). (e) The Ni-SI_a state (PDB ID 6QGR). (f) Ni-R state (PDB ID 4U9H). A bridging ligand exists in the Ni-A (μOOH^- and μOH^-), Ni-B (μOH^-), and Ni-R states (μH^-), while the bridging position is vacant in the Ni-SI_a state. Atomic coloring: Ni, green; Fe, orange; S, yellow; C, gray; O, red; N, blue.

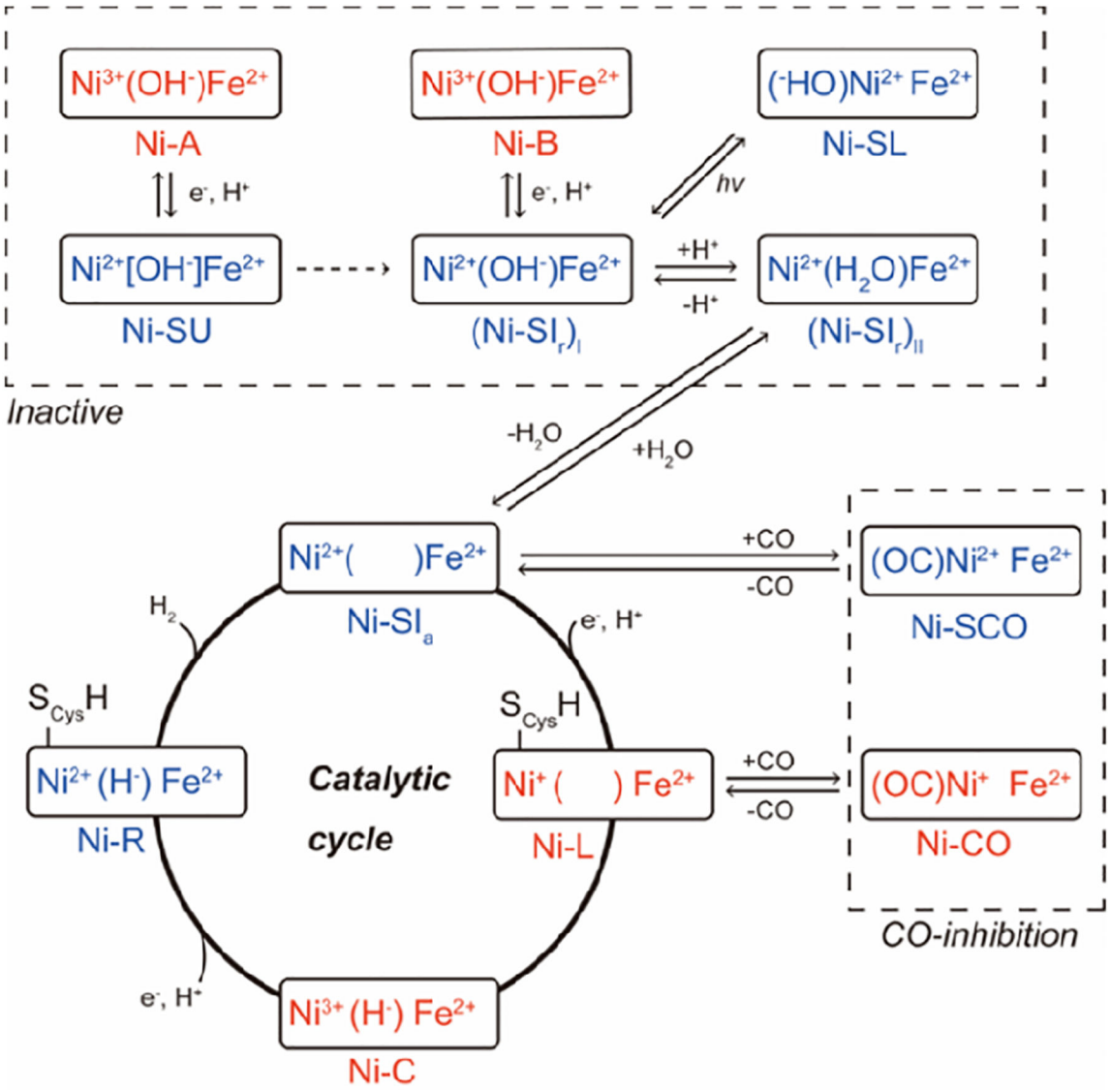

Figure 21.

Proposed catalytic cycle of [NiFe]-hydrogenase. The catalytic cycle comprises four states (Ni-SI_a, Ni-R, Ni-C, and Ni-L) that interconvert in direction of H_2 oxidation or proton reduction. The EPR-active states are shown in red, diamagnetic states are shown in blue. Among the inactive states, a μOH^- ligand is tentatively assigned in the Ni-SU state.

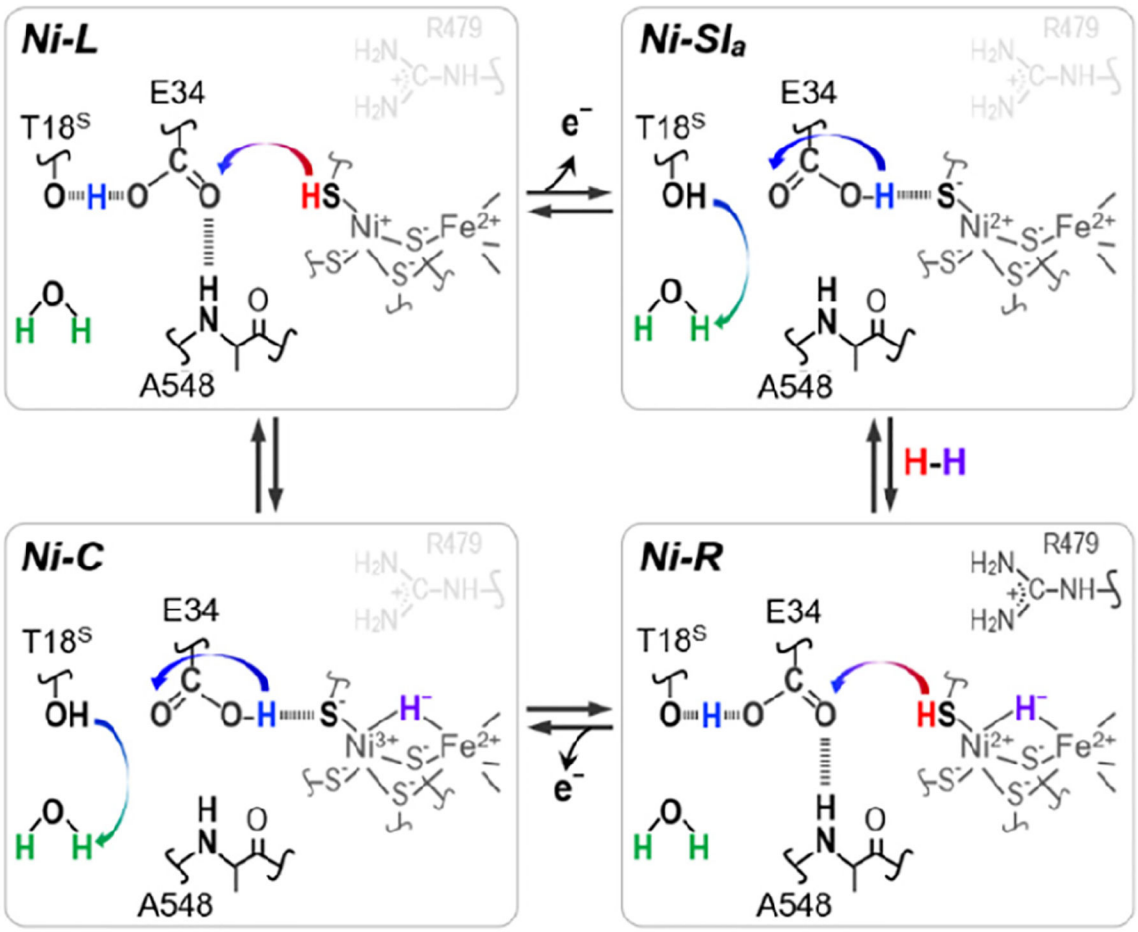

Figure 22.

Proposed proton transfer mechanism for [NiFe]-hydrogenase. The hydrogen bond network between C546 (*Dv*MF nomenclature, the respective sulfur atom is bold), E34, T18, A548, and a dangling water molecule is rearranged during the catalytic reaction. An involvement of R479 (gray) is possible. Reprinted (adapted or reprinted in part) with permission from ref 346. Copyright 2019 Wiley.

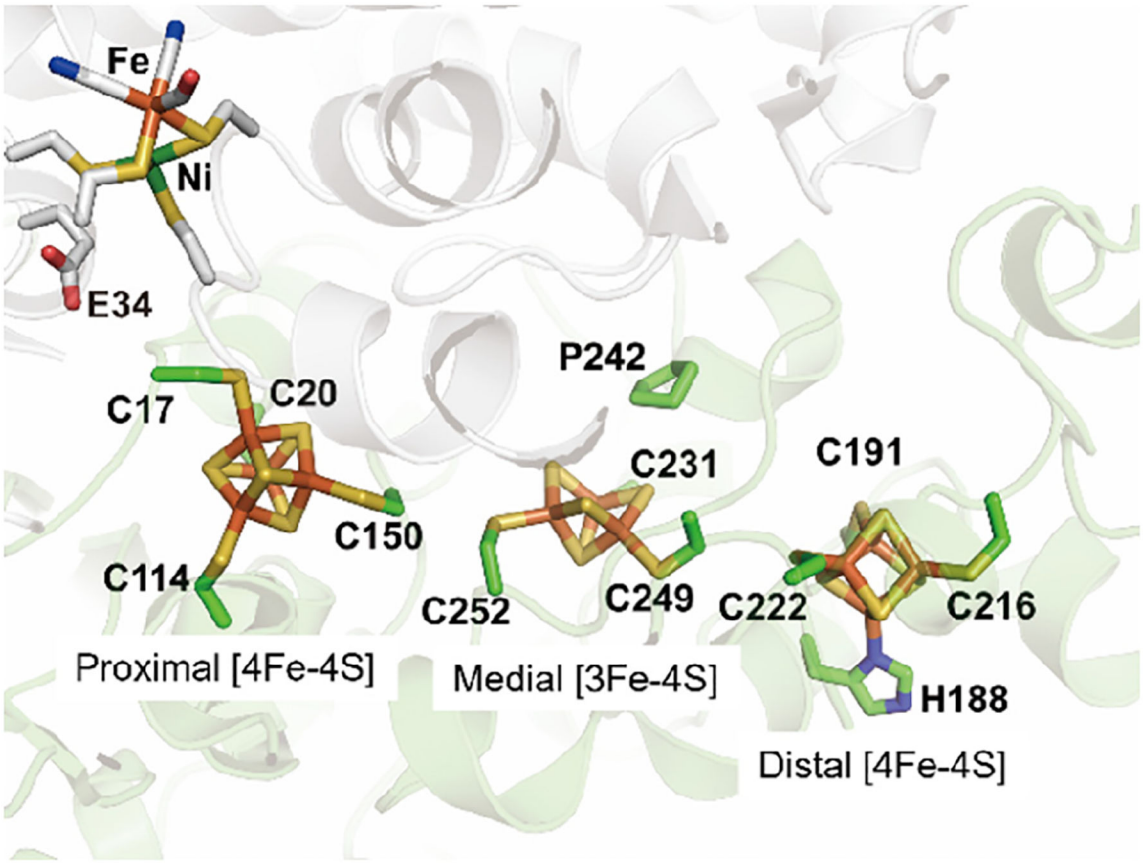

Figure 23.

Location of the accessory iron–sulfur clusters. The large subunit with the Ni–Fe cofactor is shown in white cartoon, the small subunit with the proximal [4Fe-4S], the medial [3Fe-4S], and the distal [4Fe-4S] cluster is shown in green (*Dv*MF [NiFe]-hydrogenase, PDB ID 1H2R). The three accessory iron–sulfur clusters are located almost linearly. Atomic coloring: Ni, dark green; Fe, orange; S, yellow; C, green; O, red; N, blue.

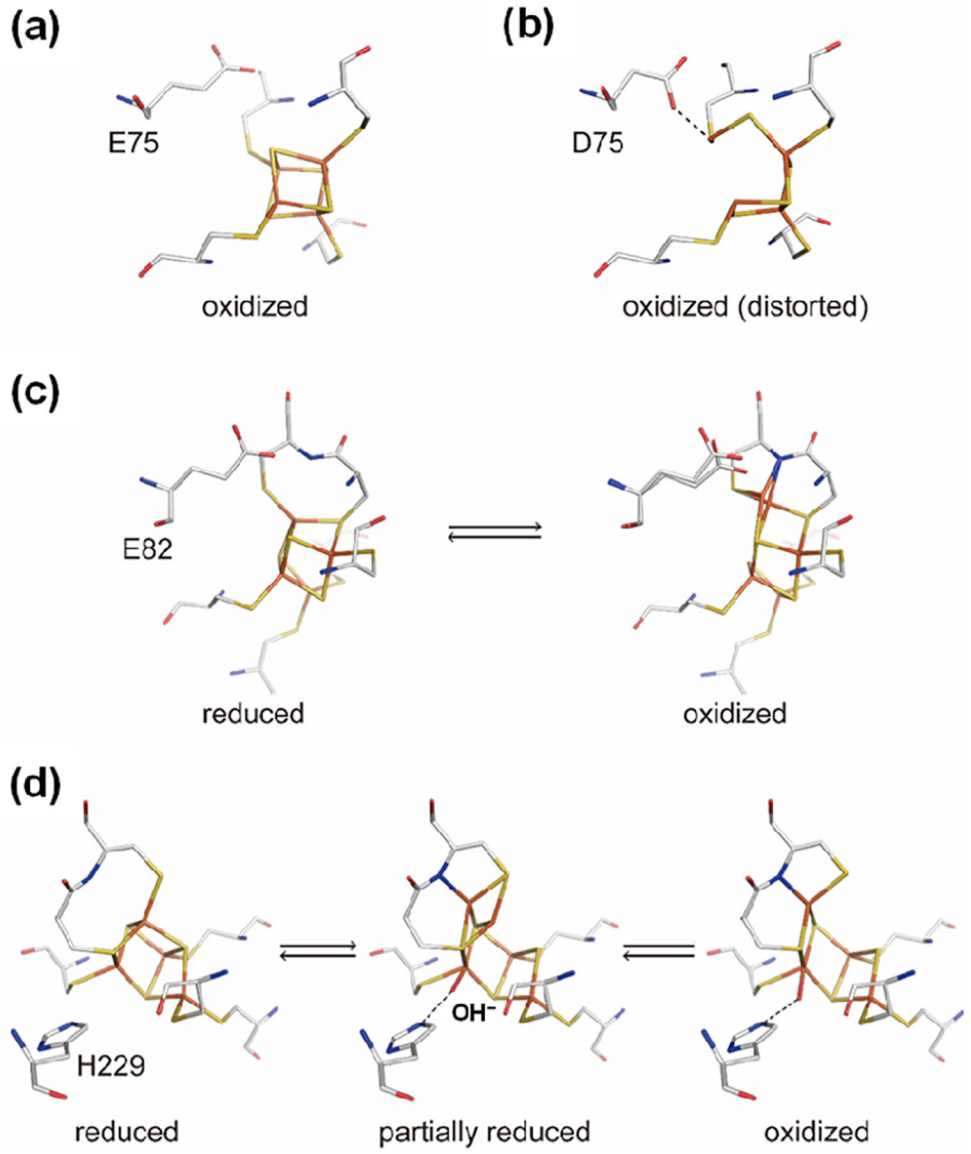

Figure 24.

Structural changes of the proximal iron–sulfur cluster in various [NiFe]-hydrogenases. (a) Oxidized form (PDB ID 1UBH) in *Dv*MF and (b) oxidized-distorted form (PDB ID 3MYR) in *Av*. (c) Reduced and oxidized forms of the [4Fe-3S] cluster in *Hm*MBH (PDB ID 3AYX and 5Y34). (d) Reduced, partially reduced, and oxidized forms of the [4Fe-3S] cluster in *Re*MBH (PDB ID 3RGW, 4IUD, and 4IUB). The proximal [4Fe-4S] cluster is distorted with one of the Fe ions bound to D75 in one of the oxidized forms (b). Atomic coloring: Ni, green; Fe, orange; S, yellow; C, gray; O, red; N, blue.

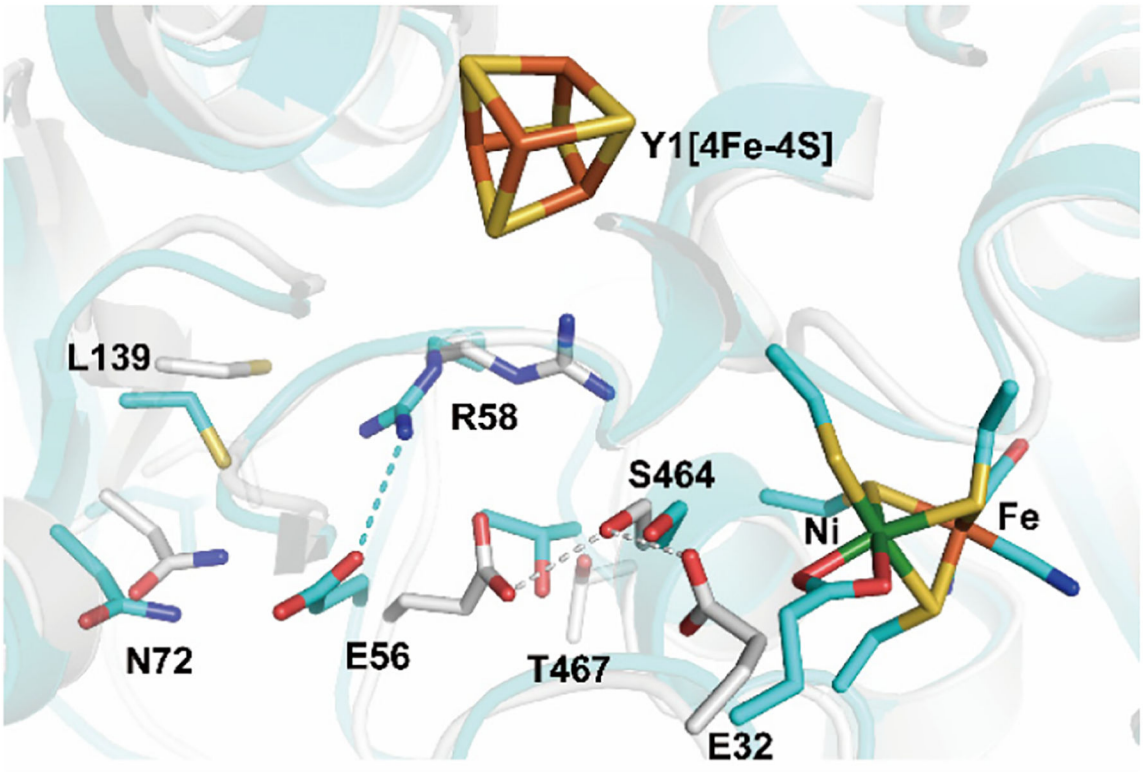

Figure 25.

Proposed proton transfer in the O_2-tolerant [NiFe]-hydrogenase *Hf*TH-1. The oxidized state is shown in cyan (PDB ID 5XF9) and the H_2-reduced state is shown in white (PDB ID 5XFA). Y1 refers to the proximal iron–sulfur cluster. The side chain of E32 binds to the Ni ion in the oxidized state, while it does not bind to the Ni ion and forms a hydrogen bond network including S464 and E56 in the reduced state. The metal centers in the reduced state are omitted for clarity. Atomic coloring: Ni, green; Fe, orange; S, yellow; C, gray; O, red; N, blue.

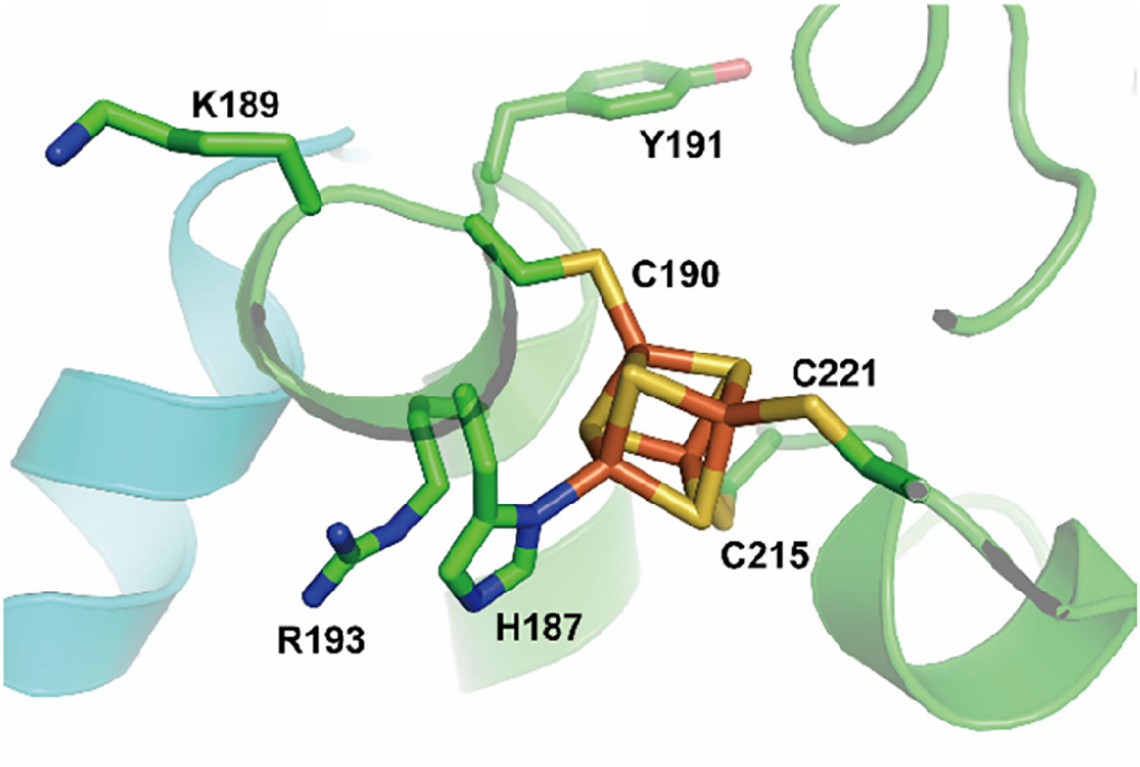

Figure 26.

Amino acids surrounding the distal [4Fe-4S] cluster. The [NiFe]-hydrogenase *Ec*Hyd-1 is shown (PDB ID 3UQY). Arginine R193 in the second sphere affects the electron transfer rate. Atomic coloring: Fe, orange; S, yellow; C, green; O, red; N, blue.

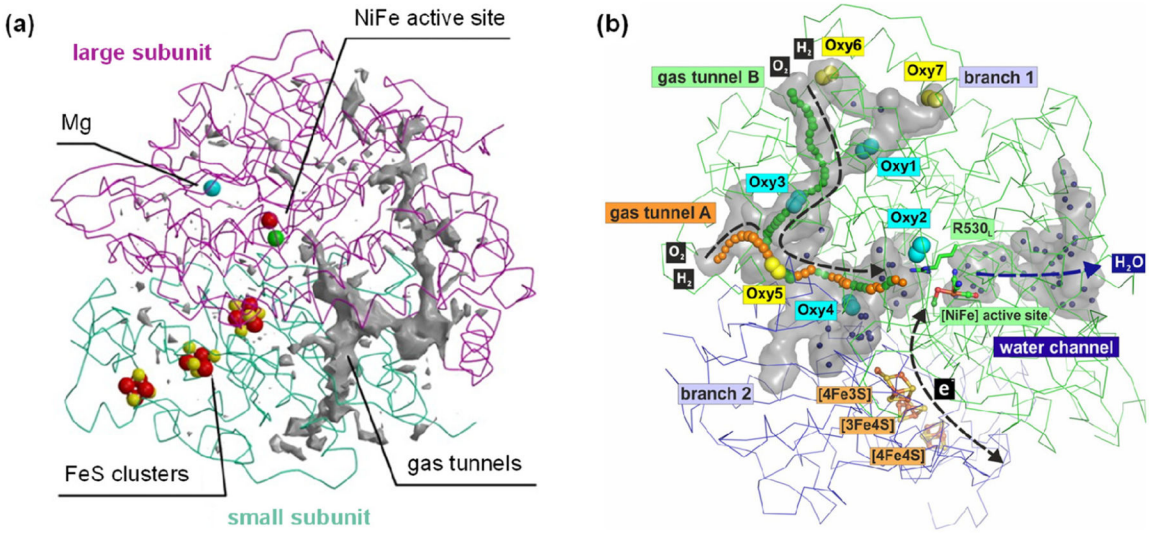

Figure 27.

Gas transfer channels. (a) Standard *Df* [NiFe]-hydrogenase. Reprinted (adapted or reprinted in part) with permission from ref 309. Copyright 2008 National Academy of Sciences. (b) O_2 pathway in O_2-tolerant *Re*MBH. Two entrances for gas transfer channels have been revealed, which are combined and extend to the Ni–Fe active site. Reprinted (Adapted or Reprinted in part) with permission from ref 400. Copyright 2018 National Academy of Sciences.

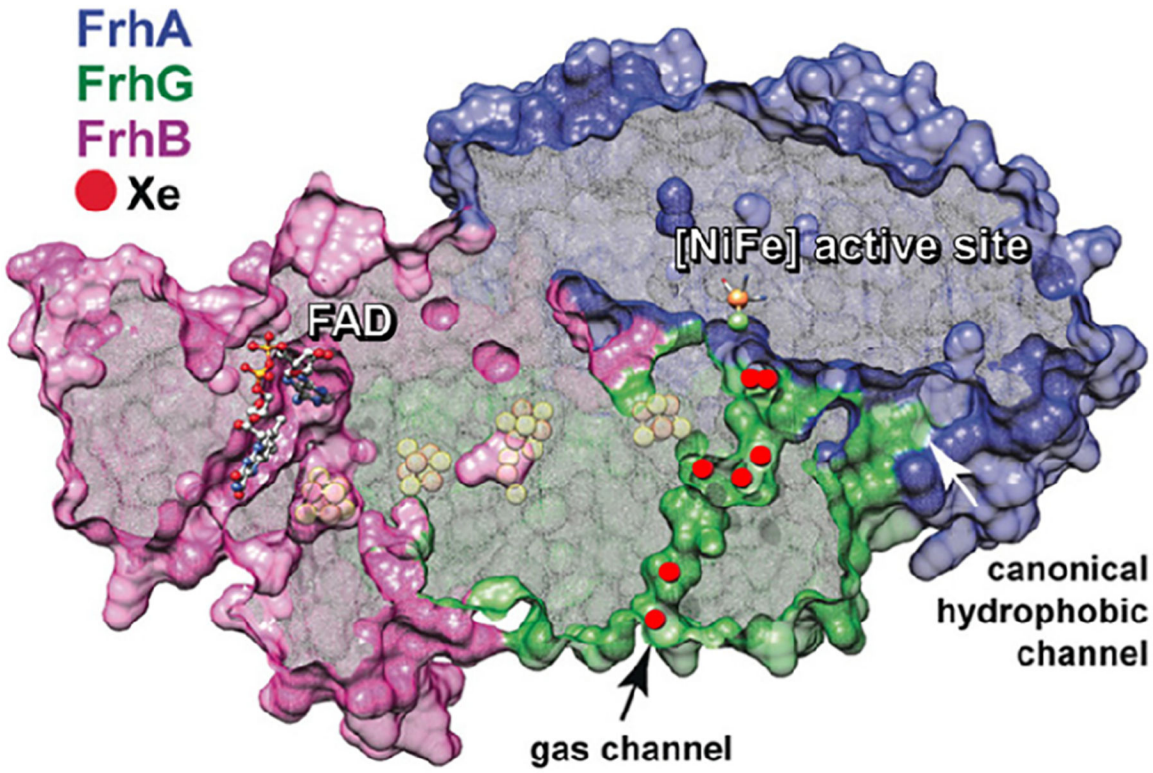

Figure 28.

Gas tunnels of *Mb* F_{420}-reducing [NiFe]-hydrogenase. Seven Xe atoms (red spheres) were detected within an additional gas tunnel from the surface to the Ni–Fe cofactor (PDB ID 6QII). Reprinted (adapted or reprinted in part) with permission from ref 339. Copyright 2019 Wiley.

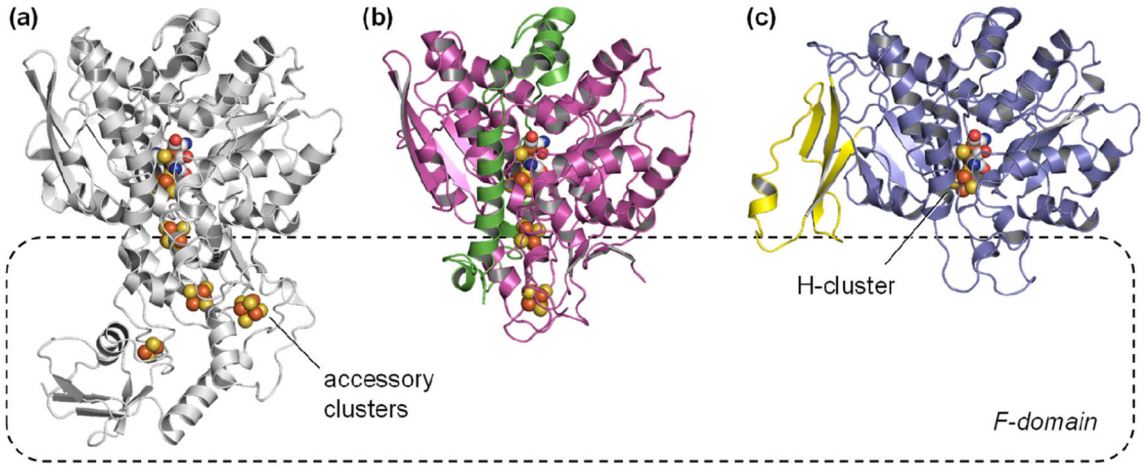

Figure 29.

Crystal structures of various [FeFe]-hydrogenases. (a) *C. pasteurianum Cp*I (PDB ID 4XDC) and (b) *D. desulfuricans Dd*H (PDB ID 1HFE). The characteristic peptide belt of *Dd*H is shown in green. Panel (c) depicts a homology model of the [FeFe]-hydrogenase from *C. reinhardtii Cr*HydA1. Here, the characteristic “loop” that is specific for this enzyme is shown in yellow. Accessory iron–sulfur clusters and the catalytic H-cluster are highlighted as spheres. Note the successive miniaturization of the F-domain from (a) to (c). Atomic coloring: Fe, orange; S, yellow; C, gray; O, red; N, blue.

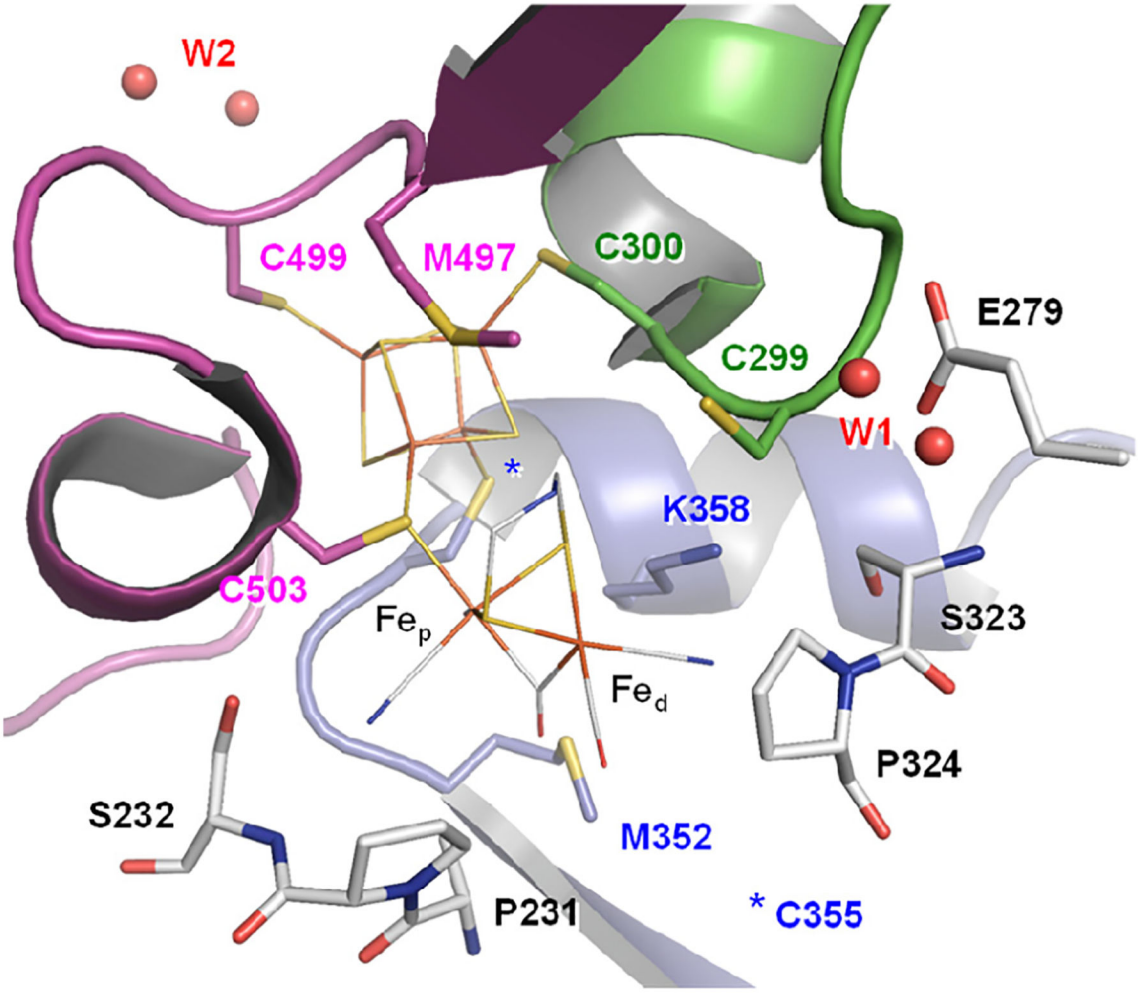

Figure 30.

Active site cavity and catalytic cofactor of [FeFe]-hydrogenase *Cp*I (PDB ID 4XDC). The H-cluster is composed of an [4Fe-4S] cluster and the diiron site. Loops 1–3 provide four cysteine residues to bind the [4Fe-4S] cluster and the diiron site. In loop 1 (green), C299 is part of the proton transfer pathway (further including water cluster W1, E279, and other groups). In loop 2 (blue), M352 may interact with the μCO ligand while K358 was suggested to form a hydrogen bond with the CN^- ligand at the distal iron ion, Fe_d. In loop 3 (magenta), M497 may form a hydrogen bond with the ADT group. Cysteine C499 was proposed to be the 1st proton acceptor of the proton transfer pathway. Serine S232 provides a hydrogen bond to the CN^- ligand of the proximal iron ion, Fe_p, presumably involving a backbone contact with P231. Atomic coloring: Fe, orange; S, yellow; C, gray; O, red; N, blue.

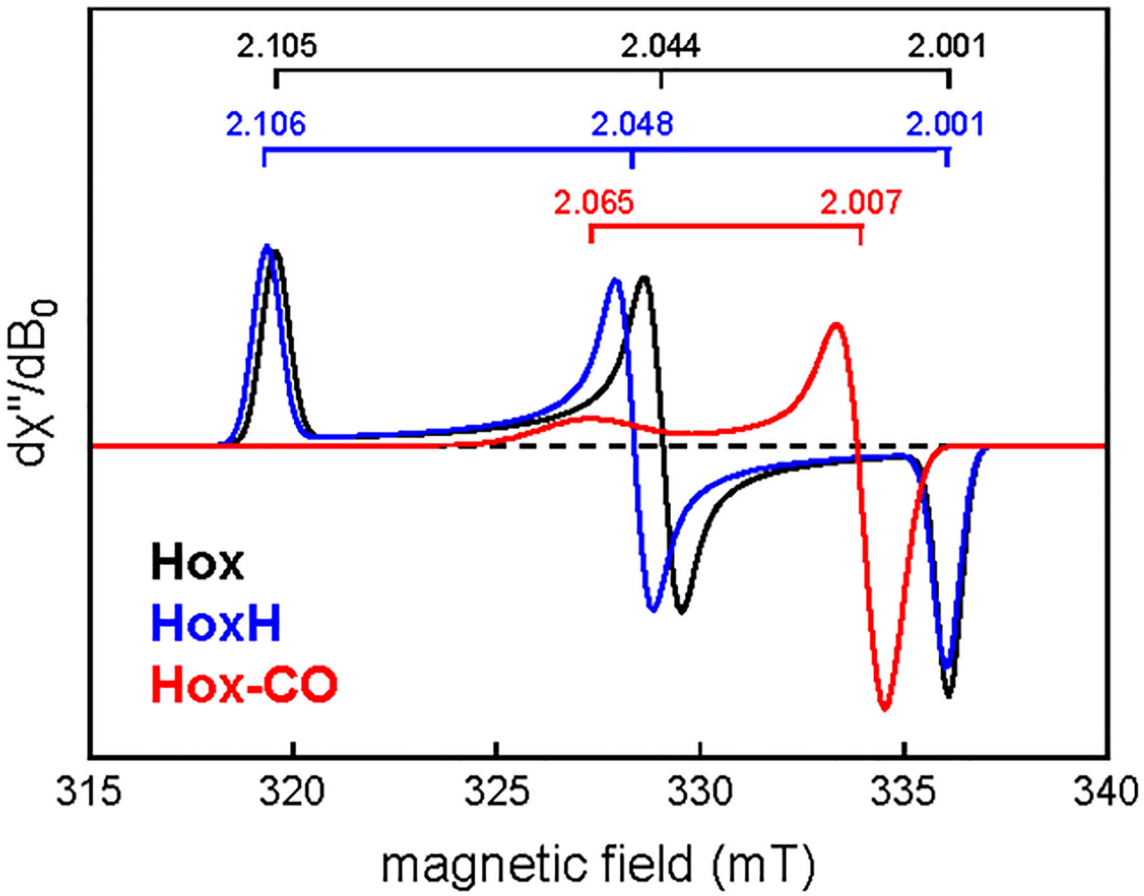

Figure 31.

EPR spectra of the oxidized H-cluster. Simulations of EPR spectra for the oxidized states H_{ox}, $H_{ox}H$, and H_{ox}-CO as observed in *Ci*HydA1. The *g*-values are indicated. Reprinted (adapted or reprinted in part) with permission from ref 267. Copyright 2020 American Chemical Society.

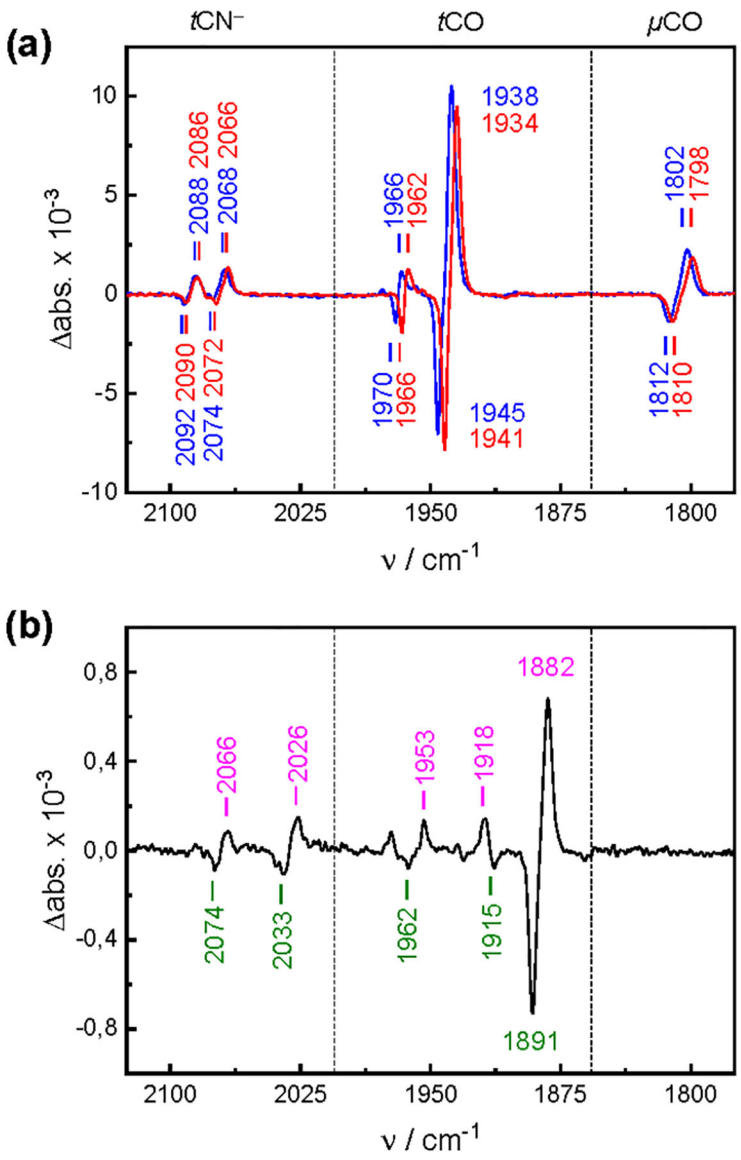

Figure 32.

Influence of the [4Fe-4S] cluster on the IR signature of the H-cluster. (a) 'H_2 − N_2' difference spectra of *Cr*HydA1 cofactor variant PDT at pH 5 ('$H_{red}'H$ − $H_{ox}H$', blue trace) and pH 8 ('H_{red}' − H_{ox}', red trace). Negative and positive bands are assigned to H-cluster states with an oxidized and reduced [4Fe-4S] cluster, respectively. The small frequency shifts between the oxidized and reduced states are assigned to a protonation at or near the [4Fe-4S] cluster. Data taken from ref 488. (b) Spectro-electrochemical difference spectrum of *Cr*HydA1 that shows the accumulation of H_{sred} (magenta labels, −650 mV vs SHE) over H_{red} (green labels, −450 mV vs SHE) at pH 9. Negative and positive bands are assigned to H-cluster states with an oxidized and reduced [4Fe-4S] cluster, respectively. At ambient temperature, the bridging carbonyl ligand (*μ*CO) converts into a terminal ligand, which results in three *t*CO bands.

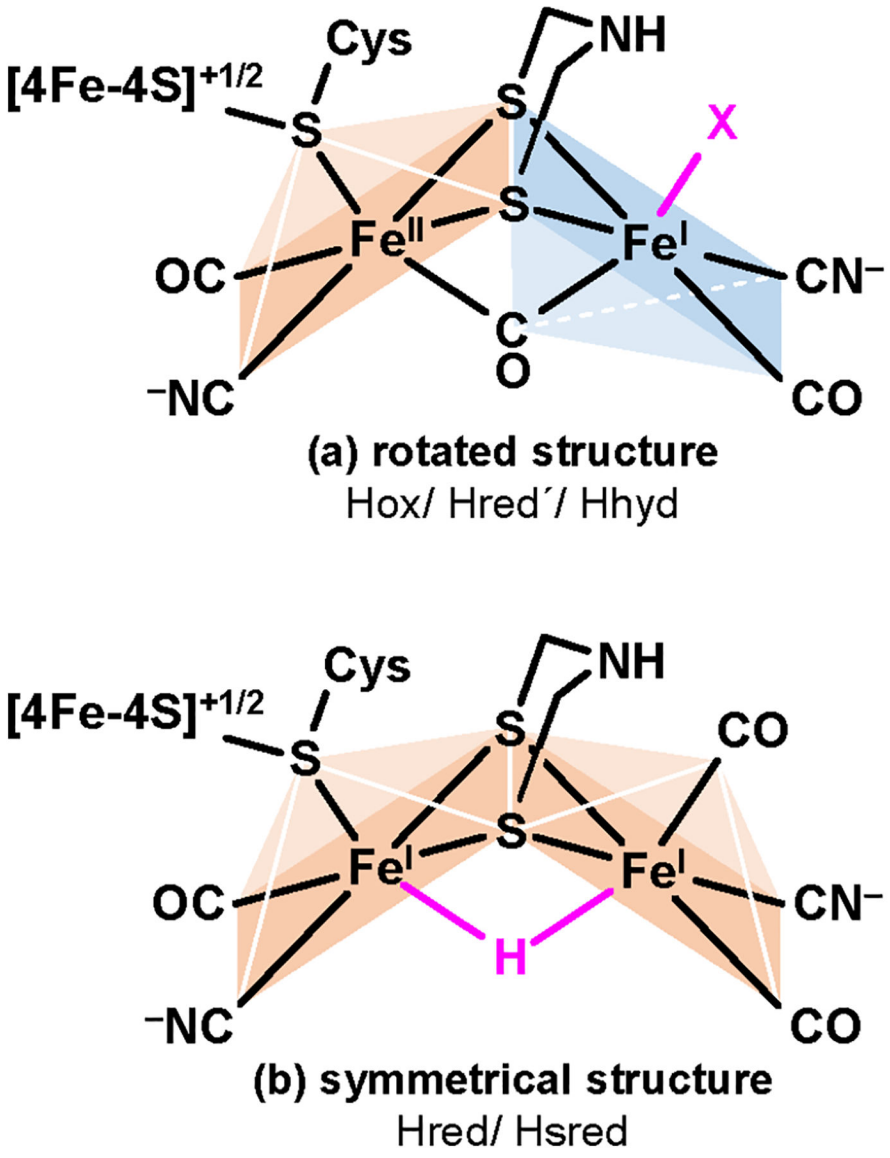

Figure 33.

Changes in geometry upon reduction. (a) In the paramagnetic II/I state of the diiron site (H_{ox} and $H_{red'}$), the μCO ligand stabilizes the "rotated structure" that is characterized by a squarepyramidal/inverted square-pyramidal arragenment and an open coordination site at Fe_d (X). In H_{hyd}, the diiron site is "superoxidized" (II/II) and X is a terminal hydride. (b) Upon reduction (I/I), the diiron site adopts the symmetrical square-pyramidal/square-pyramidal arrangement. No μCO ligand is observed in the respective redox states Hred and Hsred.

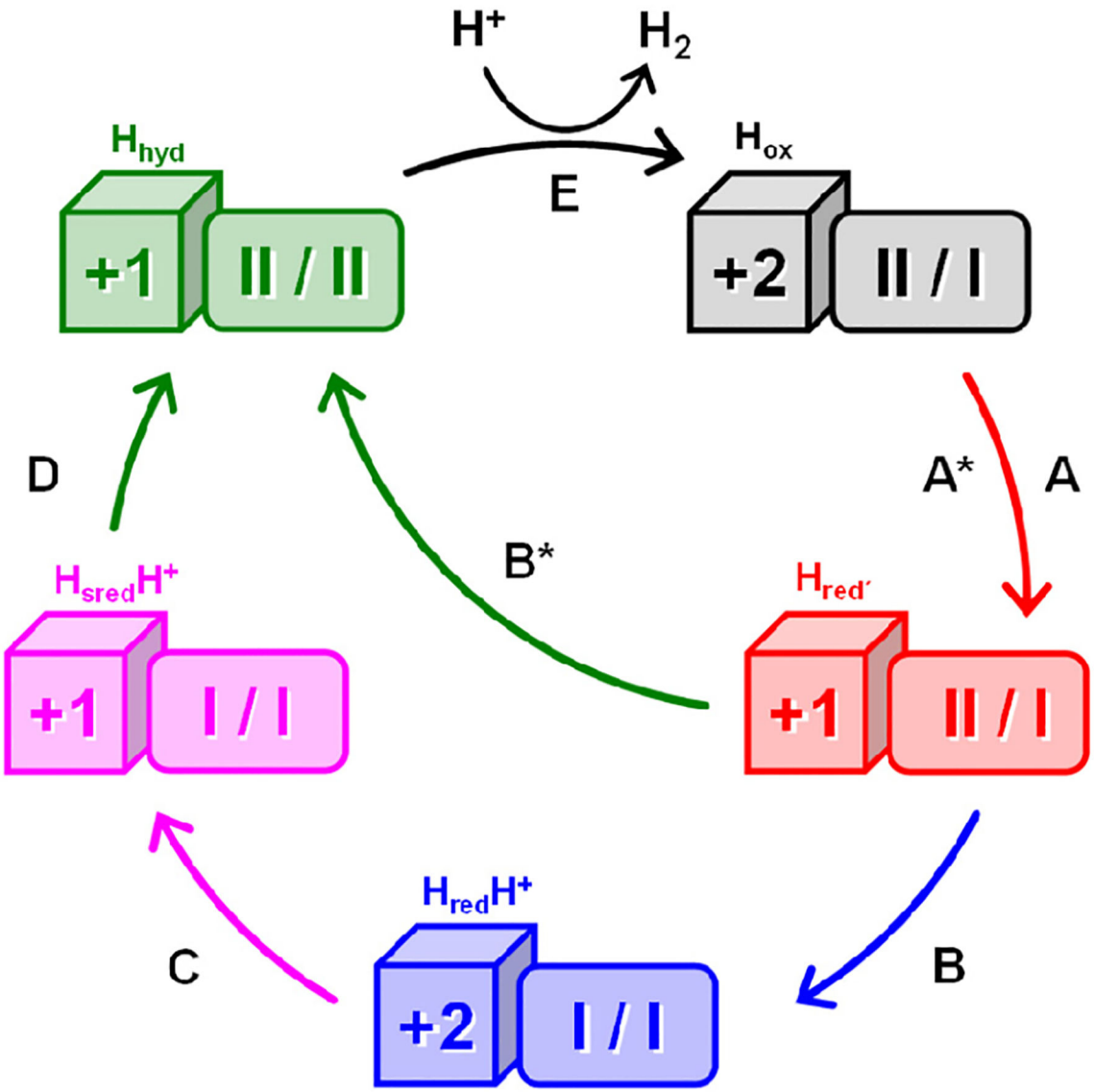

Figure 34.

Proposed catalytic cycle. The 5-step model (A–E) includes $H_{red}H^+$ and $H_{sred}H^+$, presuming the H-cluster retains the μCO ligand upon reduction of the diiron site. The 3-step model (A*–B*–E) suggests a "short-cut" from $H_{red'}$ to H_{hyd} as both species share the same geometry. The geometry of the reduced diiron site (I/I) under ambient conditions is debated. Reprinted (adapted or reprinted in part) with permission from ref 267. Copyright 2020 American Chemical Society.

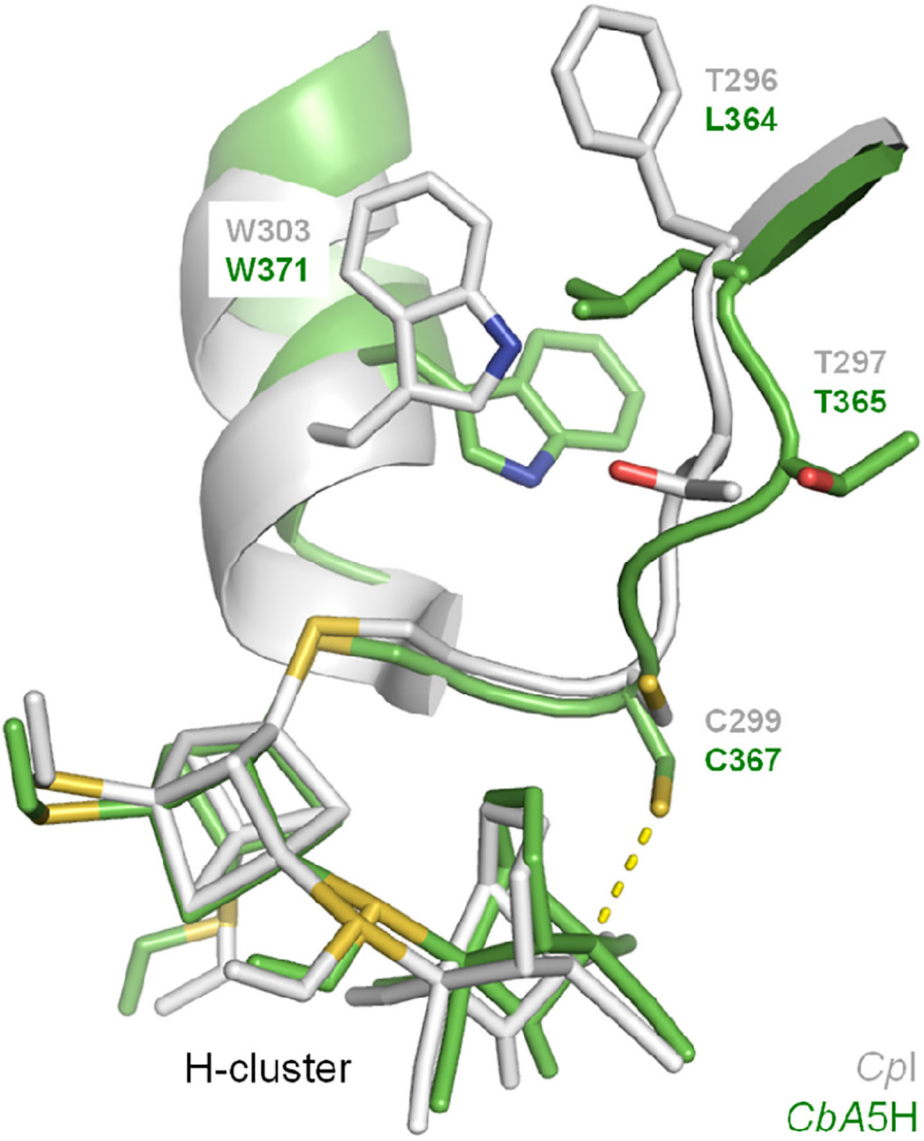

Figure 35.

Comparison of *Cp*I (white) and *Cb*A5H (green) in the H_{ox} and H_{inact} state. The distance of the sulfur atom of C299/C367 shrinks from ~6 Å to ~3 Å, making a direct coordination of the distal iron ion (Fe_d) in the H_{inact} state of *Cb*A5H likely (dashed line). The annotated amino acid residues have been identified to cause the flexibility of the unique loop in *Cb*A5H. Drawn after PDB IDs 4XDC and 6TTL.

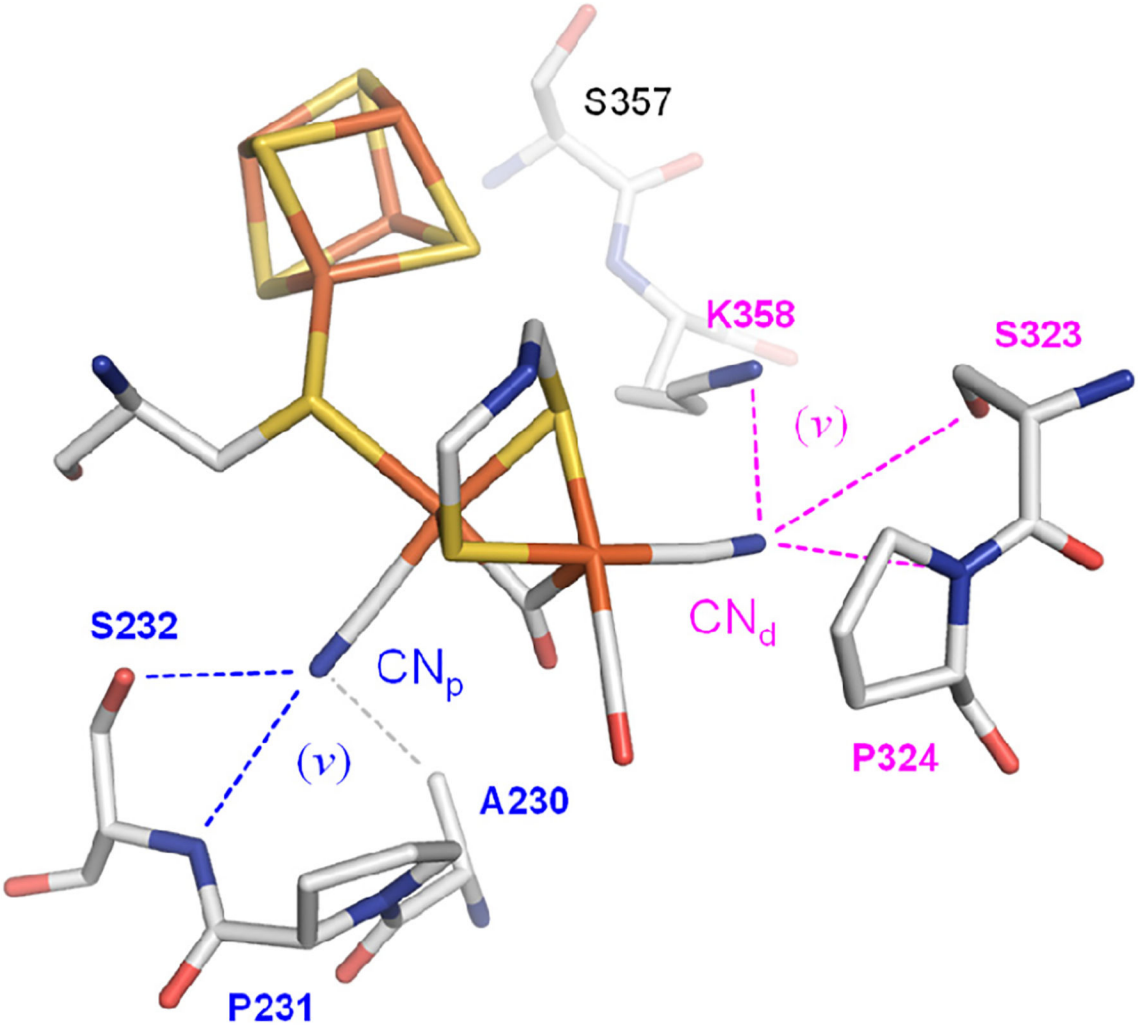

Figure 36.

Hydrogen-bonding environment of the CN^- ligands. In proximal (p) position, polar interactions (*v*) with a backbone amine, S232, and variant A230S have been experimentally verified in *Cp*I and *Cr*HydA1. The hydrophilic pocket including K358, S323, and a P324 backbone contact inspired the assignment of the CN^- ligand in distal (d) position in *Cp*I and *Dd*H. The putative hydrogen-bonding environment (*v*) is shown. Drawn after PDB ID 6NAC. Atomic coloring: Fe, orange; S, yellow; C, gray; O, red; N, blue.

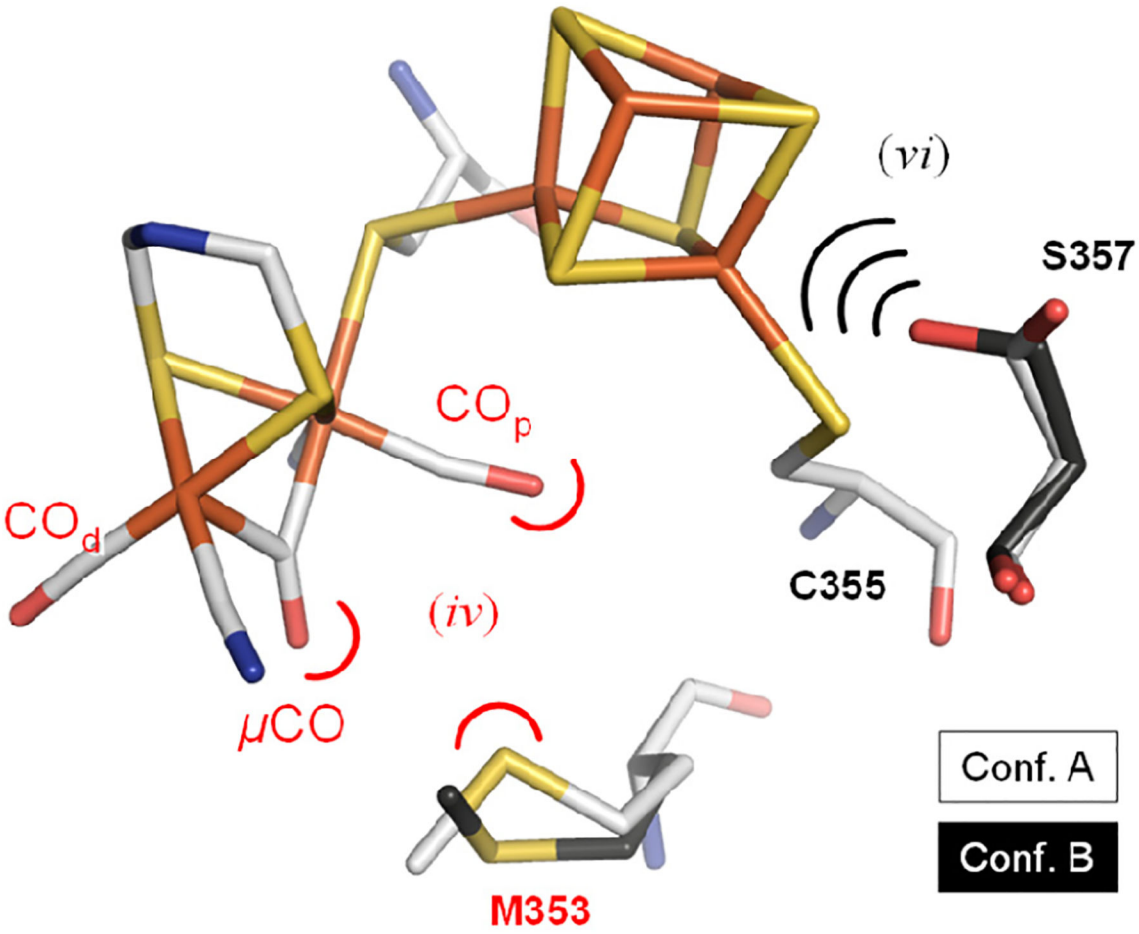

Figure 37.

Structural differences between “conformation A” and “conformation B”. The M353 side chain shifts by ~0.4 Å away from μCO and Fe$_p$-CO in the “reduced” state (equivalent conformation B), which lowers the steric constraints (*iv*). Concomitantly, the side chain of S357 switches to an orientation toward the [4Fe-4S] cluster and the cysteine ligand C355. This may influence the electron density distribution across the cluster (*vi*). Drawn after PDB ID 6NAC. Atomic coloring: Fe, orange; S, yellow; C, gray; O, red; N, blue.

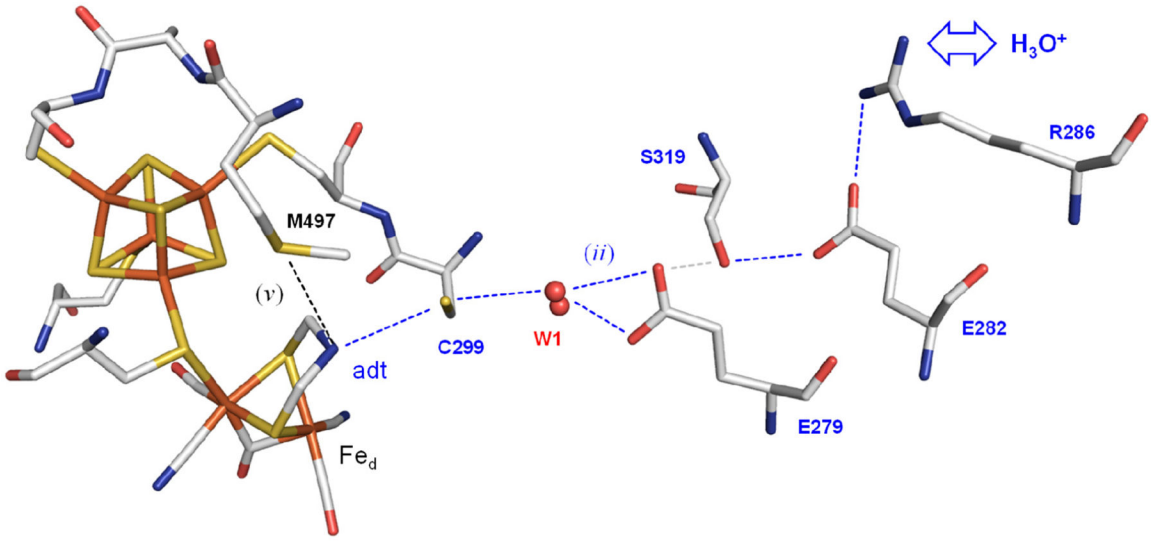

Figure 38.

The “catalytic” proton transfer pathway in [FeFe]-hydrogenase *Cp*I. The side chain of M497 may stabilizes the orientation of the ADT ligand by a hydrogen bond (*v*). Dashed blue lines represent the hydrogen-bonding network (*ii*) of the proton transfer pathway. Note that a bond between E279 and S319 is unlikely in the oxidized state (dashed gray line) but formed upon reduction and protonation of the cofactor. Drawn after PDB ID 4XDC. Atomic coloring: Fe, orange; S, yellow; C, gray; O, red; N, blue.

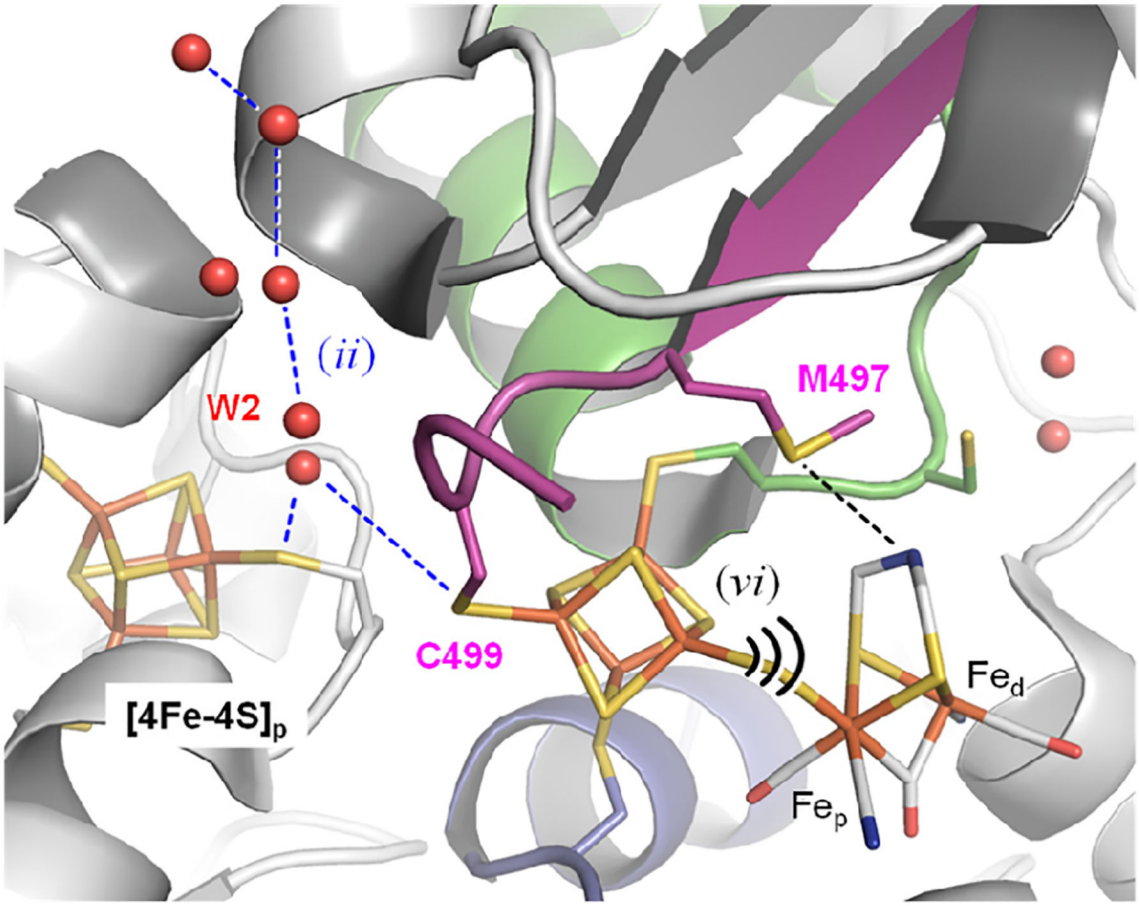

Figure 39.

The “regulatory” proton transfer pathway in [FeFe]-hydrogenase *Cp*I. In most crystal structures of *Cp*I, a trajectory of water molecules (red spheres) can be found, putatively connected by hydrogen bonds (*ii*). This water channel “W2” is located at the intersection of the accessory domain (white) and the catalytic domain (including the most proximal iron–sulfur cluster, $[4Fe\text{-}4S]_p$), leading up to cysteine C499 that coordinates the [4Fe-4S] cluster of the catalytic cofactor. Here, protonation and redox changes influence the diiron site (*vi*). Drawn after PDB ID 4XDC. Atomic coloring: Fe, orange; S, yellow; C, gray; O, red; N, blue.

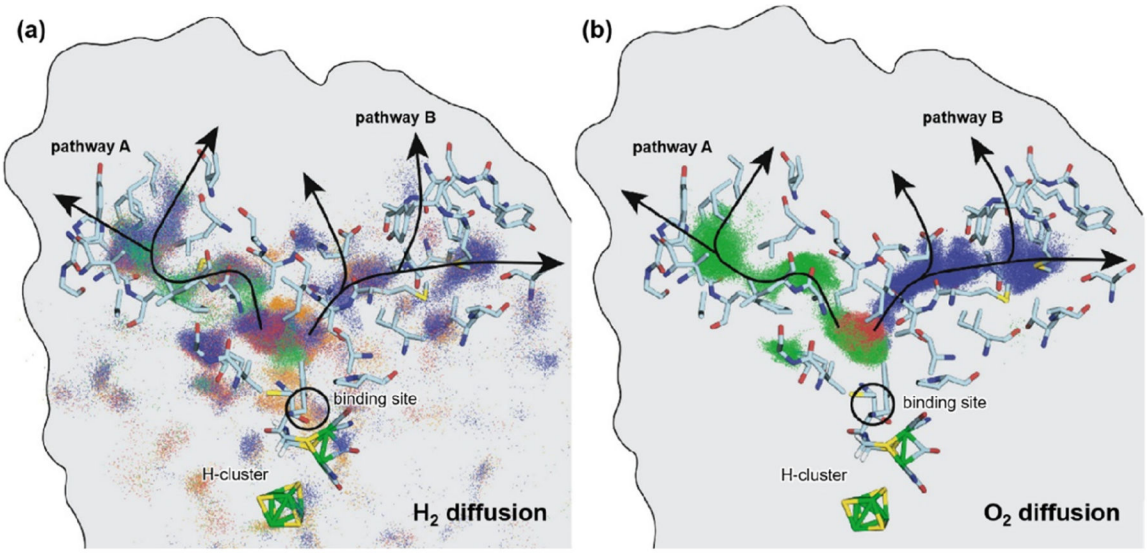

Figure 40.

Gas diffusion pathways in [FeFe]-hydrogenase. Representative simulations of 1000 copies of (a) H_2 diffusing out from the H-cluster and (b) of O_2 diffusing out from the H-cluster or from the middle of a previously identified H_2 channel. Possible exits, based on the proximity of the external solution, are highlighted with arrows. Contrary to H_2 diffusion, the O_2 molecules move collectively through the same pathway for a given simulation, though they may employ different pathways for different independent simulations. Reprinted (adapted or reprinted in part) with permission from ref 569. Copyright 2005 Cell Press.

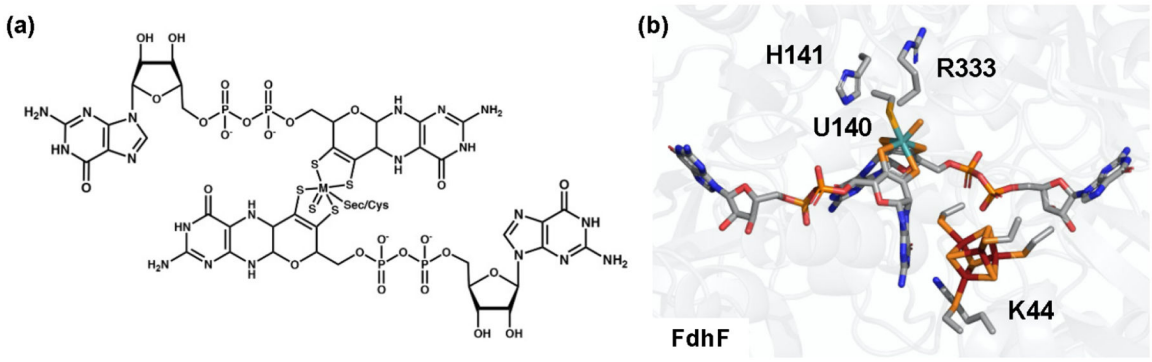

Figure 41.

Bis-metal binding pterin guanine dinucleotide cofactor (bis-MGD) present in formate dehydrogenases. (a) Members of the DMSO reductase family of molybdoenzymes bind the bis-MGD form of the cofactor in the active site. The bis-MGD in formate dehydrogenases coordinates the metal (depicted as M to be Mo or W) by the dithiolene groups from two pterin ligands with the additional ligands being a sulfido group, and a sixth ligand which is either a selenocysteine (Sec) or a cysteine (Cys) from the amino acid backbone. (b) Representative depiction of the bis-MGD cofactor coordination environment in formate dehydrogenases, of *E. coli* FdhF in the oxidized state (PDB ID 1FDO).

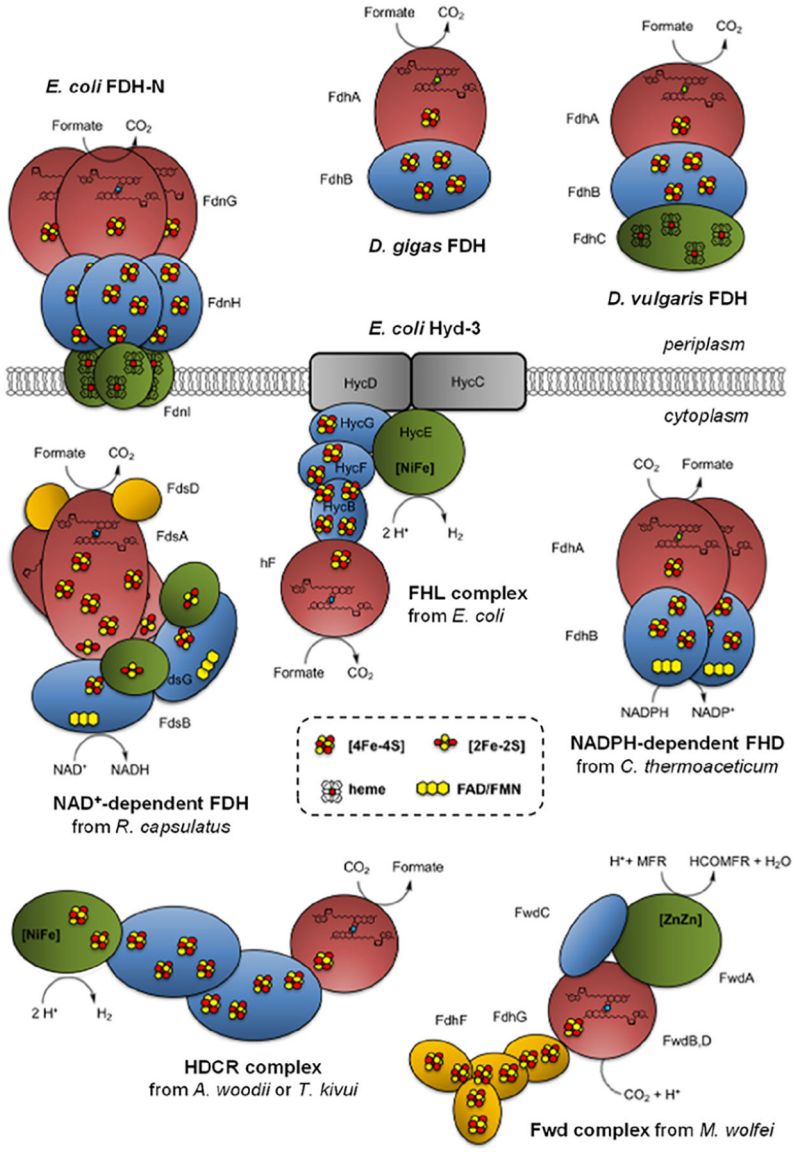

Figure 42.

Schematic overview of cytoplasmic and periplasmic FDHs. Localization of FDHs, their subunit organization and cofactor composition. Shown are the membrane bound respiratory FdnGHI from *E. coli*, the periplasmic FdhAB and FdhABC from the *D. gigas* and *D. vulgaris* Hildenborough, the formate hydrogen-lyase complex formed by (FdhF) and Hyd3 (HycBCDEFG) from *E. coli*, the cytoplasmic FDH from *R. capsulatus*, the cytoplasmic CO_2-reducing dimeric FDH (FdhAB) from the acetogen *Morella thermoacetica*, the HDCR complex from *A. woodii* (Mo-containing) or from *T. kivui* (W-containing), and the formylmethanofuran dehydrogenase complex from *M. wolfei*.

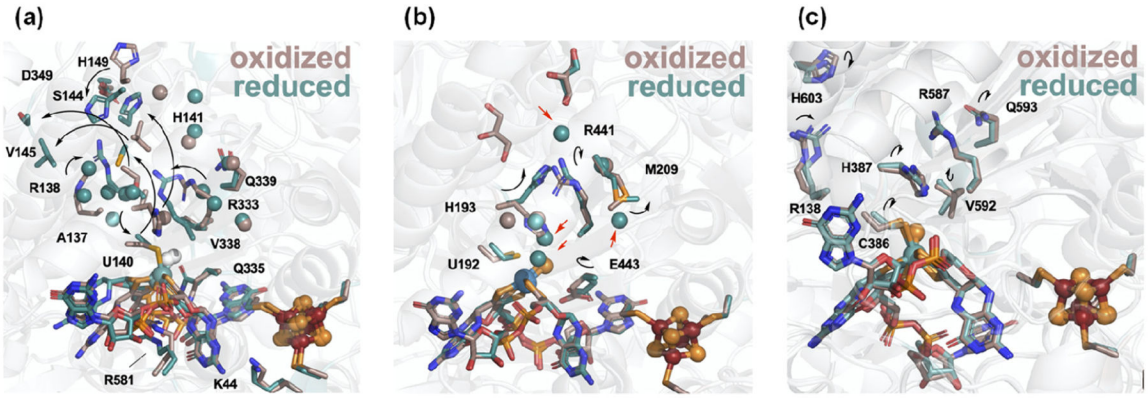

Figure 43.

Structural comparison of FDH undergoing redox change. Structures correspond to (a) *E. coli* FdhF oxidized (PDB ID: 1FDO) and formate-reduced (PDB ID: 2IV2), (b) *D. vulgaris* Hildenborough FDH oxidized (PDB ID: 6SDR) and formate-reduced (PDB ID: 6SDV), and (c) *R. capsulatus* FDH oxidized (PDB ID: 6TGA) and NADH-reduced (PDB ID: 6TG9). Participatory amino acids and bound H_2O and glycerol molecules (where appropriate) in the substrate-binding cleft of FDH are depicted in dark salmon in the oxidized state, and deep teal in the reduced state. The structural effect of specific amino acids accompanying redox changes are depicted with black arrows. The appearance of highlighted H_2O molecules in the reduced state are indicated with red arrows.

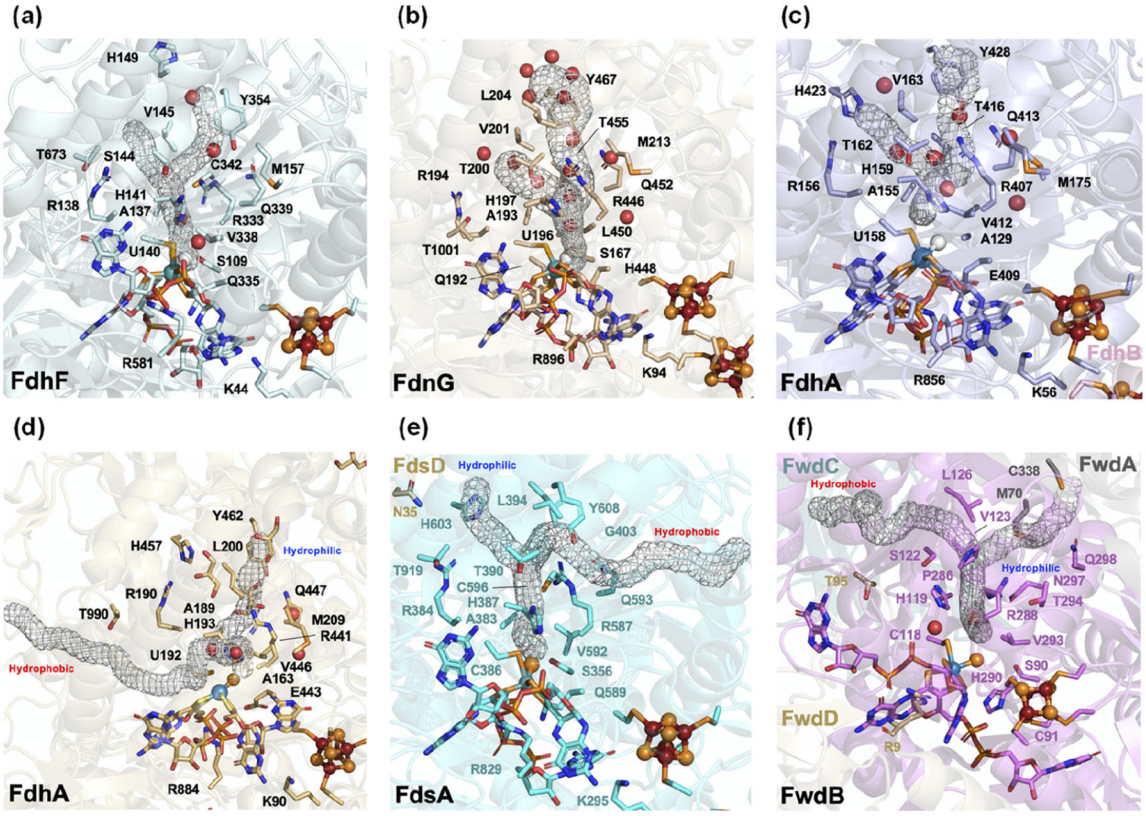

Figure 44.

Structural characterization of the active site of Mo/W–FDHs and formylmethanofuran dehydrogenases. Structures correspond to (a) *E. coli* FdhF (PDB ID 1FDO), (b) *E. coli* FdnG (PDB ID 1KQF), (c) *D. gigas* FdhA (PDB ID 1H0H), (d) *D. vulgaris* Hildenborough FdhA (PDB ID 6SDR), (e) *R. capsulatus* FdsA (PDB ID 6TGA), and (f) *M. wolfeii* formylmethanofuran dehydrogenase FwdABCD (PDB ID 5T5I). Key amino acid residues and bound H_2O molecules are depicted, where appropriate. Predicted substrate and gas channels, are noted for each enzyme; the hydrophobic channel predicted for *D. vulgaris Hildenborough* FDH was predicted from the reduced enzyme (PDB ID 6SDV). Subunits harboring the bis-MGD cofactor are labeled with black text. The hydrophilicity or hydrophobicity of the channel is noted. Channels were constructed via the CAVER plugin in PYMOL.

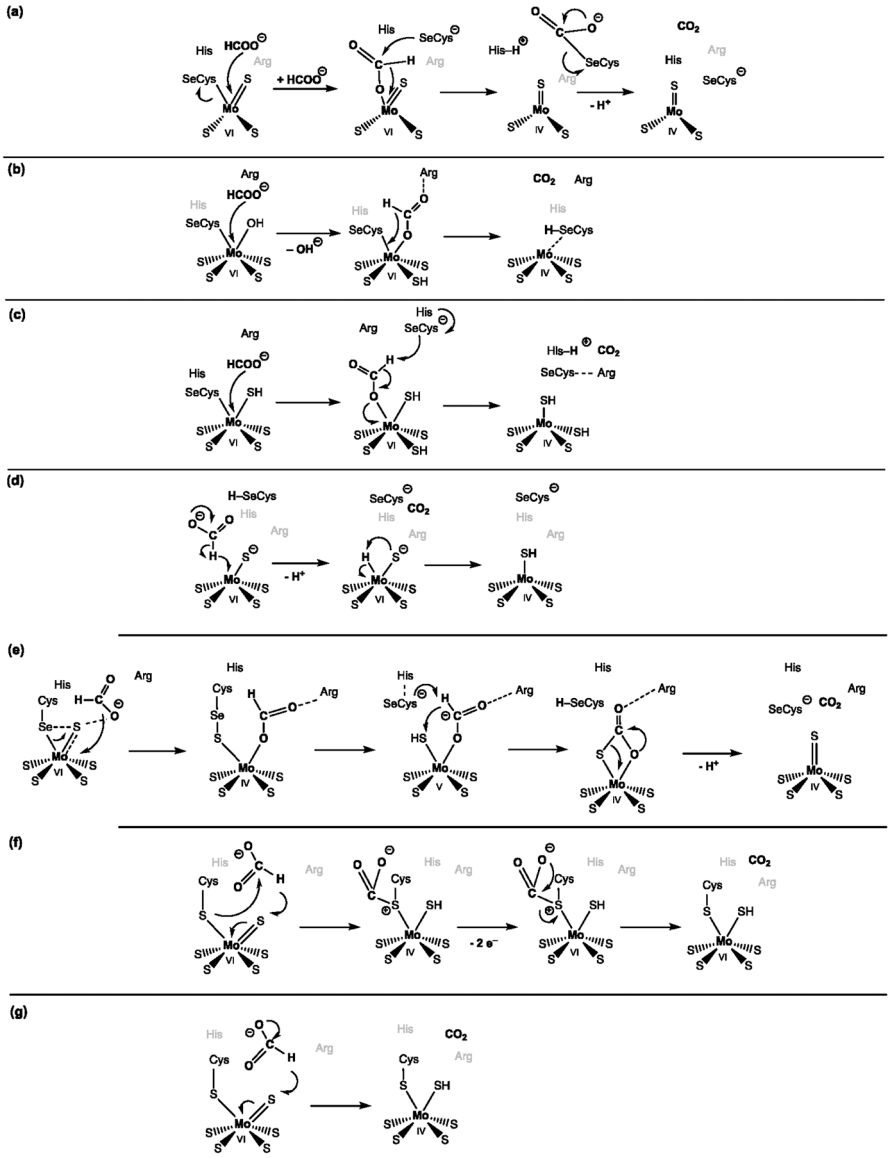

Figure 45.

Proposed reaction mechanisms for formate oxidation by FDH enzymes. (a) Mechanism proposed by Heider and Böck in 1993; (b) mechanism proposed by Sun and co-workers in 1997; (c) mechanism proposed by Raaijmakers and Romao in 2006; (d) mechanism proposed by Cerqueira, Gonzales, Moura, and co-workers in 2011; (e) mechanism proposed by Zampella and co-workers in 2012; (f) mechanism proposed by Dong and Ryde in 2018; (g) mechanism proposed by Hille and co-workers in 2016; details are given in the text. Active site residues without a defined role in an individual mechanism are depicted in gray.

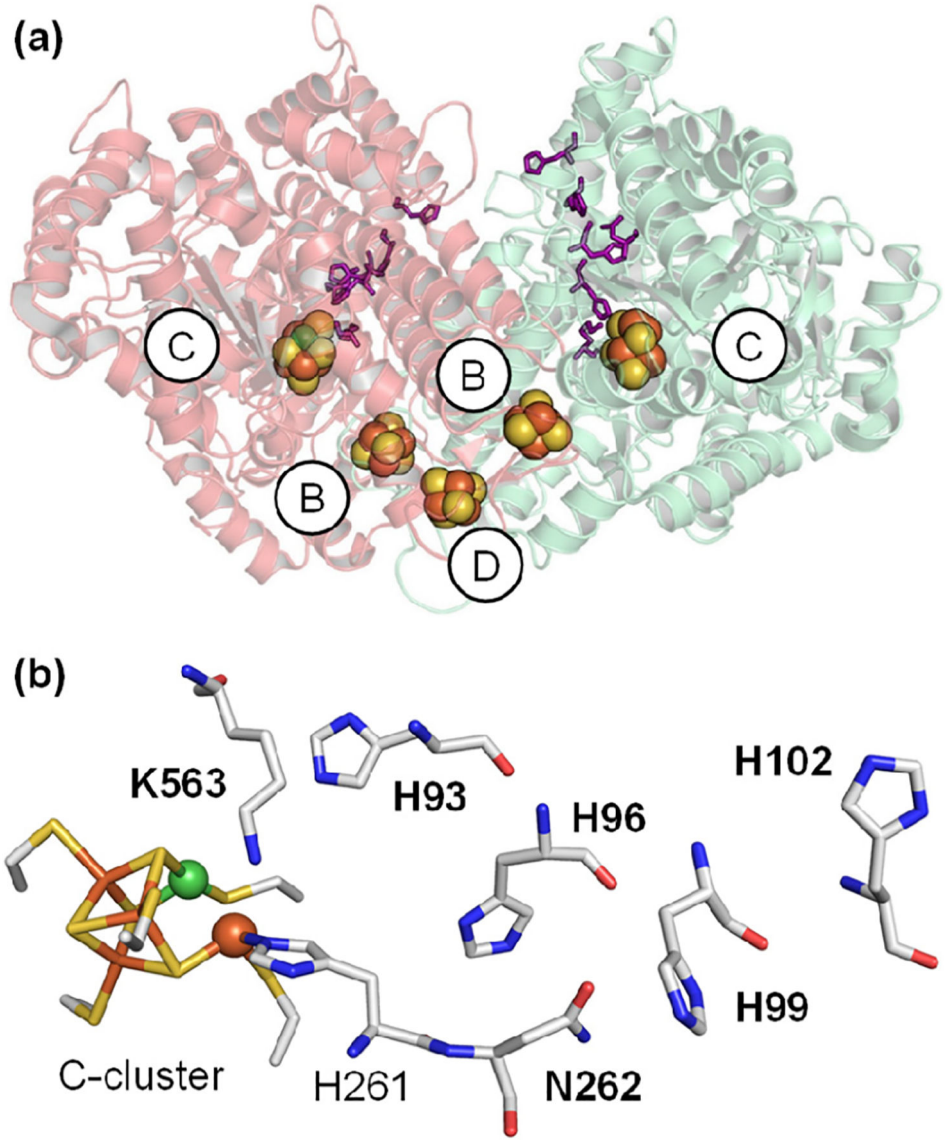

Figure 46.

Structure of CODH. Overall structure of *Ch*CODH II (PDB ID 1SU8). Each monomer of the *Ch*CODH II homodimer is represented with a different color. The spheres represent the inorganic cofactors, labeled cluster B–D. The C-cluster is the catalytic active site cofactor. The purple amino acids correspond to the putative proton transfer pathway. (b) Close up view of the C-cluster and residues putatively involved in proton transfer (PDB ID 3B52). Atomic coloring: Fe, orange; Ni, green; S, yellow; C, gray; O, red; N, blue.

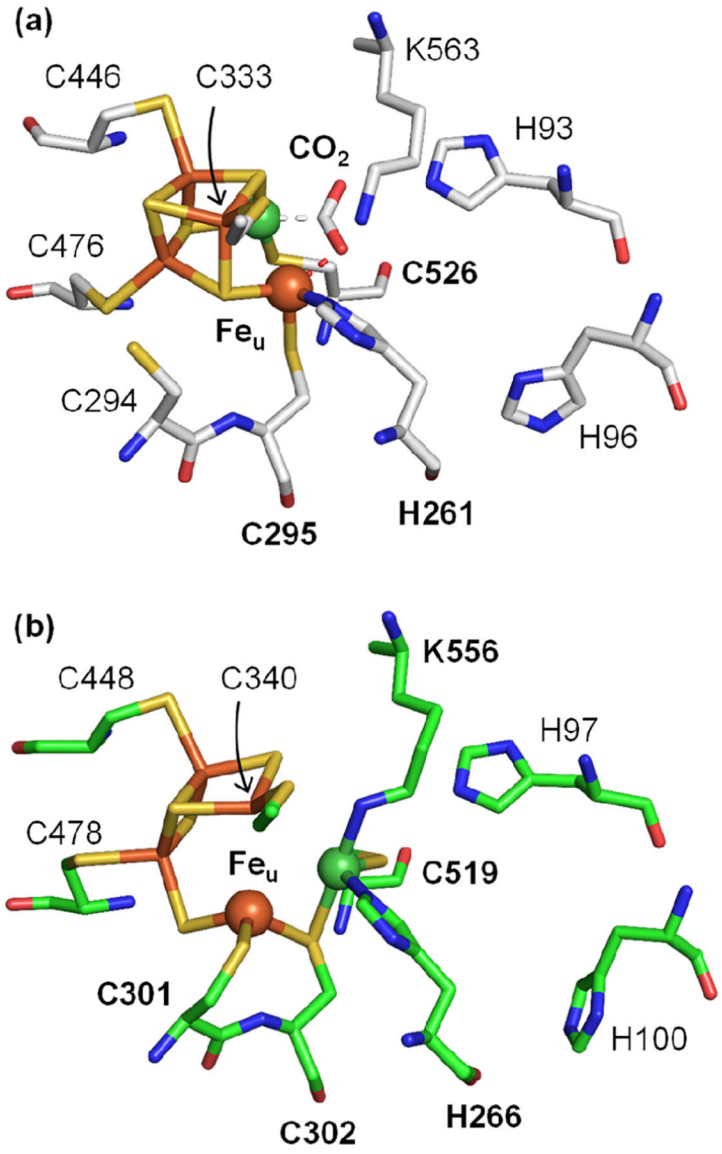

Figure 47.

Structure of the catalytic C-cluster of CODH. (a) Close up view of the CO_2-bound active site (*Ch*CODH II, PDB ID 3B52), with a representation of most of the amino acids discussed here. Fe_u refers to the "dangling" iron ion. (b) View of the active site of *Dv*CODH (PDB ID 6B6W) in the oxidized, protected state (C_{ox}). The orientation is the same as in the left panel. Metal-coordinating residues are bold. Atomic coloring: Ni, green; Fe, orange; S, yellow; C, gray; O, red; N, blue.

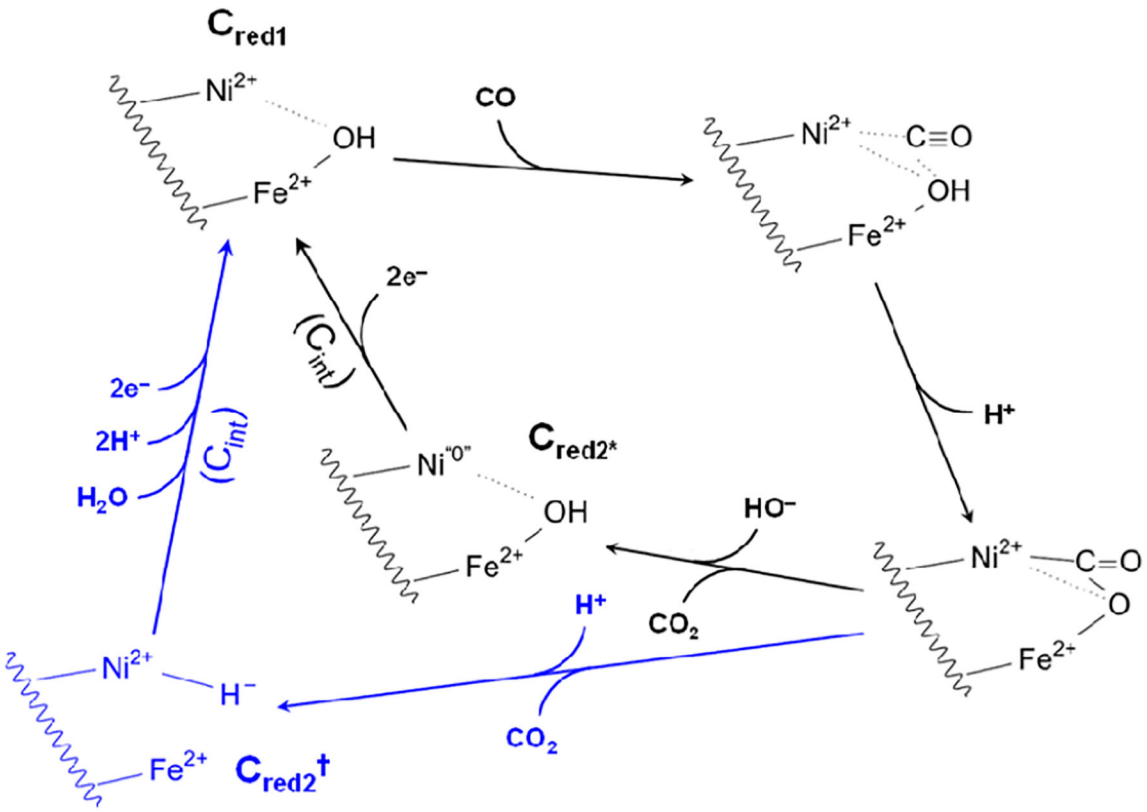

Figure 48.

Proposed mechanisms for the oxidation of CO to CO_2 by CODH. The black scheme is the original proposal by Jeoung and Dobbek.[682,691] The blue part is the modification to that scheme proposed by Fontecilla-Camps, Amara, and co-workers.[692] For the sake of clarity, we have only indicated the arrows in the direction of CO oxidation, but CO_2 reduction is supposed to follow the exact same steps in reverse order.

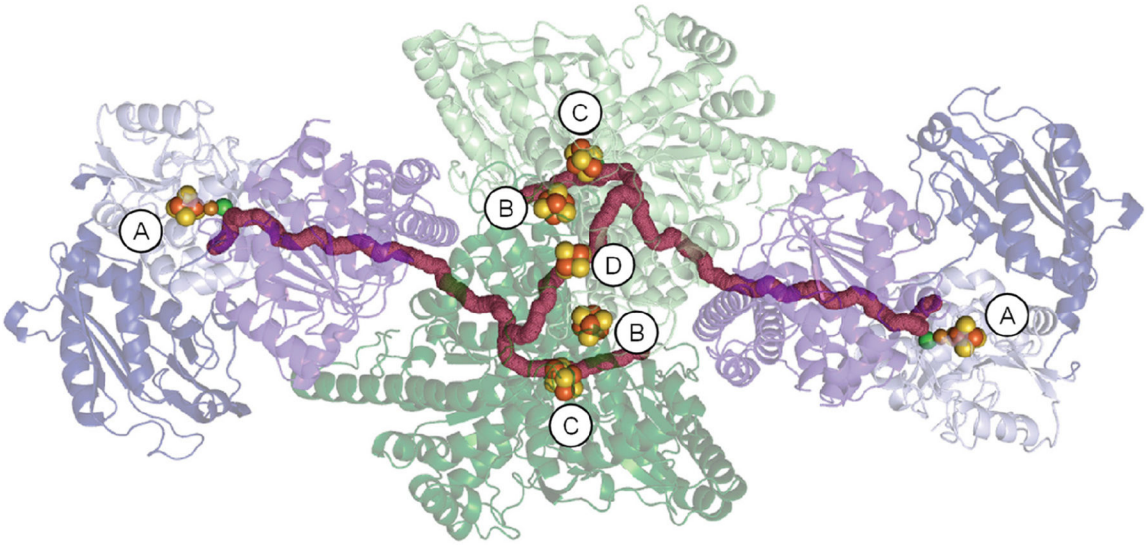

Figure 49.

Hydrophobic gas channels in CODH. Structure of the ACS/CODH from *M. thermoacetica* (PDB ID 2Z8Y), indicating the position of the clusters A–D, and marking the long hydrophobic channel that connects them. Reprinted (adapted or reprinted in part) with permission from ref 702. Copyright 2022 Elsevier.

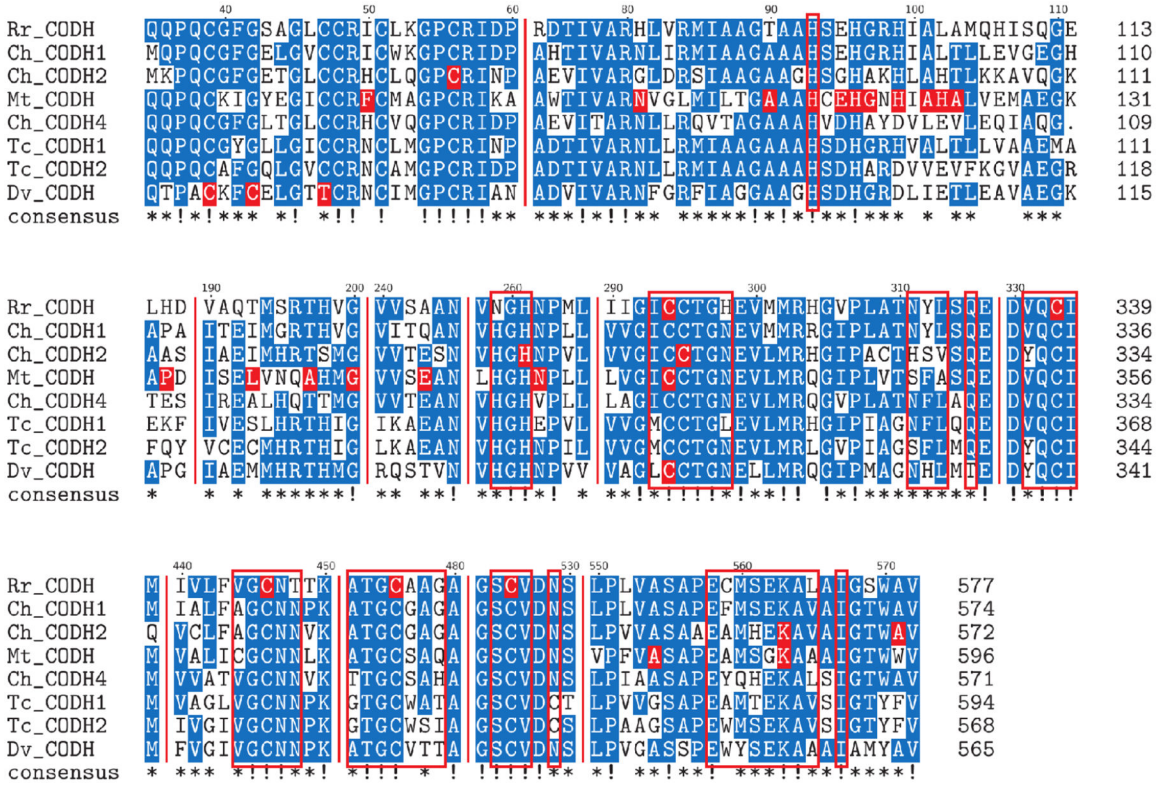

Figure 50.

Sequence alignment of the main CODHs studied so far. Conservation is indicated by a blue background. The amino acids with a red background have been modified by site-directed mutagenesis in the literature. The red frames correspond to the amino acids within 8 Å of any atom from inorganic C-cluster. The numbering is that of *Ch*CODH II.

Table 1.

List of Single Point Mutations Reported for *Azotobacter vinelandii* NifDK with Proximity to the M-Cluster Site[a,b]

NifDK residue	Arg (R)	His (H)	Lys (K)	Asp (D)	Glu (E)	Ser (S)	Thr (T)	Asn (N)	Gln (Q)	Cys (C)	Gly (G)	Pro (p)	Ala (A)	Ile (i)	Leu (L)	Phe (F)	Tyr (Y)	Trp (W)	ref
α-G69						x													174, 175
α-V70											x		x	x					176, 177, 178, 179
α-H83				x				x		x						x	x		152
α-R96		x	x						x				x		x				154, 179, 180, 181
α-Q151					x														169
α-C154						x													169
α-D161					x														169
α-C183						x													169
α-S190											x								174
α-Q191			x		x							x	x						139, 169, 174, 178, 181, 182, 183, 184, 185
α-S192	x			x	x		x	x	x						x			x	174, 186
α-H195							x	x	x		x				x		x		139, 152, 154, 179, 182, 183, 184, 187, 188, 189
α-H196	x			x	x									x	x				152
α-H274									x				x						152, 156, 158
α-C275						x													169
α-R277		x	x				x			x	x	x			x	x			181, 186, 190
α-G356[c]																			186
α-R359			x						x										154, 174, 181
α-H362				x									x						157
α-F381														x	x				154, 174
α-H442								x		x									154
α-W444											x		x			x	x		158
α-H451													x						156, 158

[a] NifD = *α*, NifK = *β*.

[b] NifDK residues listed have been mutated to the marked amino acids.

[c] No specific mutations are listed.

Table 2.

List of *A. vinelandii* NifDK Residues near the M-Cluster That Have Been Investigated through Mutagenesis

NifDK residue	location near M-cluster[a]	coordinate[b]	proposed role(s)
α-G69	outer sphere near S2B	(+, −, +)	Hydrophobic interactions with substrate
α-V70	2nd sphere near S2B	(0, −, +)	Hydrophobic interactions with substrate
α-R96	2nd sphere near S5A	(+,−, 0)	Steric/Hydrogen-bonding interactions with M-cluster, substrates
α-S190	outer sphere near S2B	(0, +, +)	Steric or hydrogen-bonding interactions
α-Q191	2nd sphere near S2B, HC	(+, +,+)	Hydrogen-bonding interactions with *R*-homocitrate ligand ofM-cluster
α-S192	outer sphere near S2B	(−, +, +)	Hydrogen-bonding interactions with conserved H_2O molecules
α-H195	2nd sphere near S2B	(−, 0, +)	Hydrogen-bonding and steric interactions with M-cluster, substrates
α-H196	outer sphere near S2B, Fe1	(−, 0, +)	Unknown
α-H274	outer sphere near Fe1, S4A	(−,−,−)	Assists with M-cluster incorporation, adjacent to α-C275
α-C275	cofactor bound	(−, 0, 0)	Ligates Fe-capped end of M-cluster
α-R277	2nd sphere near S1A	(−, +, +)	Hydrogen-bonding interactions with conserved H_2O molecules
α-G356	2nd sphere near S3A	(+, +, 0)	Hydrogen-bonding interaction with M-cluster
α-R359	2nd sphere near S5A	(0, +, −)	Hydrogen-bonding interaction with M-cluster
α-H362	outer sphere near Fe1	(−, +, −)	Assists with M-cluster incorporation
α-F381	2nd sphere between S2B, S3A	(0, +, +)	Hydrophobic interactions with M-cluster
α-H442	cofactor bound	(+, +, −)	Ligates Mo-capped end of M-cluster
α-W444	outer sphere near S4B	(+,−, −)	Hydrophobic interactions with M-cluster
α-H451	outer sphere near S4A	(−,−,−)	Assists with M-cluster incorporation

[a] Locations are based on proximity to the M-cluster atoms from the crystal structure of the resting state NifDK (PDB ID 3U7Q).[38]

[b] The general location of the amino acid side chain in the coordinate system defined in Figure 7.

Table 3.

Reactivity of Select Purified NifDK Variants[a]

NifDK protein type	NH_3[b] (N_2)	H_2[b] (N_2)	C_2H_4[c] (C_2H_2)	C_2H_6[c] (C_2H_2)	H_2[c] (C_2H_2)	H_2[d] (Ar)	NH_3[e] (N_2/CO)	H_2[e] (N_2/CO)	C_2H_4[f] (C_2H_2/CO)	C_2H_6[f] (C_2H_2/CO)	H_2[f] (C_2H_2/CO)	H_2[g] (Ar/CO)	ref
Av wild-type	860	615	1706	0	276	2494	0	2727	1134	0	959	2841	185
α-V70A	800					1800							176
α-V70I	170	1940	130	0	2000	2340							177
α-R96K	373		804			972							154
α-Q191K	0	514	40	7.2	528	540	0	182	14	2.3	340	254	185
α-H195Q	-	-	1350	0	1115	2860							183
α-H195N	-	-	535	135	355	1470							183
α-R277C						1400						2400[h]	186
α-R359K	709		1523			1587							154
α-F381L	816		1656			1844							154
Av Wild-type	989	555	2096			2211							158
α-W444Y	1036	507	2066			2069							158
α-W444F	906	505	1906			1795							158
α-W444A	212	101	364			410							158
α-W444G	0	6	8			11							158
Av Δ*nifV*						840							181
Kp Wild-type	725	471	1127	-	-	1527							196
Kp ΔnifV	318	842	1044	-	-	1242							196
Kp ΔnifV	-	812	-		202	1369	-	574	-	-	585	718	197

[a] Specific activity is reported with units of nmol product × min^{-1} × (mg protein)$^{-1}$. Gas in parentheses reflects the substrate conditions used for the assay.

[b] Assays are reported in an atmosphere of 100% N_2.

[c] Assays reported in an atmosphere of 10% C_2H_2, 90% Ar.

[d] Assays reported in an atmosphere of 100% Ar.

[e] Assays are reported in an atmosphere of 3% CO, 97% N_2.

[f] Assays are reported in an atmosphere of 3% CO, 10% C_2H_2, 87% Ar.

[g] Assays are reported in an atmosphere of 3% CO, 97% Ar.

[h] Assays are reported in an atmosphere of 10% CO, 90% Ar.

Table 4.

Conservation of Amino Acid Residues in the H-Domain of Experimentally Characterized [FeFe]-Hydrogenases[a]

	C*p*I	**C*p*II**	**C*p*III**	**C*a*I**	***Dd*H**	***Me*HydA**	**C*b*A5H**	***Cr*HydA1**	***Cr*HydA2**	***Tm*HydA**	***Tm*HydS**	***Tam*HydS**
HB	S232	S101	A162	S231	A109	A113	A294	A94	A97	A227	S79	S81
PT	E279	E148	E202	E278	E156	E151	E341	E141	E144	E274	E118	F119
PT	E282	E151	E205	E281	E159	E154	E344	E144	E147	E277	E121	E122
PT	R286	R155	R209	R285	R163	R158	R348	R148	R151	R281	G125	K126
PT	C299	C169	*C*222	C298	C178	C171	C367	C169	C172	C294	A131	A137
CC	C300	C170	C223	C299	C179	C172	C368	C179	C173	C295	C132	C138
PT	S319	S189	S242	S318	S189	S192	S387	S189	S192	S314	A151	L157
HP/HB	M353	T223	G268	M352	M232	T227	M421	M223	M226	M348	G177	S191
CC	C355	C225	C270	C354	C234	C229	C423	C225	C228	C350	C179	C193
HB	S357	A227	A272	D356	A236	A231	A425	R227	R230	A352	A181	A195
HB	K358	K228	K273	K357	K237	K232	K426	K228	K231	K353	K182	K196
HB	M497	M367	M381	M497	M376	M381	M565	M415	M426	M480	S267	L291
CC	C499	C369	C383	C498	C378	C391	C567	C417	C428	C482	C269	C293
CC	C503	C382	C387	C502	C382	C395	C571	C421	C432	C486	C273	C297
PDB IDs	6N59	-	-	-	1FEH	-	6TTL	3LX4	-	-	-	-

[a]Representative PDB accession codes for *Cp*I, *Dd*H, *Cb*A5H, and the apoprotein of *Cr*HydA1 are given in the last row. Legend: HB, hydrogen bonding; HP, hydrophobic; PT, proton transfer; CC, cluster coordination.

Table 5.

List of [FeFe]-Hydrogenase Amino Acid and H-Cluster Variants[a]

	variant	PDB ID	target	ref
***Cp*I**	G412H, G414A/H, G418A/H, G421H, G422H, K358N, R449A/H	N/A	Maturation	445
	E279A	5LA3	Proton transfer, formation of H_{hyd}	446
	C299A	6GLY	Proton transfer	447, 448, 449
	C299D	6GLZ		
	C299S	N/A		
	E279A	N/A		
	E279D	6YF4		
	E279Q	6GM0		
	E282A	6GM1		
	E282D	6GM2		
	E282Q	6GM8		
	R286A/L	6GM3		
	S319A	6GM4		
	C299S, M353L, K358N, M497L	N/A	Hydrogen bonding	450
	S31P, E47G, R86H, C153Y, N160D, D186G, T188A, I197V, K208E, K252R, I253V, A280V, N289D	N/A	Hydrogen turnover, O_2 sensitivity	451
	L192G, G194C, N189C, T356C/T/V, S357C/G/P/T, M397C, A498C	N/A	Hydrogen turnover, O_2 sensitivity	452
	M70L, M211L, M243L, M277L, M387L, M481L, M485L, M551L	N/A	O_2 sensitivity	453
	C48A, C100A, C298D	N/A	Proton transfer, electron transfer	417, 454, 455
***Cr*HydA1**	C169A/S	N/A	Proton transfer, formation of H_{hyd}	456, 457, 458, 459
	C169A/D/S	N/A	Proton transfer	448
	E141A	6GM5		
	E141D	N/A		
	E141Q	6GM6		
	E144A	6GM7		
	E144D/Q	N/A		
	R148A	N/A		
	S189A	N/A		

	variant	PDB ID	target	ref
	C417H[b]	6GL6	[4Fe-4S]	460
	C170A/D/S, C225A/D/S, C417A/D/S, C421A/D/S[b]	N/A	[4Fe-4S]	461
	T226K/V	N/A	[4Fe-4S]	462
	R171D/W[c]	N/A	Electron transfer	463
	A92S, A94S, S193C, E231D	N/A	Hydrogen bonding to CN^-	464
	C169S, M223L, K228N, M415L	N/A	Hydrogen bonding	450
	C169D, F290Y, V296F	N/A	O_2 diffusion	465
	R96Q K179Q K262Q R349Q R353Q R379Q K396Q K397E, K433Q	N/A	Interaction with ferredoxin	466
Other	L364F, C367D/A, P386L, A561F (in *Cb*A5H)	N/A	O_2 inhibition, formation of H_{inact}	424
	C48A, C100A, C298D (in *Ca*I)	N/A	Proton transfer and electron transfer	417, 454, 455
	V229T (in *Cr*HydA2)	N/A	$[4Fe]_H$	467 [c]
Cofactor Variants	PDT, ODT, SDT, and other headgroups	N/A	Maturation, hydrogen turnover	418, 468, 469, 470, 471, 472, 473, 474
	Other modifications	N/A	Hydrogen turnover	475, 476, 477, 478, 479
	ODT	5BYQ	Hydrogen turnover, hydrogen bonding	479, 480
	PDT	5BYR		
	SDT	5BYS		
	EDT	6H63		

[a] The majority of amino acid variants were produced for *Cp*I and *Cr*HydA1, with most H-cluster variants being produced for *Cr*HydA1. Other enzymes include *Ca*I, *Cb*A5H, and *Cr*HydA2.

[b] In refs 460 and 461, the numbering is different due to the deletion of 55 *C*-terminal amino acids.

[c] In ref 463, arginine R171 resembles R227 following the nomenclature used for *Cr*HydA1 in this work.

Table 6.

Vibrational and Electronic Properties of the Main H-Cluster States[a]

	νCN$^-$/cm^{-1}		νCO/cm^{-1}			[4Fe-4S]	[FeFe]	μ/t
H$_{ox}$	2088	2070	1964	1940	1802	+2	II/I	CO/−
H$_{ox}$H	2092	2074	1970	1946	1812	+2	II/I	CO/−
H$_{ox}$-CO	2091	2081	1968	1962[c]	1808	+2	II/I	CO/CN$^-$
H$_{ox}$H–CO	2094	2086	1972	1966[c]	1816	+2	II/I	CO/CN$^-$
H$_{red'}$	2084	2066	1962	1933	1792	+ 1	II/I	CO/−
H$_{red'}$H	2086	2068	1966	1938	1800	+1	II/I	CO/−
H$_{red'}$-CO	2086	2076	1967	1951[c]	1793	+1	II/I	CO/CN$^-$
H$_{red}$	2070	2033	1961	1915	1891	+2	I/I	H/CO[b]
H$_{hyd}$	2088	2076	1980	1960	1860	+1	II/II	CO/H$^-$
H$_{sred}$	2068	2026	1953	1918	1882	+1	I/I	H/CO[b]
H$_{inact}$	2106	2087	2007	1983	1848	+2	II/II	CO/?
H$_{trans}$	2100	2075	1983	1977	1836	+1	II/II	CO/?

[a] All data stem from *Dd*H (H$_{inact}$ and H$_{trans}$) or *Cr*HydA1 (other H-cluster states).

[b] Under cryogenic conditions, H$_{red}$H+ and H$_{sred}$H+ are formed that bind a bridging carbonyl ligand and are likely to feature an open coordination site (μ/t = CO/−).

[c] In the CO-inhibited states, the coupled pCO/dCO stretching vibration gives rise to an additional band at 2012 cm^{-1} (H$_{ox}$-CO), 2006 cm^{-1} (H$_{ox}$H–CO), or 2002 cm^{-1} (H$_{red'}$-CO).

Table 7.

Oxidation Kinetic Parameters of Structurally Characterized FDH and Formylmethanofuran Dehydrogenase Enzymes[a]

organism/type	*E. coli* FdhF	*E. coli* FdnGHI	*D.gigas* FdhAB	*D. vulgaris* Hildenborough FdhAB	*R. capsulatus* FdsGBAD	*M. wolfeii* formylmethanofuran dehydrogenase
catalytic subunit	FdhF	FdnG	FdhA	FdhA	FdsA	FwdB
metal	Mo	Mo	W	W	Mo	W
PDB ID	1FDO, 2IV2	1KQF	1H0H	6SDR, 6SDV	6TGA, 6TG9	5T5I
formate oxidation kinetic parameters	k_{cat} = 2800 s^{-1}	N/A	k_{cat} = 138 s^{-1}	k_{cat} = 3684 s^{-1}	k_{cat} = 36 s^{-1}	k_{cat} = 18 s^{-1}
	K_M = 26 mM			K_M = 1 μM	K_M = 281 μM	K_M = 13 μM
	K_d = 100 mM				$K_{M\ NAD+}$ = 173 μM	$K_{M\ MV}$ = 400 μM
	$K_{M\ BV}$ = 3 mM					
ref	594		590	595	596	597

[a]Reported formate oxidation kinetic parameters for *E. coli, D. gigas*, and *D. vulgaris* Hildenborough FDH represent those following the enzymatic reduction of benzyl viologen; formylmethanofuran dehydrogenase follows the enzymatic reduction of methyl viologen, while for *R. capsulatus* FDH the enzymatic reduction of NAD^+ is reported.

Table 8.

Amino Acid Comparison and Oxidation Kinetic Parameters of Active Site Variants of Structurally Characterized FDH and Formylmethanofuran Dehydrogenase Enzymes[a]

organism/ type	*E. coli* FdhF	*E. coli* FdnGHI	*D. gigas* FdhAB	*D. vulgaris* Hildenborough FdhAB	*R capsulatus* FdsGBAD	*M. wolfeii* formylmethanofuran dehydrogenase	Function	Formate Oxidation Kinetic Parameters	ref
conserved amino acids	U140	U196	U158	U192	C386	C118	substrate binding, catalytic efficiency	*E. coli* (FdhF) U140C: k_{cat} = 9 s^{-1}, K_M = 9 mM, K_D = 5 mM, $K_{M\ BV}$ = 2 mM	585
	H141	H197	H159	H193	H387	H119	proton shuttling, channel gating	*R capsulatus* H387M: k_{cat} = 34 s^{-1}, K_M = 3.6 mM *R capsulatus* H387K: k_{cat} = 1 s^{-1}, K_M = 28 mM	598
	R333	R446	R407	R441	R587	R288	substrate binding, channel gating	*R capsulatus* R587K: k_{cat} = 11 s^{-1}, K_M = 362 mM	598
	M157	M213	M175	M209	G403	I133	hydrophobic channel direction	N/A	
	V338	L450	V412	V446	V592	V293	hydrophobic interaction at bis-MGD	N/A	
	K44	K94	K56	K90	K295	I37	electron transfer to Fe–S relay	N/A	
	Q335	H448	E409	E443	Q589	H290	gating proton shuttling	N/A	
	V145	V201	V198	V197	G391	V123	hydrophobic interaction with active site Arg	N/A	
	Q339	Q452	Q413	Q447	Q593	N297	hydrophobic interaction with active site Arg	N/A	

[a]Amino acid residues in the primary or secondary coordination sphere by which a role has been assigned or postulated are noted. Enzymatic activity of reported active site variants for respective organisms follow the same electron acceptor used as reported for the WT enzyme, as reported in Table 7.